UNIVERSIDADE FEDERAL DE SANTA CATARINA
CAMPUS UNIVERSITÁRIO REITOR JOÃO DAVID FERREIRA LIMA
DEPARTAMENTO EM ENGENHARIA MECÂNICA
PROGRAMA DE PÓS-GRADUAÇÃO EM CIÊNCIA E ENGENHARIA DE MATERIAIS

Nicolás Ignacio Araya Rivera

EFFECT OF THE CHARACTERISTICS OF PORES AND SOLID LUBRICANT ON THE TRIBOLOGICAL BEHAVIOUR OF SINTERED STEEL IMPREGNATED WITH GRAPHITE

FLORIANÓPOLIS
2020

Nicolás Ignacio Araya Rivera

EFFECT OF THE CHARACTERISTICS OF PORES AND SOLID LUBRICANT ON THE TRIBOLOGICAL BEHAVIOUR OF SINTERED STEEL IMPREGNATED WITH GRAPHITE

Tese de Doutorado apresentada ao Programa de Pós-Graduação em Ciência e Engenharia de Materiais da Universidade Federal de Santa Catarina, como requisito parcial para a obtenção de título de Doutor em Ciência e Engenharia de Materiais.
Orientador: Prof. Dr. José Daniel Biasoli de Mello
Coorientador: Prof. Dr. Claudio Aguilar Ramirez

FLORIANÓPOLIS
2020

Ficha de identificação da obra elaborada pelo autor,
através do Programa de Geração Automática da Biblioteca Universitária da UFSC.

Rivera, Nicolás Ignacio Araya
EFFECT OF THE CHARACTERISTICS OF PORES AND SOLID LUBRICANT ON THE TRIBOLOGICAL BEHAVIOUR OF SINTERED STEEL IMPREGNATED WITH GRAPHITE / Nicolás Ignacio Araya Rivera ; orientador, José Daniel Biasoli de Mello, coorientador, Cláudio Aguilar, 2020.
187 p.

Tese (doutorado) - Universidade Federal de Santa Catarina, Centro Tecnológico, Programa de Pós-Graduação em Ciência e Engenharia de Materiais, Florianópolis, 2020.

Inclui referências.

1. Ciência e Engenharia de Materiais. 2. Interação lubrificante sólido/poros. 3. Impregnação à vácuo. 4. Tribología. 5. Aço poroso. I. de Mello, José Daniel Biasoli . II. Aguilar, Cláudio. III. Universidade Federal de Santa Catarina. Programa de Pós-Graduação em Ciência e Engenharia de Materiais. IV. Título.

Nicolás Ignacio Araya Rivera

EFFECT OF THE CHARACTERISTICS OF PORES AND SOLID LUBRICANT ON THE TRIBOLOGICAL BEHAVIOUR OF SINTERED STEEL IMPREGNATED WITH GRAPHITE

O presente trabalho em nível de doutorado foi avaliado e aprovado por banca examinadora composta pelos seguintes membros:

Prof. Cristiano Binder, Dr.
Universidade Federal de Santa Catarina

Rafael Arenhart, Dr.
Universidade Federal de Santa Catarina

Prof. Antonio Eduardo Martinelli, Dr.
Universidade Federal do Rio Grande do Norte

Certificamos que esta é a **versão original e final** do trabalho de conclusão que foi julgado adequado para obtenção do título de doutor em ciência e engenharia dos materiais.

Assinado de forma digital por Guilherme Mariz de Oliveira Barra:17871842854
Dados: 2020.02.20 11:12:02 -03'00'

Prof. Guilherme Mariz de Oliveira Barra Dr.
Coordenador do Programa

Documento assinado digitalmente
Jose Daniel Biasoli de Mello
Data: 20/02/2020 11:01:21-0300
CPF: 159.964.176-34

Prof. José Daniel Biasoli de Mello, Dr.
Orientador

Florianópolis, 2020

This work is dedicated to my wife Paula and to my daughter Violeta.

AGRADECIMENTOS

Ao professor Dr. Claudio Aguilar por me motivar para fazer a minha pós-graduação numa instituição de excelência e por ser um grande amigo.

Ao professor Dr. José Daniel Biasoli de Mello pela paciência e orientação ao longo do meu doutorado. Não só um excelente professor, mas também uma excelente pessoa.

Ao professor Dr. Aloisio Nelmo Klein pela maravilhosa acolhida e apoio desde a minha primeira visita no LABMAT no ano 2012.

Ao professor Dr. Cristiano Binder pelo constante apoio e preocupação desde o meu ingresso ao LABMAT, sempre disposto a brindar excelentes conselhos e sugestões.

A minha esposa Paula Aranda pela paciência e apoio durante esta fase

Ao Rogério Antônio Campos pela eficiência com a qual desempenha seu trabalho frente a secretaria do PGMAT/UFSC. Pela simpatia e disposição em sempre auxiliar os alunos.

Aos companheiros do LabMat pelo bom convívio, motivação e ajuda dispensada durante este período. Especialmente aos meus colegas e amigos (sem ordem particular) Guilherme, Isadora, Renan, Priscila, Tercius, Ricardo, Antonio, Daiany, Thiago e Gustavo.

Aos bolsistas Gustavo, Daniel, Thiago e especialmente Letycia pela sua qualidade profissional e ajuda em momentos críticos do desenvolvimento do presente trabalho.

Ao BNDES, a Embraco, e ao CNPQ e CAPES pelo financiamento da pesquisa.

E a todos aqueles que contribuíram, de maneira direta ou indireta, para o êxito na conclusão do meu doutorado.

"Where there is a tree to be planted, you plant it. Where there is an error to be corrected, correct it. There is always an effort that everybody dodges, you do it. You be the one that moves the rock away of the road". *Gabriela Mistral*, 1945.

RESUMO

A maioria dos compósitos autolubrificantes produzidos por metalurgia do pó apresentam interações metalúrgicas entre a fase lubrificante e a matriz durante o processo de síntese o que não permite isolar o efeito das características individuais destas fases no desempenho tribológico. Poucos autores têm utilizado a técnica de impregnação a vácuo de lubrificantes sólidos para promover lubricidades a seco em materiais porosos, de maneira de isolar as propriedades do lubrificante das propriedades da matriz. Dentre esses autores nenhum abordou como a interação entre os poros e o lubrificante impregnado governa o desempenho tribológico do compósito. Por esses motivos, o presente trabalho trata do estudo da interação entre o lubrificante sólido e os poros durante ensaios tribológicos e a influência desta interação no desempenho tribologico. O objetivo principal do presente trabalho foi entender como as características do lubrificante sólido e da matriz afetam separadamente o desempenho tribológico de aços porosos impregnados com grafite. Para abordar este problema, no presente trabalho foi desenvolvida uma técnica de impregnação a vácuo para impregnar, com grafite, aços porosos produzidos por metalurgia do pó. As principais variáveis estudadas foram a pressão de compactação e temperatura de sinterização para o aço poroso e o tamanho de partícula e estrutura cristalina para o grafite. Para estudar o efeito da estrutura cristalina foi utilizado grafite derivado da reação Cr_3C_2-B_4C que é um novo lubrificante sólido desenvolvido pelo Laboratório de Materiais da Universidade Federal de Santa Catarina (LABMAT). Ensaios de durabilidade e desgaste foram utilizados para realizar a caracterização tribológica, as pistas de desgaste foram analisadas por microscopia eletrônica de varredura, análise de imagem e micro-espectroscopia Raman. Os resultados mostram que o desempenho tribológico dos aços porosos impregnados com grafite dependem da capacidade do grafite ser gradativamente liberado dos poros durante os ensaios e das propriedades mecânicas do material, existindo um balanço entre a quantidade de lubrificante disponível e a resistência mecânica da matriz, ambos dependentes da porosidade. Os resultados também indicam que a degradação da tribocamada de grafite ocorre pelo aumento na densidade de defeitos e a transformação de carbono sp^2 para sp^3.

Palavras-chave: Interação lubrificante sólido/poros, Impregnação à vácuo, Grafite, Aço poroso, Tribologia, Carbono derivado de carbetos.

RESUMO EXPANDIDO

Introdução

O aumento do consumo energético a nível mundial em função do tempo junto com o incremento nas emissões de CO2 advindos desse consumo energético demanda soluções ao curto e mediano prazo enfocadas à utilização de fontes de energia não contaminantes e à redução do consumo de energia através do aumento na eficiência energética. Nesse último ponto, é projetado que a aplicação de tecnologias para a redução do atrito e o desgaste poderia diminuir o consumo de energia num 38% porcento no longo prazo. É por esse motivo que a pesquisa tribológica se torna extremadamente importante para o desenvolvimento da sociedade. Dentre as formas de reduzir o atrito e o desgaste, a lubrificação sólida é promissória em situações onde a lubrificação hidrodinâmica (ou fluida em geral) não pode ser utilizada (como em condições de temperaturas extremas ou altas pressões). Dentre as formas de aplicação de lubrificação sólida, a produção de materiais compósitos metal-lubrificante sólido produzidos por metalurgia do pó têm trazido o interesse dos pesquisadores devido ao fato de que a dispersão da fase lubrificante no volume do material permite a autorregeneração da camada lubrificante durante o fenômeno tribológico porém, nesses materiais, suas propriedades são grandemente afetadas pelas interações e transformações de fases ocorridas durante o processo de sinterização o que não permite isolar o efeito das propriedades individuais do metal e do lubrificante no desempenho tribológico do compósito. Já a técnica de impregnação de materiais porosos com lubrificante sólido permite obter materiais donde as propriedades do lubrificante são completamente independentes das propriedades da matriz o que permite avaliar o efeito delas no comportamento tribológico do sistema. Para avaliar esses efeitos, no presente trabalho foram impregnadas amostras de aço sinterizado de porosidade variável com grafite de tamanho de partícula variável e CDC produzido pela reação entre B_4C e Cr_3C_2 para avaliar o efeito da estrutura cristalina no desempenho tribológico do material.

Objetivos

O Objetivo Geral do presente trabalho foi estudar a interação entre os poros e o grafite impregnado em aço sinterizado e como essa interação influencia o comportamento tribológico do aço impregnado. Os objetivos específicos foram:

- ✓ Produzir amostras de aço sinterizado cuja fase metálica tem homogeneidade microestrutural e cujos poros variam em tamanho, forma e quantidade.
- ✓ Desenvolver um método para impregnar lubrificante sólido nos poros de aço poroso produzido surgida por metalurgia em pó.
- ✓ Desenvolver uma metodologia de análise de imagem que permita obter informações sobre a distribuição de carbono nos poros das faixas de desgaste a partir de imagens obtidas pela SEM e EDS
- ✓ Estudar a relação entre o tamanho, a forma e o número de poros no fornecimento de lubrificante sólido durante o teste tribológico.
- ✓ Estudar a influência da razão de tamanho entre partículas de lubrificante sólido e poros na impregnação e o comportamento tribológico do aço sinterizado.
- ✓ Analisar a influência da estrutura cristalina do CDC derivado da reação entre B_4C e Cr_3C_2 no comportamento tribológico do sistema que está sendo estudado.

Metodologia

Primeiro foi determinado um sistema tribológico idealizado no sentido em que as propriedades do sistema que influenciam o fenômeno tribológico eram conhecidas ou controladas e no qual ao mesmo tempo não existissem interações físico-químicas entre a fase de lubrificante sólido e

a matriz que pudessem influenciar as propriedades mecânicas dos corpos de prova. O material escolhido foi aço sinterizado poroso impregnado com grafite. Misturas de pós de Astaloy CRL + 0,6% em massa de carbono foram preparadas, compactadas a 200, 400 e 600 MPa e sinterizadas durante 1 hora a 1100, 1150 e 1200°C para obter matérias com diferentes porosidades. As amostras sinterizadas foram caracterizadas pelas técnicas de microdureza Vickers, análise de imagem, densidade volumétrica e análise metalográfico.

Uma vez obtidas as provetas, foi desenvolvido um processo de impregnação a vácuo para obter amostras de aço impregnado com grafite de D50 = a 1,10, 6,07 e 21,54 μm e com CDC derivado da reação entre B_4C e Cr_3C_2. As amostras impregnadas foram caracterizadas através de microscopia eletrônica de varredura (MEV) e ensaios tribológicos de durabilidade para avaliar o preenchimento dos poros e a lubricidade induzida pela técnica. Os ensaios de durabilidade foram realizados numa configuração de esfera (AISI 52100, 10 mm de diâmetro) sobre plano, deslizamento alternado com uma frequência de 2 Hz e percurso de 10 mm, com incrementos de carga de 7 N a cada 10 minutos.

Uma vez impregnadas as amostras, foi avaliado o efeito do tamanho de partícula no desempenho tribológico do aço impregnado através de ensaios de durabilidade e de desgaste usando a mesma configuração tribológica, porém mantendo uma carga constante de 14 N durante uma hora. Nesta etapa as pistas de desgaste foram analisadas via MEV e microscopia Raman usando um laser de λ = 514.5 nm na faixa de 300-3200 cm^{-1}. O volume das marcas de desgaste foi calculado usando a técnica de interferometria de luz branca e o software Mountains Map Universal v7.0. Na seguinte etapa avaliado o efeito da porosidade e da temperatura de sinterização no desempenho tribológico de aço impregnado com grafite de D50 = 1.10 μm e foi estudada a evolução dos poros e da distribuição de carbono nas pistas de desgaste em ensaios de carga incremental interrompidos. Para realizar essa análise foi desenvolvido um script de na linguagem Python v3.6 para analisar as imagens de elétrons retroespalhados obtidas via MEV e os mapas de carbono obtidos via EDS das marcas de desgaste. Nesta etapa a microscopia Raman foi utilizada para avaliar a evolução do material na tribocamada em função da carga nos ensaios de carga incremental.

Na última etapa do trabalho foi avaliado o efeito da estrutura cristalina de CDC sintetizado a 1200, 1300, 1400 e 1500 °C no desempenho tribológico do aço sinterizado mediante ensaios de durabilidade e de desgaste. Os CDCs foram caracterizados mediante as técnicas de granulometria, microscopia Raman e difração de raios X.

Resultados e Discussão

Os resultados da primeira etapa do trabalho mostram que é possível obter amostras com diferentes porosidades em função da sua pressão de compactação, mantendo a microdureza da matriz constante entre todas as condições, este fato foi considerado crítico para a realização do presente trabalho já que permite desconsiderar o efeito da microdureza da matriz nos análises realizados em etapas posteriores. Na segunda etapa foi desenvolvido um processo de impregnação que permitiu com sucesso induzir lubricidade em amostras de aço sinterizado através do preenchimento dos seus poros superficiais com grafite. O número de ciclos de impregnação esteve relacionado à distribuição de tamanho de partícula do grafite sendo mais difícil impregnar os grafites com D50 = a 6.07 e 21.54 μm. O estudo da influência do tamanho de partícula no desempenho tribológico do aço sinterizado impregnado revelou que a durabilidade do fenômeno de lubrificação é inversamente proporcional ao tamanho de partícula do grafite e que os grafites de 6.07 e 21.54 μm conseguiram manter lubricidade por até aproximadamente 120 m porém não tiveram a capacidade de manter a lubricidade por essa distância durante os ensaios de carga constante. Essa diferença de comportamento em função do tamanho de partícula foi atribuída ao acesso a novos reservatórios de grafite produzido pelos incrementos de carga durante os ensaios de durabilidade e também, à maior fluibilidade das

partículas de grande tamanho que faz com que sejam retiradas mais facilmente dos poros durante os ensaios tribológicos, deixando eles vazios durante os ensaios de carga constante. Na etapa seguinte o estudo do efeito dos parâmetros de processamento no desempenho tribológico do aço impregnado revelou que a durabilidade destes materiais depende da quantidade de estoques disponíveis, ou seja, é diretamente proporcional à porosidade, porém, a taxa de desgaste também aumenta com a porosidade devido à perda de propriedades mecânicas. O estudo da evolução dos poros e da distribuição de carbono durante os ensaios de carga incremental revelou que a porosidade das marcas de desgaste diminui em função da carga ao mesmo tempo que aumenta a microdureza do material dentro das marcas o que faz com que a taxa de desgaste seja mantida constante. Sobre o fechamento dos poros, as análises indicam que ele começa pela divisão dos poros de grande tamanho em poros de menor tamanho o que faz com que a porosidade diminua, porém o número de poros se mantenha quase constante em função da carga. A análise de distribuição de carbono dentro dos poros mostrou que os poros pequenos e estreitos podem melhor reter o grafite durante os ensaios tribológicos, liberando-o gradativamente conforme avança o ensaios, contrariamente, os poros de maior tamanho liberam rapidamente o grafite o que faz que ele fique baixo o nível da marca de desgaste e não participe do fenômeno de lubrificação, esse fenômeno é explicado também pela noção de fluxo de grafite desde os poros para a pista de desgaste, seções estreitas opõem resistência ao fluxo do grafite o que resulta beneficial para o desempenho tribológico do material. A análise da evolução do espectro Raman das marcas de desgaste em função da carga mostra que a densidade de defeitos de pontos (associado à produção de vacâncias) aumenta em função da carga junto com a aparição dos picos associados ao carbono sp^3. Um modelo de amorfização foi proposto onde a excessiva produção de vacâncias dentro dos planos basais do grafite devido à ação do fenômeno tribológico causa a aparição de carbono sp^3 entre as lamelas o que não permite o cisalhamento entre os planos basais e, portanto, diminui a capacidade lubrificante do grafite.

Finalmente o estudo do desempenho tribológico do aço sinterizado impregnado com CDC revelou que o desempenho tribológico do grafite melhora com o seu nível de cristalinidade nos ensaios de durabilidade, porém os ensaios de desgaste sugerem que outras variáveis além da estrutura cristalina do material devem ser consideradas.

Considerações Finais

No presente foram avaliados os efeitos dos parâmetros de processo, das características do grafite e da interação entre poros e grafite no desempenho tribológico de aço sinterizado impregnado. O presente trabalho constituí um avanço importante na utilização da técnica de impregnação de grafite como técnica para promover lubrificação em materiais sinterizados para aplicações industriais e ao mesmo tempo, representa um avanço científico no entendimento da influência do fluxo de grafite desde os poros para a superfície no desempenho tribológico do material. O análise da estrutura cristalina do grafite antes e depois dos ensaios tribológicos representa um avanço no entendimento das transformações na rede cristalina do grafite induzidas pelos fenômenos tribológicos e como esta estrutura cristalina influencia o desempenho tribológico dele, a aplicação do análise Raman desenvolvido por Cançado em 2017 para estudar tribocamadas contendo grafite é a primeira do seu tipo na literatura e constitui uma contribuição do presente trabalho. Finalmente, as técnicas desenvolvidas no presente trabalho não só estão limitadas ao estudo de aço impregnado com grafite e podem ser utilizadas para analisar uma grande gama de combinações de matriz-lubrificante sólido produzidas por impregnação ou como materiais compósitos produzidos por outras técnicas.

Palavras-chave: Interação lubrificante sólido/poros, Impregnação à vácuo, Grafite, Aço poroso, Tribologia, Carbono derivado de carbetos.

ABSTRACT

Most of the self-lubricating composites produced by powder metallurgy present metallurgical interactions between the lubricant and matrix phases during the sintering process, which do not allow to isolate the effect of the individual characteristics of each phase on the tribological behaviour of these composites. Few authors have used the solid lubricant impregnation technique to promote lubricity in porous materials while isolating the properties of the solid lubricant from the properties of the matrix. Among those authors, none of them has addressed how the interaction between pores and the solid lubricant governs the tribological performance of the material. Because of this, the present work addresses the interaction between solid lubricant particles and pores during tribological testing and the influence of this interaction on the tribological behaviour of sintered steel impregnated with graphite. The main objective of this work was to understand how the properties of the lubricant and matrix phases separately affect the tribological behaviour of porous steels impregnated with graphite. To tackle this problem, in the present work, a vacuum impregnation technique was developed in order to impregnate porous sintered steels with graphite. The main variables studied were compaction pressure and sintering temperature for the porous steel and particle size and crystalline structure for the lubricant phase. To study the effect of the crystalline structure graphite derived from the Cr_3C_2-B_4C reaction was used, this is a new solid lubricant developed in the Materials Laboratory of the Federal University of Santa Catarina (LABMAT). Scuffing resistance and wear tests were used to perform the tribological characterization of these materials. The wear tracks were analysed by scanning electrons microscopy, image analyses and Raman micro-spectroscopy. Results show that the tribological behaviour of porous steels impregnated with graphite depends on the slow release of graphite from the pores during the tribological tests and also depends on the mechanical properties of the matrix. A balance exists between the amount of solid lubricant available and the mechanical resistance of the matrix, both depending on the porosity. Results also show that the degradation of the graphitic tribolayer occurs by the increase in the point-defect density and the transformation from sp^2 to sp^3 carbon.

Keywords: Solid Lubricant/Pore Interaction, Vacuum Impregnation, Graphite, Porous steel, Tribology, Carbide derived carbon.

.

LIST OF FIGURES

LIST OF TABLES

LIST OF ABREVIATIONS AND ACRONYMS

LABMAT: Materials Laboratory of The Federal University of Santa Catarina

UFSC: Federal University of Santa Catarina

HOPG: Highly Ordered Pyrolytic Graphite

CDC: Carbide Derived Carbon

SEM: Scanning Electron Microscope

EDS: Energy-Dispersive X-Ray Spectroscopy

COF: Coefficient of Friction

XRD: X-ray diffraction

ANOVA: Analysis of Variance

TABLE OF CONTENTS

1 INTRODUCTION

In the last decades, the worldwide energetic demand has increased exponentially, mainly due to the industrialisation and development of countries like China and India (BP P.L.C., 2015). As a product of this continuous rise in the energetic demand there are a significant number of researchers and engineers working in the development of new energy sources (DINCER, 2000; PANWAR; KAUSHIK; KOTHARI, 2011; ZENG et al., 2017) and new ways to increase energetic efficiency (TUNG; MCMILLAN, 2004; SUGIMURA, 2017). In that second aspect, the development of new and better lubricants becomes a priority to the technological and industrial growth of nations (HOLMBERG; ERDEMIR, 2017). As an example, 33% of the energy consumption in cars, buses and trucks is dissipated as heat produced by friction (HOLMBERG; ANDERSSON; ERDEMIR, 2012; HOLMBERG et al., 2014). By the application of new technologies in lubrication and protection against wear, energetic losses due to friction can be potentially reduced by 40% in the long term (15 years) and by 18% in the short term (8 years) (HOLMBERG; ERDEMIR, 2017). This results in a considerable motivation for the development of new materials capable of inducing lubrication in a wide range of applications.

The most commonly used form of lubrication is hydrodynamic, where a film of fluid lubricant completely separates the surfaces in relative motion (STACHOWIAK; BATCHELOR, 1993). This results in a significative reduction in the coefficient of friction and wear rates of the system when compared to the same system without lubrication. (BUSHAN, 2013). However, there are situations where fluid lubrication cannot be used (like high vacuum or extreme temperatures) or is undesirable (like in the food industry or in optical equipment). It is in these situations where solid lubrication appears as an interesting alternative over conventional lubrication methods (CLAUSS, 1972; SLINEY, 1982; MIYOSHI, 2001a).

Solid lubricants can be applied in a variety of ways (as summarized in figure 1). The oldest and simplest method is to powder of rub the material in the surfaces to be lubricated. Some solid lubricants can be dispersed in an aerosol and sprayed directly in the areas of tribological contact (ERDEMIR, 2000). As powders, these materials can be dispersed in fluid lubricants, producing a synergic effect between the two materials (ZHANG et al., 2011, 2017; MARUYAMA; HOKAO, 2017). They also can be strongly adhered to a surface if mixed with

an appropriate binder or resin (STACHOWIAK; BATCHELOR, 2014a) or deposited by physical vapour deposition (PVD), chemical vapour deposition (CVD) or plasma-assisted techniques (ERDEMIR; ERYILMAZ, 2014; OSS GIACOMELLI et al., 2018). However the restricted nature of the lubricating layer of these systems limits the duration of the lubricity phaenomena; because of this, self-replenishment mechanism of the lubricating layer are needed (ERDEMIR, 2000).

Figure 1: Methods for the application of solid lubricants.

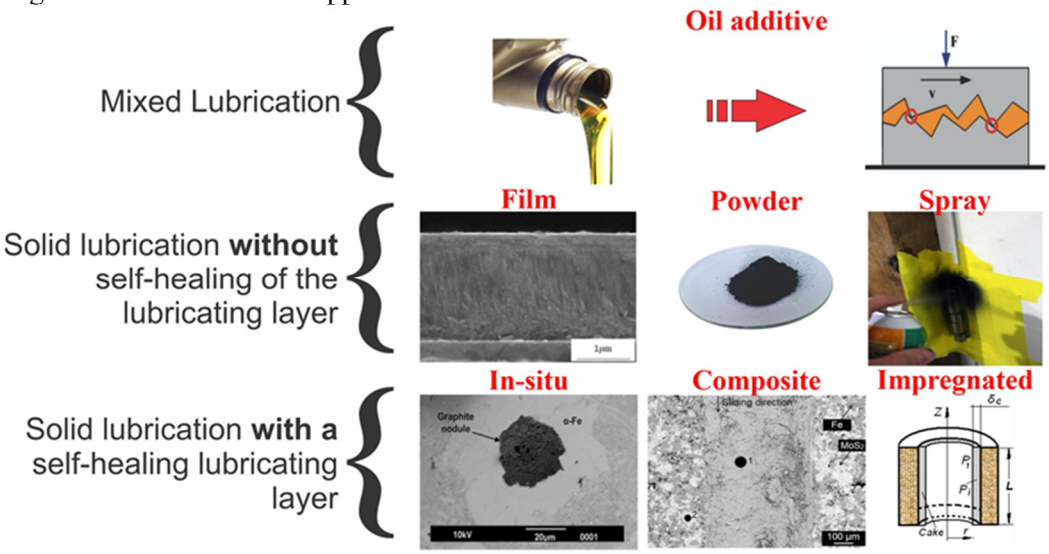

Source: Author.

Among the forms of inducing solid lubrication that are presented in figure 1, the ones providing the self-replenishment of the tribo-layer are the in-situ generation of the lubricating phase (BINDER et al., 2010; KLEIN et al., 2015); the incorporation of solid lubricants in composite materials (CUI et al., 2012, 2013; FURLAN et al., 2012, 2017; PARUCKER et al., 2013) and the impregnation of a porous substrate (RAPOPORT et al., 2002; WIŚNIEWSKA-WEINERT, 2014). The two first methods allow the obtention of a self-lubricating material produced by powder metallurgy where the lubricating phase is dispersed in the bulk of the specimen, and consequently, can be supplied to the tribological contact as the material wears (DE MELLO et al., 2011; HAMMES et al., 2014). Nevertheless, in those two methods, by their nature, there are interactions between the lubricating phase and the matrix phase during the sintering cycles that make it hard to separate the effect of the properties of the lubricating phase from those of the matrix phase in the tribological performance of the material.

The impregnation of porous materials with solid lubricant allows the supply of solid lubricant in the tribological contact, which is released as the material experiences wear

(RAPOPORT et al., 2003). The amount of lubricant that will be supplied during the tribological phaenomena depends on the number of pores impregnated and the penetration of the lubricant into the matrix (LESHCHINSKY et al., 2002; RAPOPORT et al., 2002; WIŚNIEWSKA-WEINERT, 2014). This method has the advantage that the mechanical, microstructural and physical-chemical properties of the matrix are independent of the material being impregnated, which allows to study the effect of both materials (matrix and solid lubricant) independently. The impregnation method needs open pores at the surface. A common method to obtain a material with these characteristics is by powder metallurgy. In conventional pressing and sintering, size and number of pores are strongly related to the compaction pressure used during the moulding process. Higher pressures produce more packing and plastic deformation of the powders, which lead to densification and reduction of the porosity of the green body (GERMAN, 2005). In the sintering process and due to the second law of thermodynamics, the pores inside the green body are rounded in order to reduce their surface energy (HRYHA; DUDROVA, 2011; HÖGANAS, 2013a. This rounding is proportional to the sintering temperature and time implemented (HAYNES, 1991; KULECKI; LICHAŃSKA; SUŁOWSKI, 2015). The presence of pores heavily influences the mechanical properties of sintered materials. Besides being empty spaces, pores act as stress risers, which reduces the elastic module and mechanical strength of sintered materials (HAYNES, 1971, 1991; HAYNES; EGEDIEGE, 1989) also reducing their impact toughness (HÖGANÄS AB, 2004). However, for a constant porosity, mechanical properties are influenced by the shape of pores. Round pores do not rise stresses as much as irregularly shaped pores, so mechanical properties are improved when pores are rounded (HAYNES, 1991; DOBRZAŃSKI et al., 2007)

To study the tribological behaviour of impregnated porous materials, the effect of pores must be addressed. Sub-superficial pores have a negative effect on the wear resistance, facilitating the nucleation and growth of cracks beneath the surface, which results in severe wear (DUBRUJEAUD; VARDAVOULIAS; JEANDIN, 1994; DESHPANDE; LIN, 2006). Although this effect is critical, other studies have reported that the presence of open pores at the surface during the tribological phaenomena has a positive impact on the wear resistance. This is because open pores act as traps for debris, which reduces the accumulation of abrasive particles between the moving surfaces and reinforces the porous surface (LEHEUP; ZHANG; MOON, 1994, 1998; SIMCHI; DANNINGER, 2004; ISLAM; FARHAT, 2011). Studies

conducted in sintered steels treated by steam-oxidation show that pore size and free mean path between pores have an impact on the wear resistance of these materials. In these it was observed that in ball-on-flat tests the durability of the oxide layer (which is proportional to the wear resistance of these materials) is negatively affected by the porosity (MOLINARI; STRAFFELINI, 1995).

On the other hand, the reduction of the mean free path between pores (which depends on the number and size of pores) increases the durability of the oxide layer in these materials (DE MELLO; HUTCHINGS, 2001). In abrasion tests, de Mello et al. proved that although open pores acted as traps for the abrasive particles during the tribological tests, this effect depends on the pore size distributions, in summary: as pores increase in size, it becomes more difficult for them to be filled with debris which makes them detrimental to the wear resistance of these materials (DA SILVA; BINDER; DE MELLO, 2005).

Once pores are filled with solid lubricant, their influence in the tribological behaviour of the material changes because of the effect of the solid lubricant in the tribological contact (RAPOPORT et al., 2001; KANG; CHUNG, 2003). Rapoport et al. have studied the tribological behaviour of sintered materials impregnated with WS_2 particles in block-on-ring tests (RAPOPORT et al., 1997), dry or dispersed in oil (LESHCHINSKY et al., 2002). In these, it was found that the tribological behaviour changed with the atomic arrangement of the impregnated material (120 nm WS_2 fullerenes being better than 4 μm lamellar WS_2) however, the effect of their differences in size was not addressed.

Considering the latter, there is a gap in the literature in three crucial aspects:

1. The effect of the number, size and shape of the pores on the tribological behaviour of impregnated materials and the evolution of these characteristics throughout the tribological tests.
2. The effect of the solid lubricant particle size on the tribological behaviour of these materials.
3. The effect of the crystalline structure of the solid lubricant (without significative changes in particle size) on the tribological behaviour of these materials.

To address these topics, the present work studied the interaction between pores and solid lubricant in porous low alloy steels produced by compaction and sintering impregnated graphite. Graphite was chosen because it is a widely available, easy to characterize and its tribological behaviour has been vastly covered by literature (HATATE et al., 2001;

DIENWIEBEL et al., 2004; KUMAR et al., 2011; CUI et al., 2012; FURLAN et al., 2017; SAKKA et al., 2017). In this system, the effect of particle size was studied by impregnating specimens with graphite of D50 = 1.10, 6.07 and 21.54 μm and characterising them using incremental and constant load tests in a reciprocating ball on flat configuration. Then the evolution of pores and solid lubricant distribution was studied by using image analysis techniques on the scanning electron microscopy (SEM) images of the wear tracks produced by incremental load tests. Finally, the effect of the crystalline structure of the graphite was studied by impregnating the specimens with a new kind of carbide-derived carbon (CDC) produced by the solid-state reaction between boron carbide (B_4c) and chromium carbide (Cr_3C_2), which is a product of the doctoral work of the Msc. Guilherme Neves. This reaction produces graphite with varying degrees of crystallinity depending on the reaction temperature. The coefficient of friction, wear rates and scuffing resistance of the specimens impregnated with CDC was measured and compared with the results obtained using crystalline graphite.

The impregnation of porous materials with solid lubricants is an easy way to promote lubricity in materials produced by powder metallurgy and can improve their tribological performance by taking advantage of their residual porosity. This work addresses the effect of the porosity and sintering temperature of the sintered steel as well as the effect of the particle size on the tribological performance of impregnated steel, as well as the tribological performance of the new CDC being produced by the Laboratório de Materiais from the Federal University of Santa Catarina (LABMAT). For all of this, it constitutes an advance towards the development of self-lubricating materials and to the understanding of the solid lubrication phaenomena.

1.1 OBJECTIVES AND MOTIVATION

This work addresses the interaction between the solid lubricant and the lubricant stocks (pores) during the tribological phaenomena and the effect of the solid lubricant characteristics on the tribological behaviour of the system. Most self-lubricating composites have intricated relationships between the lubricating phase and its metallic matrix, mainly because the lubricating phase is not completely inert in relation to the matrix. This causes that the properties of the lubricant and the properties of the matrix cannot be isolated which makes it difficult to study the effect of their individual properties in the tribological performance of the composite.

The material chosen to perform this work was sintered steel impregnated with graphite, both crystalline and derived from carbides, in order to address the influence of the size, shape and number of pores and the size and crystalline structure of graphite in the tribological behaviour of the system. This work is part of one of the LABMAT research lines involving the characterisation and development of solid lubricant and self-lubricating composites for industrial applications. Its main motivation is to understand the role of the lubricant reservoirs in dry lubrication conditions and the effect of the properties of the solid lubricant in its tribological performance. Considering this the general and specific objectives of this work were defined as follows.

1.1.1General Objective

To study the interaction between the pores of sintered steel and the impregnated graphite and how this interaction influences the tribological behaviour of the impregnated steels

1.1.2 Specific objectives

- ✓ To produce samples of sintered steel whose metallic phase has microstructural homogeneity and whose pores vary in size, shape and quantity.
- ✓ To develop a method to impregnate solid lubricant into the pores of porous steel produced by powder metallurgy.
- ✓ To develop an image analysis methodology that allows obtaining information about the carbon distribution in the pores of the wear tracks from images obtained by SEM and EDS
- ✓ To study the relationship between the size, shape and number of pores in the supply of solid lubricant during the tribological test.

- ✓ To study the influence of the size ratio between solid lubricant particles and pores in the impregnation and the tribological behaviour of the sintered steel.
- ✓ To analyse the influence of the crystalline structure of CDC in the tribological behaviour of the system being studied.

To fulfil the objectives of the present work, it was divided into 5 steps, each one with its own objective and scope. A summary of these steps is shown in figure 2.

Figure 2: Objectives and scope of each step of the present work.

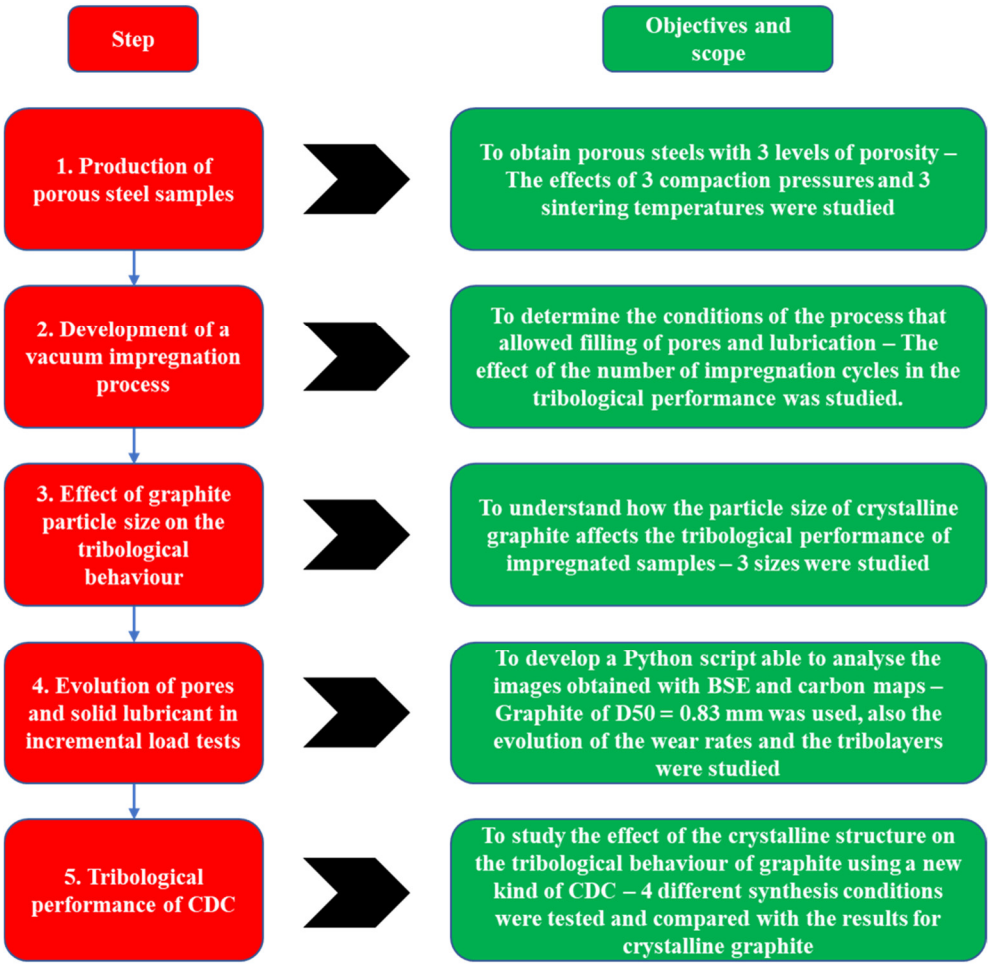

Source: Author

2 LITERATURE REVIEW

In this section, the relevant topics to better understand the motivation and objectives of this work will be presented. First, solid lubrication will be introduced, and powder metallurgy will be presented as a method to produce porous materials. Then the techniques to impregnate porous materials will be discussed, and the theory behind vacuum impregnation will be addressed. The Raman spectra of graphite and graphite-related materials will also be discussed. Finally, the computational techniques for image analyses and the tribological applications of CDCs will be presented. It must be highlighted that CDCs produced by solid-state reactions between two carbides are new materials developed by the LABMAT's research team.

2.1 SOLID LUBRICATION

Friction and wear in mechanical systems are caused by the contact and relative motion between two surfaces. The most common method to reduce both effects is the intercalation of a lubricating layer which separates the moving surfaces and induces low friction. This lubricating layer can be supplied as a fluid, a thin film, in the form of powders or a mixture of those three options (BRISCOE, 1992; MIYOSHI, 2001a).

Fluid lubricants like oils and greases have a wide array of applications when they can be successfully applied. However, in conditions like extreme temperatures, extreme loads, or high vacuum solid lubrications appears as a promising solution. Table 1 presents a list of conditions were fluid lubrication is unsuitable or undesired.

Table 1 - Applications where fluid lubricants are undesirable or unsuited.

Requirement	Application
To avoid contamination of the product or the environment	Food processing
	Space telescopes
	Microscopes and cameras
	Paper processing
	Medical equipment
To provide and maintain lubrication in hard to reach areas	Planes
	Space vehicles
	Satellites
	Nuclear reactors
Abrasion resistance in dirty environments	Space rovers
	Cars
	Mining equipment
	Off-road vehicles
	Construction equipment
To provide stationary service	Planes
	Train engines
	Missile components
	Telescope frames
	Furnaces
High vacuum	Vacuum products
	Space mechanism
	Space telescope mounts
	Space platform

Source: Adapted by the author from MIYOSHI (2001)

Solid lubrication is obtained by the utilisation of self-lubricating solids or the inclusion of a third solid body with the ability to induces low coefficients of friction between the moving surfaces (CLAUSS, 1972; STACHOWIAK; BATCHELOR, 2014a). According to Miyoshi, a solid lubricant film must have the capacity of inducing coefficients of friction below 0.3 and wear rates below $10^{-6}mm^3/N.m$ (MIYOSHI, 2001b). In a later work by de Mello and Binder, the lubricity regime of a solid lubricant film was defined as the region where the film induces coefficients of friction below 0.2 (DE MELLO; BINDER, 2006). This concept has been extended to self-lubricating composites (DE MELLO et al., 2011, 2017a; FURLAN et al., 2017) and was the criteria to define the lubricity regime in the specimens produced in this work.

Solid lubricants can be classified into several subclasses. Table 2 presents a classification of more commonly used solid lubricants based on their chemical composition and crystalline structure (ERDEMIR, 2000).

Table 2: Classification of solid lubricants according to their chemical composition and crystalline structure

Classification	Key Examples	Typical friction coefficients*
Lamellar solids	MoS_2	0.002 - 0.24
	h-BN	0.15 - 0.7
	Graphite	0.07 - 0.5
	Graphite fluoride	0.05 - 0.15
	H_3BO_3	0.02 - 0.2
Soft metals	Ag	0.2 - 0.35
	Pb	0.15 - 0.2
	Au	0.2 - 0.3
	In	0.15 - 0.25
	Sn	0.2
Mixed oxides	Cuo-Re_2O_7	0.1 - 0.3
	CuO-MoO_3	0.2 - 0.35
	PbO-B_2O_3	0.1 - 0.2
	CoO-MoO_3	0.2 - 0.47
	NiO-MoO_3	0.2 - 0.3
Single oxides	B_2O_3	0.15 - 0.6
	Re_2O_7	0.2
	MoO_3	0.2
	TiO_2 (sub- stoichiometric)	0.1 - 0.6
	ZnO	0.1 - 0.6
Halides and sulphates from alkaline metals	CaF_2, BaF_2, SrF_2	0.2 - 0.4
	$CaSO_4$, $BaSO_4$, $SrSO_4$	0.15 - 0.2
Carbon-based solids	Diamond	0.02 - 1
	DLC	0.003 - 0.5
	Vitreous carbon	0.15
Organic materials/polymers	Zinc stearate	0.1 - 0.2
	Waxes	0.2 - 0.4
	Soaps	0.15 - 0.25
	PTFE	0.04 - 0.15
Bulk or thick-film composites (> 50 μm)	Metal-, polymer-, and ceramic-matrix composites consisting of graphite WS_2, MoS_2, Ag, CaF_2, BaF_2, etc.	0.05 - 0.4
Thin films (< 50 μm)	Nanocomposite or multilayer coatings consisting of MoS_2, DLC, Ti, etc.	0.05 - 0.15
	Electroplated Ni and CR films consisting of PTFE, graphite, diamond, B_4C, etc., particles as lubricants	0.1 - 0.5

*Friction values given in this table represent friction measurements made on each solid lubricant over a wide range of test conditions, environments, and temperatures. The objective here is to show how friction varies depending on test conditions, as well as from one solid to another.
Source: Adapted by the author from Erdemir (2000).

In this work, the solid lubricant chosen was graphite, which is a lamellar solid that possesses a strong interaction between the atoms in the basal planes but a weak interplanar interaction (due to Van der Waals forces). This facilitates shear and (among other factors) grants

it his lubricating properties (CLAUSS, 1972). Under certain conditions, crystalline graphite is known as one of the most effective solid lubricants. The tribological performance of graphite in dry lubrication has been characterized by tests performed in graphite blocks KUMAR et al., 2013, 2015b) and as the lubricating phase in composite materials (ROHATGI; RAY; LIU, 1992; MOUSTAFA et al., 2002; CUI et al., 2012; FURLAN et al., 2017).

For tribological applications, another interesting form of graphite is turbostratic graphite. Turbostratic graphite is a carbon allotrope with an sp^2 hybridisation state which presents a parallel random stacking with no three-dimensional order. In turbostratic graphite the net spacing (c axis) is ≥ 0.34 nm, exceeding those of crystalline graphite which is of 0.334 nm (DRESSELHAUS, 1997; WELZ, 2003; REBELO, 2014). The turbostratic stacking can be found mainly in carbon materials obtained at temperatures below 3000 °C, where the hexagonal layers are usually small, and few of them are parallel stacked. Turbostratic graphite is produced mainly due to lattice defects such as stacking faults, vacancies and dislocations (WELZ, 2003). Figures 3 and 4 show the difference between crystalline graphite and turbostratic graphite stacking.

Figure 3: Difference between crystalline (a) and turbostratic (b) graphite stacking

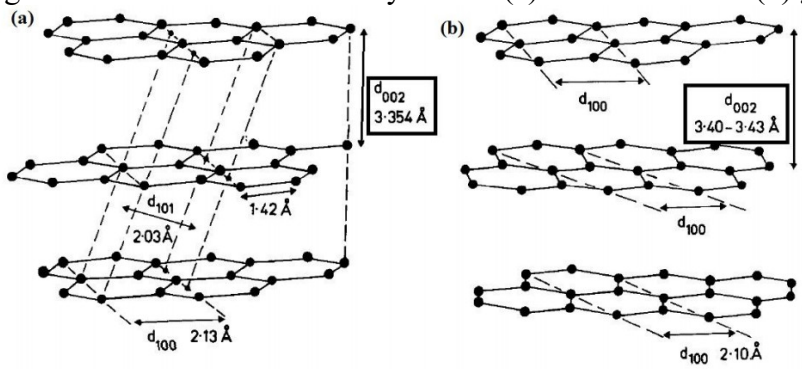

Source: Knox et al. (1986).

Figure 4: Upper view of graphite layers for crystalline stacking (a) and turbostratic stacking (b)

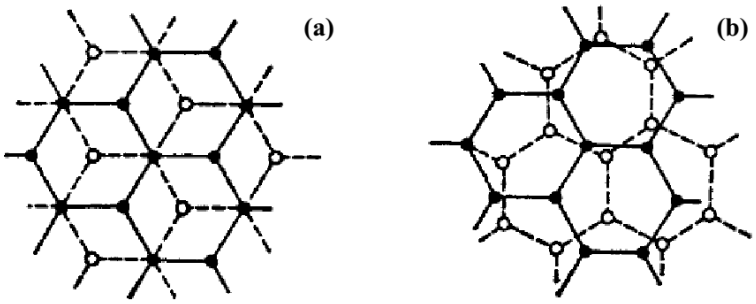

Source: Rebelo (2014).

Crystalline graphite shows a regular array of graphite layers stacked in order to minimise the spacing between layers; meanwhile, turbostratic graphite has a random stacking order in the c axis (DIENWIEBEL et al., 2004). In the atomic scale, turbostratic graphite exhibits super-lubricity due to incommensurable contact between the basal planes. Under certain conditions, this translates into extremely low friction coefficients (BINDER, 2009; KUMAR et al., 2011).

This carbon allotrope is important as can be found in carbide-derived carbon which is one of the subjects of the present work. Another subject of the present work is the role of pores in the mechanical and tribological properties of materials. These topics are presented in the next section.

2.2 POWDER METALLURGY AND POROUS MATERIALS

2.2.1 Manufacture of porous materials by powder metallurgy

Powder metallurgy is a fabrication process that combines mechanical forming (moulding) and subsequent densification processes (ASM INTERNATIONAL HANDBOOK COMMITTEE, 1998). These densification steps have the objective of obtaining a finished or semi-finished product called sintered body (GERMAN, 2005). Among all the techniques for moulding and sintering (like metal injection moulding, hot isostatic pressing, powder forging, etc.) the simplest most widely used process in the industry is press and sinter (CAPUS, 2005a). This process starts with the mechanical densification of powders inside a rigid mould by applying pressures in the order of 650 MPa (HÖGANAS, 2013b). Under the influence of the compaction pressure, the particles undergo plastic deformation and a certain amount of cold welding of their surfaces (GERMAN, 2005; HÖGANAS, 2013a) which provides the compacted piece with enough mechanical strength (green strength) for its handling in later steps. Sintering is a process where the compacted material is transformed into a coherent solid by applying temperatures below its melting point (NOWACKI; KLIMEK, 1993; HÖGANAS, 2013b). The main driving force behind the sintering process is the reduction of the Gibbs free energy of the

compact, mainly in terms of surface energy and chemical potential of the powder mixture (NOWACKI; KLIMEK, 1993; GERMAN, 2005).

The main advantages of the powder metallurgy techniques in comparison with other alternatives like casting or machining are:

- Precise control over the chemical composition
- Minimum material losses
- Dimensional accuracy
- The flexibility of chemical compositions
- Microstructural control during the process without the need for further treatments (GERMAN, 2005; BINDER et al., 2010)

Nevertheless, the expensive raw materials, moulding tools and processing equipment in general limit the application of these techniques (CAPUS, 2005b). In general, powder metallurgy fabrication is justified when medium/high complexity components are required or to produce identical components in high quantities (ASM INTERNATIONAL HANDBOOK COMMITTEE, 1998).

Depending on the moulding and sintering methods used is possible to manufacture components with varying degrees of porosity, from metal foams (GOODALL, 2013; MONDAL et al., 2015; WANG et al., 2015), meso and microporous materials (NISHIYABU; MATSUZAKI; TANAKA, 2007; GÜLSOY; GERMAN, 2008; NISHIYABU, 2012) to fully densified components, with mechanical properties equal or sometimes higher than those of materials produced by conventional techniques (ASM INTERNATIONAL HANDBOOK COMMITTEE, 1998).

The systematic study of the variables involving the evolution of the porosity from the green compact to the sintered body is important due to its impact on the final properties of the components (ASM INTERNATIONAL HANDBOOK COMMITTEE, 1998; GERMAN, 2005). To better understand this point and to help with the comprehension of the terminology used in the present work is important to define some concepts that are inherent to porous materials. This will facilitate the understanding of the phenomena that occurred during the tribological characterisation of the impregnated specimens. These concepts are:

Porosity: Ratio between the pore volume and the total volume of the part (Vp/Vt). Porosity is related to the density of the material by equation 1.

$$\text{Porosity (\%)} = 100x\ (1 - \frac{\rho}{\rho_0}) \qquad (1)$$

Where ρ is the density of the sintered material and ρ_0 is the density of the material without pores. Porosity is a fundamental parameter for porous materials and a key factor to their physical and mechanical properties. Depending on their relation to the surface of the sintered material, porosity can be communicating (figure 5(a)), open-blind (figure 5(b)) or closed (figure 5 (c)) (DULLIEN, 1992).

Figure 5: Classification of pores according to their relationship with the surface

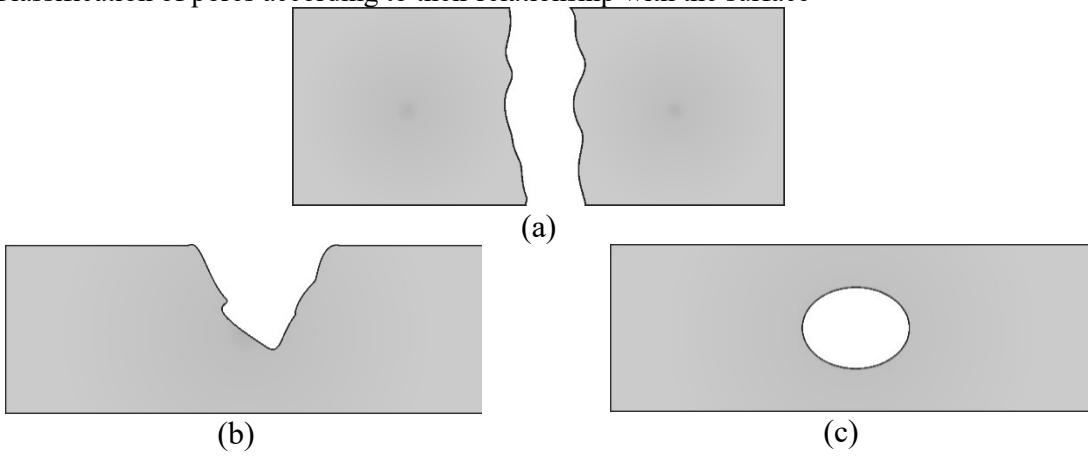

Source: Author.

Pore size: Defined as the nominal diameter of the pores inside the material. It can be represented as the max diameter, mean diameter or as a size distribution. Figure 6 presents the four most common ways to define pore diameter by image analysis:

- As the mean diameter of a circle with the same area as the pore (figure 6(a)).
- As the diameter of the circle with the same perimeter of the pore (figure 6(b)).
- As the longitude of the line that bisects the pore, also known as Martin diameter (figure 6(c)).
- As the distance between two tangent lines in opposite sides of the pore, also known as Feret diameter (figure 6(d)).

Figure 6: Definitions of pore diameters by image analysis: (a) Diameter of the equivalent circle with the same area of the pore (b) Diameter of the equivalent circle with the same perimeter of the pores, (c) Martin diameter, (d) Feret diameter.

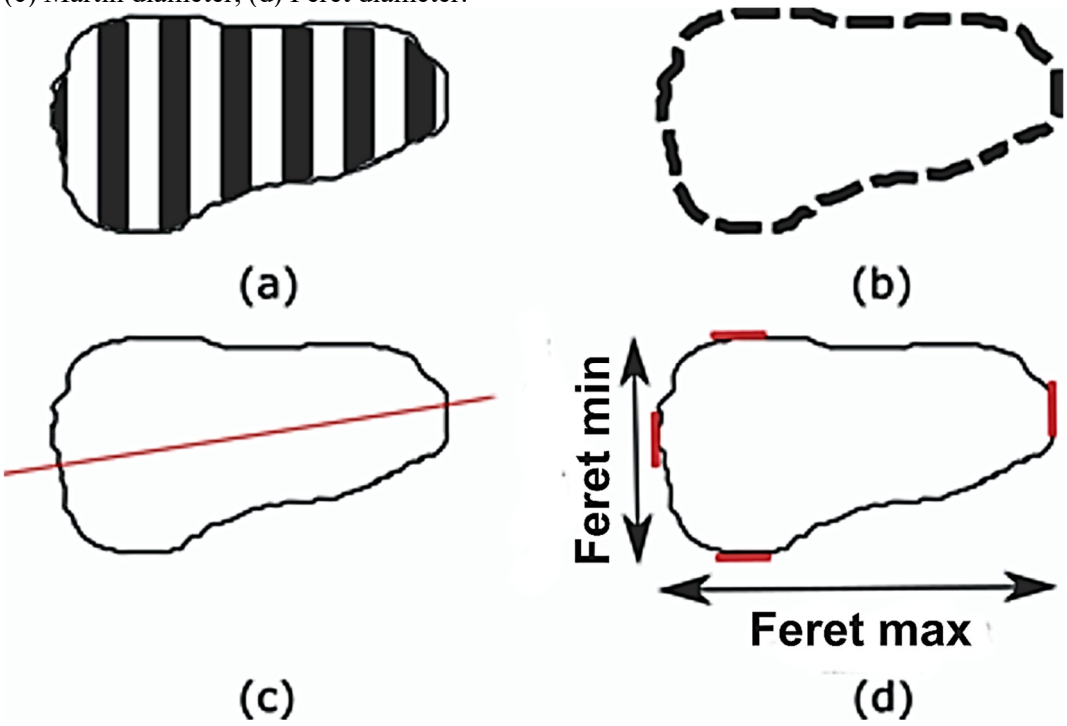

Source: Author

Feret and Martin's diameters offer significative information about the size of the pores, even if they are irregular (FRIEL et al., 2000). In the present work, mean Feret diameter was used to describe pore sizes as is a commonly used definition for pore size in powder metallurgy products. Pore size is directly correlated with the capacity of the material of being impregnated (LIU; CHEN, 2014a); this will be addressed in section 2.3 of the present work.

Pore shape: Pore shape is measured by a-dimensional parameters called shape factors. These parameters measure the deviation of the shape of the pores from a pre-established model (FRIEL et al., 2000). In this work, three shape factors were calculated: Eccentricity, Circularity and Solidity.

Eccentricity is defined as the ratio of the focal distance over the major axis length of the ellipse with the same second-moments as the pore (VAN DER WALT et al., 2014). Figure 7 presents an example of this measure.

Figure 7: Definition of the eccentricity shape factor

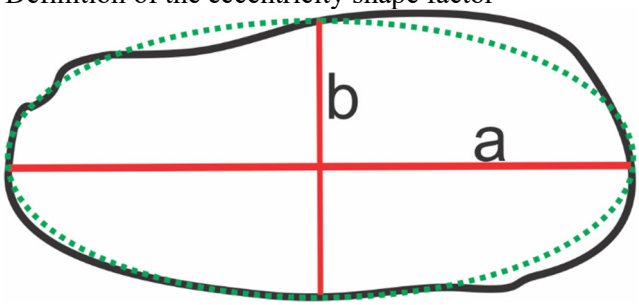

Source: Author

Eccentricity is calculated using equation 2:

$$b^2 = a^2(1 - e^2) \qquad (2)$$

Where a and b are one-half of the major and minor axes and e is the eccentricity of the ellipse. When the eccentricity equals 0, the ellipse becomes a circle.

Circularity is defined as the ratio between the area of the pore and the perimeter of its equivalent circle and is calculated using equation 3:

$$C = \frac{4\pi A}{P^2} \qquad (3)$$

Where C is the circularity, A is the area of the pore and P is its perimeter. When the circularity equals 1, the pore becomes a circle (FRIEL et al., 2000).

Finally, solidity is the ratio between the area of the pore and the area its convex hull (SCIKIT-IMAGE, 2019). An example of this concept is shown in figure 8.

Figure 8: Pore (left) and its convex hull (right)

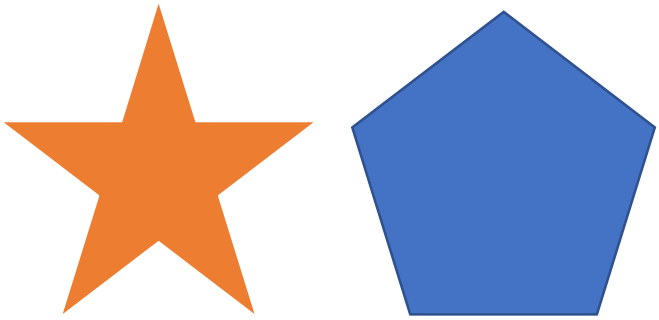

Source: Author.

If solidity equals 1, it means that the pore is solid (it has no concavities). If solidity is less than 1, it means that the pore boundary is irregular or has concave regions.

Mean free path (λ): Is a measure of the spatial distribution of the pores, defined as the mean distance between the pore boundaries. It is calculated according to equation 4:

$$\lambda = d\frac{(1-V_{vp})}{V_{vp}} \qquad (4)$$

Where d is the mean pore diameter and V_{vp} is the total porosity. The mean free path is related to the capacity of the lubricant reservoirs to provide lubrication as each stock of lubricant (pores in the case of impregnated materials) can cover a limited area (BINDER et al., 2010), therefore, if they are far apart of each other, lubrication will be deficient.

In the production of parts by pressing and sintering, the compaction pressure, powder particle size, sintering temperature and sintering time are the main parameters that affect porosity, pore size and pore shape (ASM INTERNATIONAL HANDBOOK COMMITTEE, 1998; DE MELLO et al., 2001; KULECKI et al., 2016). These effects can be summarised as follows:

2.2.1.1 Effect of compaction pressure and particle size

Compaction pressure is the main responsible for the densification of a component produced by powder metallurgy (GERMAN, 2005). The exact nature of this effect depends on the pressing method, shape, size and mechanical properties of the powders to be compacted and

of the use of lubricant during the pressing process (POQUILLON et al., 2002). The influence of compaction pressure on the green density can be studied by constructing a compressibility chart. An exemplary compressibility chart is shown in figure 9.

Figure 9: Compressibility chart for Fe-1C-1W

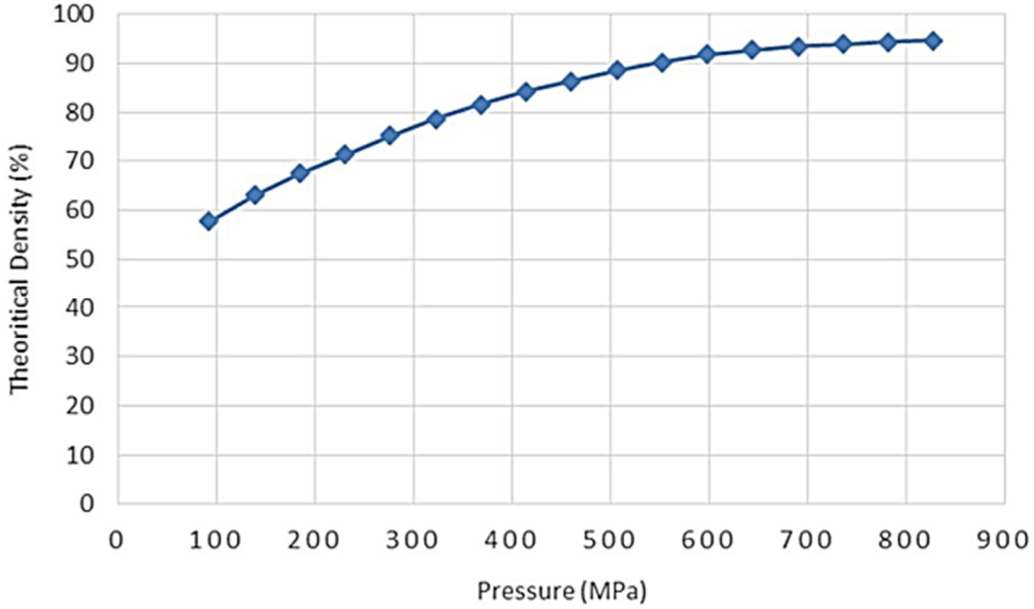

Source: Prabu et al. (2014)

The compressibility chart allows obtaining an estimate for the final density for components produced by conventional press and sinter. Compaction pressure also influences the size and shape of pores; in simple terms, when porosity is high, the pores are interconnected (GOODALL, 2013). This interconnection forms big and irregular pores. As compaction pressure rises, pores start to lose their connectivity becoming isolated, small and with more regular shapes. An example of this is presented in figure 10. At constant compact pressure, powder particle size influences compactability and therefore, the porosity of the sintered components. In comparison with powders with big particle sizes, small particles have a higher specific surface area, which causes more friction between the particles and less plastic deformation during pressing (as the applied force is divided by a bigger surface area). As a consequence, the porosity of a sintered body is inversely proportional to the powder particle size (GERMAN, 2005).

Figure 10: Effect of compaction pressure in the size and shape of pores (schematic)

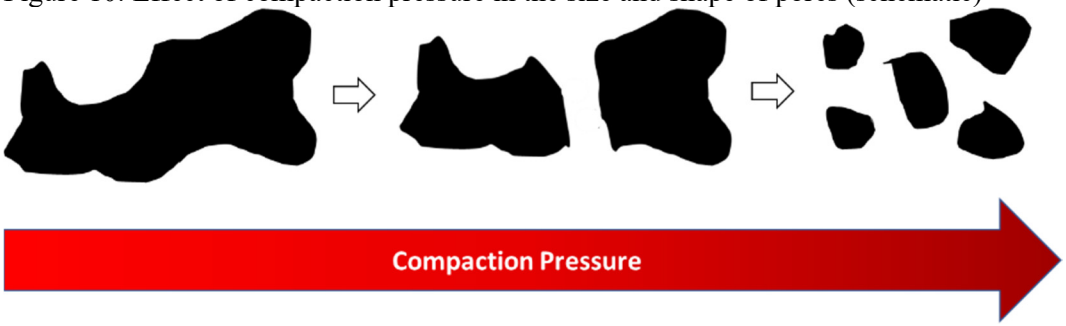

Source: Author

Compaction pressure and particle size have a conjunct influence in the mean free path of the sintered components. Figure 11 shows the effects of these parameters for sintered iron.

Figure 11: Mean free path between pores as a function of compaction pressure and particle size

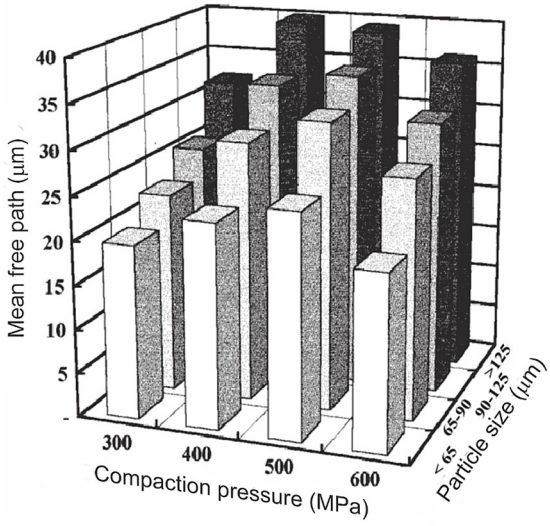

Source: Adapted by the author from de Mello et al. (2001)

In figure 11, it can be observed that compaction pressure has the effect of reducing the mean free path for a constant particle size due to the diminution of pore sizes and porosity. For a constant compaction pressure, the mean free path is reduced along with particle sizes. In this work, the particle size of pre-alloyed iron was fixed in the 75-125 µm range to reduce the influence of particle size on the characteristic of the pores and the porosity.

2.2.1.2 Effect of sintering time and temperature

Besides compaction pressure, sintering temperature and time also influence the final shape and size of the pores in the sintered parts. During the sintering process, the points of contact between the particles start to grow into necks. The formation and grow of these necks increase the metallurgical bond between the particles which in turn increases the mechanical properties of the sintered body. The creation of necks and changes in porosity follow the tendency of the system to reduce the surface energy and chemical potential between the powder particles (LIU; CHEN, 2014b).

The effect of sintering temperature and time in the densification of the material depends on the characteristics of the powders being used. Summarizing, smaller irregular powders (with high surface energy) will be sintered at higher rates than big, spheroidal powders (GERMAN, 2005). Figure 12 presents the steps of neck formation and the densification of compacted bodies during sintering.

Figure 12: The effect of sintering time in the shape of pores

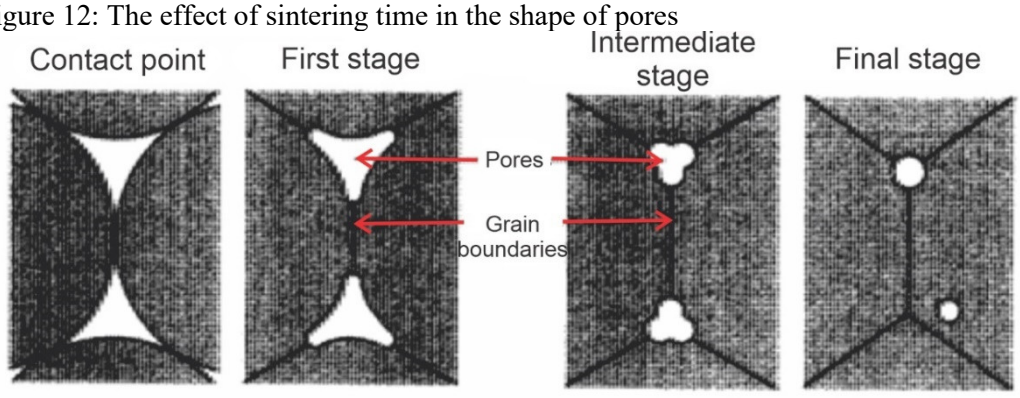

Source: Adapted by the author from German (2005)

Sintering temperature accelerates the sintering process (and the rounding of pores) due to the rise in atomic mobility of the material. Pore rounding reduces the number of stress risers which improves the mechanical properties of the sintered bodies (HAYNES; EGEDIEGE, 1989; CHAGNON; TRUDEL, 1997; DOBRZAŃSKI et al., 2007). Now that the concepts

regarding pores and porosity have been discussed, the effect of the pores in the mechanical and tribological properties of sintered materials will be addressed.

2.2.2 Effect of porosity in the mechanical and tribological properties of powder metallurgy materials

A considerable number of studies has been focused on how porosity affects the mechanical properties of sintered materials (HAYNES, 1991; YE; LI; EADIE, 2001; CHAWLA; DENG, 2005; YALCIN, 2009; KULECKI et al., 2016). In this context, Beiss et al. proposed equation 5 to estimate the mechanical properties of a sintered steel.

$$P = P_0 \left(\frac{\rho}{\rho_0}\right)^m \qquad (5)$$

Where P is the mechanical property to be estimated, P_0 is the property of the material without pores, ρ is the density of the sintered material, ρ_0 is the density of the material without pores and *m* is a constant ranging between 1 and 3 depending on the powder properties and the sintering technique used. An schematic plot of the increase in mechanical properties with sintered density for powder metallurgy materials is shown in figure 13, according to the figure, the route used to densify is not as relevant as the density itself (BEISS, 2003; HÖGANÄS AB, 2004). However, the sintering time and temperature affect the shape and size of pores and therefore, the mechanical properties of the sintered material (HAYNES, 1991; DOBRZAŃSKI et al., 2007). Figure 14 presents an example of the effect of sintering time on the mechanical properties of pure iron.

The effect of porosity in the mechanical properties is well understood; however, the effect of porosity in the wear resistance of sintered materials is more complex and will be strongly dependent of the conditions in which the materials were tested (CHEN; LI; COOK, 2009; LI; OLOFSSON, 2017). In one hand, the presence of pores in the surface reduces the effective contact area between the sintered material and the counter-body, which increases the real contact pressure and the wear rates (DESHPANDE; LIN, 2006; YALCIN, 2009). Its have also been found that, depending on their shape and size, pores beneath the surface can act as stress risers, facilitating crack nucleation and growth. These cracks can propagate between

interconnected pores, causing detachment of material from the surface (VARDAVOULIAS; JOUANNY-TRESY; JEANDIN, 1993; YE; LI; EADIE, 2001). An example where wear rates increase with porosity is presented in figure 15.

Figure 13: Increase of the mechanical properties of sintered steel with sintered density (Schematically).

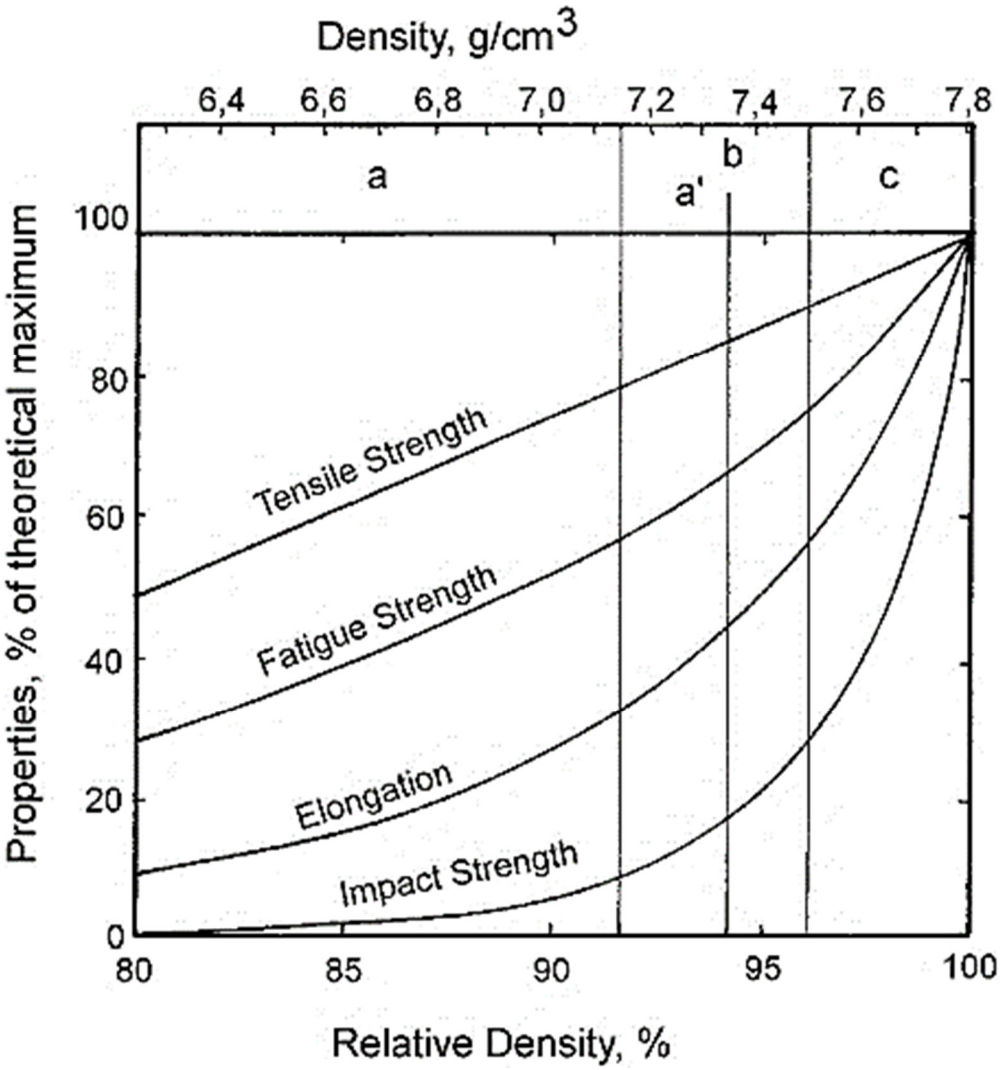

* Letters inside the graph indicate common processing routes with their density ranges: a = press and sinter, a' = hot pressing, b = pressing + pre-sintering, re-pressing and sintering, c = powder forging.
Source: Adapted by the author from Höganäs AB, (2004)

Figure 14: Effect of sintering time in Young's modulus for atomized iron powders sintered at 1200°C

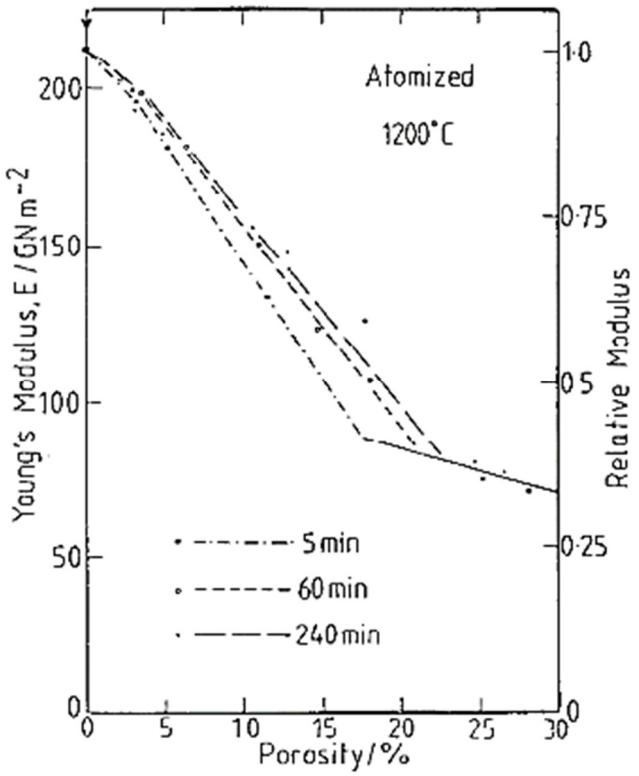

Source: Haynes (1991)

Figure 15: Wear rate of Cu/WC composites sliding against SiC as a function of porosity and load in pin-on-disk tests

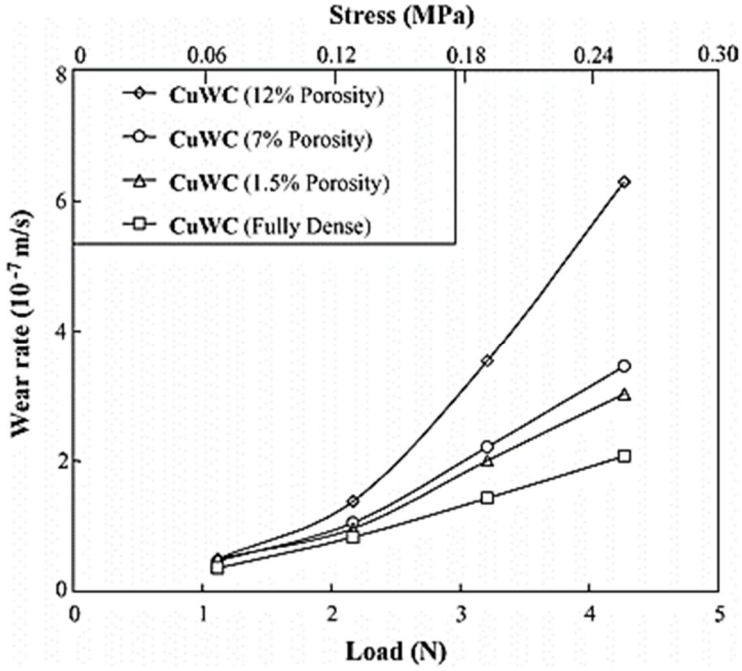

Source: Deshpande (2006)

On the other hand, some studies have pointed out that pores at the surface have a positive effect on the wear resistance. Depending on the size and number of pores, they can act as deposits for debris (figure 16), this has the effect of reducing the number of abrasive particles, avoiding their agglomeration. This also reduces the mass loss during the sliding and rises the real contact area during the test (DUBRUJEAUD; VARDAVOULIAS; JEANDIN, 1994; SIMCHI; DANNINGER, 2004; PRABU et al., 2014; MARTIN; GARCÍA; BLANCO, 2015). Other authors have determined that the predominance of the effect mentioned before depends on the test condition and the size and shape of pores (SIMCHI; DANNINGER, 2004; ISLAM; FARHAT, 2011). Simchi and Danninger found that for sintered iron, there are certain porosity levels where the positive effect of the accumulation of debris in the surface pores was balanced by the negative effect of stress rising and loss of mechanical properties at the surface. This behaviour is shown in figure 17.

Figure 16: SEM images presenting the cross-section of the wear track of sintered iron. The image shows: (a) and (b) closed pores due plastic deformation at the surface, (c) and (d) pores containing debris

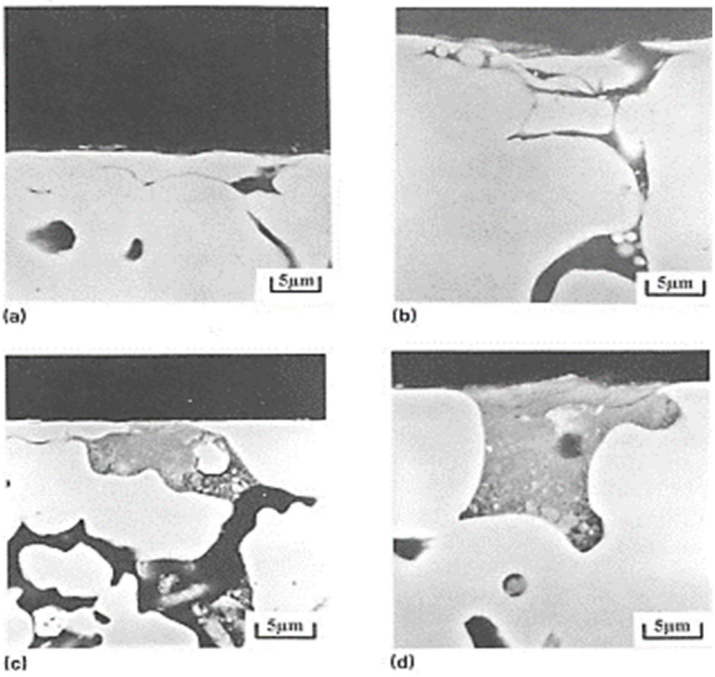

Source: Adapted by the author from Dubrujeaud et al. (1994)

Figure 17: Wear rate of sintered iron as a function of total porosity at different applied loads

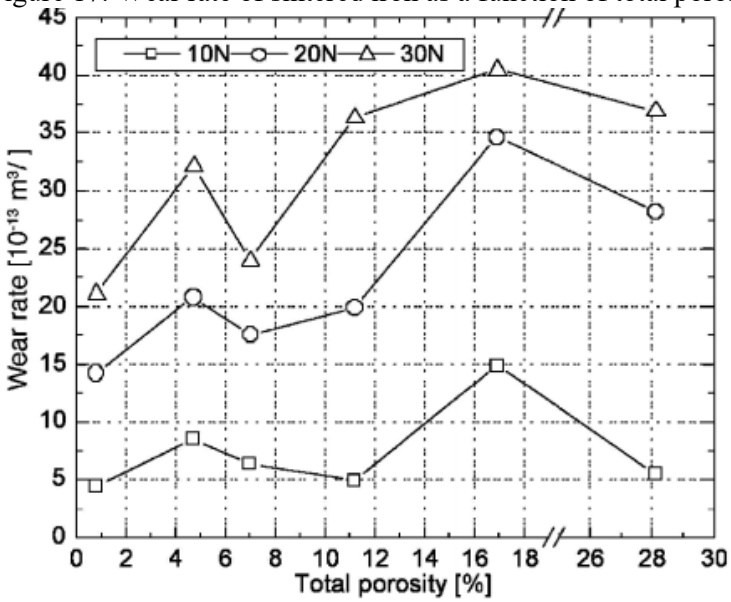

Source: Adapted by the author from Simchi and Danninger (2004)

Besides the quantity, the size distribution of pores has an important effect on the tribological behaviour of sintered materials. Figure 18 shows the changes in wear rates as a function of mean pore sizes in the micro-abrasion tests performed in steam-oxidised sintered iron.

Figure 18: Evolution of the wear coefficient as a function of pore size in micro-abrasion test on steam-oxidized sintered iron using: (a) Alumina, (b) Silica, the numbers besides the symbols (1,2,3 and 4) indicate the abrasive powders sizes (<65, 65–90, 90–125 and >125μm respectively)

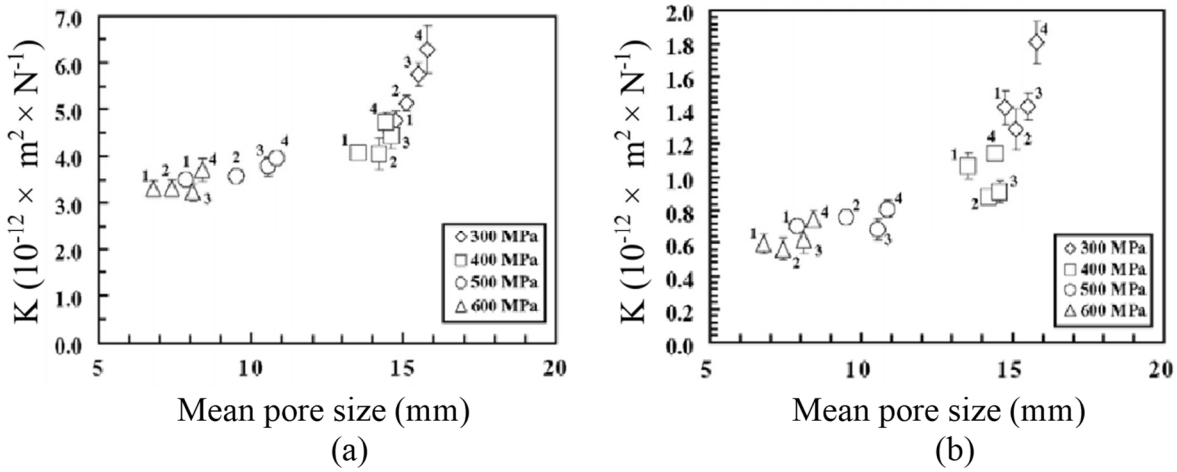

Source: Adapted by the author from da Silva et al. (2005)

In figure 18, the term K is the wear coefficient calculated as the wear volume divided by the load and the sliding distance used in micro-abrasion tests. In this configuration, the wear coefficient rises as a function of pore size. This is explained by the fast filling of small pores with abrasive particles at the start of the test (figure 19 (a)) which increases the mechanical and wear resistance at the surfaces. Bigger pores are slowly or partially filled with abrasive particles and remain open during the tests, so they do not contribute to increase the wear resistance of the material (DA SILVA; BINDER; DE MELLO, 2005).

In another work, de Mello and Hutchings proved that the mean free path also contributes to the durability of the oxide layer in steam-oxidised sintered iron. The durability of the oxide layer is directly related to the wear resistance of these materials (DE MELLO; HUTCHINGS, 2001). Figure 20 shows the influence of the mean free path in the durability of the oxidised layer in a ball-on-flat reciprocating test.

Figure 19: Surface pores inside the wear tracks of sintered iron with mean pore sizes of (a) 10 μm and (b) 20 μm

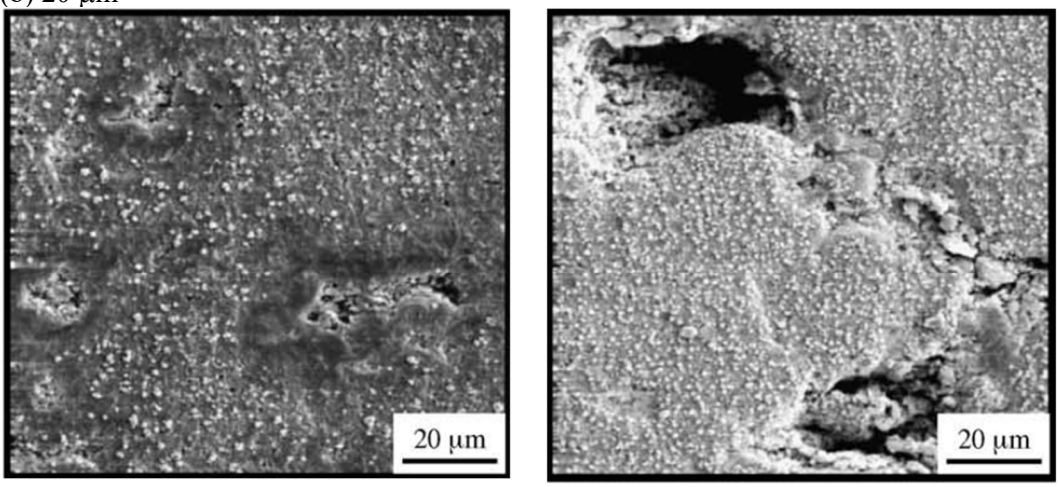

(a) (b)

Source: Adapted by the author from da Silva et al. (2005)

Figure 20: Influence of the mean free path (M.F.P) on the durability (D_d) of the oxide layer in steam-oxidised sintered iron compacted at 300, 400, 500 and 600 MPa

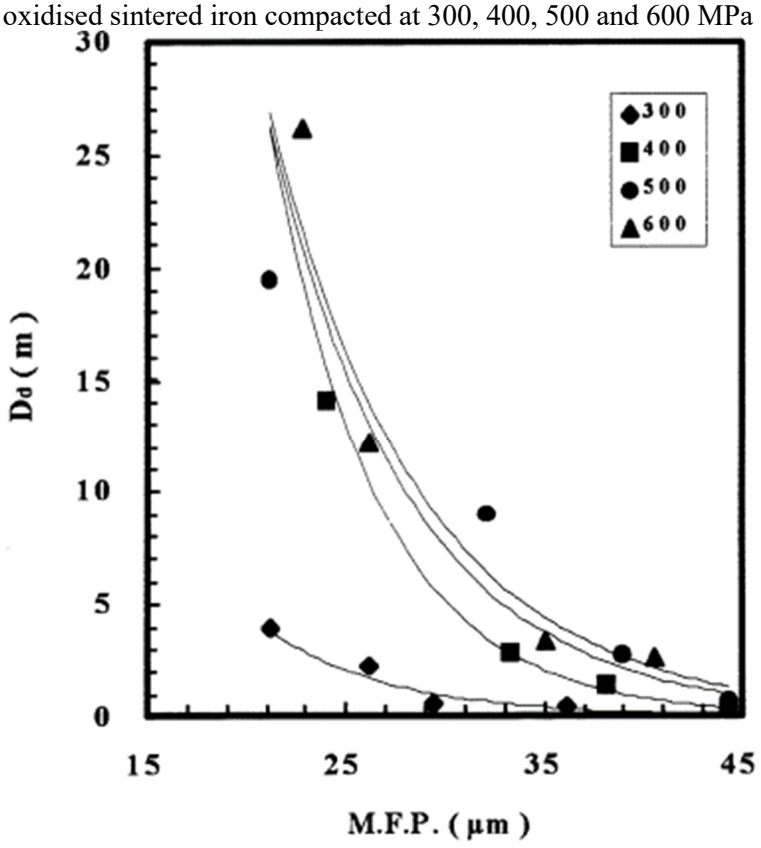

Source: de Mello and Hutchings (2001)

In conditions where lubrication is present, the wear rate is reduced as a function of the porosity because pores act as lubricant reservoirs during tribological testing (MARTIN; GARCÍA; BLANCO, 2015; LI; OLOFSSON, 2017). This capacity of pores to stock lubricant allows the use of porous materials for tribological applications. In this work, vacuum impregnation was used to obtain samples of sintered steel containing graphite in its pores. The following section explains how the vacuum impregnation process works.

2.3 VACUUM IMPREGNATION OF POROUS MATERIALS

The impregnation of porous materials can modify their properties and is widely used in the industry. Impregnation processes are applied to the sealing of pores and cracks in high-performance materials (ASM INTERNATIONAL HANDBOOK COMMITTEE, 2002), to include a reinforcement phase in structural materials (XU et al., 2017) and to include a

lubricating phase (liquid or solid) in materials for tribological uses (BRAITHWAITE, 1964; LIU; CHEN, 2014c; STACHOWIAK; BATCHELOR, 2014b) (to name some examples). The impregnation process begins by submerging the part that will be impregnated in a liquid or dispersion. Then, impregnation can happen in three ways:

1. Using pressure above the atmospheric to force the penetration of the fluid in the pores of the material.
2. To use vacuum to extract the air inside the pores of the porous material, then break to vacuum, so atmospheric pressure forces the penetration of fluid into the pores.
3. Vacuum impregnation followed by the application of pressures above the atmospheric pressure with the sample still submerged in the fluid.

The first method has the advantage to allow the penetration of fluids with low wettability but, to obtain an adequate level of penetration of fluid, the impregnation equipment must have the capacity to withstand extremely high pressures with safety. This is also a disadvantage of the third method. Vacuum impregnation is a process easy to implement and operate, where the penetration of the fluid will be determined by the wettability of the fluid and the vacuum applied (SHELL; WALFORD, 1956).

Figure 21 shows a schematic of an impregnation cycle. To simplify the process, a system of 3 interconnected pores of diameters d_1, d_2 e d_3 where $d_3 < d_1 < d_2$ is considered according to figure 21 (a). With this in mind, the impregnation cycle can be summarised in the following steps:

1. The porous material is submerged in a dispersion of graphite in acetone (figure 21 (a)), the dispersion fills some surface pores until reaching the equilibrium condition given by equation 6.

   $$P_{g1} = P_l = P_{atm} + P_C \qquad (6)$$

   Where P_g is the air pressure inside the pores, P_l is the pressure in the liquid, P_{atm} is the atmospheric pressure and P_c is the capillary pressure given by the Young-Laplace equation

   $$P_c = \frac{2\sigma}{R} \qquad (7)$$

   Where σ is surface tension and R is the curvature radius of the pore.

2. Then the system is placed under vacuum ($P = P_{vacuum}$). In this condition, the air inside the pores is extracted from the material following the pressure gradient until the air pressure inside the pores is in equilibrium with P_{vacuum} (figure 21 (b)).
3. Once the extraction of the air inside the pores is finished, the atmospheric pressure is restored. As now the pressure of the air inside the pores is less than the pressure outside, the liquid can access new pores, compressing the gas until the equilibrium condition given by equation 8 is reached (figure 21 (c)).

$$P_c = \frac{2\sigma}{R} \qquad (8)$$

4. Finally, the material is taken out of the dispersion and placed at a temperature that allows the evaporation of the fluid, leaving only the solid materials inside the pores (figure 21(d)).

Figure 21: Impregnation cycle (schematic)

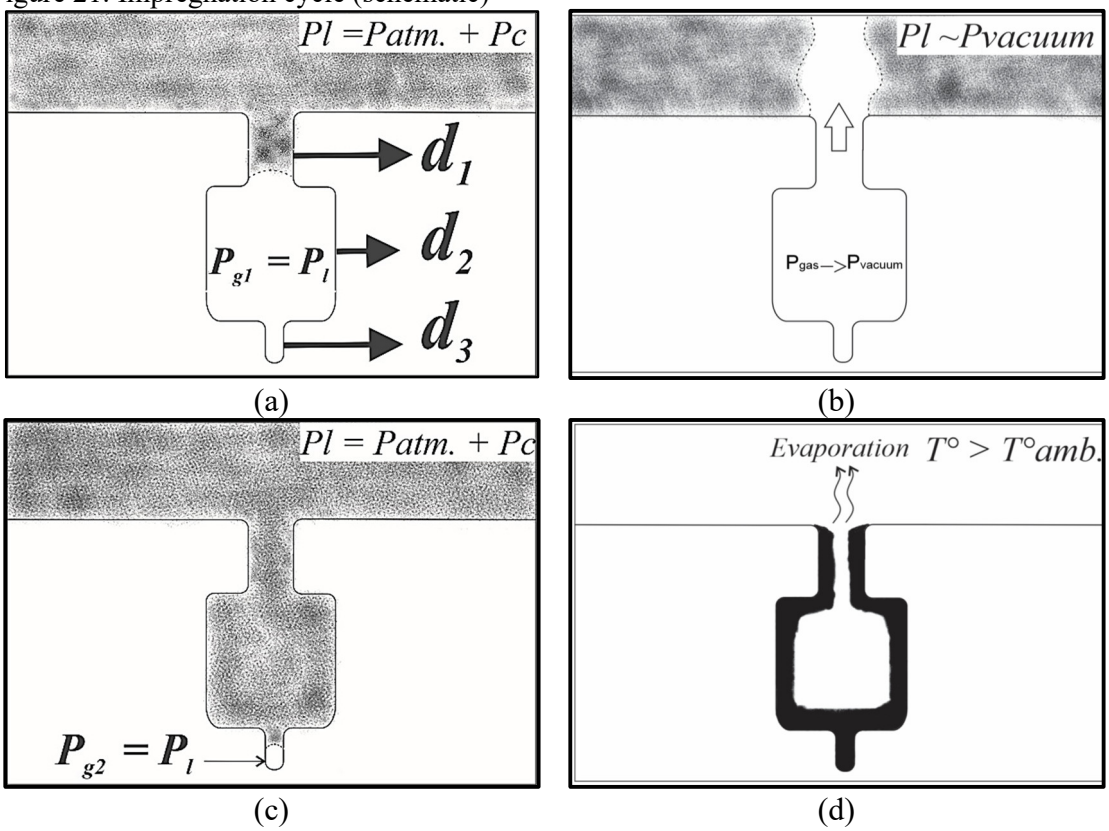

Source: Author

As capillary pressure is inversely proportional to the curvature radius of the pores, small pores are more easily impregnated by a wetting fluid. However, when the impregnating

fluid is a suspension, the minimum size of pores that will be impregnated is determined by the particle size of the impregnated solid.

2.4 RAMAN SPECTROSCOPY APPLIED TO GRAPHITE AND GRAPHITE-RELATED MATERIALS

The Raman effect is the change in wavelength of light being scattered by a solid or fluid material due to the interactions between the incident photons and the electronic bands of the material (FERRARO; NAKAMOTO; BROWN, 2003b). The Raman scattering effect is a very weak effect; only one in a million of the scattered photons exhibits this change in wavelength. Even so, as the change in wavelengths depends on the electronic bands, hence, the chemical bonds and structure of the materials, the scientific community quickly realised its power as a non-destructive characterization tool (BOHNING, 1998). More details about the physics involved in Raman scattering can be found in references (FERRARO; NAKAMOTO; BROWN, 2003a; JORIO et al., 2011a; LARKIN, 2011; TAN, 2019).

In Raman spectroscopy, a monochromatic light (Laser) is directed towards the sample to be analysed. This light is reflected by the sample resulting in a spectrum where the Y-axis is the intensity of the scattered photons and the X-axis is the change in wavelength denoted as Raman Shift (cm^{-1}).

With the advent of laser technology, the Raman spectroscopy of completely black materials like carbon black and graphite became a possibility. In 1970, F. Tuinstra and J.L. Koenig published their seminal work entitled “Raman Spectrum of Graphite” where they successfully applied a laser source to mono and polycrystalline graphite (TUINSTRA; KOENIG, 1970b). In their work, they identified the two main features of the Raman spectra of graphite: The G and D bands which are shown in figure 22. The G band located at 1575 cm^{-1} is a first-order vibrational mode with E2g resonance which means that its intensity is related to the excitation and relaxation (breathing) of the atomic bonds located in the basal planes of graphite (WU; LIN; TAN, 2019) as shown in figure 23. The disorder-induced D band is produced by the break on symmetry induced by the presence of defects inside the basal planes

of graphite. These defects (mainly dopants, vacancies and boundaries) activate new vibrational modes that are forbidden for perfectly crystalline structures (JORIO et al., 2011b).

Figure 22: Raman spectra of mono (a) and poly (b) crystalline graphite

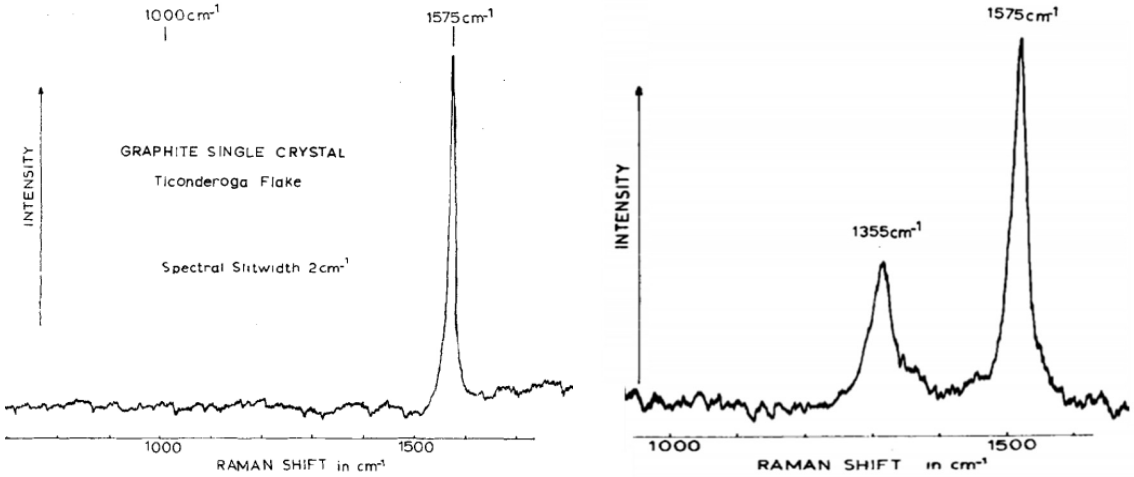

(a) (b)

Source: Adapted by the author from Tuinstra and Koenig (1970)

Figure 23: Breathing mode of the basal planes of graphite

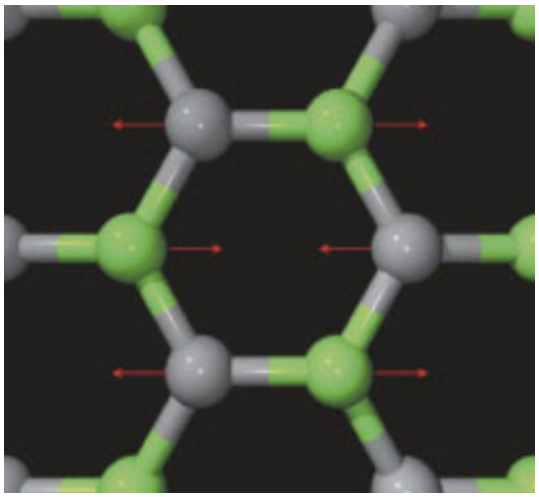

Source: Jorio et al. (2019)

Figure 24 shows the Raman spectra inside and outside a graphite crystallite deposited on a glass substrate. As shown in figure 24, the D (and D') bands are active in the crystallite boundaries that are regions of disorder. In these regions, the crystal lattice is not perfectly symmetric which activates the vibrational modes related to the D band.

The Raman spectrum of graphite also shows the so-called second-order bands which are bands produced by double resonance processes. These double resonance processes involve

one photon creating two phonons and generally include overtones and combinations of the D and G bands (JORIO et al., 2011c). In the second-order Raman spectrum, the most interesting feature is the 2D (also called G') band. The 2D band is observed for all sp^2 carbons as a peak (or multipeak feature) in the range 2500-2800 cm^{-1} depending on laser energy (JORIO, 2012). The number of peaks and bandwidth of this feature is sensitive to the stacking order and the number of layers (in the case of graphene) being analysed (MARTINS FERREIRA et al., 2010). This makes this feature a powerful tool to quantify the number of layers in a graphene film and to obtain information about the stacking order in graphitic materials (FERRARI; BASKO, 2013; MOGERA et al., 2015).

Figure 24: Confocal Raman images of a 6 nm-high highly ordered pyrolytic graphite (HOPG) crystallite deposited on a glass substrate: Raman image obtained by plotting the spatial dependence of the G-band intensity (a), Raman image obtained by plotting the spatial dependence of the D-band intensity (b) and their corresponding Raman spectra (c)

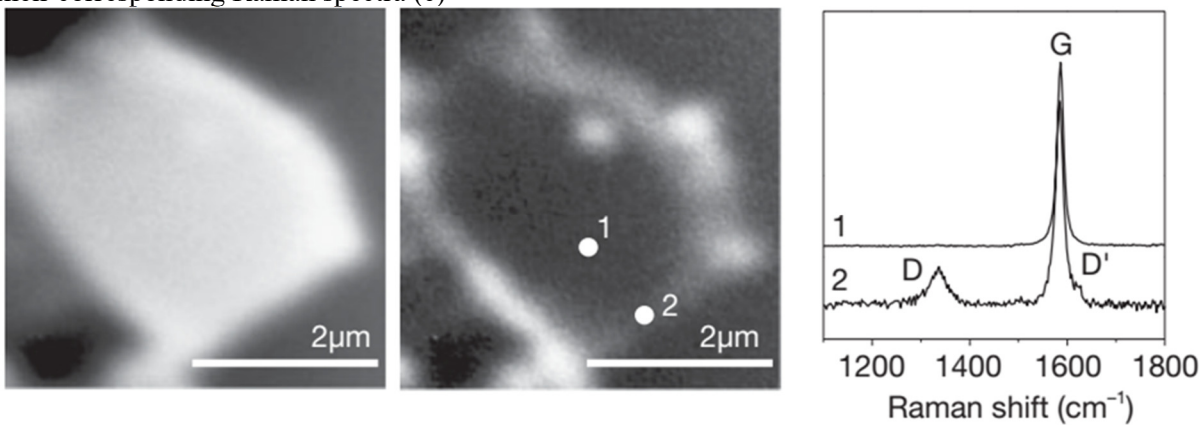

(a) (b) (c)

Source: Jorio et al. (2011)

The changes in the 2D band as a function of number of layers and stacking order are summarized in figure 25. In this work, the number of peaks of the 2D band was used to assess the differences in the structural order in the c-axis between crystalline graphite and CDC.

Figure 25: Evolution of the 2D band for: 1 (a), 2 (b), 3 (c) and 4-layer graphene. Also, for highly ordered pyrolytic graphite (HOPG) (e) and turbostratic graphite (f)

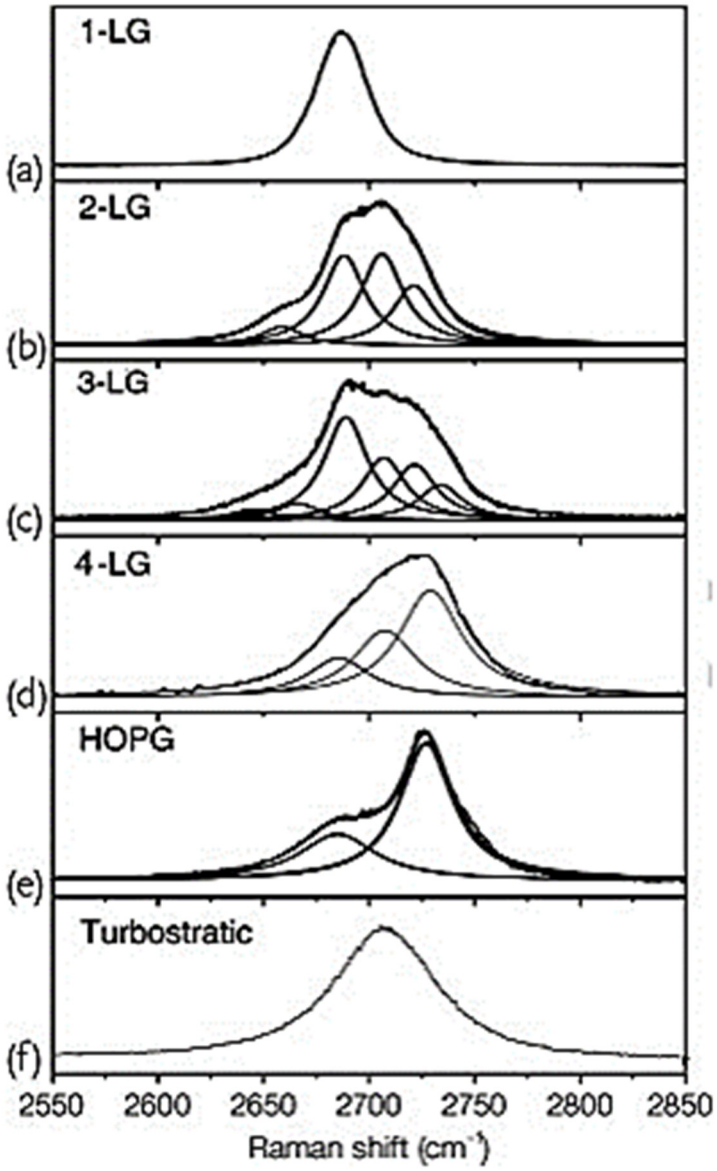

Source: Jorio et al. (2011).

In another work also published in 1970, Tuinstra and Koenig used x-ray diffraction to calculate the crystallite sizes of various types of polycrystalline graphite fibres. They then correlated the results with the intensity ratios of the D and G bands (ID/IG), as shown in figure 26, resulting in the Tuinstra-Koenig equation: I(D)/I(G) = 4.4 /La, where La is the crystallite size in nm (TUINSTRA; KOENIG, 1970a).

Figure 26: Crystallite sizes measured by x-ray diffraction of graphite fibres as a function of their ID/IG ratios obtained from their respective Raman spectra

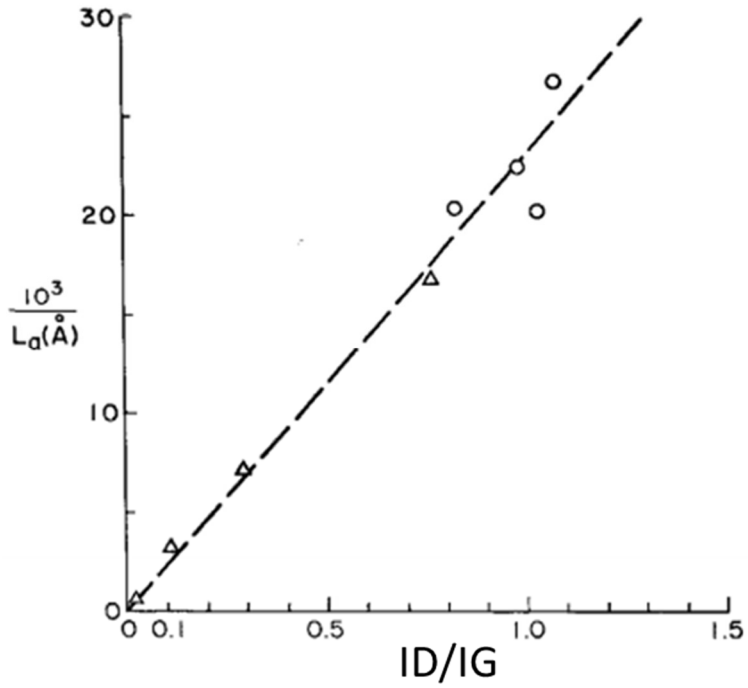

Source: Adapted by the author from Tuinstra Koenig (1970)

In 1990 Wang, Alsmeyer & Mc Creery showed that the D band is not only related to the crystallite size, but also the breaking of symmetry due to the presence of any defect which is enough to activate this vibrational mode (WANG; ALSMEYER; MC CREERY, 1990). Continuous efforts were made in order to correlate the intensities of the D and G bands with the crystallite size of graphite. In 2000, Ferrari and Robertson found that the position of the G band, as well as the ID/IG ratio, changed not only with crystallite size but also with the fraction of sp^3 hybridization inside the material. The sp^2 carbon changes to an sp^3 hybridization state by the introduction of structural defects in the lattice. This process of transition between and ordered sp^2 graphite and disordered sp^3 amorphous carbon is called amorphization trajectory (FERRARI; ROBERTSON, 2000). The evolution of the position of the G band and the ID/IG ratios as a function of sp^3 hybridization is shown in figure 27. As shown in the figure, first crystalline graphite transforms to nanocrystalline graphite (NC-graphite), then it becomes amorphous carbon when the quantity of sp^3 bonds reaches 20% finally, when the quantity of sp3 reaches 85% it becomes tetragonal amorphous carbon (ta-C).

Figure 27: Amorphization trajectory, showing a schematic variation of the G position and ID/IG ratio

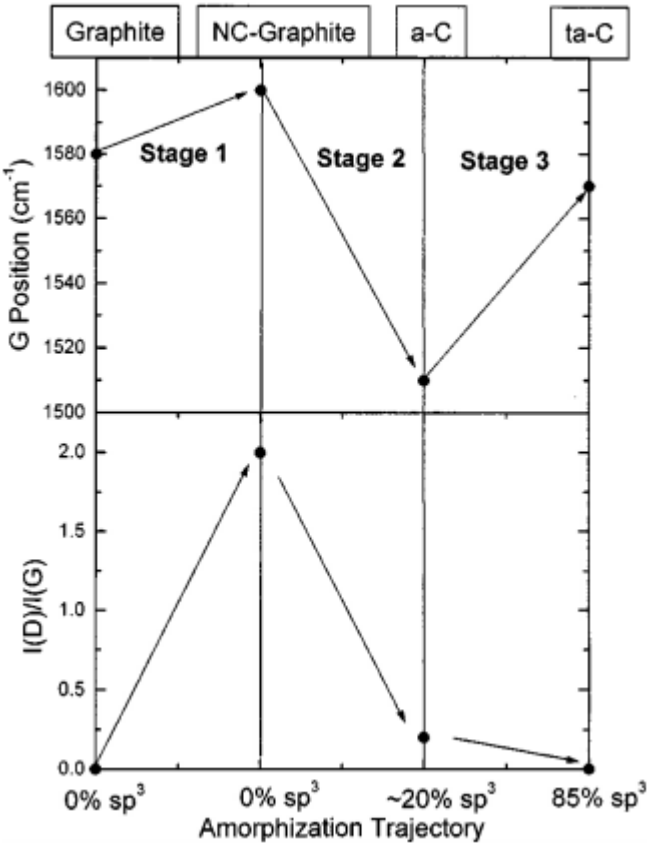

Source: Ferrari & Robertson (2000)

Considering how the ID/IG ratios depend not only on the crystallite boundaries but also on other kinds of defects, Cançado et al. developed the Tuinstra–Koenig\Cançado relation shown in equation 9.

$$\left(\frac{A_D}{A_G}\right) = \frac{\frac{560}{E_L^4}}{L_a} \qquad (9)$$

Where A_D and A_G are the integrated intensities (areas under the curve) of the D and G bands respectively, E_L is the laser energy and L_a is the crystallite size in nm (CANÇADO et al., 2006). This equation is only valid for crystallite sizes above 20 nm and without the presence of defects other than boundaries.

In 2017 Cançado et al. tackled the problem of disentangling the contribution in the Raman spectrum of point (0D) and line (1D) defects. Vacancies, impurities and dopants are considered as point defects as they break the symmetry of the lattice only around the point where they are located. They affect a circular area around their location (shown in green in

figure 28(a)) and the distance between them is called L_D. With this distance, the point defect density (σ) can be calculated as $\sigma = 1/(L_D)^2$. Crystallite boundaries are considered line defects; they break symmetry in the boundaries between crystallites affecting the area around them (shown in green in figure 28(b)). The mean distance between line defects is called La and corresponds to the mean crystallite size of the material. Finally, figure 28 (c) shows how a more realistic disordered graphite is structured with line and point defects randomly distributed.

Figure 28: Illustration of graphite with point defects (a), line defects (b) and both (c)

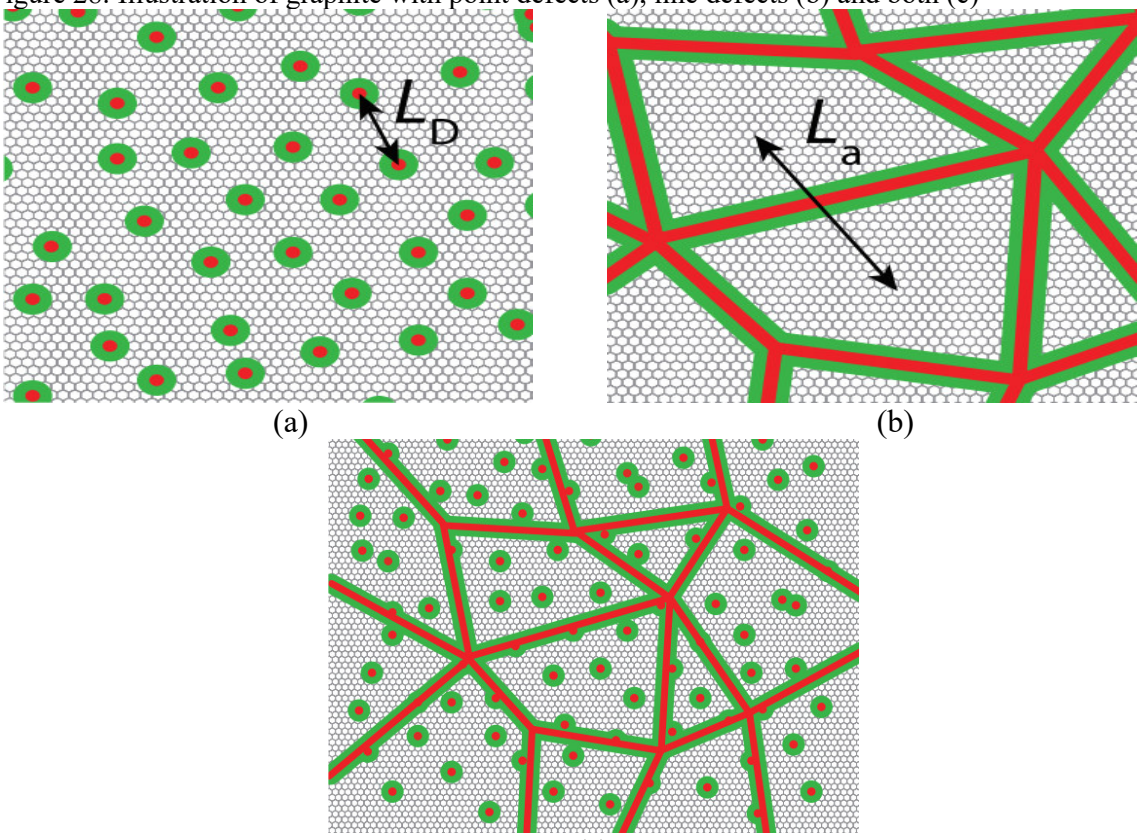

(a) (b)

(c)

Source: Adapted by the author from Cançado et al. (2017)

To disentangle the contributions of point and line defects to the Raman spectra of sp^2 carbon, Cançado et al. prepared two types of samples:

1. Samples of HOPG in which, L_a is considered to approach infinity and the L_D was decreases by ion bombardment. The quantity of point defects (and consequently L_D) as a function of the ion dosage was known from previous works (CANÇADO et al., 2011).
2. Samples of HOPG amorphized by laser ablation and then heat-treated at different temperatures to obtain increasingly larger crystallite sites (which were determined by x-ray diffraction). In these samples is considered that $L_D \rightarrow \infty$.

As two types of defects were being quantified, two spectral features were needed. In this case the authors used the ratio between the integrated intensities of the D and G bands times the laser energy to the power of four ($(A_D/A_G)*E^4_L$) and the full width and half maximum of the G band (Γ_G) as both features have been extensively used to quantify defects in graphitic materials (FERRARI; ROBERTSON, 2000; CANÇADO et al., 2004; CANÇADO, 2006; FERRARI, 2007; JORIO; FILHO, 2016). The extensive analysis of the Raman spectra and computational simulations (whose details are out of the scope of the present work) derived in the creation of the Raman diagrams (shown in figure 29. The Raman diagrams (and their related equations) allow obtaining the point defect distance (L_D) and line defect distance (L_a) of any graphitic material by fitting the first order D and G bands of the Raman spectra. Details about how the Raman diagrams are obtained can be found in (CANÇADO et al., 2017), details of how the spectra are fitted can be found in (RIBEIRO-SOARES et al., 2015). It must be considered that this model only works for spectra whose parameters fall between the dashed and continuous lines in figure 29 or corresponds with some of the coloured experimental curves shown in the figure. It also must be noticed that for some combinations of L_a and L_D it is possible to find more than one combination of $(A_D/A_G)*E^4_L$ and Γ_G as both parameters are influenced by the line and point defects simultaneously.

Figure 29: Raman diagram for point (a) and line (b) defects.

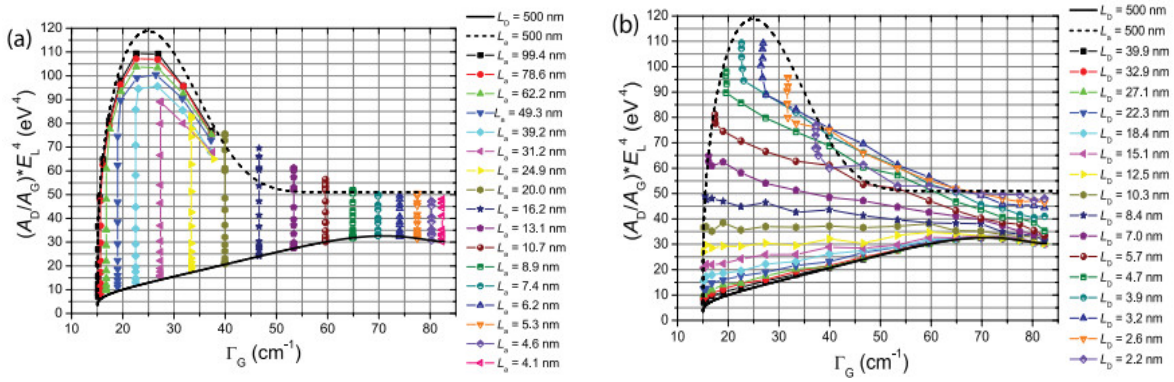

Source: Cançado et al. (2017)

Up to date, this is the most advanced use of the Raman spectra to quantify defects in graphitic materials and has been used to develop a parameterized principal component analysis (PCA) for large scale analysis and characterization of sp^2 carbon materials (for example as a quality control tool in the production of graphene) (CAMPOS et al., 2018). In this work, this method was used to characterize the graphite present in the tribolayers generated by the scuffing resistance test and to characterize the carbide-derived carbon used in this work. The carbide-derived carbons are presented in the next section.

2.5 SYNTHESIS OF CARBIDE DERIVED CARBONS AND THEIR TRIBOLOGICAL APPLICATIONS

Carbide derived carbons (CDCs) are carbonaceous materials derived from the decomposition of carbides by chemical or physical methods (WANG; GAO, 2009). The most common CDCs are produced by the reaction between one or more carbides with halogen gases like F_2 or Cl_2 (URBONAITE, 2008). In recent years progress has been made in the development of a new way to obtain CDCs by solid-state reactions. These reactions can be between carbide and a transition metal (BINDER et al., 2017) or between two carbides. This last method is under development and is part of the doctoral thesis of M. Sc. Guilherme Neves from the LABMAT-UFSC.

The production method determines the tribological applications of the CDCs. Now a brief review of the tribological performance of these materials will be presented.

2.5.1 CDCs produced by solid-gas reactions

The first synthesis of CDC was performed at the beginning of the 20th century, but the objective at the time was to obtain metal chlorides, leaving carbon as a residue (URBONAITE, 2008). In the last decades, the CDCs have been extensively studied due to their electric properties (WANG; GAO, 2009), high surface area (URBONAITE, 2008), and tribological properties (CHUN; LIM, 2014).

For tribological applications, the CDCs are usually synthesised by the selective etching of SiC, B_4C or TiC with chlorine of fluorine gases. The product of this process is a lubricating film deposited in a ceramic substrate, as shown in figure 30.

Figure 30: Cross-section of a CDC film grown as a film in its precursor

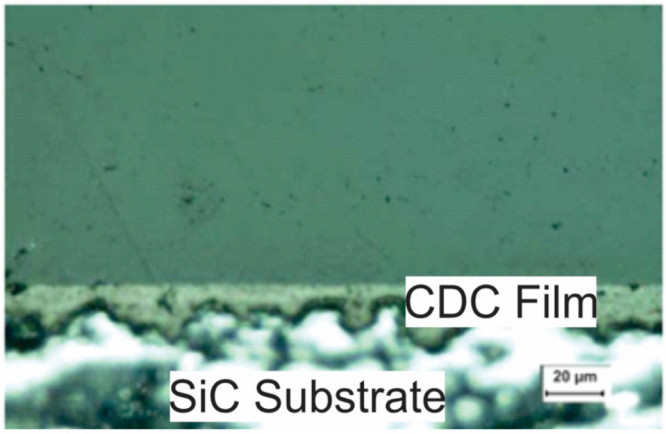

Source: Adapted by the author from McNallan et al. (2005)

Depending on the processing parameters, the allotropes present and the degree of graphitisation of the CDC are affected, which in turn affect the tribological behaviour of the material (CHUN; LIM, 2014). At low synthesis temperatures, the CDC presents a mixture of sp^2 and sp^3 hybridization resulting in an amorphous material (URBONAITE; HÄLLDAHL; SVENSSON, 2008). At higher temperatures, carbon starts to organise, increasing the amount of sp^2 hybridisation and becoming more graphitic. The ratio between sp (linear), sp^2 (planar) and sp^3 (three-dimensional) hybridisation determines the allotropes present in the CDC, as presented in figure 31.

Figure 31: Ternary phase diagram for carbon allotropes

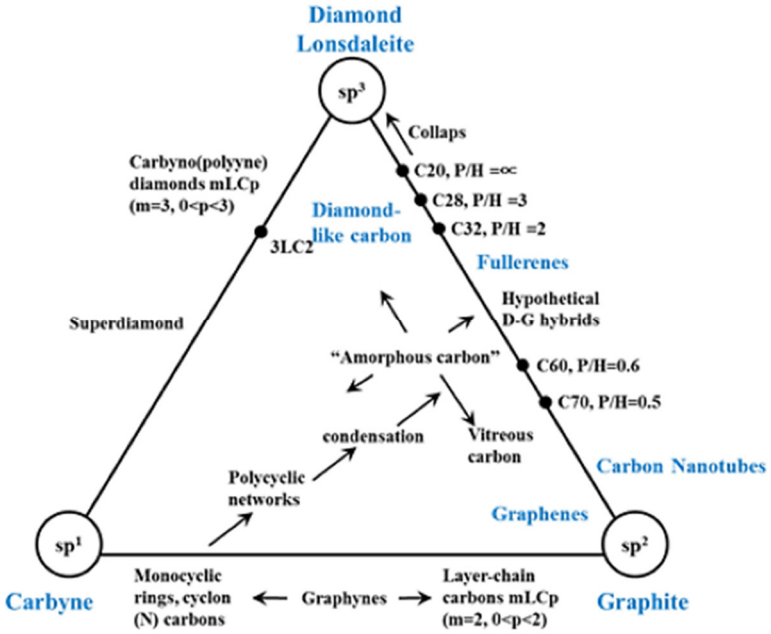

Source: Chun and Lim (2014)

Figure 31 is relevant because a significative difference in the tribological performance of carbon materials as a function of the type of hybridisation and allotropes present has been reported in the last decades (ZHAI et al., 2017). For example, Bushan and Gupta proved that fullerene coatings could induce coefficients of frictions below (0.12) of those induced by common DLC films (0.2) in Al_2O_3-TiC pairs at atmospheric conditions (BHUSHAN; GUPTA, 1994). Also, Mabuchi et al. studied the effect of the sp^2/sp^3 ratio on the tribological performance of DLC films. They found that the coefficient of friction in air induced by these films in pin-on-disk tests diminishes when the amount of sp^3 bonds increases (MABUCHI; HIGUCHI; WEIHNACHT, 2013). Finally, a study performed by Kumar et al. proved that the tribological behaviour of graphite blocks tested under N_2, Ar and air is heavily influenced by the amount of sp^2 hybridisation and the density of defects in the material (KUMAR et al., 2011). In the case of CDCs the presence of nano-onions and turbostratic graphite has been credited as the origin of the low friction coefficients induced by these materials (WELZ, 2003; WELZ; MCNALLAN; GOGOTSI, 2006). However, depending on the synthesis condition these solid-gas reactions CDCs can present other structure like amorphous carbon, nano-diamonds, carbon nanotubes, Buckminster fullerenes and crystalline graphite (CHUN; LIM, 2014) so addressing

the exact influence of each allotrope in the tribological behaviour of these materials becomes challenging and more research in this topic is needed.

The effect of the test atmosphere and the inclusion of hydrogen during the synthesis process have also been investigated. Hydrogen is usually added in the synthesis process to control the reaction rates and to refine the crystalline structure of the CDC (ERDEMIR et al., 2004). The utilisation of hydrogen lowers the coefficient of friction of CDCs grown in SiC substrates (figure 32) due to the passivation of dangling bonds inside the material (CHUN; LIM, 2014).

The application of solid-gas reaction CDCs allows obtaining a ceramic material with high wear resistance and low coefficients of friction but the fact that the CDC is bonded with ceramic material and that the process requires the use of halogen gases at high temperatures severely limits the applications for these CDCs.

Figure 32: Friction behaviours for as-received and hydrogen-treated CDC films in open air and dry nitrogen

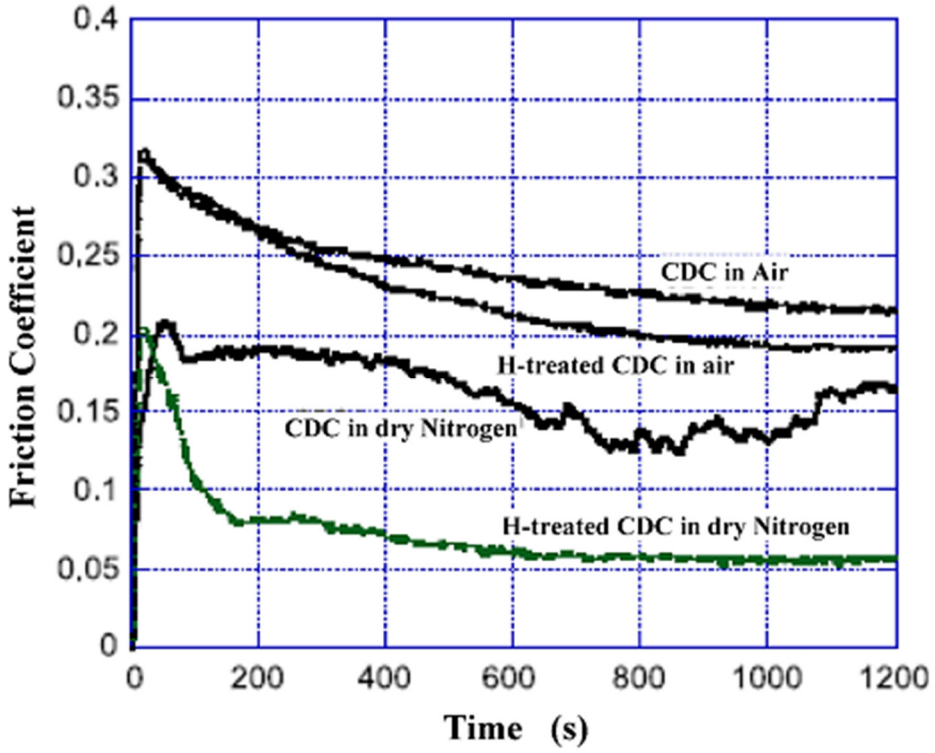

Source: Chun and Lim (2014)

Another promising route to obtain CDCs for tribological application is the solid-state reaction route which is presented in the next section.

2.5.2 CDCs produced by solid-state reactions

Chamberlain first reported solid-state reactions between SiC and Ti in SiC substrates sputtered with Ti in 1980 (CHAMBERLAIN, 1980). In 1989 Backhaus-Ricoult extensively studied the reactions between SiC and Ni, Fe, and Ti (BACKHAUS-RICOULT, 1989). Later in 1991, Cho, Joshi & Wadsworth extended this study to Co and Pt (CHOU; JOSHI; WADSWORTH, 1991). In these works, the SiC-metal reaction is studied by using diffusion pairs where two solid blocks (one made of SiC and one made of metal) are put under pressure and reacted at high temperatures. In these works, several carbides and silicides were found along with carbon which was considered as a residue as the goal of the studies was to obtain tightly bonded metal-ceramic materials and carbon was detrimental to this bonding. Tang et al. studied in detail the reaction between Fe-SiC in 2002 but again, no special attention was given to the carbon by-products (TANG et al., 2002).

In 2009 the doctoral thesis of Dr. Cristiano Binder focused on the development of self-lubricating sintered steels based on the reaction between Fe and SiC during sintering (BINDER, 2009). In that work, SiC particles are mixed with iron and alloy elements. At the sintering temperature SiC starts to dissociate, silicon and carbon start to diffuse into the steel matrix until the concentration of Si around the SiC particle reaches a critical point where it stabilises α-Fe. The presence of α-Fe around the particle “traps” the remaining carbon which ends up forming a graphite nodule. Figure 33 (a) shows an schematic model of this process and figure 33 (b) presents the typical microstructure of these self-lubricating steels consisting of graphite nodules surrounded by a steel matrix.

Figure 33: Schematic model of the SiC dissociation process (a), typical microstructure of self-lubricating steels (b)

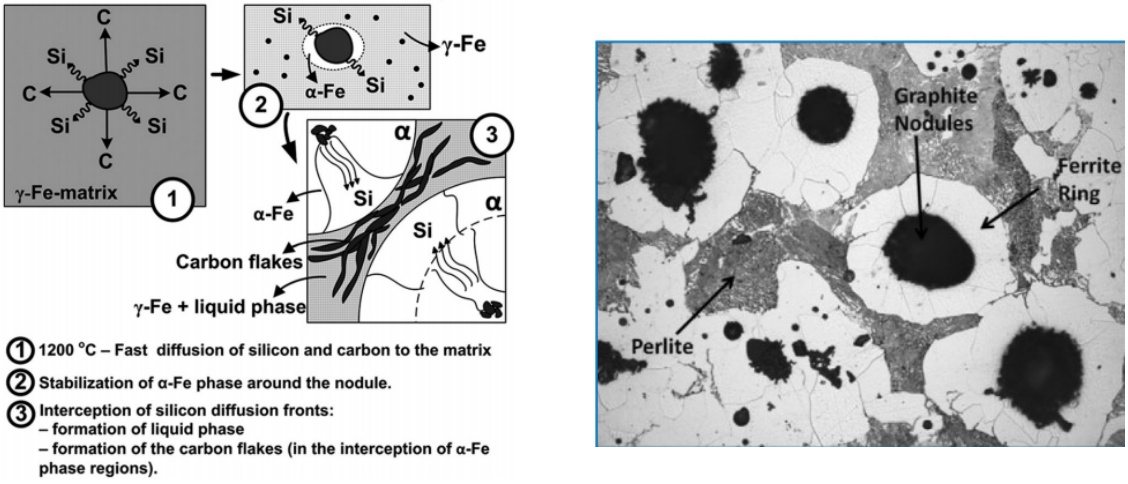

(a) (b)

Sources: Binder et al. (2016) (a) and Schroeder et al. (2010) (b)

The graphite contained in these materials is effectively a solid-state reaction CDC and provides solid lubrication. Figure 34 shows the evolution of friction coefficient and scuffing resistance (durability) as a function of SiC content for self-lubricating steels sintered 1 hour at 1150°C.

Figure 34: Friction coefficient and durability as a function of SiC content measured in Fe + 0.6 wt.%C + variable SiC content (expressed in weight percent) sintered 1h at 1150°C

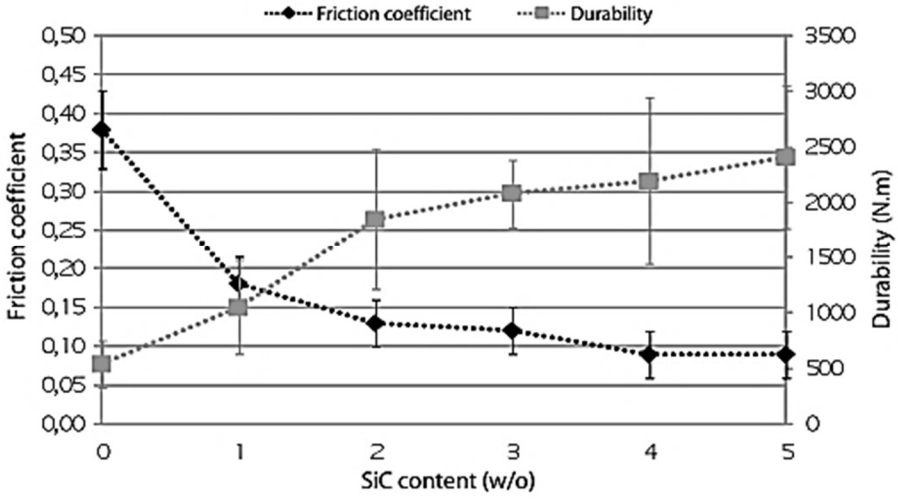

Source: Binder et al. (2010)

Depending on the alloy elements and sintering conditions, self-lubricating steels can induce friction coefficients as low as 0.04 (DE MELLO et al., 2013). The excellent tribological behaviour of these materials has been attributed to the presence of turbostratic graphite (BINDER et al., 2017). As discussed in section 2.1, turbostratic graphite is a carbon allotrope with no three-dimensional order and weak interactions between its basal planes, which facilitates its shearing.

The applications of CDCs produced by this method is limited to self-lubricating steels. However, recent works have been focused on the synthesis of solid-state reactions CDCs in the form of powders to increase the number of possible applications. These studies have been focused on the separation of the turbostratic graphite produced by the Fe-SiC reaction by mechanical (PEREIRA, 2019) and chemical methods (JACQUES DIAS, 2019).

3 METHODOLOGICAL APPROACH

As this work addresses the interaction between the solid lubricant and the lubricant stocks (pores) during tribological testing, it was crucial to develop a methodology which allowed to obtain a self-lubricating composite without physicochemical interactions between the lubricant and the matrix phase (for example due to chemical reactions during sintering). To overcome this difficulty and to understand how the lubricant reservoirs evolve and how the solid lubricant is released, an "ideal system" was designed where the properties of the solid lubricant are completely separated from the properties of the matrix, this was achieved by impregnating porous steels with graphite. The production of specimens with open pores in their surfaces using powder metallurgy was chosen over other techniques such as selective laser ablation (in order to produce superficial pores) o similar texturizing techniques because powder metallurgy is a simple, widely used technique so the results obtained in this works will be more easily translated into industrial applications. The main tribological variables involved in this "ideal" tribological system are presented in figure 35.

Figure 35: Tribological variables involved in the present study

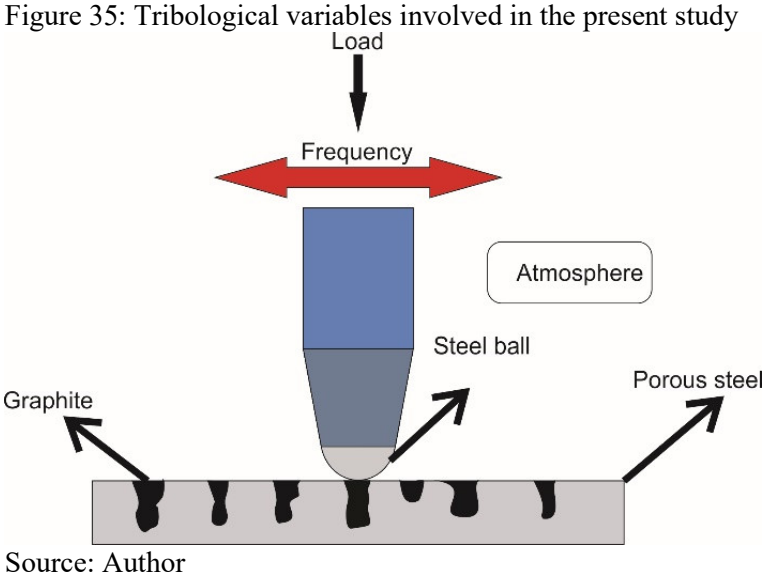

Source: Author

From the variables involved, the material of the counter body, as well as the frequency and the atmosphere were known and remained constant in all the tests. Incremental normal loads were chosen over constant load tests to study the sealing of pores during the tests. This

was because it is expected that the load increments would accelerate the process of pore sealing and, at the same time, would allow to study the effect of the load in the pore sealing process.

The number, size and shape of pores in the specimens and the characteristics of the graphite were varied in order to study their individual effects; a summary of this concept is shown in figure 36.

Figure 36: Schematic representation of the impregnated specimens showing the variables addressed in this work

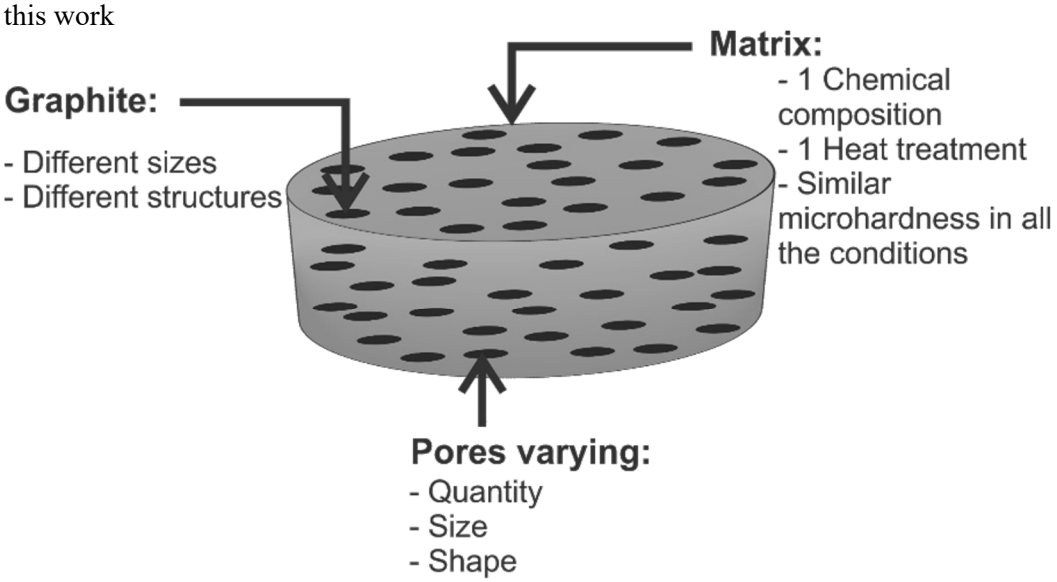

Source: Author

Once the research project was outlined taking into account the considerations and simplifications presented, the materials and characterization techniques necessary in order to achieve the objectives of this work were defined and are presented in the next chapter.

4MATERIALS AND METHODS

4.1 RAW MATERIALS

The technical data of the powders used in this work is listed in table 3. Porous specimens were pressed and sintered from a mixture of Astaloy CRL pre-alloyed iron (a SEM image of the powder is shown in figure 37) and elemental carbon powder (D_{50}= 6.07 μm, shown in figure 38 (c)) in order to obtain porous steels with microhardness above 2000 MPa. This limit is the average hardness of pearlite (PAVLINA; VAN TYNE, 2008) and was defined to obtain a metallic matrix strong enough to delay the sealing of pores during tribological testing.

Table 3: Raw materials

Chemical Composition	**Commercial Name**	**D_{50} (μm)**	**D_{90}/D_{50}**	**Purity (%)**	**Supplier**
Fe + 1.5 Cr + 0.2 Mo	Astaloy CRL	104	3.1	98.84	Höganas
C	Micrograf 9930 MA	21.54	2.1	99.92	Nacional de grafite
C	Micrograf 99507 UJ	6.07	2.2	99.96	Nacional de grafite
C	Micrograf 99501 UJ	1.10	1.9	99.95	Nacional de grafite
C	CDC (B4C-Cr_3C_2)	1.2 - 1.4	2.6 – 2.9	99	LABMAT

Source: Data provided by the suppliers

Figure 37: SEM image of Astaloy CRL powder

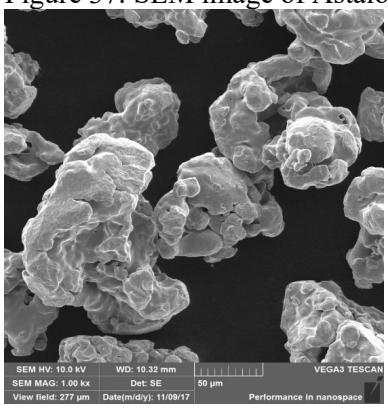

Source: Author

Carbon powders with D_{50} of 1.10, 6.07 and 21.54 μm listed in table 3 were used to study the effect of the particle size in the tribological behaviour of the impregnated steels. Figure 38 shows SEM images of the graphite powders used.

Figure 38: SEM images of the 1.10 μm (a), 6.07 μm (b) and 21.54 μm (c)* crystalline graphite used in this work.

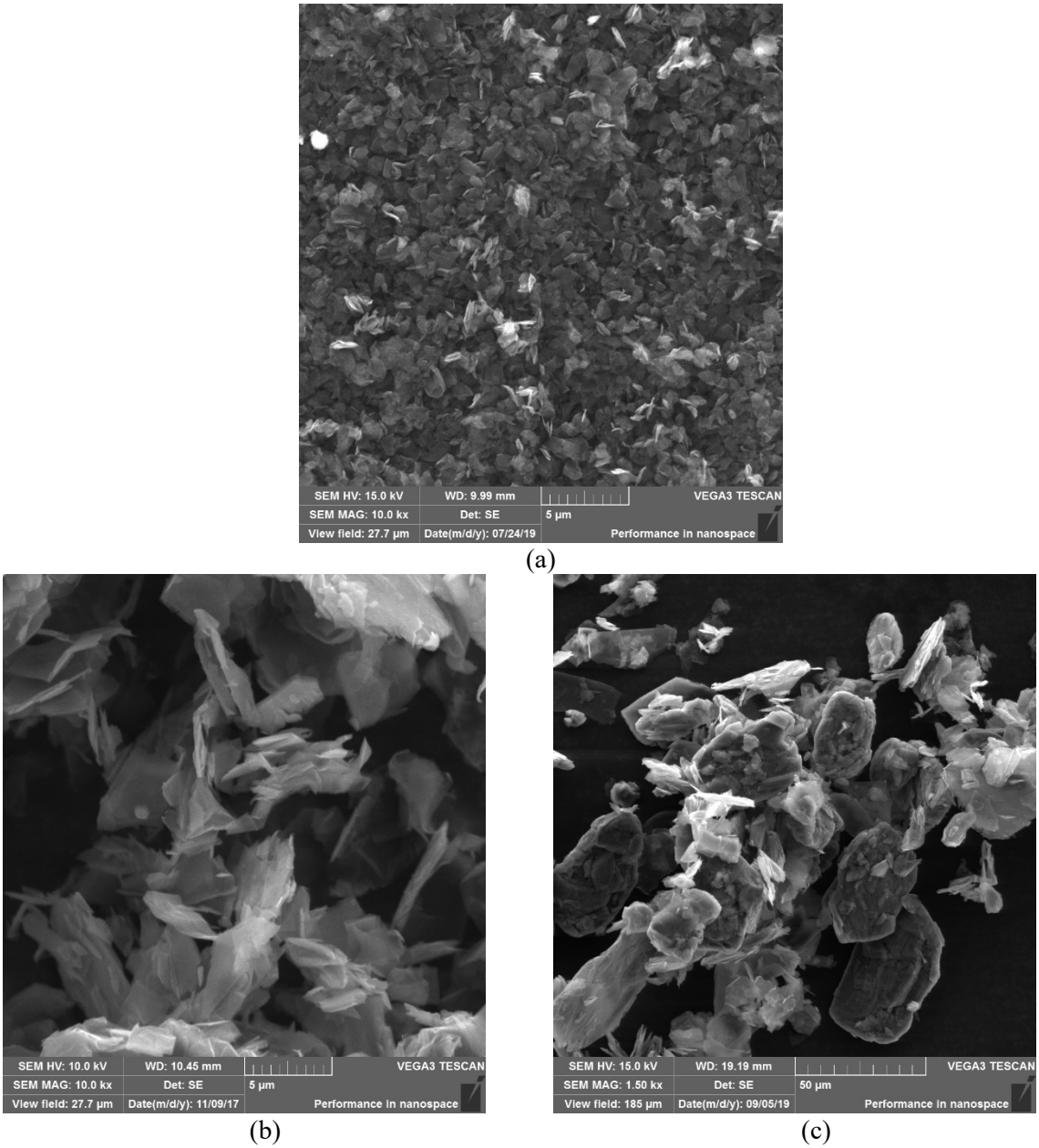

*Figure 36 (c) is zoomed-out for visualisation purposes
Source: Author.

The CDC (carbide-derived carbon) produced by the reaction between Cr_3C_2 and B_4C was supplied by the ongoing doctoral work of the Ph.D. student Guilherme Oliveira Neves and

was used to study the effect of the crystalline structure of graphite in the tribological behaviour of the impregnated sintered steel. A SEM image of the CDC is shown in figure 39.

Figure 39: SEM of the CDC produced by the reaction between Cr_3C_2 and B_4C

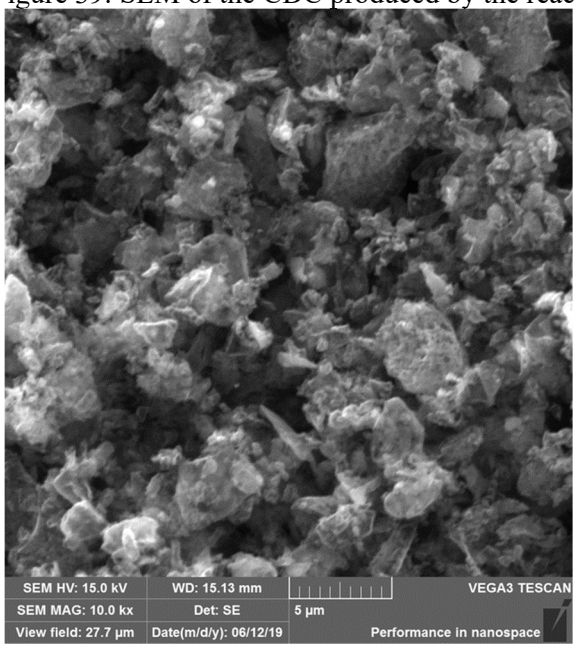

(a)

Source: Author

4.2 MOULDING

Astaloy CRL powder was sieved in the range between 125 and 75 mm and then mixed with 0.6 wt.% carbon powder using an Alphie-3 three-dimensional mixer with a velocity of 60 RPM for 30 minutes. From this mixture, 2 types of samples were produced:

1. Cylindrical samples of 9.9 mm of diameter and 10 mm thickness for microhardness, optical microscopy and image analysis of the porosity.
2. Cylindrical samples of 20 mm of diameter and 15 mm thickness for impregnation and tribological testing.

Samples of 9.9 mm diameter were pressed using a double effect matrix with a Sky uniaxial manual press. Samples of 20 mm diameter were compacted using the same kind of matrix in a Gabrielli semi-automatic press. Compaction pressures used were 200, 400 and 600 MPa to obtain 3 different porosities and pore size distributions.

4.3 SINTERING

The specimens were sintered in a Jung tubular furnace using an Ar - 25vol.% H_2 atmosphere, with a flow rate of 1 L/min. The heating rate was 10° C/min and the time at the sintering temperature was 1 hour. The sintering temperatures used were 1100, 1150 and 1200 °C and the cooling rates after sintering was 7 °C/min with the tube inside the furnace down to 930 °C. Then the tube was pulled from the furnace and cooled at approximately 65 °C/min using mechanical ventilation. Figure 40 presents a schematic diagram of the thermal cycles.

Figure 40: Thermal cycles (schematic)

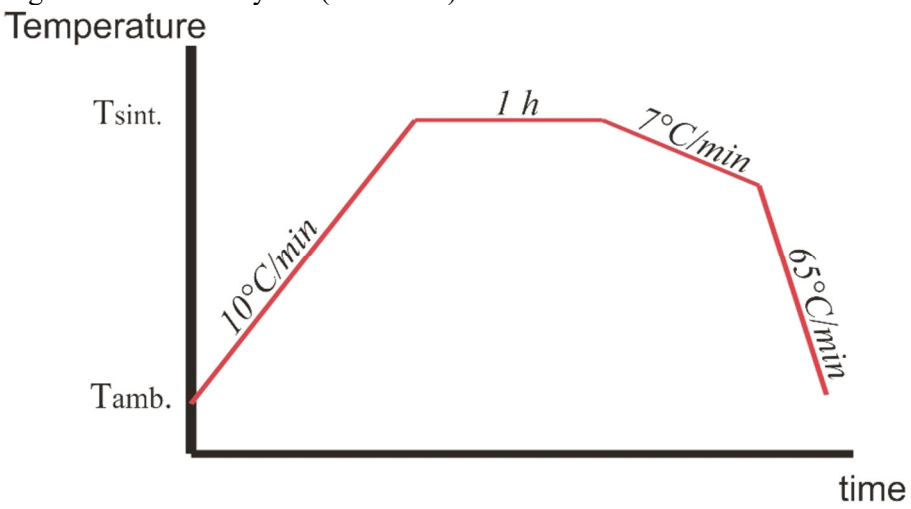

Source: author

4.4 VACUUM IMPREGNATION

Samples were vacuum impregnated in an airtight container connected to an 0.94 kW Eberle vacuum mechanical pump as schematically shown in figure 41. Inside the container, cylindrical samples were placed in a suspension of acetone and graphite. When vacuum is applied, the air inside the porous specimens leaves the specimen. When atmospheric pressure is restored, it pushes the suspension inside of the porous body.

Figure 41: Impregnation system (schematic)

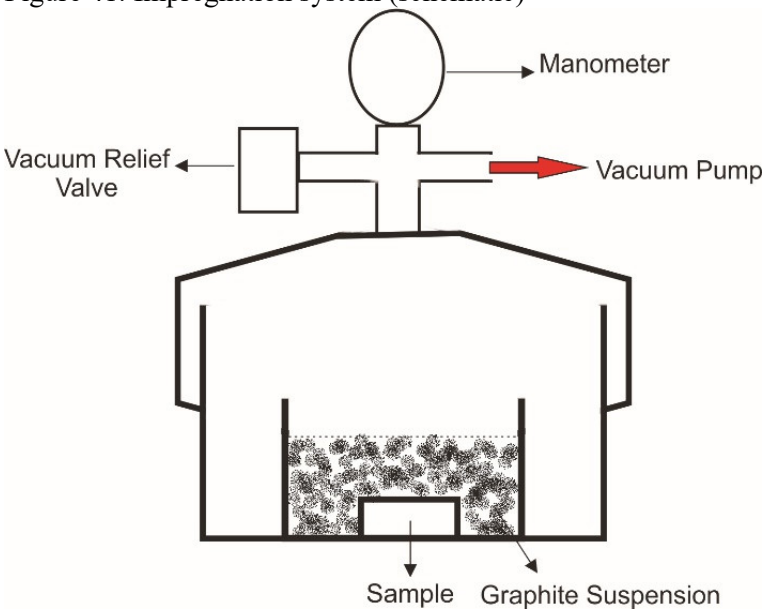

Source: Author

Once the samples are impregnated with the suspension, acetone is volatilized using hot air. This process of impregnation and volatilisation was repeated until the pores were filled with graphite. To achieve a correct impregnation of graphite without leaving residues, a suitable vehicle must be chosen. Table 4 shows the candidate materials that were considered to act as a vehicle for graphite. As graphite in atmospheric conditions is hydrophobic and its sp^2 bonds are non-polar, it must be suspended in a fluid of low polarity (KOZBIAL, 2016). Among the candidates, acetone had the lowest polarity and the highest vapour pressure which made it ideal to both create a stable suspension of graphite and to volatilize afterwards.

Table 4: Polarity and vapour pressure of the available impregnation fluid candidates

Vehicle	**Polarity in relation to water**	**Vapour pressure at 20°C (mm Hg)**
Ethylic alcohol	0.655	44
Isopropyl alcohol	0.617	32
Acetone	0.355	185

Source: Adapted by the author from Reichardt and Welton (2010)

4.5 CHARACTERIZATION TECHNIQUES

4.5.1 Technological properties of the powder mixture

The mixture of Astaloy CRL and carbon was characterised using the flowability test (MPIF standard 03), apparent density (MPIF standard 04) and compressibility (MPIF standard 45).

4.5.2 Sintering dilatometry

Samples of 9.9 mm diameter were sintered 1 hour at 1200 °C using a heat rate of 10 °C/min in a Netzsch 402C dilatometer to study the volumetric changes during the sintering process. The atmosphere was a mixture of Argon – 25vol.% H_2.

4.5.3 Density measurements

The geometric density of the green and sintered specimens was measured using a Metler Toledo XS205 scale with a resolution of 0.01 mg. The dimensions of the cylinders were measured with a Mitutoyo calliper with 0.001 mm of resolution. 9 samples per condition were measured.

4.5.4 Image analysis

For assessment of the shape and size of the pores after sintering, samples were vacuum mounted using an epoxy resin according to the MPIF 69 standard. Images of the surfaces were obtained using a Leica DM 4000 M optical microscope and then analysed with a custom Python 3.6 script built using the Scikit-image package. Python is an interpreted, object-oriented, high-level programming language commonly used in scientific computing due to its user-friendly interface (PYTHON SOFTWARE FOUNDATION, 2019) and Scikit-image is a collection of open source and peer-reviewed algorithms for image processing (SCIKIT-IMAGE, 2019).

The Python script was also used to study the evolution of pores and the carbon distribution in the wear tracks during incremental load tests.

To study the evolution of the number, size and shape of pores, backscattered electrons (BSE) images were processed using a median filter and then binarized. The median filter is used to clean the image, removing the dark regions of the BSE image that do not correspond to pores (marked by the red arrows in figure 42 (a)), so only pores are conserved in the binarized image (figure 42 (b)). The BSE images were chosen over the secondary electrons (SE) images in order to avoid the effect of the topography in the analysis and because it is easier to work with images where there is a sharp contrast between pores (black) and metal (light grey).

Figure 42: BSE picture of the wear track from a specimen impregnated with graphite (a) and the same image after being filtered and binarized (b).

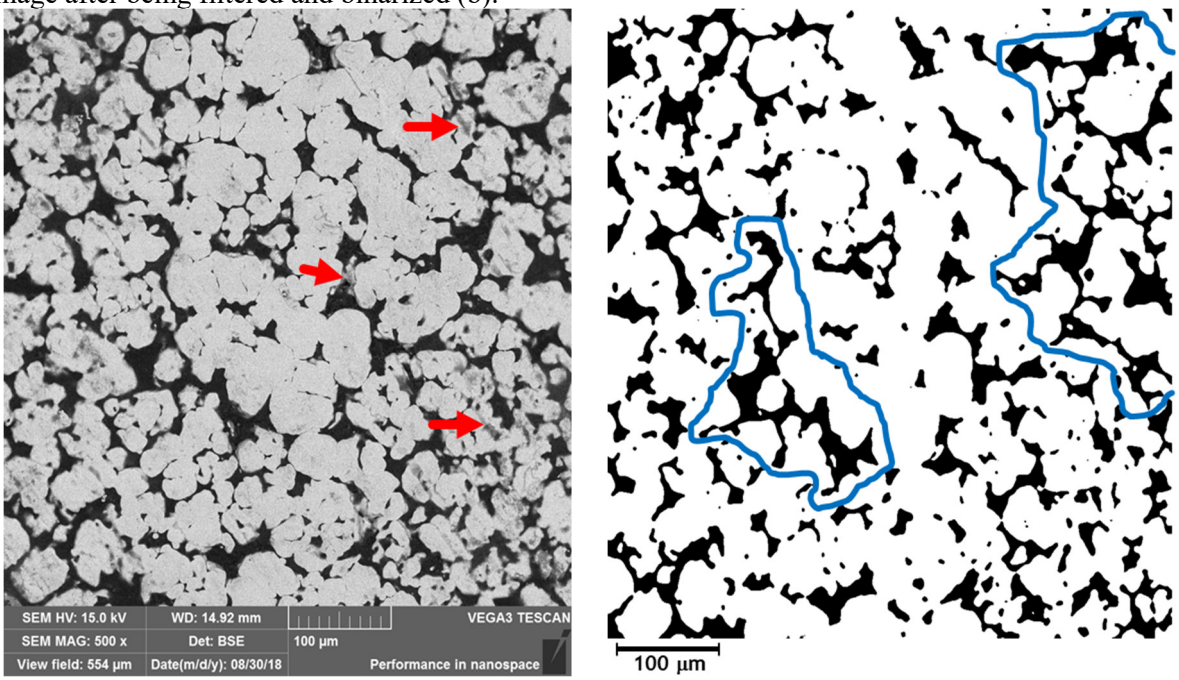

(a) (b)

Source: Author.

Pores at the surface establish interconnected networks (as shown by the blue lines in figure 42 (b)). To analyse the size and shape of individual pores these networks must be segmented; otherwise, the script recognizes them as being one pore and no valuable information would be extracted. In order to segment these lattices, a water-shedding was used. The water-shedding algorithm used starts by creating a distance map of the binarized image. A distance map replaces each point with the distance from that point to the nearest boundary, this makes that inside each continuous region there will be points whose distance from the boundaries is

greater than the distance for the points in its vicinity (these points are called local maxima). Then the points connected with these points are labelled as separated regions inside the initial interconnected area. The labelling of the points connected with the local minima continues until they reach a boundary, or another region being labelled. When two labelling processes collide a virtual boundary is created inside the original interconnected region, this process stops when all the regions have been labelled and the network becomes successfully segmented (WOJNAR, 1999), an schematic representation of this process is shown in figure 43.

Figure 43: Schematic of the water-shedding process

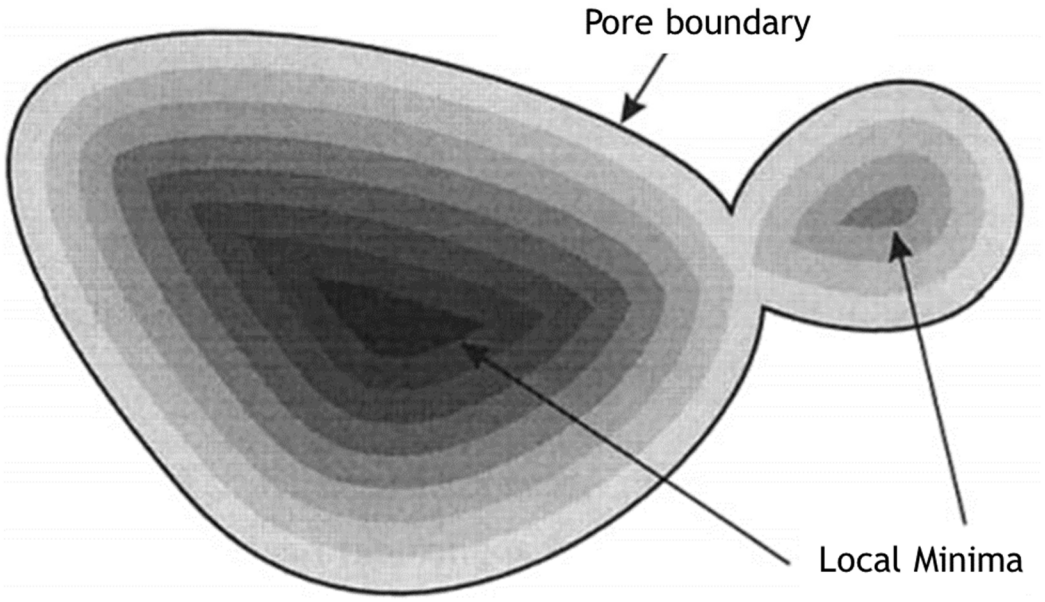

Source: Adapted by the author from Wojnar (1999)

In this work, the algorithm used was developed by J. Gostick et al. in 2019 using Python. The code is open source and free-to-use. The code and details about the algorithm can be found in reference (GOSTICK et al., 2019). Figure 44 corresponds to a watershed and labelled image. In image analysis a label is a way to identify a feature by assigning a number to each individual region, in figure 44 a colour was assigned to each label (number) in order to visualize the results of the watershedding algorithm. In the case of this image, although there are continuous networks of pores, the software will recognize each labelled (coloured) region as a separate feature, having its own size and shape.

With the images properly filtered, binarized and segmented the extraction of the morphological parameters was performed using the tools available in the Scikit-image and Porespy modules of Python. The morphological properties extracted were Feret diameter,

circularity, solidity and eccentricity. The orientation angle of the pores was also measured. The orientation angle is defined as the angle between the x-axis and the major axis of the ellipse that has the same second-order moments as the region ranging from - 90° to 90° (SCIKIT-IMAGE, 2019).

Figure 44: Watershed image from a wear track of an impregnated specimen.

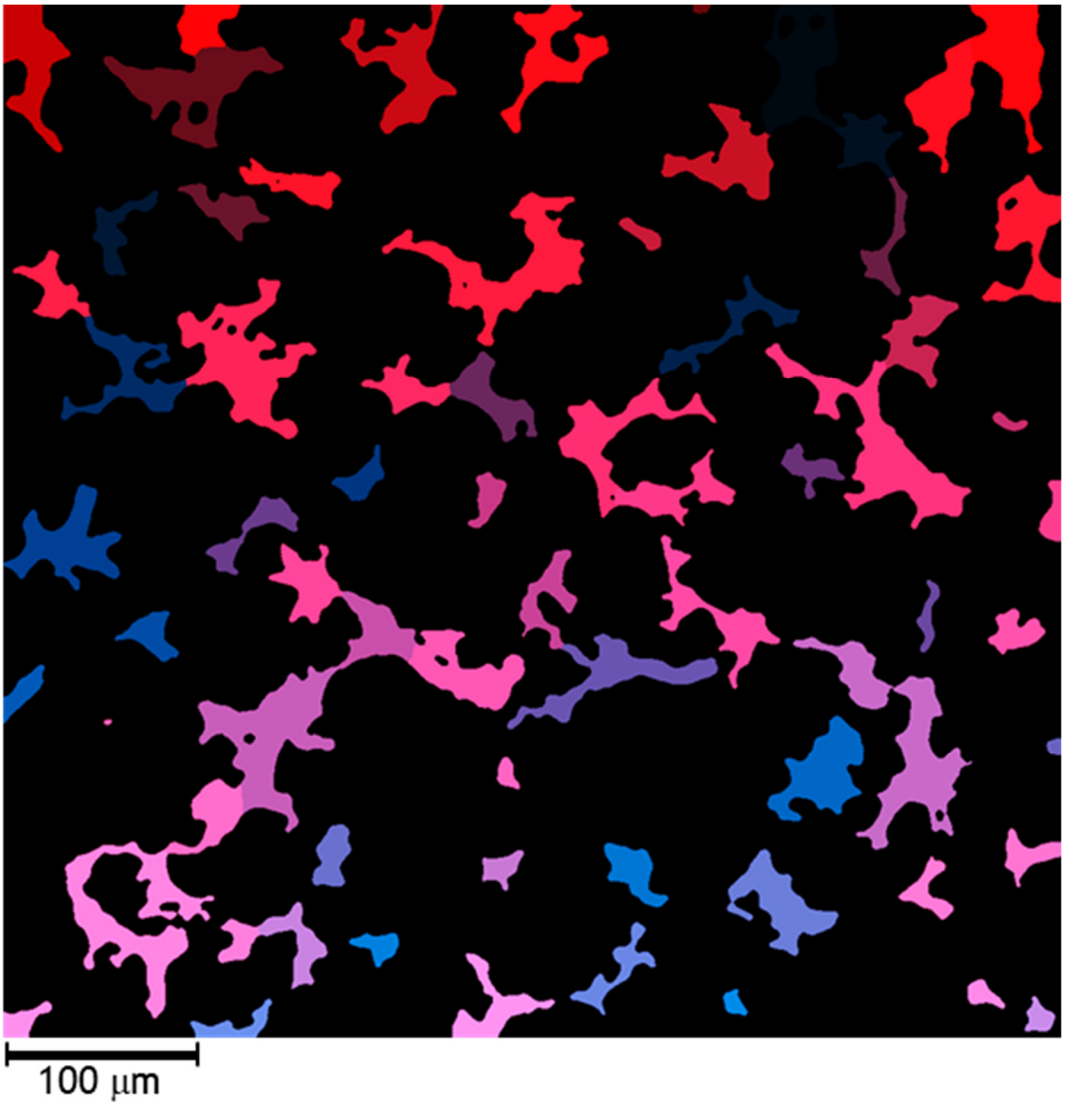

Source: Author

Figure 45 presents the binarized image of a wear track with the red arrow showing the movement axis of the counter-body during the tribological tests (figure 45 (a)) and an example of how the orientation angle is measured in a single pore (figure 45 (b)). In this work, the

absolute value of the orientation angle (|θ|) was used. The motivation behind this measure was to see if the movement of the counter-body influences the orientation of the pore during the scuffing resistance tests. In this case, if the angle is negative or positive is not relevant for the analysis. Furthermore, using the absolute value of the angle helps to visualize if the pores are aligned with the sliding axis (|θ| → 90) or not.

Figure 45: Binarized image of a wear track showing the axis of movement of the counter-body (a) and an example of how orientation angle is measured (b)

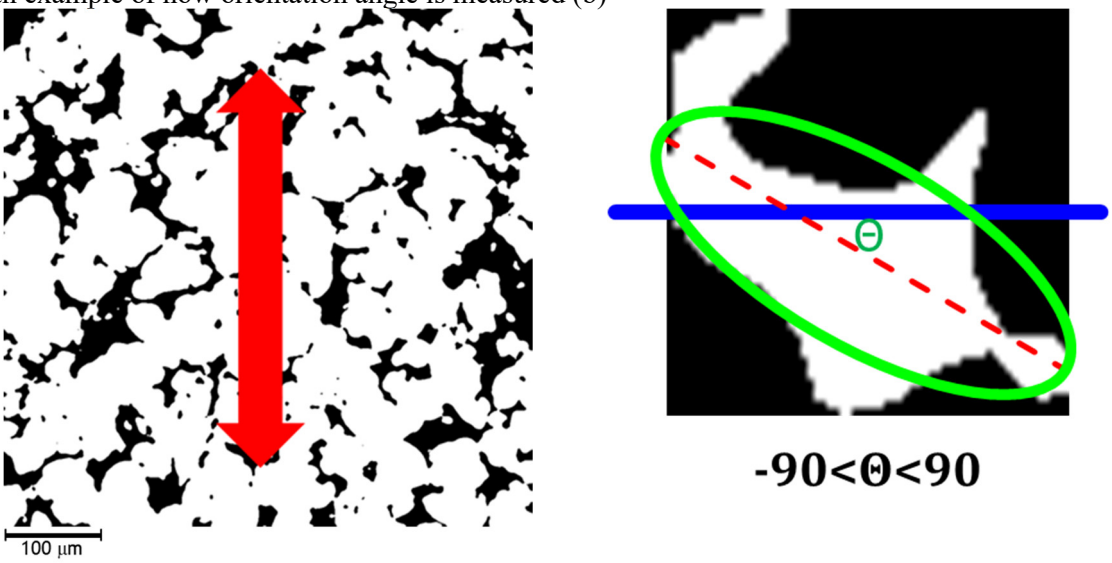

(a) (b)

Source: Author

To analyse the changes in the distribution of graphite during the tribological tests., carbon elemental maps of the wear tracks were used. In order to perform this analysis, the binarized images of the wear tracks and their corresponding carbon elemental maps were digitally superimposed. The elemental carbon maps images due to the nature of the analysis does not cover the exact same area than the images from the BSE detector and some distortion in the position of pores and carbon is created due to this factor. In order to superimpose those images, first the boundaries of the binarized image and the elemental carbon maps were extracted, then the elemental carbon image was modified in order to minimize the distance between the boundaries of the binarized image and the carbon image finally, when this minimum was reached a superimposed image was created.

By superimposing the images, each labelled pore gains a new property called “mean carbon intensity” which is the information about the quantity of carbon contained in that region provided by the elemental maps. Figure 46 shows an example of the superimposed images.

Figure 46: Binarized image of a wear track (a) with its corresponding elemental map (b) and the superposition of both images used to measure the amount of carbon in each pore (c)

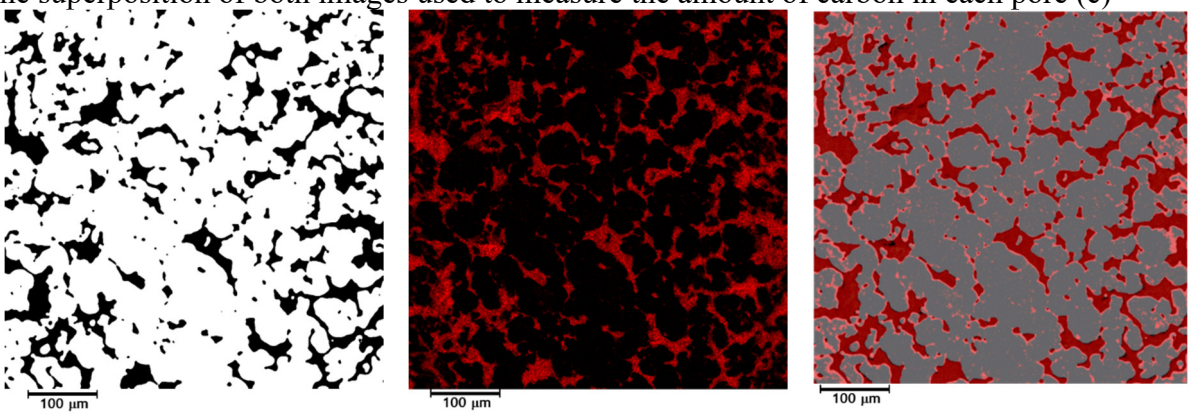

(a) (b) (c)

Source: Author

Once all the parameters were extracted, graphical and statistical analyses of the data were performed using the software Origin 2019 ®.

4.5.5 Optical microscopy

To study the microstructures, the samples were mounted and prepared according to the ASTM E3-11 standard and then etched with Nital 2 vol.%. The surfaces were analysed using a Leica DM 4000 M optical microscope, and the images were captured using a Leica DC 300 digital camera in greyscale with a resolution of 2088x1550 pixels.

4.5.6 Microhardness

Microhardness was measured using a Vickers indenter with a load of 10 gf according to the ASTM B933-16 standard. Nine measures in three samples per condition were performed. The equipment used was a Shimadzu HMV 2000 microhardness tester.

4.5.7 Scanning electron microscopy

A Tescan Vega 3 scanning electron microscope (SEM) coupled with an Oxford Instruments INCA X-act energy dispersive spectroscopy (EDS) probe was used to analyse the

wear tracks. Secondary electrons (Se) images were obtained to study the surfaces of the wear tracks. Backscattered electrons (BSE) images were used to study the evolution of pores during the tribological tests using image analysis. Finally, EDS maps were used to study the changes on the distribution of graphite on the pores during the tribological testing.

4.5.8 Micro Raman spectroscopy

The graphite used in this work and the tribolayers left before the tribological test were analysed by micro Raman spectroscopy using a Renishaw model 2000 Raman microscope, with an argon laser excitation (λ = 514.4 nm). Seven acquisitions for each condition were obtained in the region of 300-3200 cm^{-1}.

4.5.9 X-ray diffractometry

The atomic structure of the graphite used in this work was analysed using x-ray diffractometry (XRD) using a PANalytical X'pert Pro diffractometer in a Brag-Brentano $\theta/2\theta$ configuration. The x-ray source was Cu (Kα, 40KV, 40ma) with a secondary Kβ filter and a X'celerator detector. The diffractograms were acquired in the 2θ range between 20° and 100° with a step of 0.02° and a rate of 2 s/step.

4.5.10 Tribological characterisation

A CETR model UMT tribometer was used to perform the tribological tests. The configuration used was a reciprocating ball on flat. The incremental load tests were performed using the following parameters.:

- Counter body: AISI 52100 steel ball with 10 mm of diameter;
- Load: Started in 7 N with increments of 7 N in 10 minutes steps;
- Frequency: 2 Hz;
- Amplitude: 10 mm;
- Atmosphere: Air at ambient pressure, humidity and temperature;

These parameters were chosen according to the methodology developed by de Mello and Binder in 2006 (DE MELLO; BINDER, 2006). Scuffing resistance was computed as the value of load*distance where the coefficient of friction (COF) is consistently under 0.2. To

calculate the scuffing resistance, three tracks in three different samples (totalizing 9 data points) per condition were used. To perform the image analyses in the interrupted tests, three wear tracks from three different samples were used for each analysed load and condition.

From the scuffing resistance tests the conditions for the constant load tests were determined as it will be explained in chapter 4. The monitored parameters in all the tribological tests were frequency, normal and tangential loads (and therefore the COF) and the contact's electrical resistance as it indicates the presence of isolating tribochemical compounds in the contact area. The wear volumes of the counter bodies were measured by optical microscopy and the wear volumes of the specimens were measured using the digitalized surfaces obtained by white light interferometry. To obtain the wear rates and coefficients of friction, three wear tracks in two specimens per condition were used, the wear rates were calculated as the wear volume divided the product between the load and the distance travelled by the counter-body.

Finally, the wear tracks were analysed by SEM to identify the wear mechanisms involved and by micro-Raman spectroscopy to study the characteristics of the tribolayers.

4.5.11 White light interferometry

To measure the wear volume of the specimens and consequently, the wear rates, a Zygo Newview 7300 interferometer was used. Data acquired by this equipment was analysed using the software Mountainsmap v7.1.

4.5.12 Particle size analysis

Graphite particle size distributions were obtained using a Cilas 1190 laser particle size analyser. The particle sizes are obtained by laser diffraction based in the Fraunhofer diffraction MIE scattering theories (GOUESBET; GRÉHAN, 1988). The optic system of the analyser is composed of three laser sources and a CCD camera. The range of sizes that can be analysed from 0.04 to 2500 μm.

5 RESULTS AND DISCUSSION

5.1 PRODUCTION OF POROUS STEEL SAMPLES

The objective of this step was to obtain porous steels with different levels of porosity but with metallic matrixes of similar microhardness and microstructure. Figure 47 shows the processing route for this step.

Figure 47: Characterization route for step 1 of the present work.

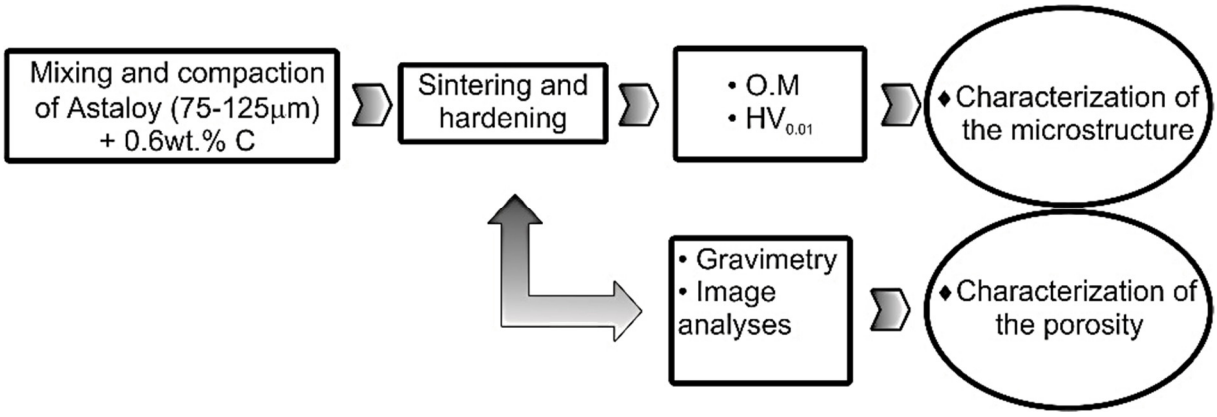

Source: Author

In order to proceed with the sintering of the porous steels first, the technological properties of the mixture were evaluated. Table 5 shows the flowability and the apparent density of the powder mixture. The compactability curve is presented in figure 48. The excellent compactability of the mixture which allows obtaining significant differences in density in the range 200-600 MPa was a crucial factor to the execution of the present work. Once the technological properties of the mixture were evaluated, the specimens were prepared by compacting the mixture at 200, 400 and 600 MPa and sintering the green bodies during 1 hour at 1200 °C in the dilatometer to study the sintering process. The dilatometry curves for each condition are shown in figure 49. The three conditions present the characteristic retraction of the beginning and the end of the austenitic transformation in the range between 737 and 777°C. All the samples experiment considerable retraction at the sintering temperature, which indicates that sintering occurred even in the samples with low compaction pressures. At cooling it can be noticed an expansion in the range between 670 and 620 °C which indicates the transformation from austenite to pearlite. There was also a slight expansion in the range 485-460 °C (encircled in red) that might indicate a bainitic or martensitic transformation due to the alloy elements

contained in the pre-alloyed powders. A considerable retraction was observed for all the specimens at the sintering temperature, which is proof of the excellent sinterability of the Astaloy CRL powders as has been reported by Kulecki et al. (KULECKI; LICHAŃSKA; SUŁOWSKI, 2015; KULECKI et al., 2016).

Table 5: Technological properties of the powder mixture

Technological Properties	
Flowability (s/50g)	34.50 +/- 0.17
Apparent Density (g/cm^3)	3.397 +/- 0.042

Source: Author

Figure 48: Compressibility chart of the powder mixture

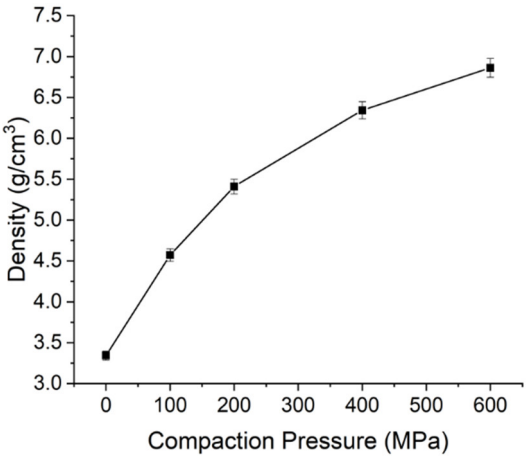

Source: Author

Figure 49: Dilatometric curves for samples compacted at 200(a), 400(b) and 600(c) MPa

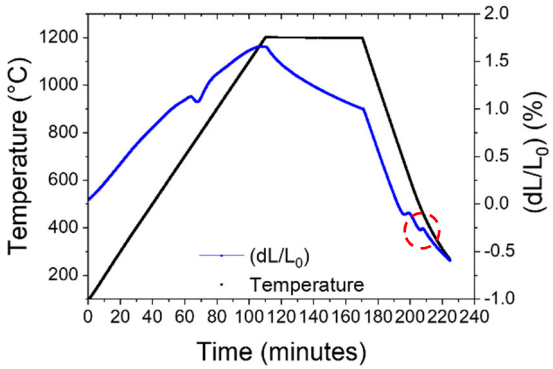

(a)

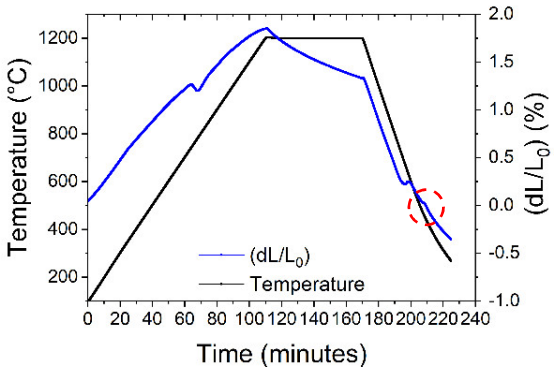

(b)

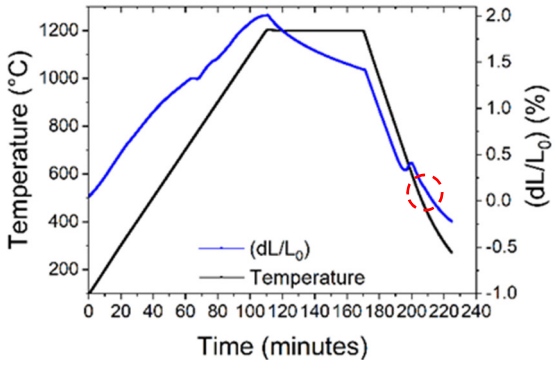

(c)

Source: Author

As the powder mixture sintered without difficulties, a sintering temperature of 1100°C was chosen as a baseline to study the effect of the compaction pressure on the porosity of the samples. Figure 50 shows the micrographs of samples compacted at 200, 400 and 600 MPa and sintered 1 hour at 1100°C, vacuum impregnated with epoxy resin and polished. These micrographs were used to perform the image analyses shown in this step. From figure 50 it is clear that the compaction pressure heavily influences the number and size of pores. As discussed in section 2.2.1.1 (literature review), at low compaction pressures pores are big and more interconnected which confers their irregular shapes (figure 50 (a)). At higher pressures the pores lose connectivity and become smaller with regular shapes (figure 50 (b) and (c)) (POQUILLON et al., 2002; GERMAN, 2005). A compaction pressure of 400 MPa was chosen to study the effect of sintering temperature in the shape and size of pores. These samples were sintered at 1100, 1150 and 1200 °C. Figure 51 shows the porosity of the specimens calculated by their geometric density and by image analyses. Geometric porosity and image analysis porosity results are in partial agreement. This was expected as geometric porosity measures a three-dimensional property (volume) while image analysis measures a bidimensional property (area) whose results would be similar if the samples where perfectly homogeneous (which is not the case for sintered materials). Also the porosity determined by image analysis is influenced by the preparation of the samples and the parameters used for the analysis like the thresholds for binarization and segmentation (FRIEL et al., 2000).

Figure 50: Optical micrographs of samples compacted at 200 (a), 400 (b) and 600 (c) MPa and sintered 1 hour at 1100°C

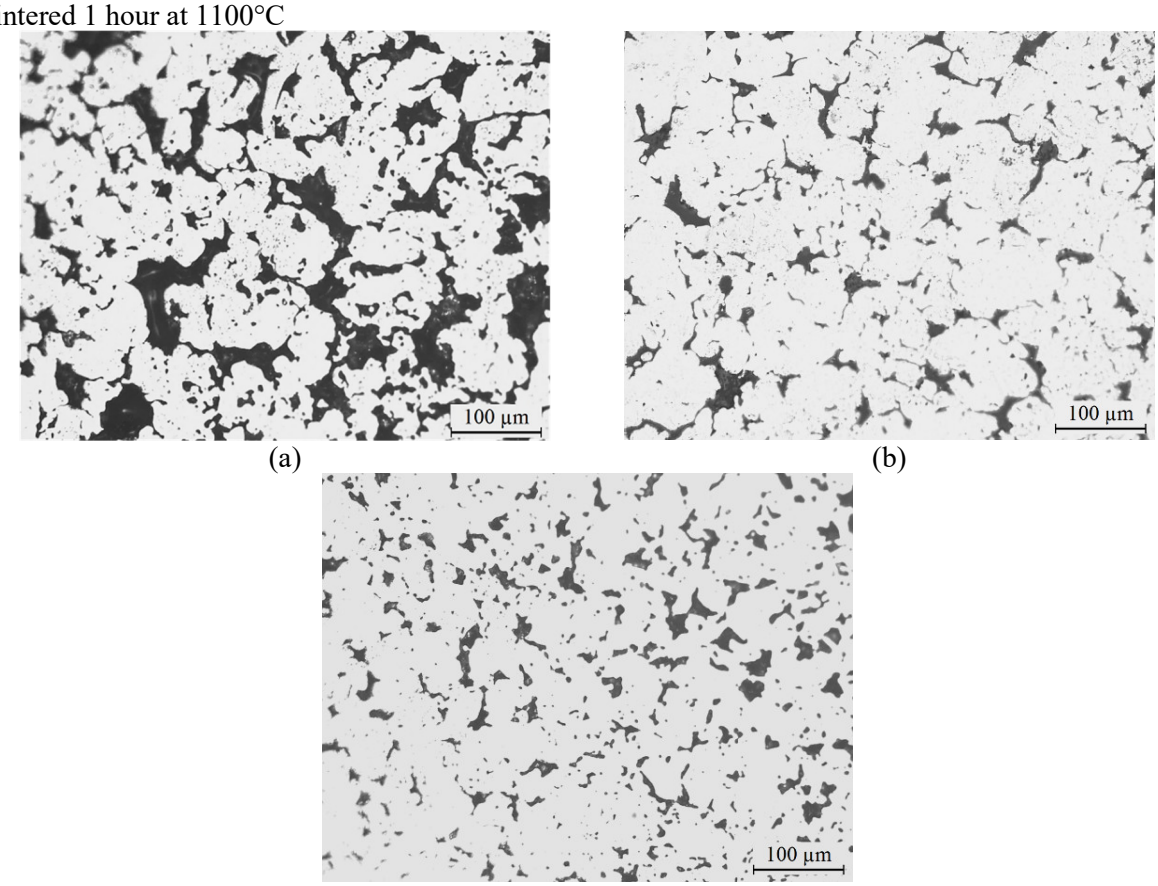

(a) (b)

(c)

Source: Author

The effect of compaction pressure and sintering temperature in the number and median Feret diameters (D_{50}) of pores in the sintered samples are shown in figure 52. As expected, an increment in the compaction pressure reduces the mean diameter of pores (the ANOVA and post-hoc analyses found in appendix A confirm that the populations and their medians are different). The overall number of pores, however, depends on both the compaction pressure and sintering temperature. Pressure tends to reduce the interconnectivity between pores thus reducing their size and increasing the number of isolated pores (which increments the pore count), on the other hand sintering temperature reduces the number of small pores by coalescence in order to minimize the Gibb's free energy of the system (GERMAN, 2005; KULECKI; LICHAŃSKA; SUŁOWSKI, 2015) as was discussed in section 2.2.1.2.

Figure 51: Porosity of the specimens calculated by their geometric density and by image analysis

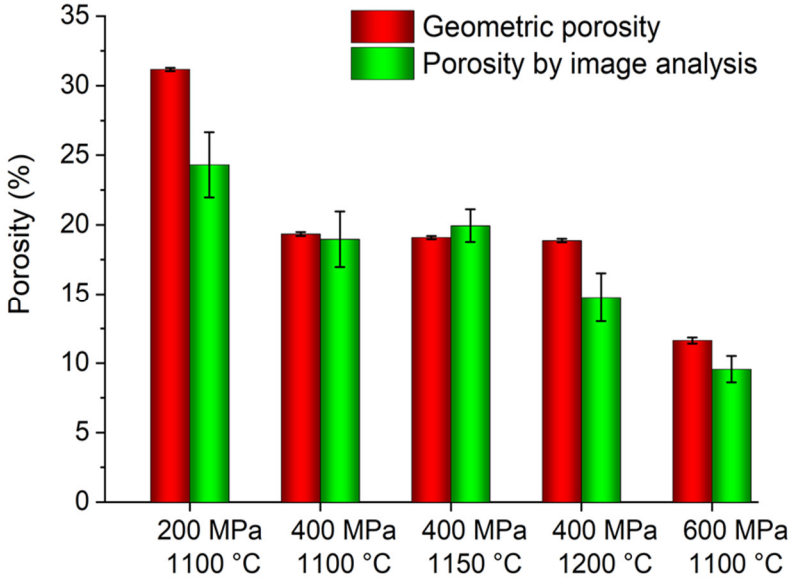

Source: Author

Figure 52: Pore count and median Feret diameter of pores.

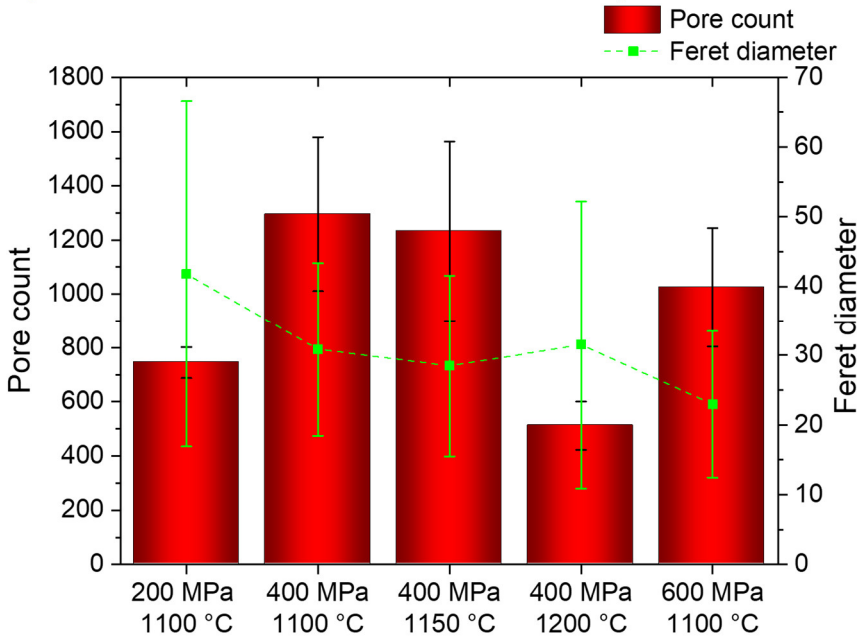

Source: Author

To better understand this point, figure 53 shows the effect of the compaction pressure in the size and circularity distributions of the pores of samples sintered at 1100 °C. As expected, compaction pressure reduced the number of big pores by reducing the interconnectivity among them as discussed in section 2.2.1.1. Circularity did not show a strong tendency toward more regular pores as a function of the compaction pressure as was expected. This was mainly

because the small pores left in the specimens compacted at 600 MPa did not have enough time to become spherical during sintering.

Figure 53: Effect of compaction pressure on the size distributions and pore circularity of samples sintered 1h at 1100°C and compacted at 200 MPa (a)-(b), 400 MPa (c)-(d) and 600 MPa (e)-(f)

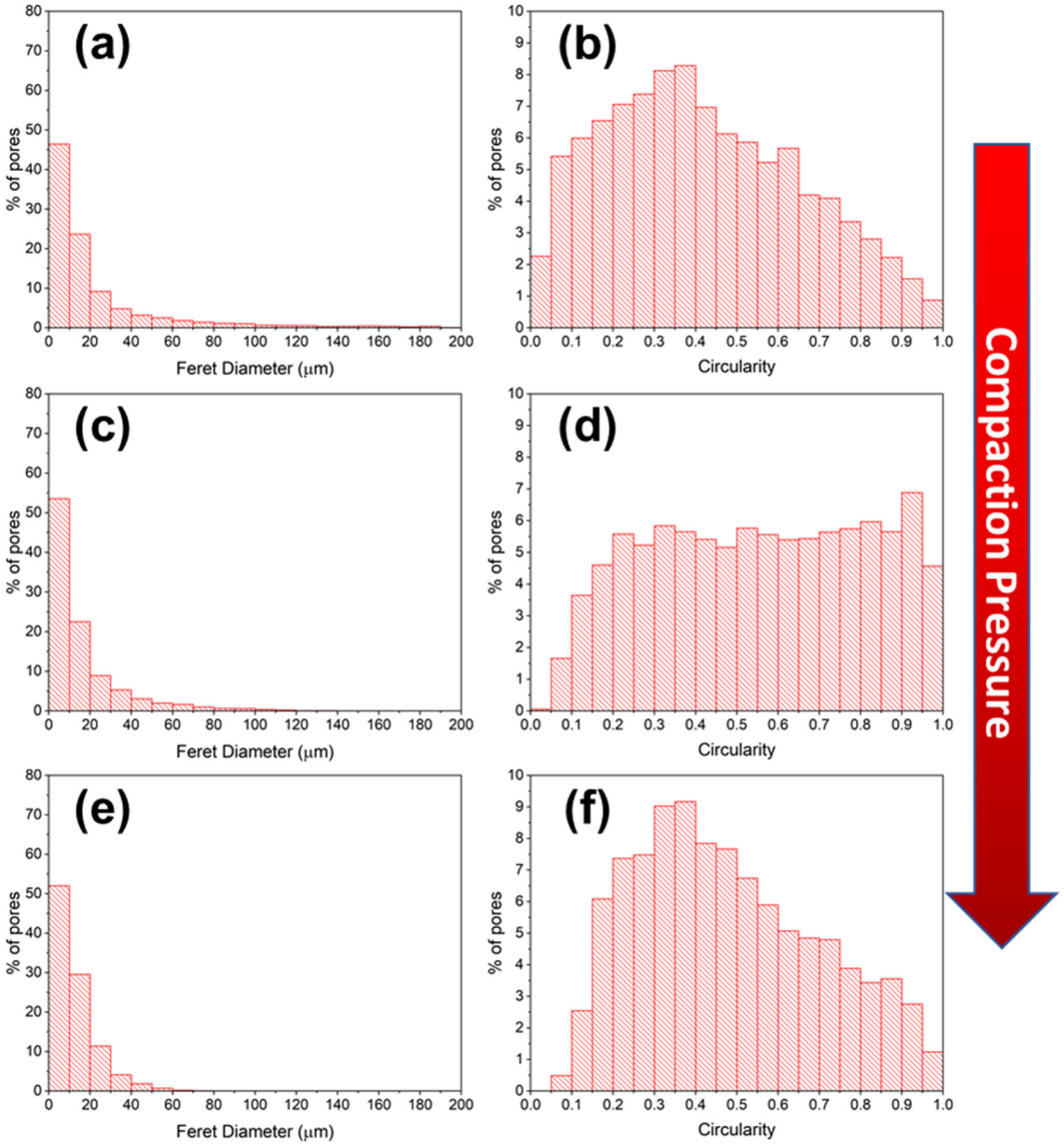

Source: Author

Figure 54 shows the effect of the sintering temperature in the size and shape distributions of pores from samples compacted at 400 MPa and sintered at 1100, 1150 and 1200 °C. Sintering temperature did not have a significative impact on the pore size distribution besides the diminution of the number of pores in the 0-10 μm range in favour of pores in the 10-40 μm range. This was expected as sintering temperature generates coalescence of pores,

reducing the number of small pores in order to minimise the surface energy of the system. However, this was not translated in a significative rounding of the pores as shown by the circularity distributions.

Figure 54: Effect of sintering temperature on the size distributions and pore circularity of samples compacted at 400 MPa and sintered at 1100 °C (a)-(b), 1150 °C (c)-(d) and 1200 °C (e)-(f)

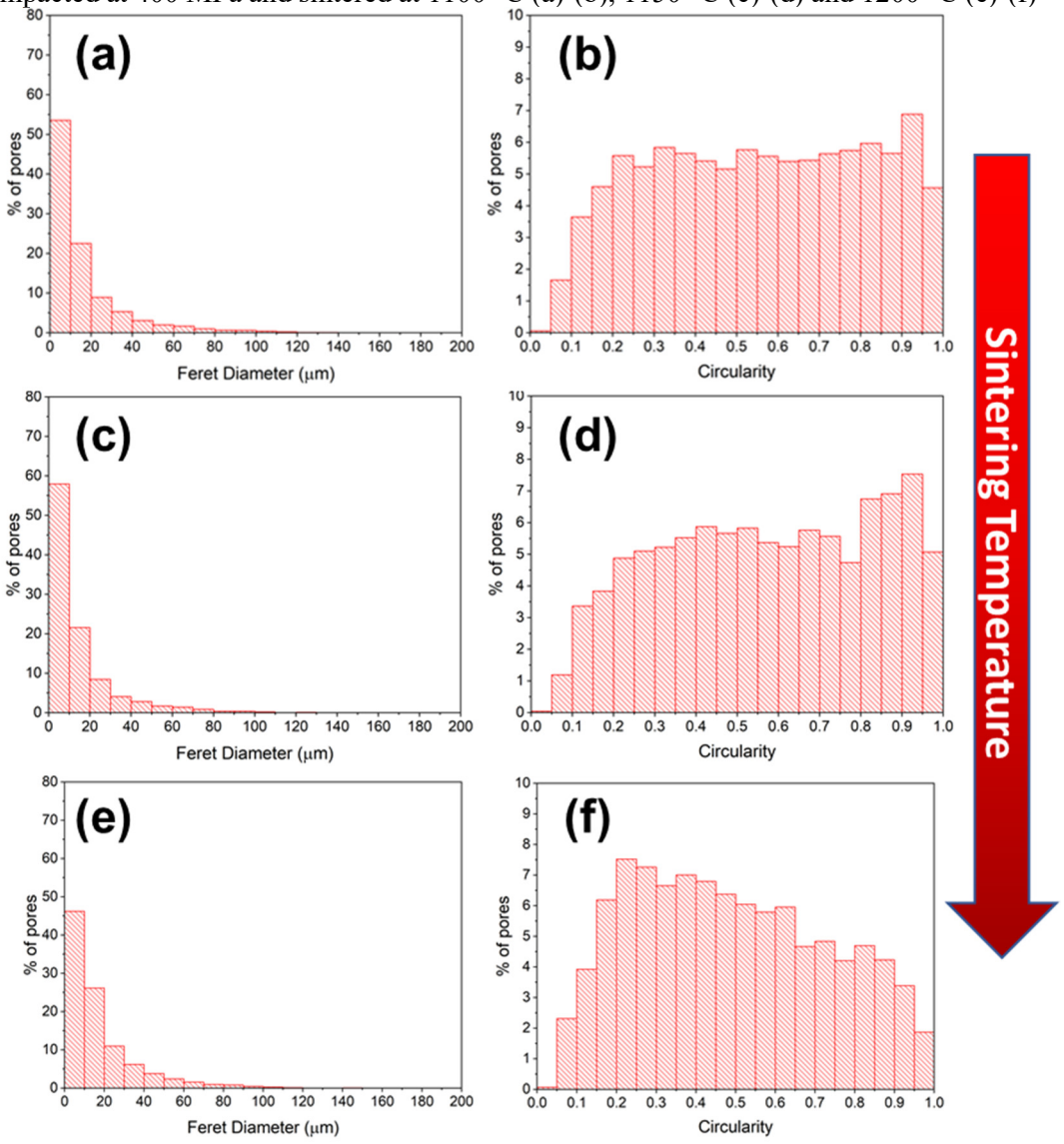

Source: Author

The microstructure of a sample compacted at 400 MPa and sintered at 1100°C is shown in figure 55. The microstructure consists of some pores deformed by the grinding and polishing process and mixtures of pearlite, bainite and martensite. These particular microconstituents were present in all the samples for all the conditions and are expected according to the work of Sulowski, Kulecki and Radziszewska (SUŁOWSKI; KULECKI; RADZISZEWSKA, 2014)

but are hardly distinguishable one from another in the micrographs. In order to correctly identify them SEM analyses paired with nano-hardness measures are needed (NAVARRO-LÓPEZ et al., 2017). The microstructure also presents some precipitates in grain boundaries (pointed by the red arrow), these precipitates have also been found in other works involving Astaloy powders (PIECZONKA; SUŁOWSKI; CIAŚ, 2012; SUŁOWSKI; KULECKI; RADZISZEWSKA, 2014; KULECKI; LICHAŃSKA; SUŁOWSKI, 2015) and are attributed to chromium and molybdenum carbides precipitation at grain boundaries during cooling.

Figure 55: Optical micrographs of samples compacted at 400 MPa and sintered at 1100 (a), 1150 (b) and 1200 °C (c) etched using 2 vol% Nital.

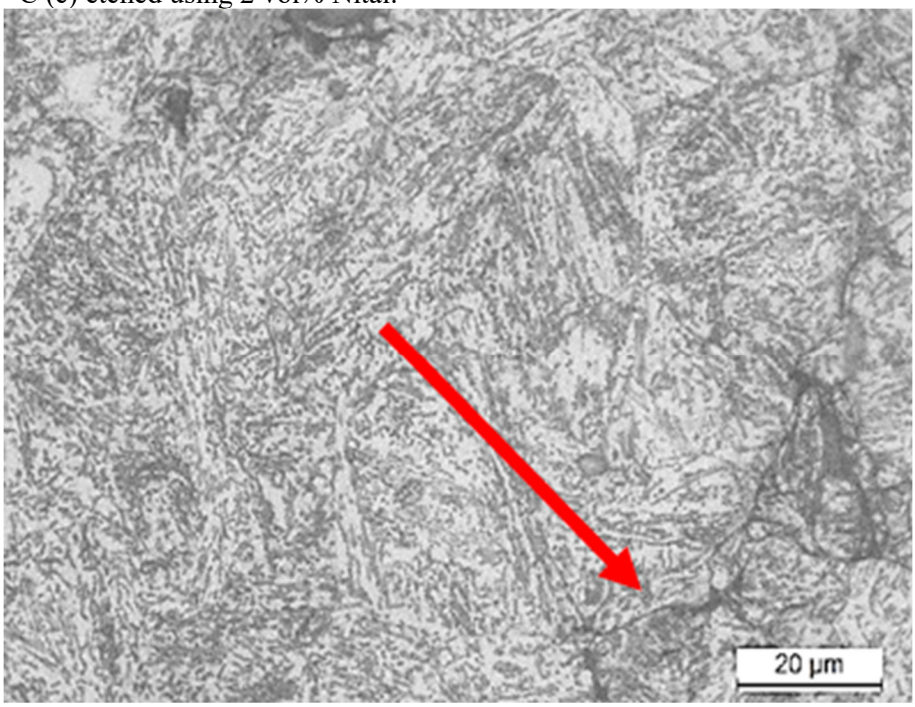

Source: Author

Finally, the effect of the processing parameters on the hardness of the specimens and the microhardness of the metallic phase was measured. These results are shown in Figure 56.

Figure 56: Vickers hardness of the specimens (a) and microhardness of the metallic phase (b) as a function of the processing parameters.

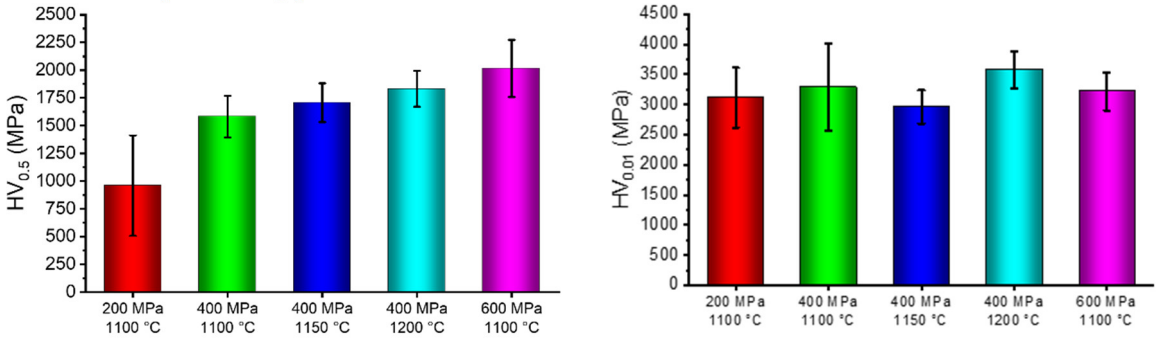

(a) (b)

Source: Author

The Vickers hardness of the specimens was measured using 500 gf to gauge the effect of the pores in the mechanical resistance of the sintered steels (figure 56 (a)). As expected, the mean hardness increments with the compaction pressure and, slightly, with the sintering temperature. The samples compacted at 200 MPa had a particularly high dispersion in their hardness due to their porosity, as the probability of having pores affected by the indentations (which introduces noise in the measurements) is higher than in the other conditions. Sintering temperature improves sintering between the particles as was discussed in section 2.2.1.2 which translates in an improvement on the hardness of the specimens. The microhardness of the metallic matrix was measured using 10 gf, so it was not affected by the porosity. As shown in figure 56 (b) **the microhardness of the matrix was not significatively affected by the compaction pressures nor by the sintering temperatures**. This was one of the main objectives of this step as differences in the tribological behaviour between these conditions will not be attributed to differences in the hardness of the metallic phase of the sintered samples. Once this step was completed, the development of a vacuum impregnation process started.

5.2 DEVELOPMENT OF A VACUUM IMPREGNATION PROCESS

Figure 57 shows the processing route for the 2nd step of the present work. The objective of this step was to develop an impregnation process suitable for all the types of graphite that were studied.

Figure 57: Processing route for step 2 of this work

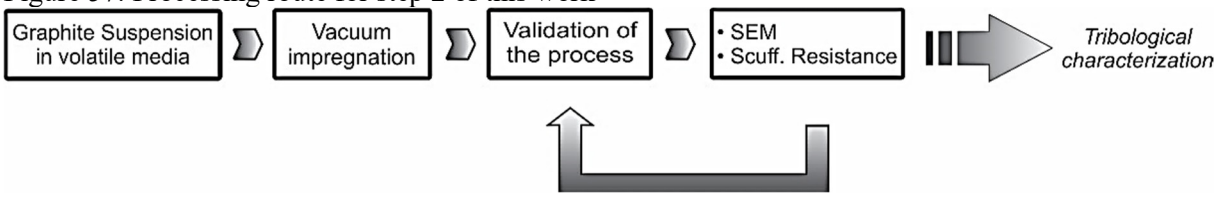

Source: Author

The criteria to define an impregnation process as successful was to find filled pores at the surface of the specimens and that graphite penetrated the sample at least 10 μm. This limit was defined as that was the expected penetration of the counter-bodies during the tribological tests based preliminary tests and other works under similar conditions, if graphite does not penetrate that much, changes in the tribological behaviour could be attributed to the depletion of lubricant and not to the sealing of pores during testing as it was planned. On the other hand, the impregnated samples had to exhibit some degree of lubricity (COF < 0.2); this was determined using scuffing resistance tests. To evaluate the penetration of graphite into the specimens after one impregnation cycle, the impregnated specimens were notched, placed 20 minutes in liquid nitrogen and then fractured by impact. Figure 58 shows SEM images of the transversal fracture of a sample compacted at 400 MPa and sintered at 1100 °C after 1 cycle of vacuum impregnation with graphite (D50 = 1.10 μm) and drying. As shown in figure 60 (a), after 1 impregnation cycle, graphite can be found below 366 μm from the surface (a graphite stock is shown in figure 58 (b)). This fact alone validated the vacuum impregnation process as an excellent way to introduce solid lubricant into the pores in a simple manner. Once the convenience of the vacuum impregnation process was established, the number of cycles necessary to fill the pores was determined. Figure 59 shows SEM images of the surface of samples with 1 and 2 impregnation cycles. In these samples, not enough graphite was found inside the pores, so 4 and 8 cycles were tested.

Figure 58: SEM images of samples compacted at 400 MPa and sintered at 1100 °C after 1 impregnation cycle.

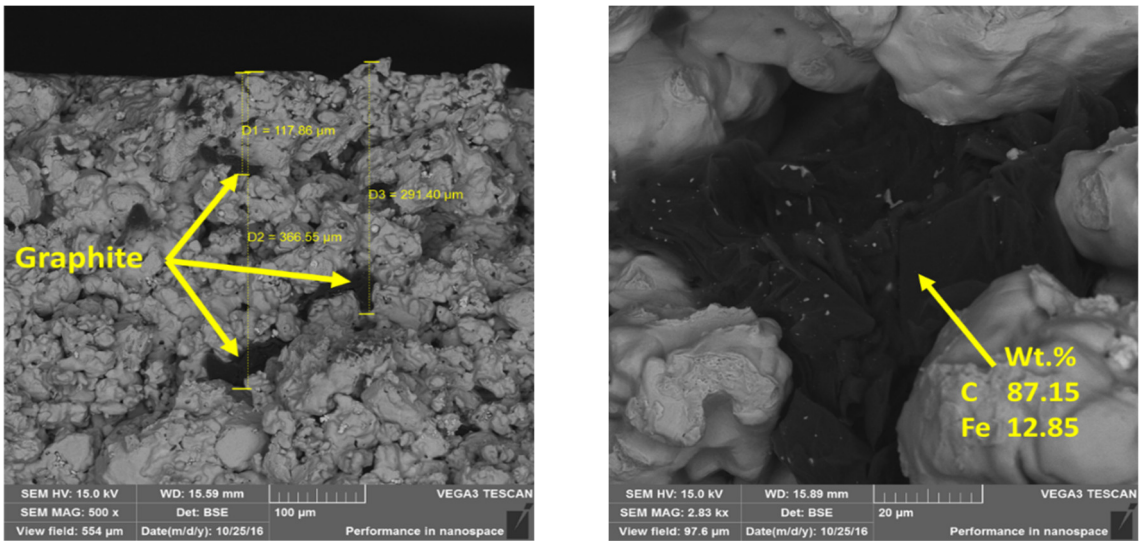

(a) (b)

Source: Author

Figure 59: SEM images of the surface of samples after 1 (a) and 2 (b) impregnation cycles

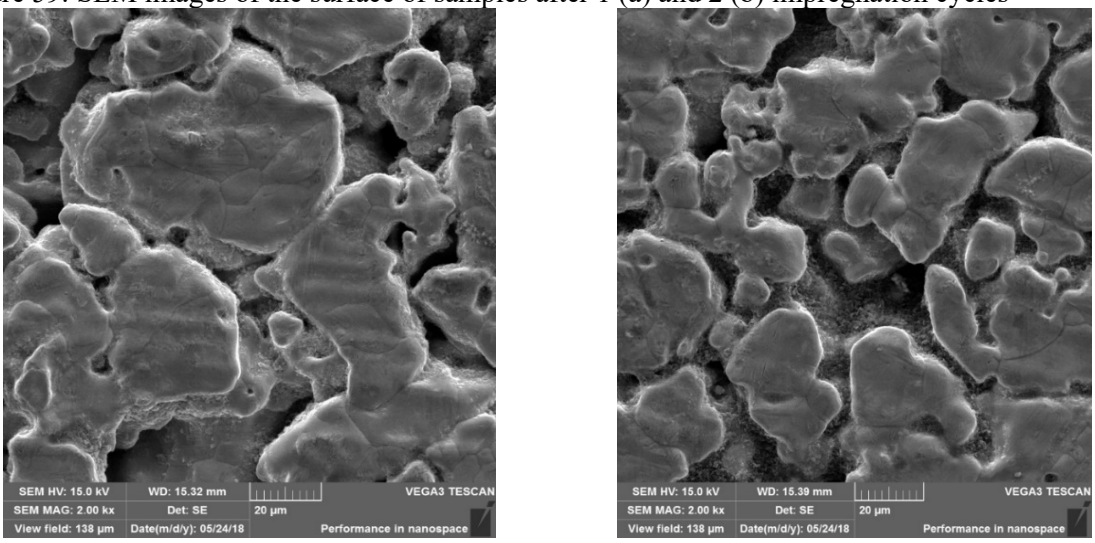

(a) (b)

Source: Author

After 4 and 8 impregnation cycles, the porous steels showed filled pores on their surfaces, but a closer look inside the pores (as shown in figure 60) showed that at 4 cycles there were still pores not filled with graphite. The effect of this incomplete filling was reflected in by the poor tribological behaviour of these samples, as shown in figures 60 (c) and (d).

Figure 60: SEM images of impregnated pores from samples compacted at 400 MPa and sintered at 1100 °C after 4 (a) and 8 (b) impregnation cycles with their corresponding scuffing resistance curves (c) and (d)

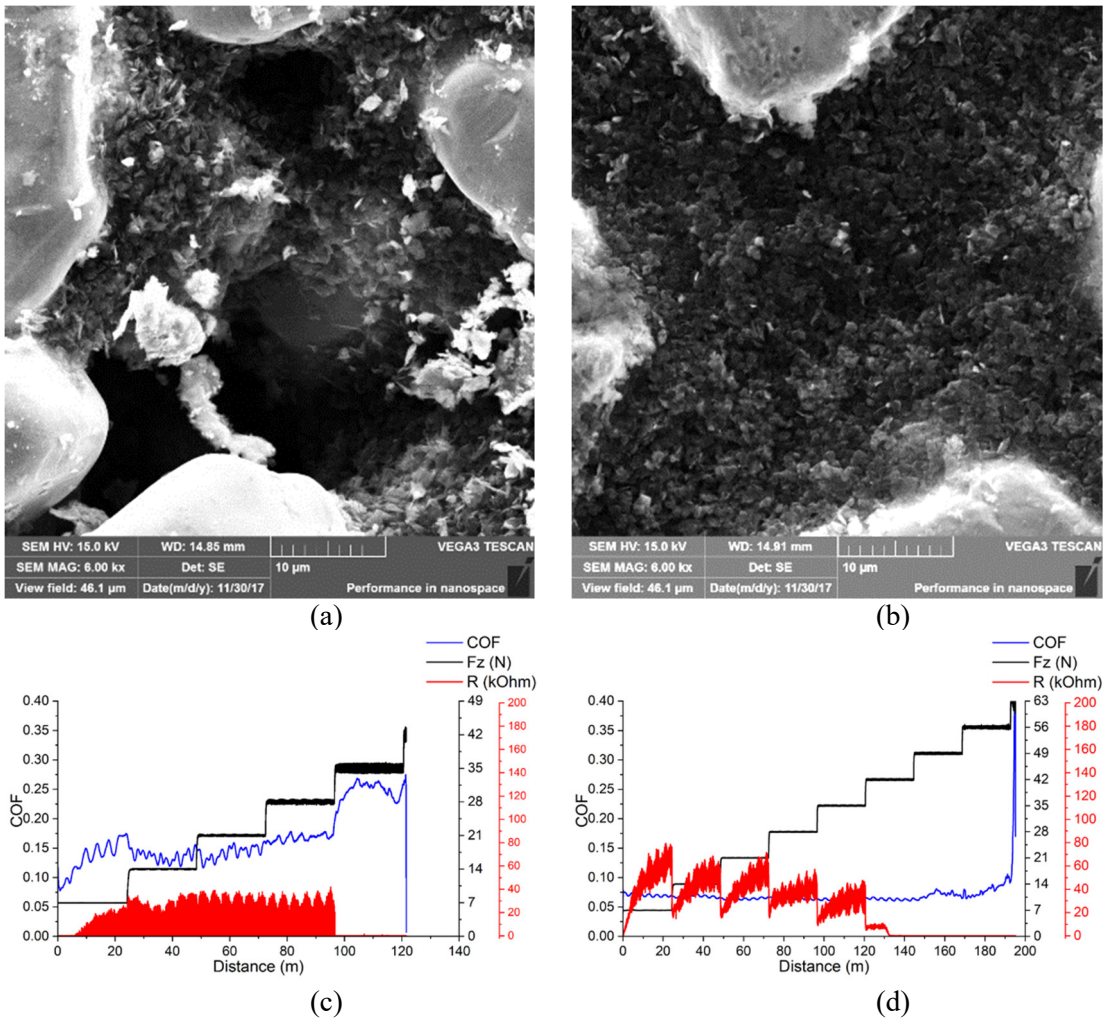

Source: Author

Figure 61 shows SEM images of a transversal fracture (using the same method described earlier) of the region below the wear track whose behaviour was shown in figure 60(d). Graphite was found below the wear track at the end of the lubricity regime. This indicates that lubrication stops because of pore sealing and not by the depletion of lubricant.

Figure 61: Transversal section, secondary (a) and backscattered (b) electron SEM images from a wear track at the end of the lubricity regime of a sample compacted at 400 MPa and sintered at 1100 °C after 8 impregnation cycles

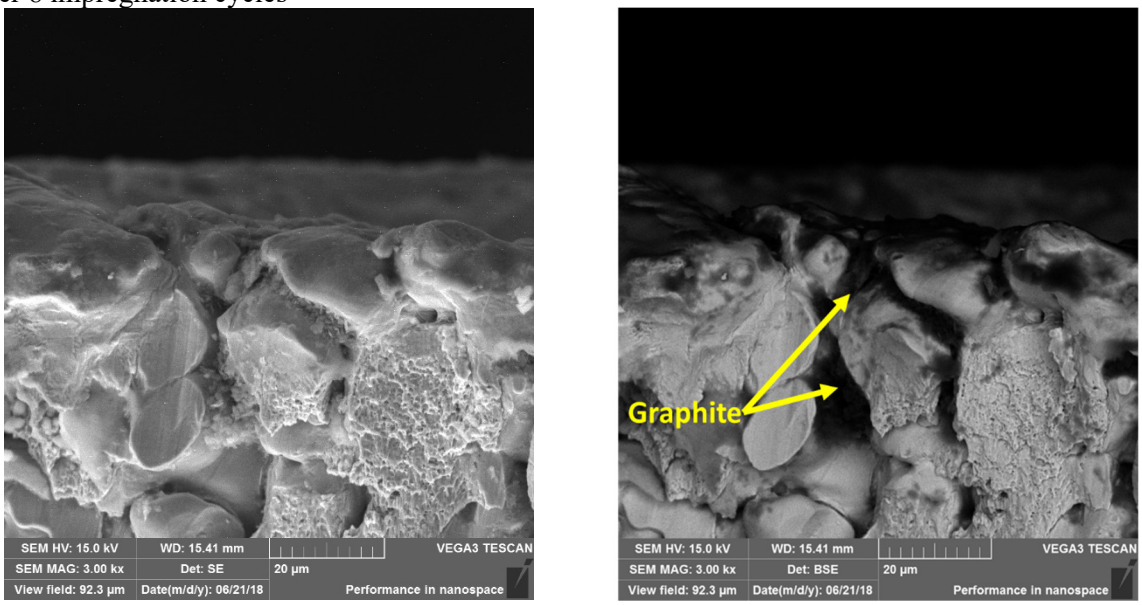

(a) (b)

Source: Author

Sixteen cycles of impregnation were performed to evaluate if the tribological behaviour would improve with more cycles. However, as shown in figure 62, this was not the case, therefore for graphite of D50 = 1.10 µm, eight impregnation cycles were defined as the optimal number of cycles.

Figure 62: Evolution of the coefficient of friction in a scuffing resistance test of a sample compacted at 400 MPa and sintered at 1100 °C after 16 impregnation cycles

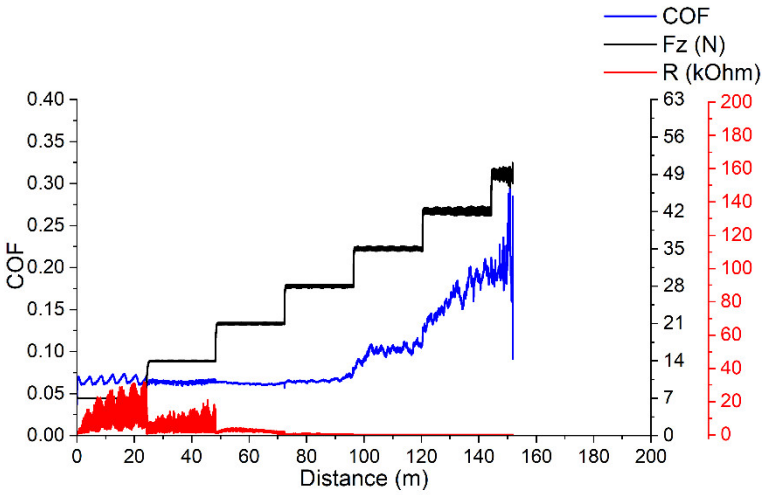

Source: Author

To study the effect of the particle size in the impregnation process, graphite with D50 = 21.54 μm was impregnated using 8 and 16 impregnation cycles. Figure 63 shows SEM images obtained using secondary electrons (figure 63 (a) and (c) and elemental maps obtained by EDS (figure 63 (c) and (d)) for these specimens. In figure 63 (b) and (d), iron is shown in green, carbon in red and oxygen in blue (this convention is valid for all the elemental maps throughout the text).

At eight cycles (figure 63 (a) and (b)), unfilled pores can still be found on the surface of the sintered steel (marked by the yellow circle). This was probably because large particles are harder to disperse due to the formation of large agglomerates. Large agglomerates do not remain in suspension because the surface energy that keeps particles suspended is outweighed by the difference in density between graphite and acetone (in other words, as graphite is denser than acetone, it only can remain suspended when the particle sizes are small) (WIESE; HEALY, 1970). At sixteen cycles (figure 63 (c) and (d)) The superficial pores were filled, so this number of cycles was chosen as the processing condition to impregnate this graphite and the graphite with D50 = 6.07 μm. A secondary electrons SEM image and an elemental map of a sample impregnated with the 6.07 μm graphite using sixteen cycles are shown in figure 66 (a) and (b). Figure 64 (c) shows the tribological response of these samples in the scuffing resistance tests. As expected, the specimen was able to provide lubricity to the system in an effective manner.

Figure 63: Secondary electrons SEM images of samples impregnated with graphite D50 = 21.54 µm after 8 (a) and 16 (c) impregnation cycles and their corresponding elemental maps (b) and (d)

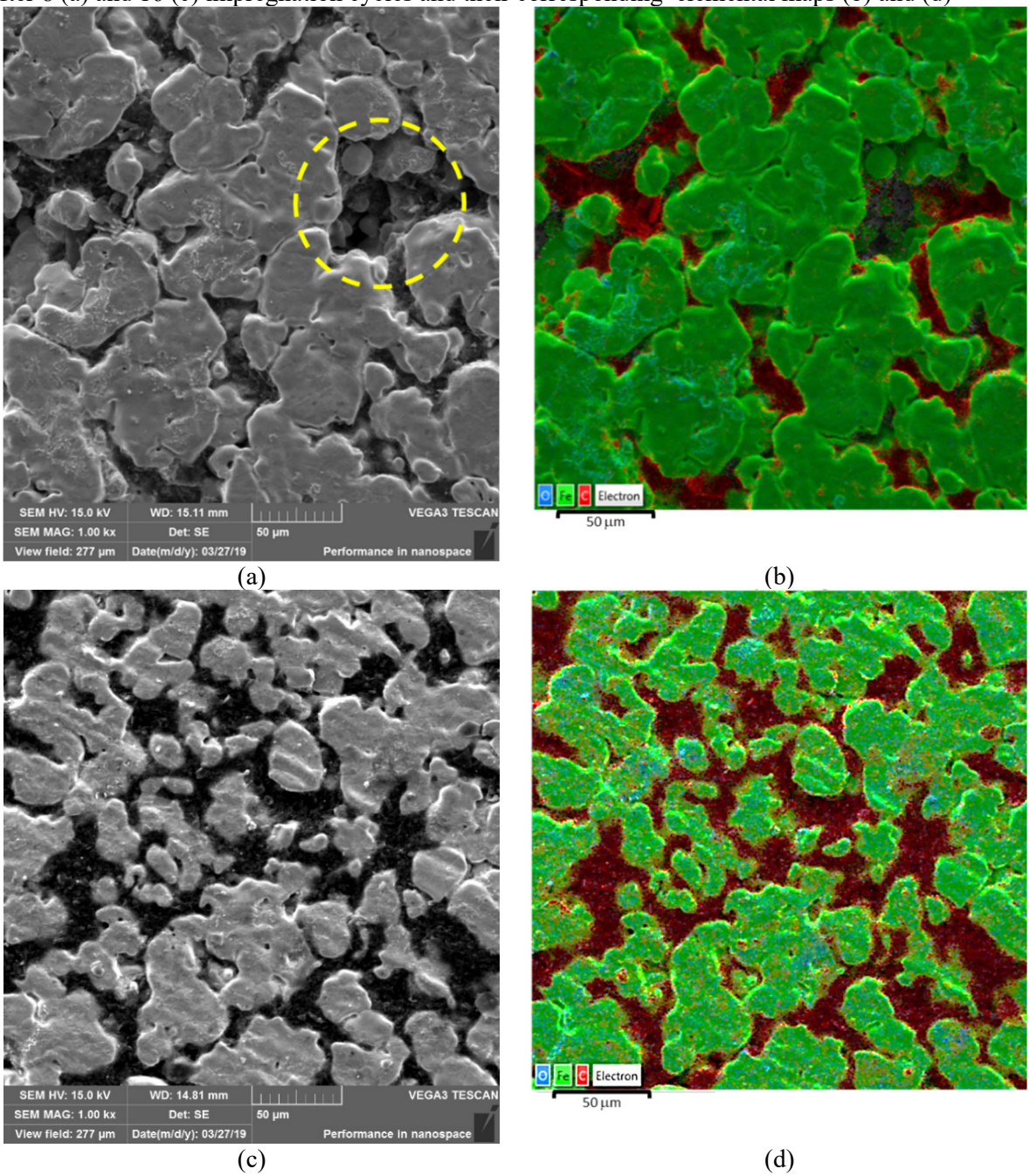

Source: Author

Figure 64: Secondary electron SEM image (a) elemental map obtained using EDS (b) and evolution of the friction coefficient with load in a scuffing resistance test (c) of a sample compacted at 400 MPa and sintered at 1100 °C after 16 impregnation cycles with the 6.07 µm graphite.

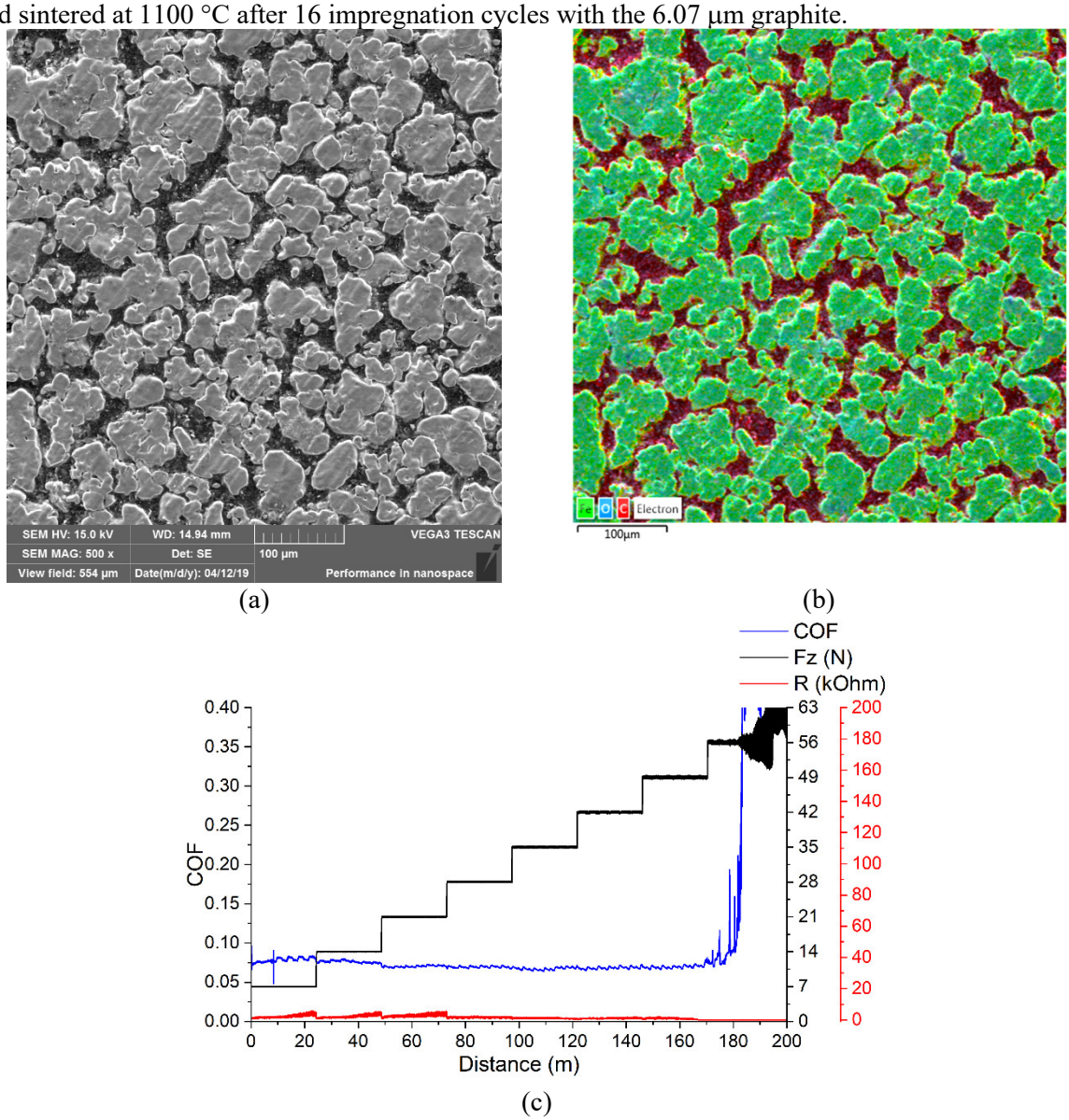

Source: Author

The final step was to determine the impregnation conditions for the CDCs produced by the reaction between B_4C and Cr_3C_2. The following is a brief description of the synthesis process as it is relevant to the discussion in this chapter, a detailed description of the synthesis process can be found in reference (NEVES et al., 2020).

1. A mixture of 23.5 wt.% B_4C and 76.5 wt.% Cr_3C_2 is prepared by conventional methods.

2. The mixture is put into an Al_2O_3 recipient which in turn is put into a tubular furnace.
3. The carbides are reacted inside the furnace at a temperature above 1200 °C in an atmosphere of $Ar/5H_2$ for 1 hour.
4. The products of the reaction are carbon and chromium borides. These borides are dissolved in chloridric acid.
5. Finally, the leftover graphite is filtered and neutralised in water.

Once the graphite was ready, it was impregnated into porous samples (400 MPa, 1100°c) using sixteen impregnation cycles. Sixteen cycles were chosen because it proved to be enough to fill the pores for much larger graphite. However, as shown by the elemental maps in figure 65 (a), oxides (in blue) were found in the impregnated sample. This corrosion was attributed to the presence of adsorbed acid in the particles of some residual salts. To address both theories, a 6^{th} step of purification was implemented, which consist of purifying the filtered graphite in an atmosphere of $Ar/5H_2$ for 1 hour at 1000°C. As shown in the elemental map of figure 65 (b) this eliminated the corrosion of the impregnated specimens.

Figure 65: Elemental maps obtained using EDS for samples impregnated with as-produced CDC (a) and with CDC after a thermal purification step (b)

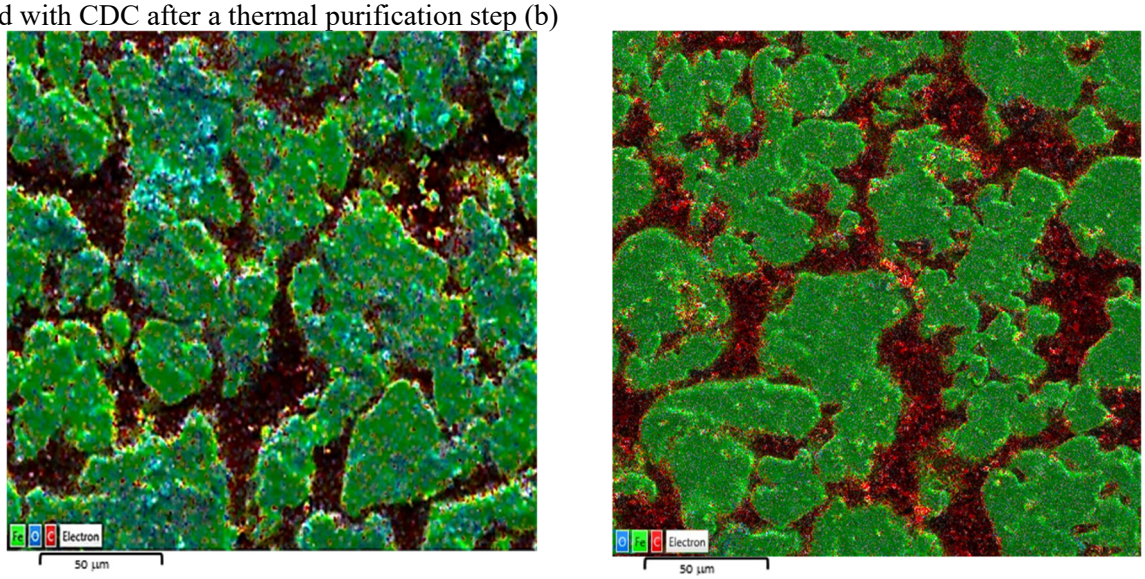

(a) (b)

Source: Author

As the pores were filled and the samples were free of corrosion, the tribological tests proceeded. Figure 68 shows the tribological results of scuffing resistance tests performed on a

sample compacted at 400 MPa and sintered at 1100 °C impregnated with CDC synthesized at 1500°C. As shown in the figure the specimen was able to maintain lubricity up to the 9th load.

Figure 66: Evolution of the coefficient of friction in a scuffing resistance test of a specimen impregnated with purified CDC

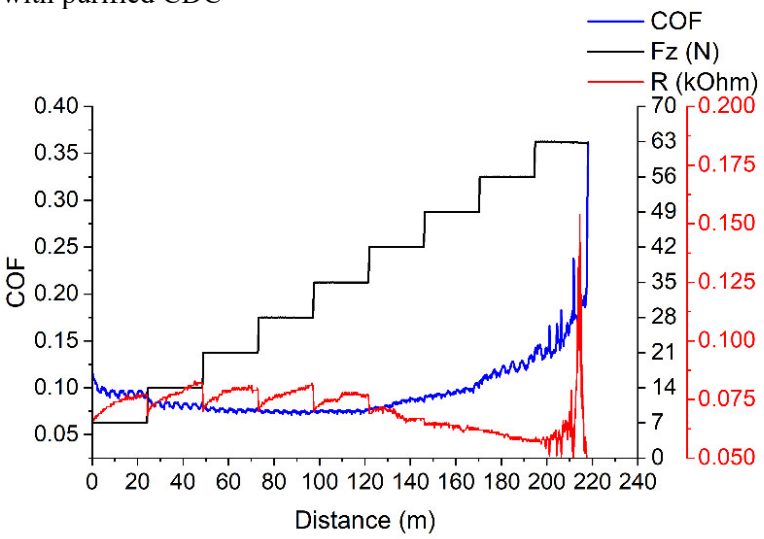

Source: Author

Since all the graphite tested were able to provide lubricity the impregnation conditions were established as summarized in table 6.

Table 6: Impregnation conditions for all the graphite particles used in this work

Graphite	N° of impregnation cycles	Comments
Crystalline 1.10 µm	8	Beyond the saturation point, incrementing the number of cycles did not improve its tribological behaviour
Crystalline 6.07 µm	16	The number of cycles was determined considering the results obtained with the 21.54 µm graphite
Crystalline 21.54 µm	16	Particle size influenced the capacity of the particles to enter the pores.
CDCs (synthesis temperatures: 1200, 1300, 1400 and 1500 °c)	16	Corrosion was found in samples impregnated with the as-produced CDC, so an extra purification step was needed to prevent this corrosion.

Source: Author

Once the impregnation conditions were established, the study continued to step 3: the study of the effect of graphite particle size on the tribological behaviour of porous steel.

5.3 EFFECT OF GRAPHITE PARTICLE SIZE ON THE TRIBOLOGICAL BEHAVIOUR OF POROUS STEEL

In this step, samples compacted at 400 MPa and sintered at 1100°C were impregnated with 1.10, 6.07, and 21.54 μm graphite in order to study the effect of the particle size in the tribological behaviour of the sintered steels.

Figure 67 shows the size distribution of pores from the sample compacted at 400 MPa and sintered at 1100 °C and the impregnated graphite for comparison. Graphite of D50 = 1.10 μm falls in the range between 0.1 and 10 μm so when compared with the pore sizes, it was able to enter in all the pores of the sample. This explains why fewer impregnation cycles were needed for this particle size. Almost half of the graphite with D50 = 6.07 μm is above 10 μm which is 53 % of the total number of pores of the sample; this situation is even more pronounced in the graphite of 21.54 μm where most of the particles are bigger than half of the pores on the sample. This helps to explain why these conditions needed more impregnation cycles to possess enough filled pores to provide lubricity.

Scuffing resistance tests were performed to study the effect of the particle size in the ability of the samples to maintain a lubricating layer in a condition of incremental loads. As shown in figure 68 (a), even with particle sizes bigger than half of the pores of the samples, graphite with sizes of 6.07 and 21.54 μm were able to provide lubrication in the tests. Figure 68 (b) shows the scuffing resistance as a function of the graphite particle size. Both quantities are inversely proportional, meaning that larger graphite cannot maintain lubrication at high loads.

Figure 67: Size distribution of pores from a sample compacted at 400 MPa and sintered at 1100 °C (a); size distributions of graphite with D50 = 1.10 (b), 6.07 (c) and 21.54 µm (d)

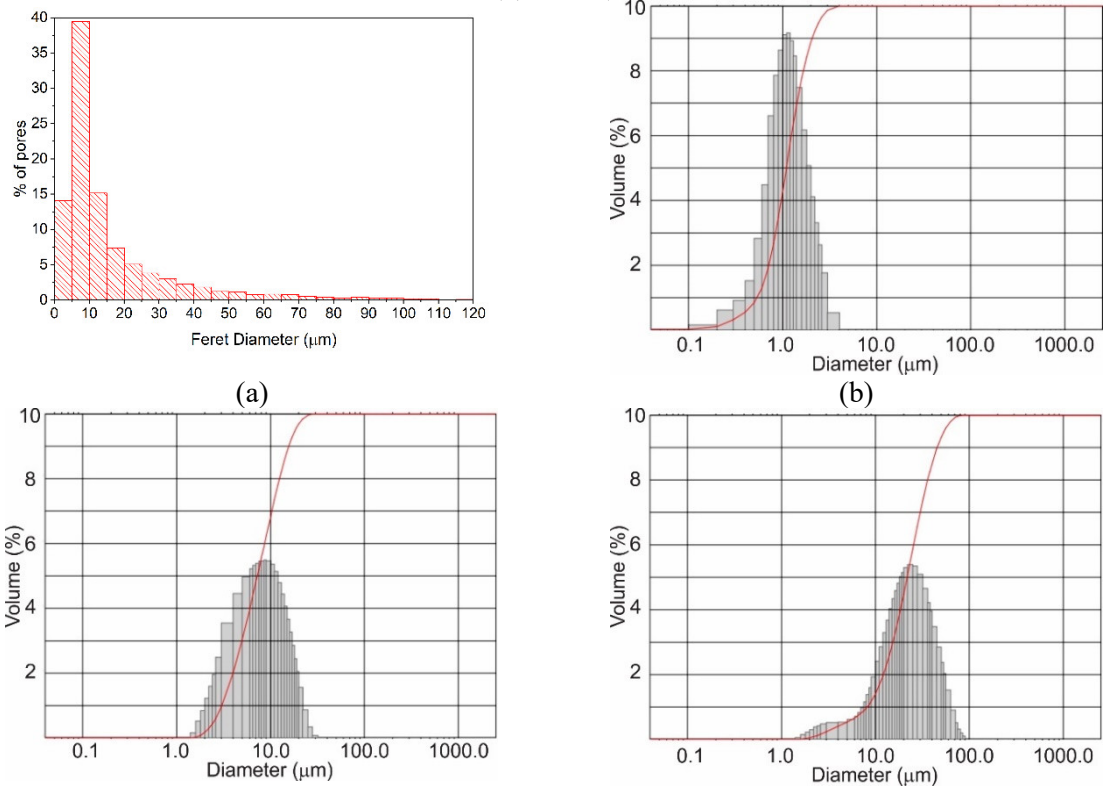

(a) (b) (c) (d)

Source: Author

Figure 68: Evolution of the coefficient of friction during the scuffing resistance tests (a) and mean scuffing resistances (b) of specimens impregnated with the 0.83, 6.07 and 21.54 µm graphite

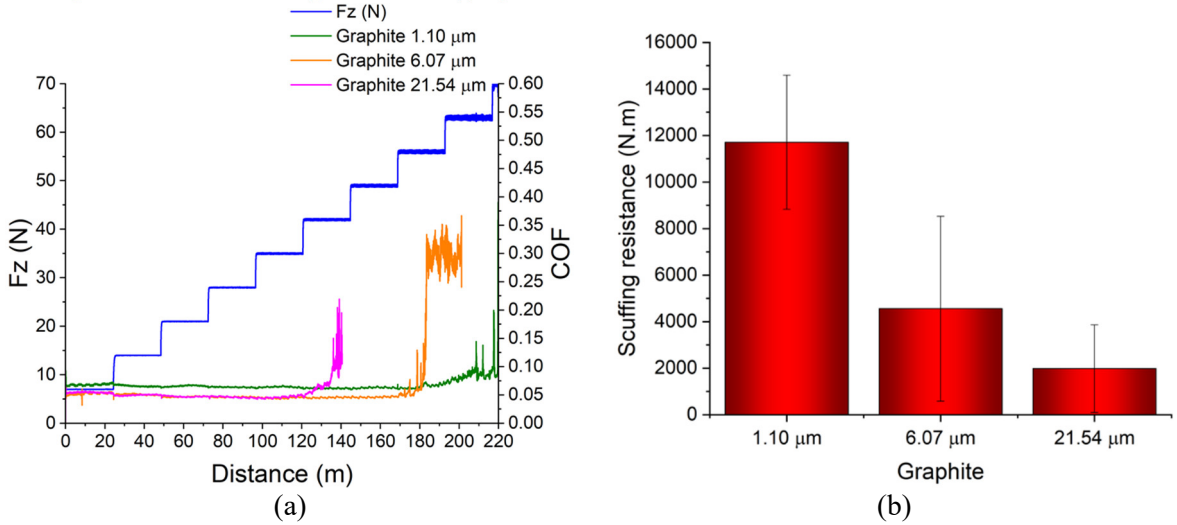

(a) (b)

Source: Author

To further study the influence of the particle size on the tribological response of the system. Constant load test with a load of 14 N and a duration of 1 hour were performed on the samples. From these tests, the average coefficients of friction as well as the wear rates of the specimens and the counter bodies were determined. As it is shown in figure 79, wear rates increase with particle size. The wear rates of specimens and counter-bodies had an increment of one order of magnitude, and there was no significative difference between 6.07 and 21.54 μm.

Figure 69: Wear rates of specimens impregnated with graphite of D50 = 1.10, 6.07 and 21.54 μm

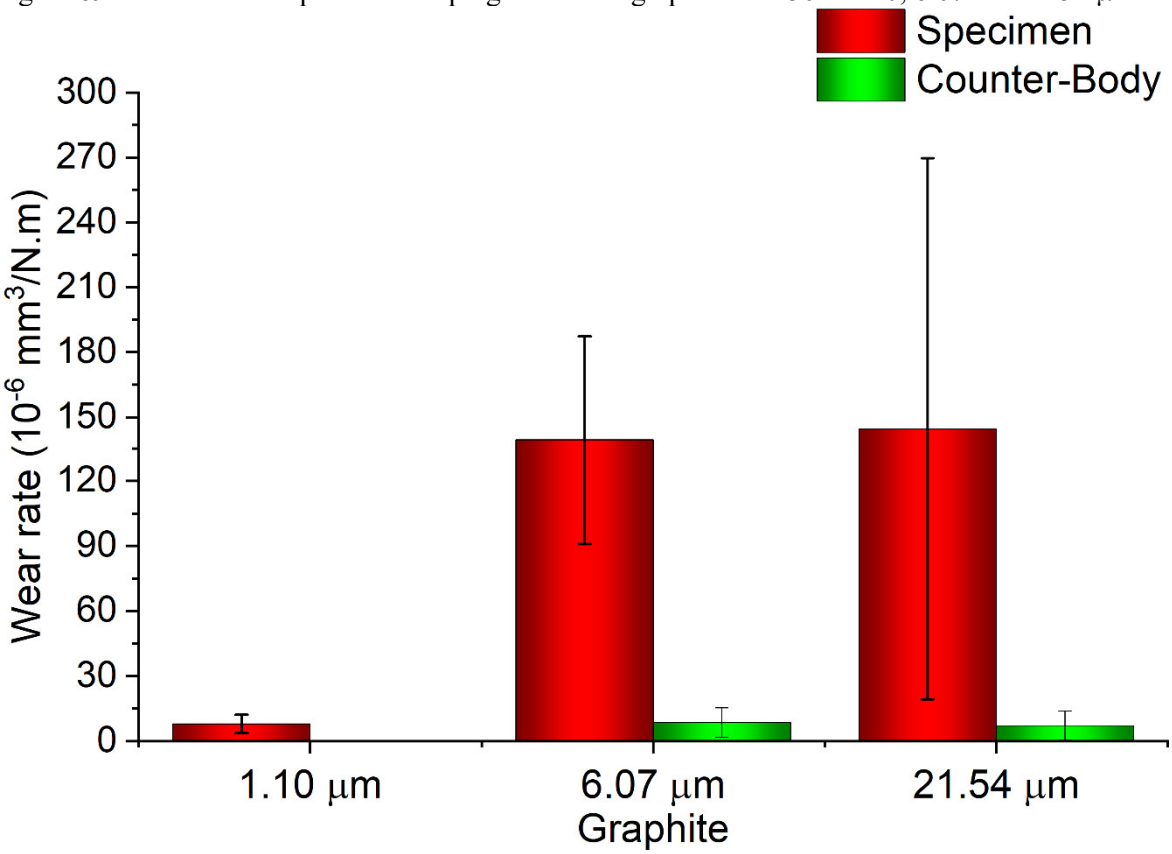

Source: Author

The wear rate of the counter-body for the 1.10 μm graphite in figure 71 was so low that it is not visible the scale of the figure. For the 6.07 and 21.54 μm graphite, the dispersion of the data was particularly high. This was because, as shown in figure 70 (b) and (c), the friction coefficient for this condition did not always remain in the lubricity regime (COF < 0.2) for the duration of the tests.

From figure 70 it comes to attention that for the larger particle sizes, there as a difference in behaviour between the incremental load and the constant load tests. At constant

load, particles of 6.07 and 21.54 µm cannot maintain lubricity for the first 100 m as was the case in the incremental load tests. This indicates that, for these particle sizes, the load increments helped to maintain and heal the lubricating layer. In other words, as the counter-body penetrated the specimen, it gained access to new reservoirs of graphite. This graphite was sheared and spread in the tracks, thus maintaining lubricity. Two mechanisms are proposed to explain this situation which are shown schematically in figures 71 and 72.

Figure 70: Evolution of the friction coefficient in the constant load test form specimens impregnated with 1.10 (a), 6.07 (b) and 21.54 mm (c) graphite

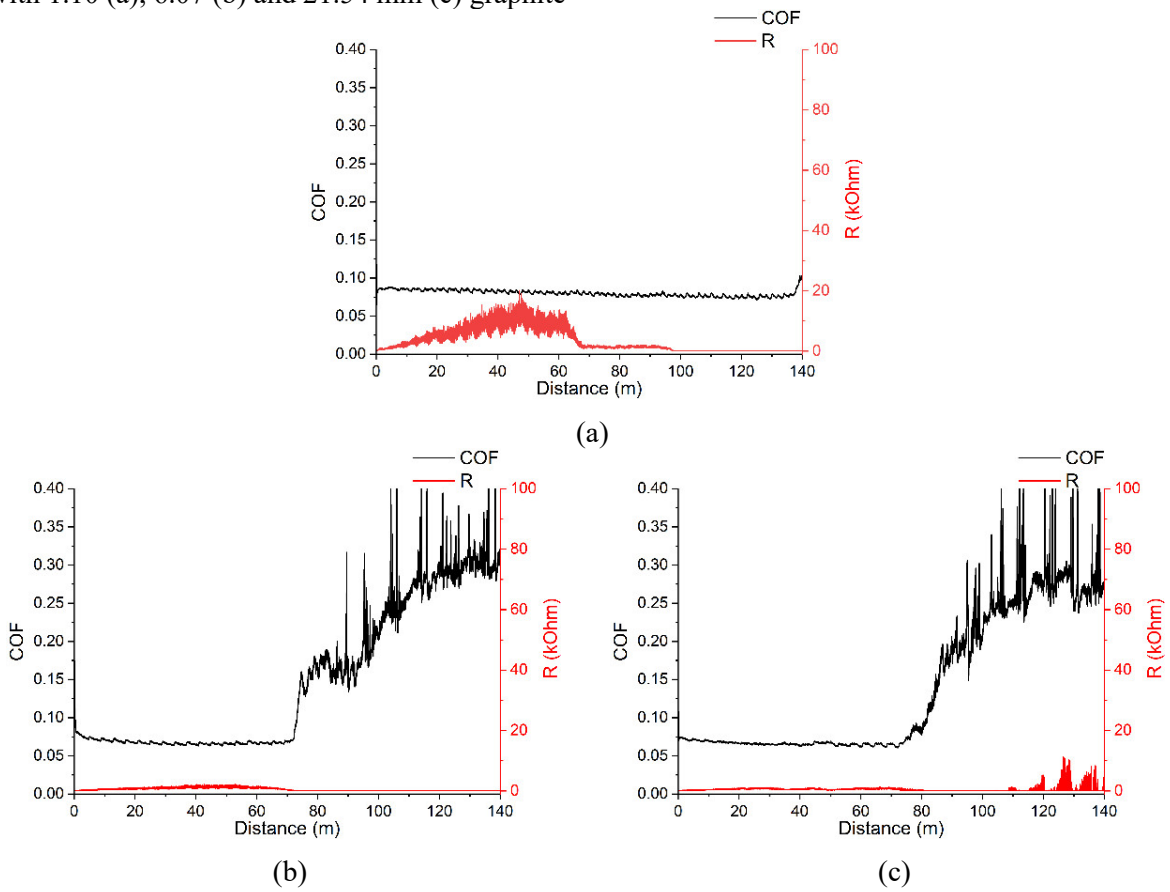

Source: Author

In the first mechanism proposed (shown schematically in figure 71), initially the contact area between the specimen and the counter-body and the width of the wear track are A_1 and w_1, respectively. When the load increases the contact area and the wide of the wear track increase to A_2 and w_2, this causes pores that were not being accessed by the counter body (yellow exes in figure 71) now supply graphite to the contact. If the load were to remain

constant, the supply of graphite ends when the pores inside w_1 get sealed. Figure 72 shows the second mechanism proposed.

Figure 71: Mechanism by which the counter body accesses new impregnated pores as load increases in incremental load tests (schematic)

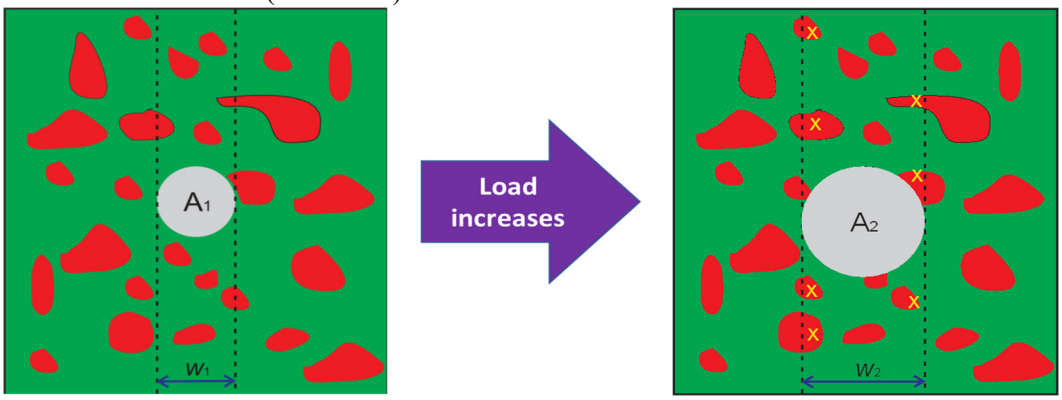

Source: Author

The second proposed model involves the differences in the flowability of powders derived from their different particle sizes. There is not a clear-cut fundamental equation of motion for powder lubrication (WORNYOH; JASTI; FRED HIGGS, 2007). However, rheological studies have proven satisfactory to describe the motion of powders (PODCZECK; MIA, 1996; FU et al., 2012; HAO, 2015). According to Higgs et al., several variables affect the flowability of powders (e.g., particle size, shape, density, surface energy, atmosphere, etc.).

Figure 72: Schematic representation of the graphite releasing process for the 1.10 µm graphite at constant load (a) and for the 6.07 and 21.54 µm graphite at constant (b) and incremental (c) loads

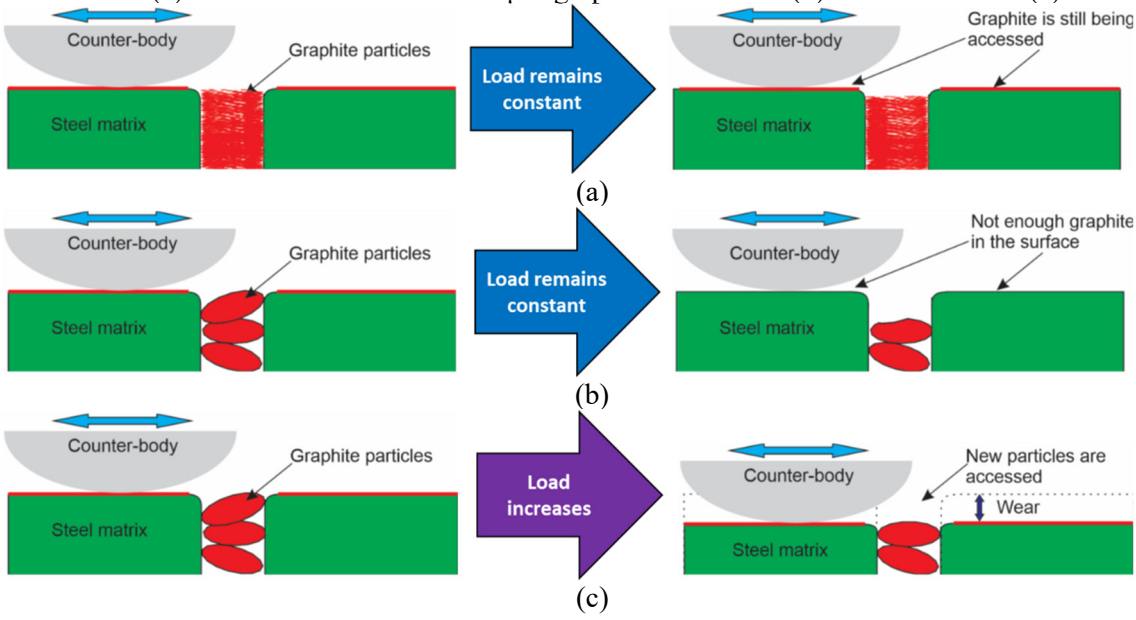

Source: Author

Among all the variables involved in the flow of powders, it has been established that for fine powders (< 150 μm) the cohesive van der Waals forces between particles greatly affect the flowability of powders (LÉONARD et al., 2017). These van der Waals forces increase with decreasing particle sizes, which result in a strong decrease in flowability (or an increase in powder viscosity) with decreasing particle sizes (FU et al., 2012; SHI et al., 2018). Taking this into consideration, the second model proposes that fine powders are slowly released from the impregnated pores at constant loads, forming and maintaining the lubricating tribo-layer as shown in figure 72 (a).

On the other hand, larger particles are more free-flowing, so they are quickly released from the pores (figure 72 (b)) during the constant load tests so they cannot maintain the lubricating tribo-layer. This situation was partially remediated by the increments in load during the scuffing resistance test, which increments the penetration of the sphere into the specimens, so it founds the graphite that was left inside the pores as shown in figure 72 (c). In their studies with nanometric WS_2 Rapoport et al. also pointed out the importance of the slow release of solid lubricant from the impregnated pores to maintain lubricity but no releasing mechanism was proposed (RAPOPORT et al., 2001; LESHCHINSKY et al., 2002). Regarding the force behind the flux of powders from the pores to the wear tracks may come from the elastic and plastic deformations of pores that squishes the graphite out of the stocks and from the van der Waals forces and electrochemical interactions between graphite and the counter body which causes graphite to leave the pores and to adhere to the AISI52100 balls.

The different mechanisms of graphite releasing lead to different tribological responses during the wear tests. To study these differences, the wear tracks were analysed using SEM and EDS as shown in figure 73. Figure 73 (a) shows the middle of the wear track of a sample impregnated with 1.10 μm graphite. Inside the track, it was possible to find open pores containing graphite as is confirmed by the elemental map (last image in figure 73 (a)). Figures 73 (b) and (c) show the half of the wear track and half of the rest of the specimen for samples impregnated with 6.07 and 20.54 μm graphite respectively. Severe plastic deformation and spalling of the tribolayer are present in both specimens (encircled in red). Figure 74 shows a zoomed image and its chemical analysis of the region encircled in blue in figure 73 (a)

Figure 73: Secondary and backscattered electrons SEM images along with their corresponding elemental maps of the wear tracks from specimens impregnated with 1.10 (a), 6.07 (b) and 21.54 µm (c) graphite

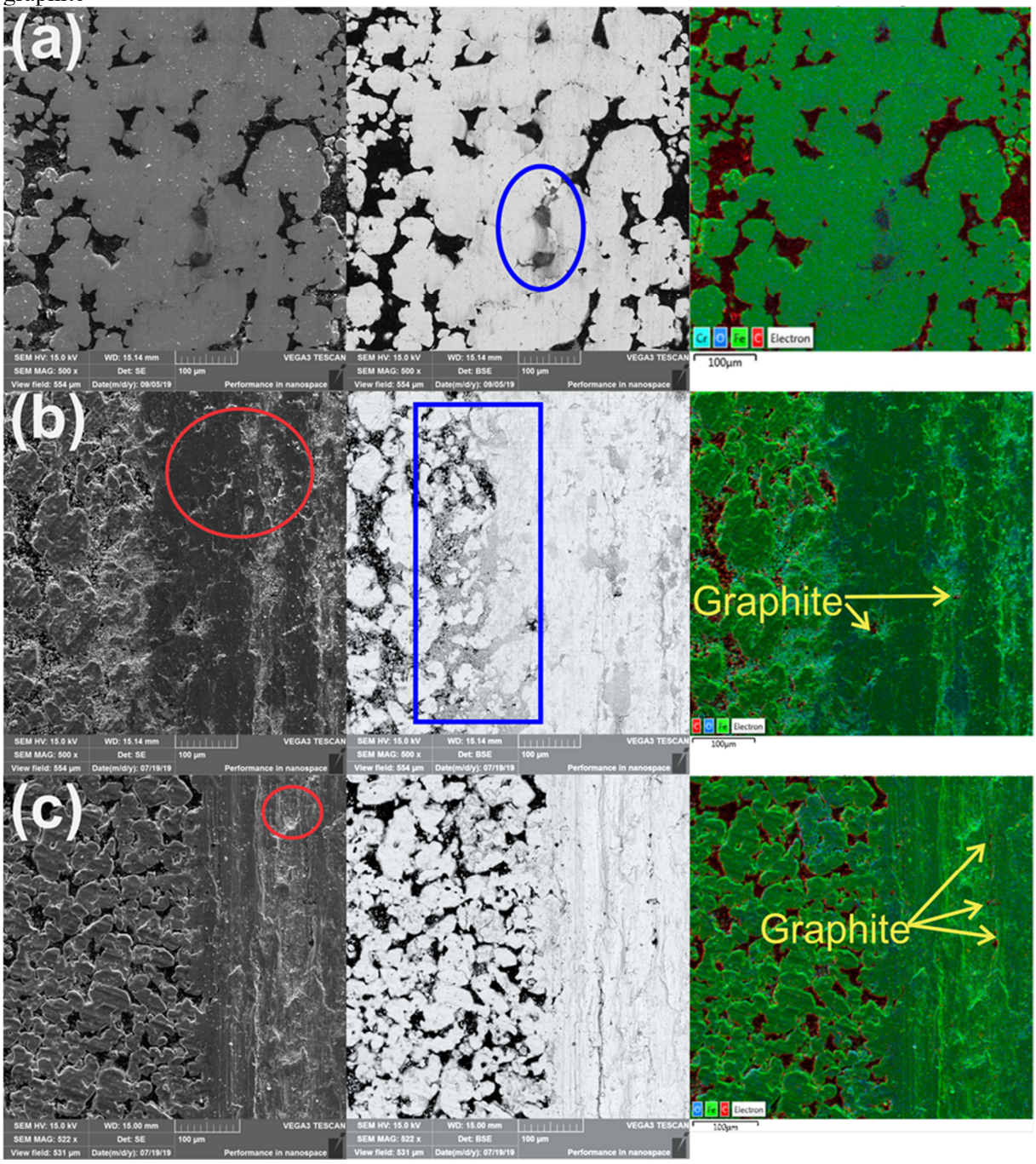

Source: Author

Figure 74: Zoomed image of a wear particle with graphite trapped in a pore of a sample impregnated with 1.10 µm graphite and its chemical analysis

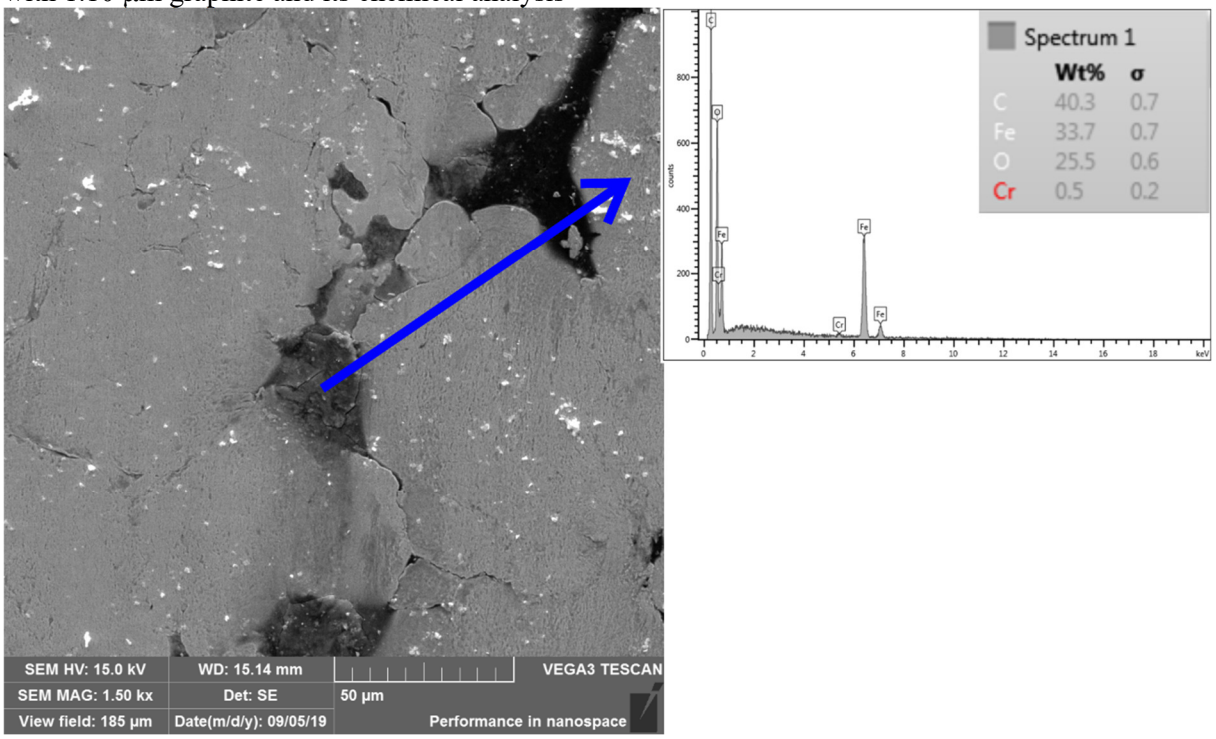

Source: Author

Figure 74 shows wear particles trapped in a pore. The chemical analysis suggests that these particles were mixed with the graphite that was inside the pore. This shows that even in conditions were the pores are filled with lubricant, they still act as traps for debris as was discussed in section 2.2.2. For the sample impregnated with the 6.07 µm graphite, the pores at the boundary of the wear track (marked by the blue rectangle in figure 73 (b)) are filled with debris (this was confirmed by the EDS map). On the other hand, there is a clear cut between the wear track and the rest of the specimen for the sample impregnated with the 21.54 µm graphite. This indicates that by the time the tests stopped, all the pores inside the track were sealed and the reciprocating action of the sphere removed the debris. Some graphite stocks can be found inside the tracks in figures 73 (b) and (c). To analyse how these stocks are different from those found in figure 73 (a), they were observed at higher magnification using SEM as shown in figure 77. Figure 75 (a), (b) and (c) shows the graphite stocks found in the wear tracks of samples impregnated with the 1.10, 6.07 and 21.54 µm graphite respectively. EDS analyses confirmed the presence of graphite (yellow arrows) and oxides (red arrows) inside the tracks. Graphite in figure 75 (a) is located inside a deformed pore and at surface level, the presence of

graphite particles around the stock suggests that it still possesses the capacity to release graphite and provide lubrication. Stocks in figures 75 (b) and (c) are below the level of the wear track

Figure 75: Zoomed pores containing graphite from wear tracks of specimens impregnated with 1.10 (a), 6.07 (b) and 21.54 µm (c) graphite

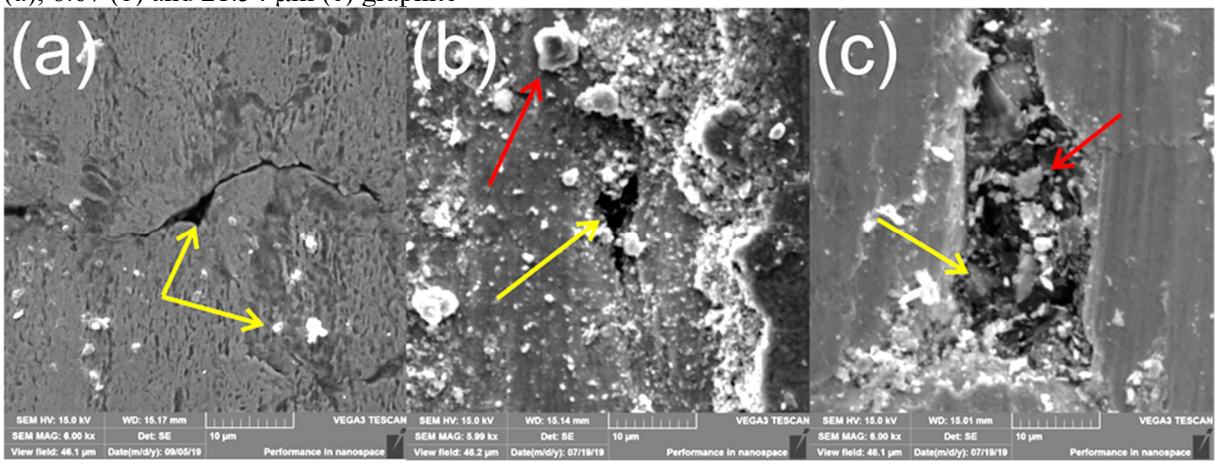

Source: Author

The zoomed-out image of these stocks shown in figure 76 suggests that these impregnated pores were exposed by the detachment of the tribolayer above them due to the action of the counter-body

Figure 76: Zoomed out SEM image of the exposed stocks shown in figure 77 (b) and 77 (c) respectively

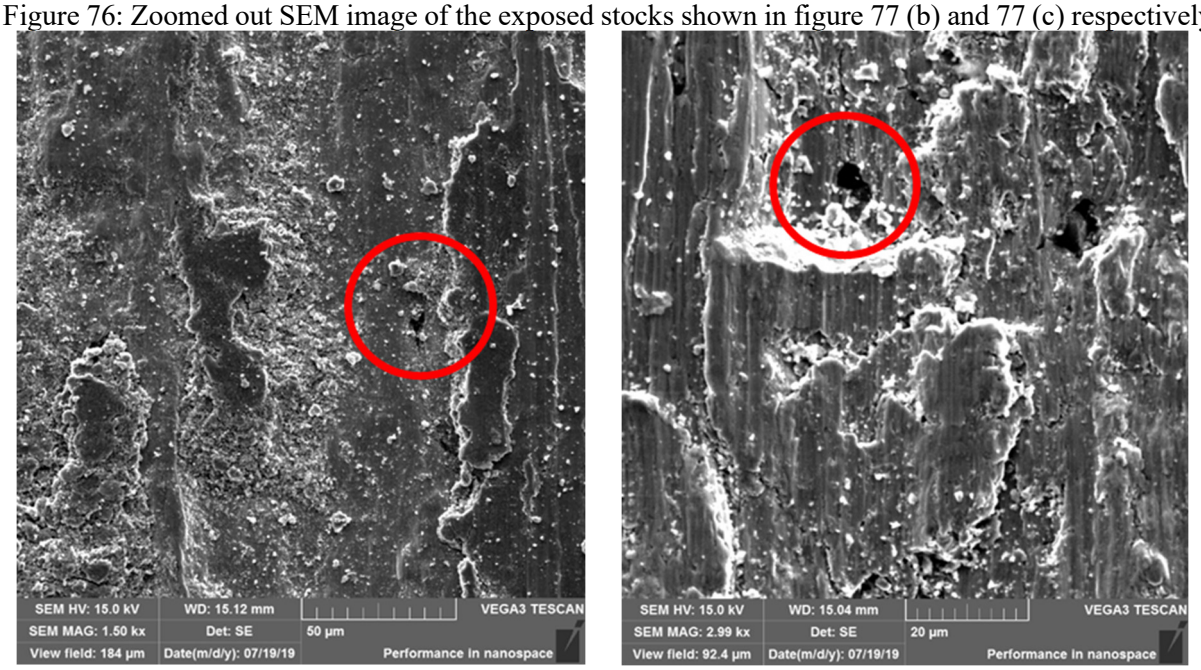

(a) (b)

Source: Author

The wear tracks were also investigated by Raman microscopy. The objective of the analysis was to observe if there were differences in the tribolayers generated by the different conditions and to try to correlate these differences with their tribological behaviour. Figure 77 shows the Raman spectra of crystalline graphite powder and of the wear tracks of samples impregnated with 1.10, 6.07 and 21.54 μm graphite. The Raman spectrum of crystalline graphite shown in figure 77 (a) exhibits the typical D, G and 2D bands. The low ID/IG ratio and the fact that the 2D band can be fitted by two peaks show that this graphite is highly ordered (as was discussed in section 2.4). The Raman spectra shown in figures 77 (b), (c) and (d) show the additional T band , which is associated to ta-C with sp^3 hybridization (FERRARI; ROBERTSON, 2001), and also the D+G and G+2D bands (which are overtones of the D and G bands (MARTINS FERREIRA et al., 2010)). These bands are associated with the amorphization process of graphite from an sp^2 to an sp^3 hybridization (FERRARI; ROBERTSON, 2000). Peaks marked with red asterisks correspond to bands located at ~ 650 and ~1150 cm^{-1}. These bands can be attributed to iron oxides produced during the tribological tests as they are close to the peaks reported for iron oxides in the literature (HANESCH, 2009; BARBOSA et al., 2015; KHAEMBA; NEVILLE; MORINA, 2015; DE MELLO et al., 2017a).

In the case of the Raman spectrum of the sample impregnated with 6.07 μm graphite, the intensities of the T, D and the oxide bands in relation with the G band are higher than in the other samples. This indicates that the carbon present in the tribolayer was highly amorphized and oxidation in the track was extensive (this correlates with the presence of debris inside the track). Also, the lack of a 2D band (which indicates 3D stacking order (JORIO, 2012)) points to the lack of stacking in the z-axis, supporting the idea of almost completely amorphous carbon.

Figure 77: Exemplary Raman spectrum of crystalline graphite powders (a) and Raman spectra obtained from the wear tracks of specimens impregnated with 1.10 (b), 6.07 (c) and 21.54 μm (d) graphite

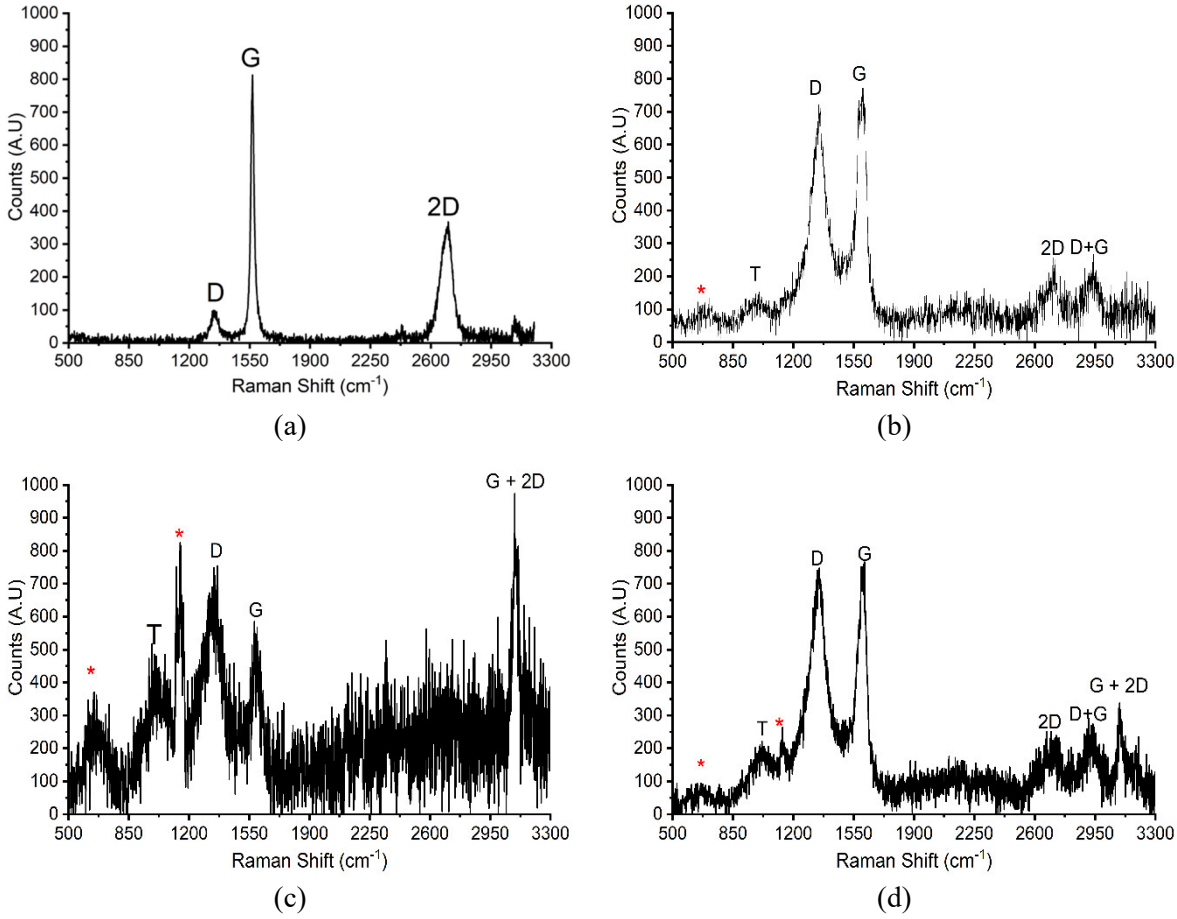

Source: Author

In this chapter, the influence of the graphite particle size in the tribological behaviour of impregnated porous steel was studied. The results show that small particle size is crucial to provide enough lubrication during the tribological testing. Inadequate lubrication due to the insufficient release of graphite during testing resulted in increased wear rates and coefficients of friction above the 0.2 threshold. It was also observed that to maintain lubricity, carbon in the wear tracks must retain some crystallinity. The release of graphite and crystallinity of carbon in the wear tracks were further explored in step 4.

5.4 EVOLUTION OF PORES AND SOLID LUBRICANT DURING INCREMENTAL LOAD TRIBOLOGICAL TESTS

To study the interaction between the pores and the solid lubricant particles during the tribological testing, 1.10 μm graphite was impregnated in samples compacted at 200, 400 and 600 MPa and sintered at 1100 °C. Also, to study the effect of the sintering temperature in this interaction samples compacted at 400 MPa and sintered at 1150 and 1200 °C were also impregnated with graphite.

First, the scuffing resistance of the impregnated samples was measured. Figure 788 shows the typical evolution of the coefficient of friction and contact resistance for the studied conditions. For all the samples, contact resistance tends to increase while the load remains constant and then drops when the load changes. This indicates an insulating tribolayer forms between the specimens and the counter-bodies. Contact resistance reached its minimum 2-3 loads before the end of the tests. This may signal that the healing process of the lubricating layer stops a few loads before the lubricity regime ends or that this healing process was no longer measurable by the evolution of the contact resistance, however, the study of this phenomena requires sophisticated techniques in order to analyse the tribolayers right before and after the load increases. These techniques include the analysis of the tribolayers using a focused ion beam to extract the tribolayers and then analysing them by TEM and XPS techniques, however, these studies are beyond the scope of this work.

The scuffing resistance for all the conditions studied in this step is shown in figure 79. As shown by the figure, the scuffing resistance of the samples was proportional to the porosity of the samples. These results were expected as samples with more pores, possessed more available graphite in their surfaces, so they were able to retain lubricity for longer. Sintering temperature had no significant effect on porosity, but it was effective in maintaining lubricity for longer. In principle, this was attributed to better mechanical strength at the surfaces due to better sintering between the metal particles, as is suggested by the hardness measurements presented in figure 56 (a). As it will be shown, the duration of the lubricity effect depends (amongst other parameters) on the resistance of the pores to being sealed, and this resistance in turns depends on the bulk mechanical properties of the sintered specimens.

Figure 78: Evolution of the friction coefficient and contact resistance during scuffing resistance test of specimens sintered at 1100°C and compacted at 200 (a), 400 (b) and 600 MPa (d). Also, for a specimen compacted at 400 and sintered at 1200 °C (c)

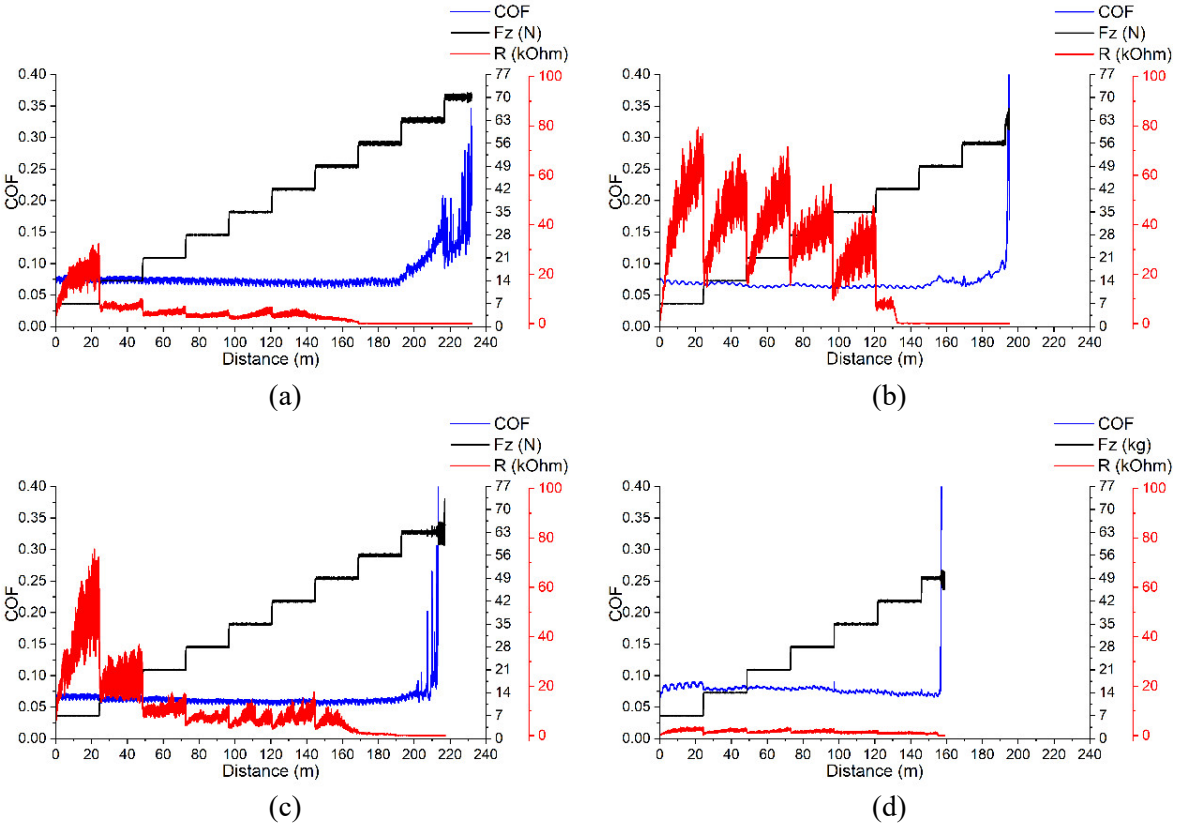

Source: Author

To study if the positive effect of porosity in the scuffing resistance translated to the wear resistance of the specimens, constant load tests were performed. As the scuffing resistance of the specimens sintered at 1150 °C was not statistically different from those sintered at 1100 and 1200 °C this condition was discarded.

Figure 79: Influence of the sintering temperature and compaction pressure in the scuffing resistance of specimens impregnated with 1.10 μm graphite

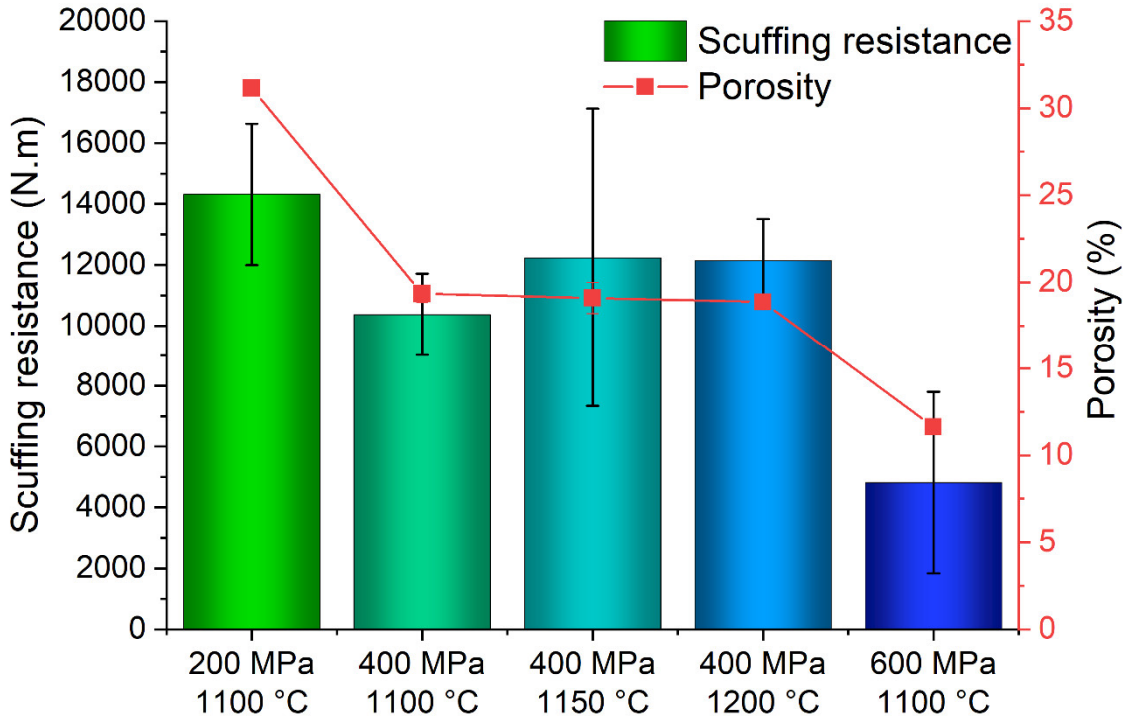

Source: Author

Figure 80 shows the typical evolution of the coefficient of friction and contact resistance during the constant load tests, figure 81 (a) shows the wear rates and the coefficients of friction measured in the studied samples, figure 81 (b) shows the wear rates of the counter bodies in a zoomed scale for visualisation purposes and figure 81 (c) shows the wear rates of the specimens as a function of their porosity. For all the conditions, the coefficients of friction remained steady over the entire test with some minor disturbances at the end. Contact resistance reached a maximum in the first half of the tests and then decreased (samples compacted at 200 MPa had this maximum in the second half of the test). This behaviour was different from what was found in the scuffing resistance tests and supports the idea that, for these materials, incremental loads are beneficial to the regeneration of the lubricating layer as graphite was gradually being accessed with each increment in load. In the case of constant load tests, the regeneration of the lubricating layer will depend only on the ability of the graphite to slowly leave the reservoir and participate in the formation of the tribolayer. This notion was already proposed back in step 3 (figures 72 and 73).

Figure 80: Evolution of the coefficient of friction and contact resistance for specimens sintered at 1100°C and compacted at 200 (a), 400 (b) and 600 MPa (d). Also, for the specimens compacted at 400 and sintered at 1200 °C (c)

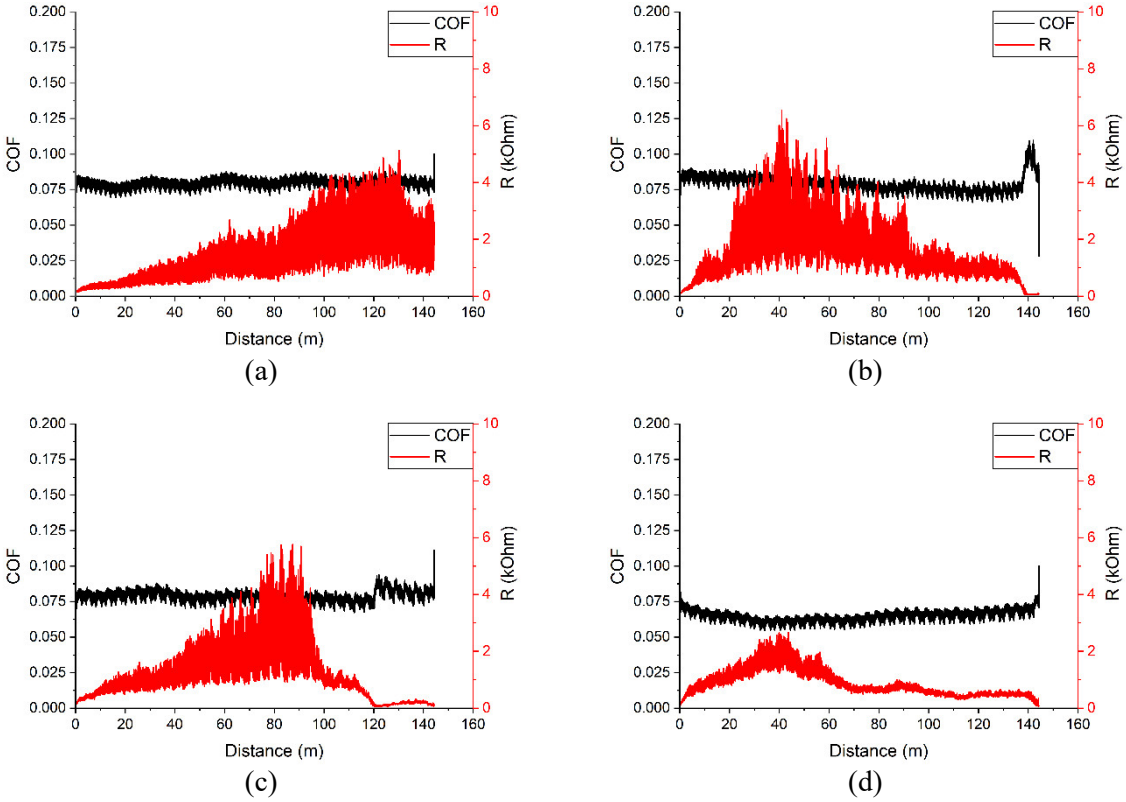

Source: Author

As shown by figure 81 (c), the wear rates of the specimens and counter-bodies were proportional to the porosity of the samples. If these results are compared with the results of scuffing resistance shown in figure 81, it is clear that even if more stocks of lubricant were available, the wear rate of the system was heavily influenced by the bulk mechanical strength of the sintered steel, which decreases with porosity. The differences in the wear rates of samples sintered at 1100 and 1200 °C also supports this hypothesis. In summary; scuffing resistance depends more on the amount of lubricant being accessed by the counter body (in other words, in the ability of the lubricating layer to heal) and wear resistance depends more on the mechanical properties of the samples (remembering that the microhardness of the metallic phase was equal for all the conditions).

Figure 81: Wear rates of the specimens studied in this step and their counter-bodies (a); zoomed wear rates of the counter-bodies (b); wear rates as a function of the porosity (c).

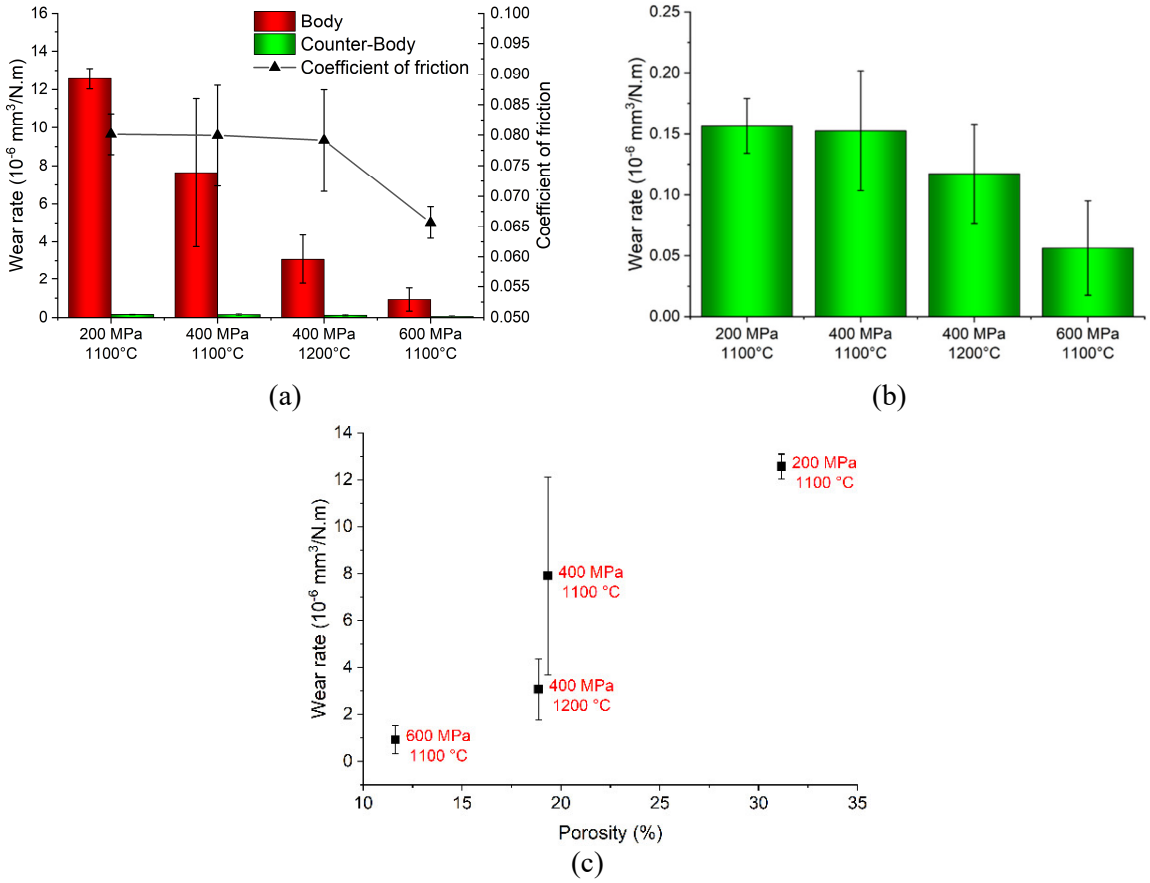

Source: Author

From figure 81 (a), it comes to attention that the coefficient of friction observed in samples compacted at 600 MPa was consistently lower than for the other conditions (0.065 vs. 0.080 for other samples). These friction coefficients were in themselves low when compared with those found in similar conditions for iron-graphite materials like grey cast irons (COF ~ 0.1(ZHANG, 2011)), ADI (COF ~ 0.2 – 0.6 (GHADERI; NILI AHMADABADI; GHASEMI, 2003; BEDOLLA-JACUINDE et al., 2015)) and Fe-Si-Graphite composites (COF ~ 0.11 (DE MELLO et al., 2017a)). The friction coefficients were close to those found in self-lubricating steels (COF ~ 0.04 – 0.2 (BINDER, 2009)) and in pure graphite pins vs steel disks (COF ~ 0.06 – 0.12 (JRADI; SCHMITT; BISTAC, 2009)). The reduction of the coefficient of friction for the samples with the lowest porosity indicates that, at a constant load, the lubrication phaenomena does not only depend on the number of stocks available but also on the

characteristics of the tribolayers produced. In order to elucidate this point, the wear tracks were analysed by SEM, as shown in figure 82.

Figure 82: Secondary electron SEM images from the wear tracks of specimens sintered at 1100°C and compacted at 200 (a), 400 (b) and 600 MPa (d). Also, for a specimen compacted at 400 and sintered at 1200 °C (c)

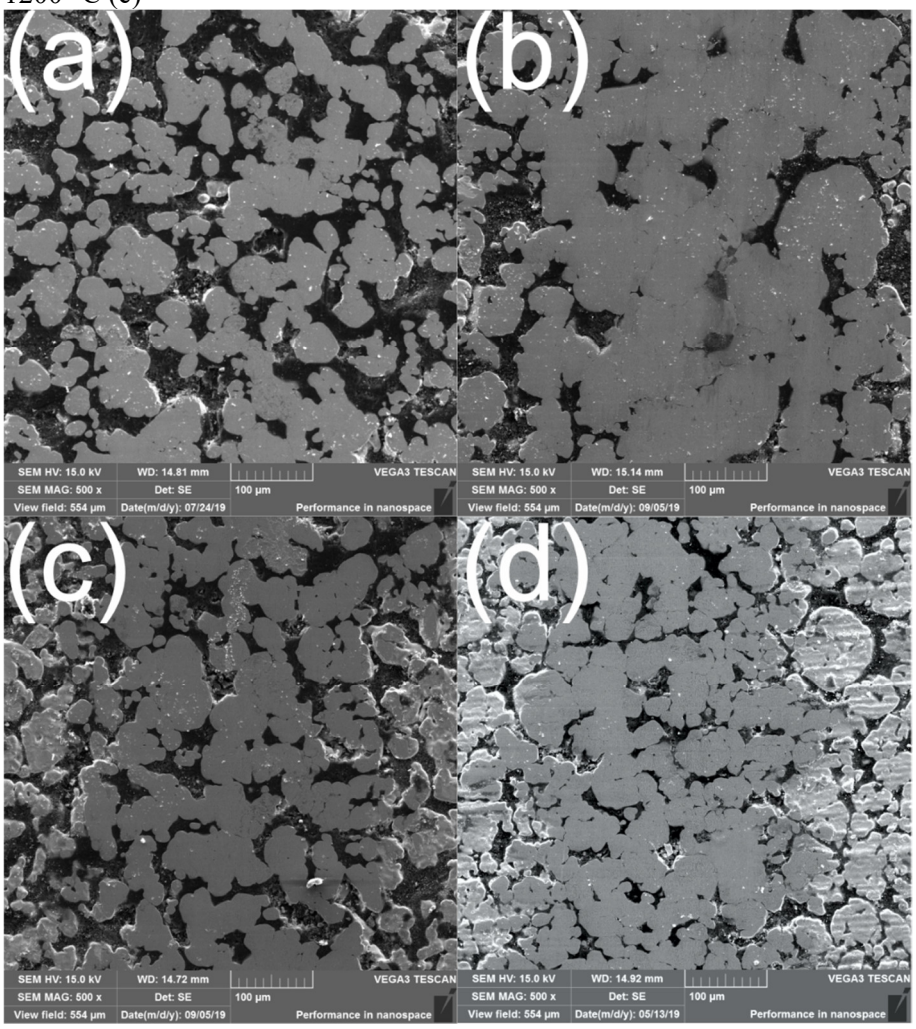

Source: Author

SEM images of the wear tracks reveal the differences between the amount of available graphite for all the conditions. The wear track of the sample compacted at 200 MPa (figure 85 a)) was the widest and shows more graphite stocks than the other conditions. This can be correlated with the fact that for these conditions, contact resistance peaked near the end of the test. This means that there were enough available stocks to heal the lubricating layer up to the end. The sintering temperature in samples compacted at 400 MPa (figure 82 (b) and (c)) influenced the number of graphite stocks available at the end of the test (this is also correlated to when the contact resistance peaked for both conditions). Better sintering between the metal particles caused the material to be more resistant to the sealing of pores during testing. Lastly,

samples compacted at 600 MPa (figure 82 (d)) have the narrowest wear tracks with impregnated pores still available at the surface and debris inside some pores (marked by the blue circle). A zoom of the graphite stocks (shown in figure 83) was done in order to characterize the tracks further.

Figure 83: : Zoomed secondary electrons SEM images from the wear tracks of specimens sintered at 1100°C and compacted at 200 (a), 400 (b) and 600 MPa (d). Also, for a specimen compacted at 400 and sintered at 1200 °C (c)

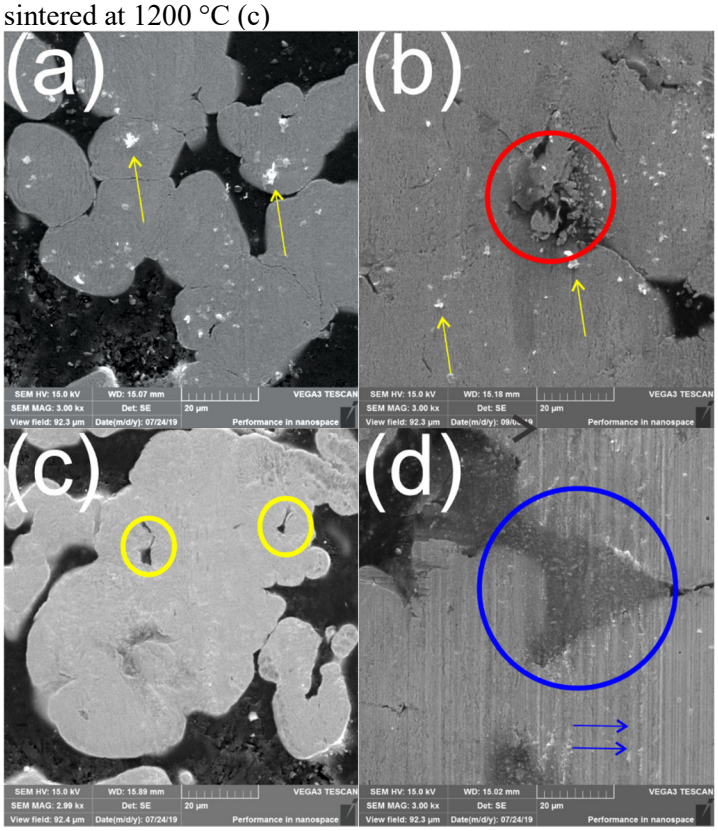

Source: Author

In figure 83, the yellow arrows point to graphite particles that were found inside the wear tracks. Also, in the sample compacted at 400 MPa and sintered at 1100°C (figure 83 (b), some pores filled with flake-shaped debris were found (marked by the red circle). As this was the condition with the least open pores inside the track, it can be expected that the lubricating layer was not homogenous, so certain areas were more directly exposed to the action of the counter body. Figure 83 (c) shows some pores containing graphite about to be closed (yellow circles) inside the wear track of a sample compacted at 400 MPa and sintered at 1200 °C. These pores exhibit plastic deformation and show the importance of the mechanical resistance of the graphite stocks to maintain lubrication in this system. They also show that smaller pores tend

to close faster than the bigger pores around them. Finally, figure 83 (d) shows a close up of a wear track from a sample compacted at 600 MPa and sintered at 1100 °C. Inside the track, abrasion marks can be found (pointed by the blue arrows), also pores filled with carbon and oxides (as confirmed by the elemental map shown in figure 82) like the one highlighted by the blue circle can be found throughout the track.

Figure 84: Elemental map obtained by EDS analyses of a pore containing graphite and oxides from the wear track of a specimen compacted at 600 MPa and sintered at 1100 °C

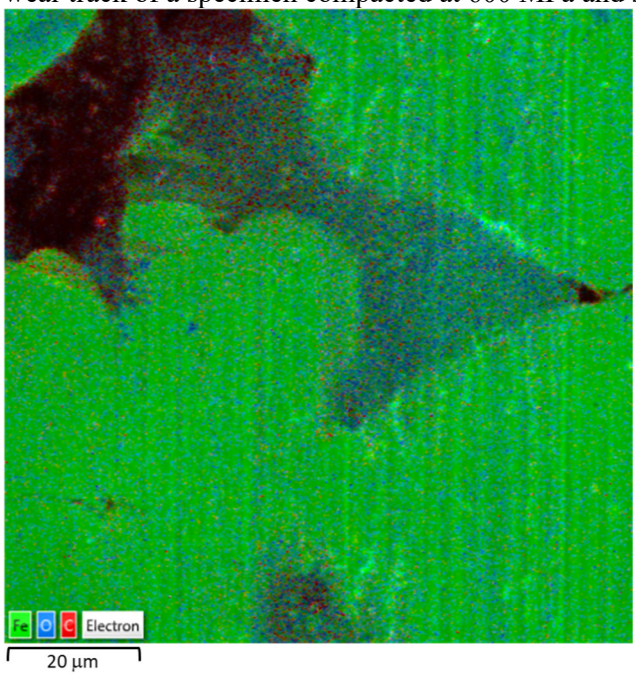

Source: Author

The presence of a mixture of fine oxides (tribolayer) and graphite inside the pores may have a synergic effect in reducing the coefficient of friction as has been found in previous studies (SLINEY, 1982). The formation of these fine oxides can be explained by the low amount of graphite at the start of the test (due to the low porosity of the sample) which did not adequately protect the wear track from oxidation, thus generating these lubricious tribolayers. On the other hand, studies conducted on self-lubricating steels have found that better mechanical properties of the substrate improve the performance of the solid lubricant, which reduces their coefficient of friction (DE MELLO et al., 2013). To determine the exact cause of this drop in the coefficient of friction, more modern techniques to isolate and analyse the tribolayers produced by the impregnated specimens are required.

Raman analyses of the wear tracks (figure 85) did not show significant differences amongst the samples. The disorder-induced bands D+G and G+2D appear in some of the spectra

along with the T band. At this level of amorphization, the ID/IG ratio is no longer a good measure of disorder or crystallite size (FERRARI; ROBERTSON, 2000) and require more sophisticated analysis methods as those presented in section 2.4.

Figure 85: Raman spectra of the wear tracks from samples sintered at 1100 °C and compacted at 200 MPa (a), 400 MPa (b) and 600 MPa (d). (c) shows the spectra from a sample sintered at 1200 °C and compacted at 400 MPa.

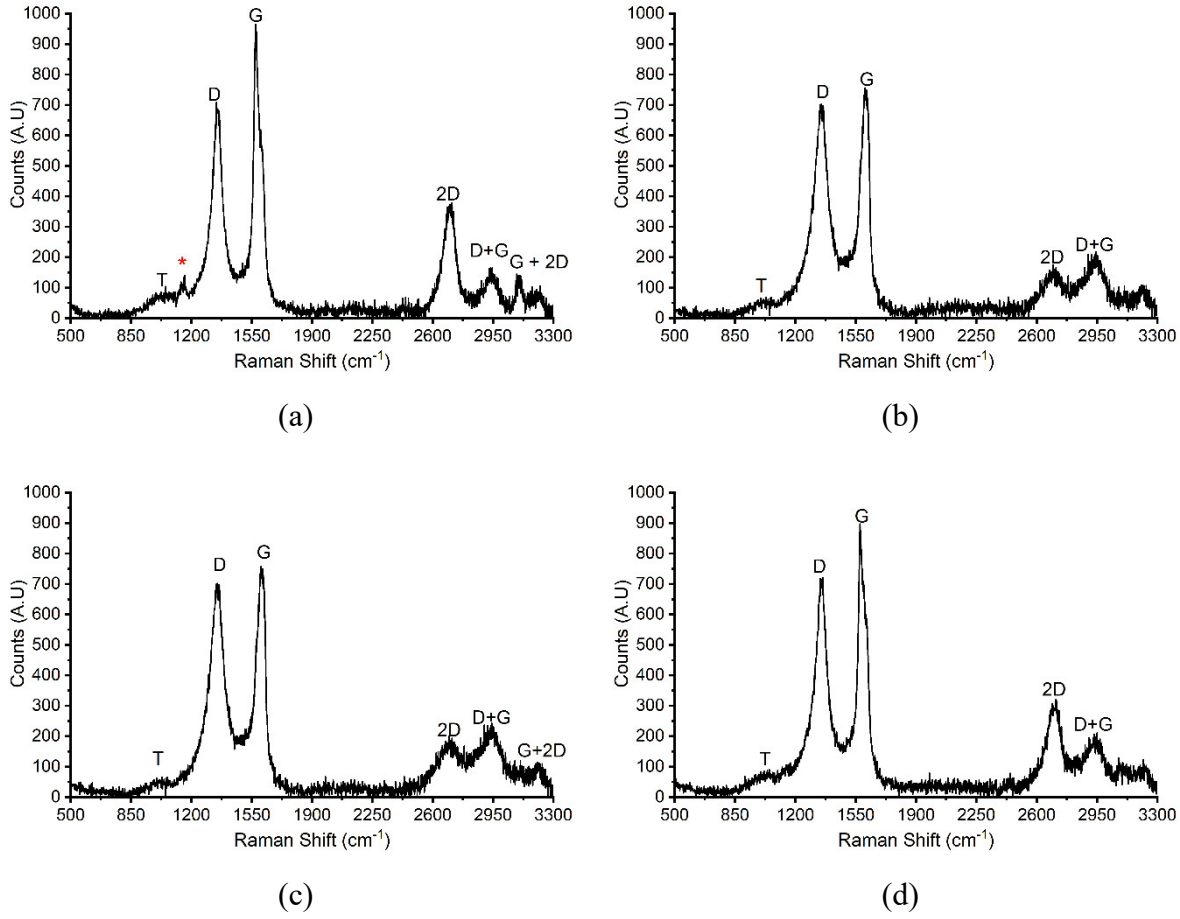

Source: Author

Several points have been raised and discussed, among them the effect of the graphite stocks in the tribological performance of the sintered samples, the role of the release of graphite from the stocks and the amorphization process of graphite during the tests. To address these topics, for each condition, the scuffing resistance tests were stopped at the end of each load up to the point where lubricity ended. Figure 86 shows an example of where the tests were stopped.

Figure 86: Evolution of the coefficient of friction during a scuffing resistance test showing the points (green arrows) where the tests were stopped for the image analysis

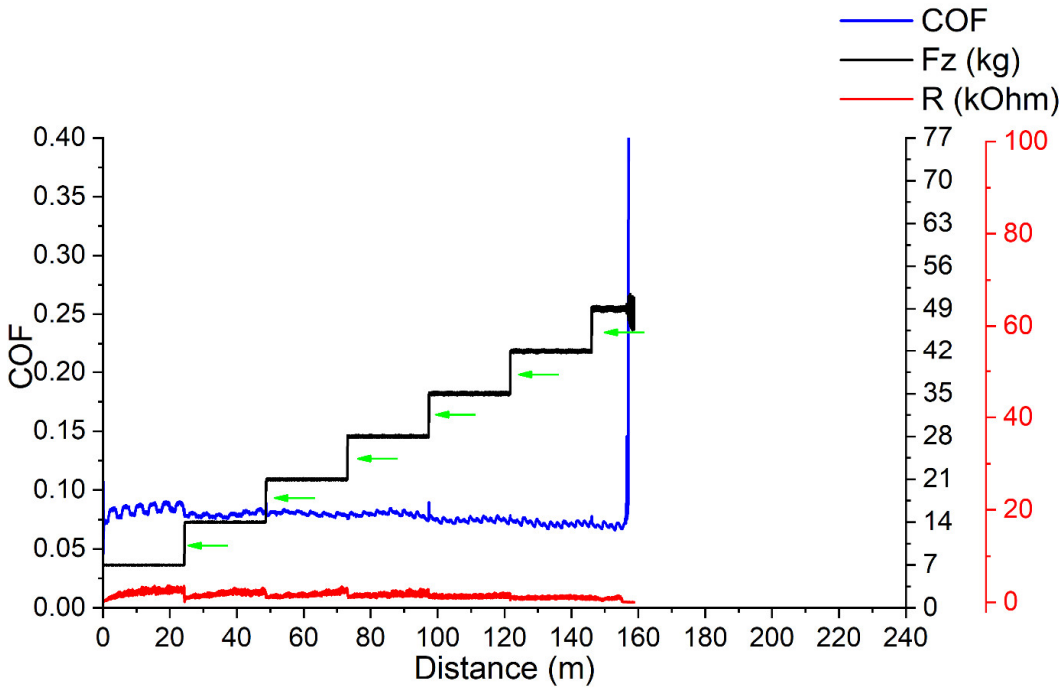

Source: Author

Image analyses of the SEM images and EDS carbon maps obtained from the wear tracks produced in these tests were analysed using a custom-made Python 3.6 script. The details of the analysis procedure were presented in section 3.5.4.

Figure 87 shows the evolution of the porosity and the wear rates as a function of the load where the tests were interrupted. The wear rates were calculated as the wear volume of the track divided by the area under the curve of the load vs distance graph . Samples compacted at 200 MPa had a drastic decrease of porosity in the wear tracks as a function of load. Wear rates also had a drastic decrease up to the 28 N load where it almost stabilized. For the other samples, porosity did not decrease drastically until the end of the test was reached and all the graphite reservoirs were closed. By comparing figures 87 (a) and (b), it can be deduced that wear rates were balanced by the sealing of pores meaning that, as load increased, the porosity of the samples decreased proportionally, keeping the wear rates constant in the lubricity regime. Samples compacted at 200 MPa took up to the fourth load to reach this balance between pore closing and wear rates.

Figure 87: Evolution of porosity (a), wear rates (b) and hardness (c) in the lubricity regime as a function of the load where the tests were interrupted

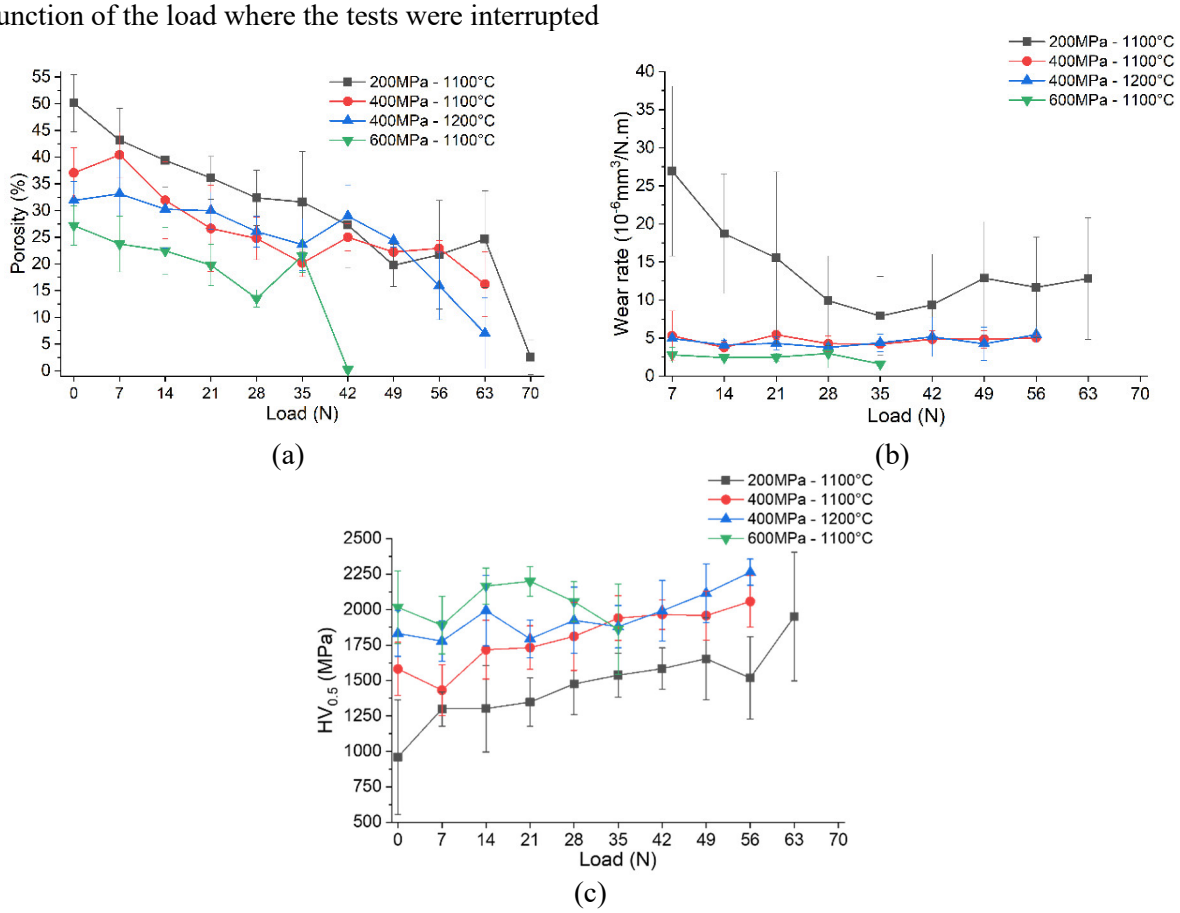

Source: Author

Figure 87 (c) shows the microhardness of the wear tracks as a function of load; for specimens compacted at 200 and 400 MPa the microhardness increases as a function of the load which corresponds with the sealing of pores with load. This increment in hardness was more pronounced for the sample compacted at 200 MPa as the pore sealing rate was more dramatic for this condition due to its initially low hardness. For the specimens compacted at 600 MPa, the analysis of variance (found in appendix A) reveals that there are no significant changes of hardness as a function of load for this condition in the lubricity regime.

To analyse the pore sealing process in more detail, the number, size, shape and orientation of pores were analysed. Figure 88 shows the evolution of the numbers of pores, pore size and orientation as a function of load during the scuffing resistance tests.

Figure 88: Evolution of the number of pores, porosity, Feret diameter and pore orientation for of specimens sintered at 1100°C and compacted at 200 ((a) and (b)), 400 ((c) and (d)) and 600 MPa ((g) and (h)). Also, for a specimen compacted at 400 and sintered at 1200 °C ((e) and (f))

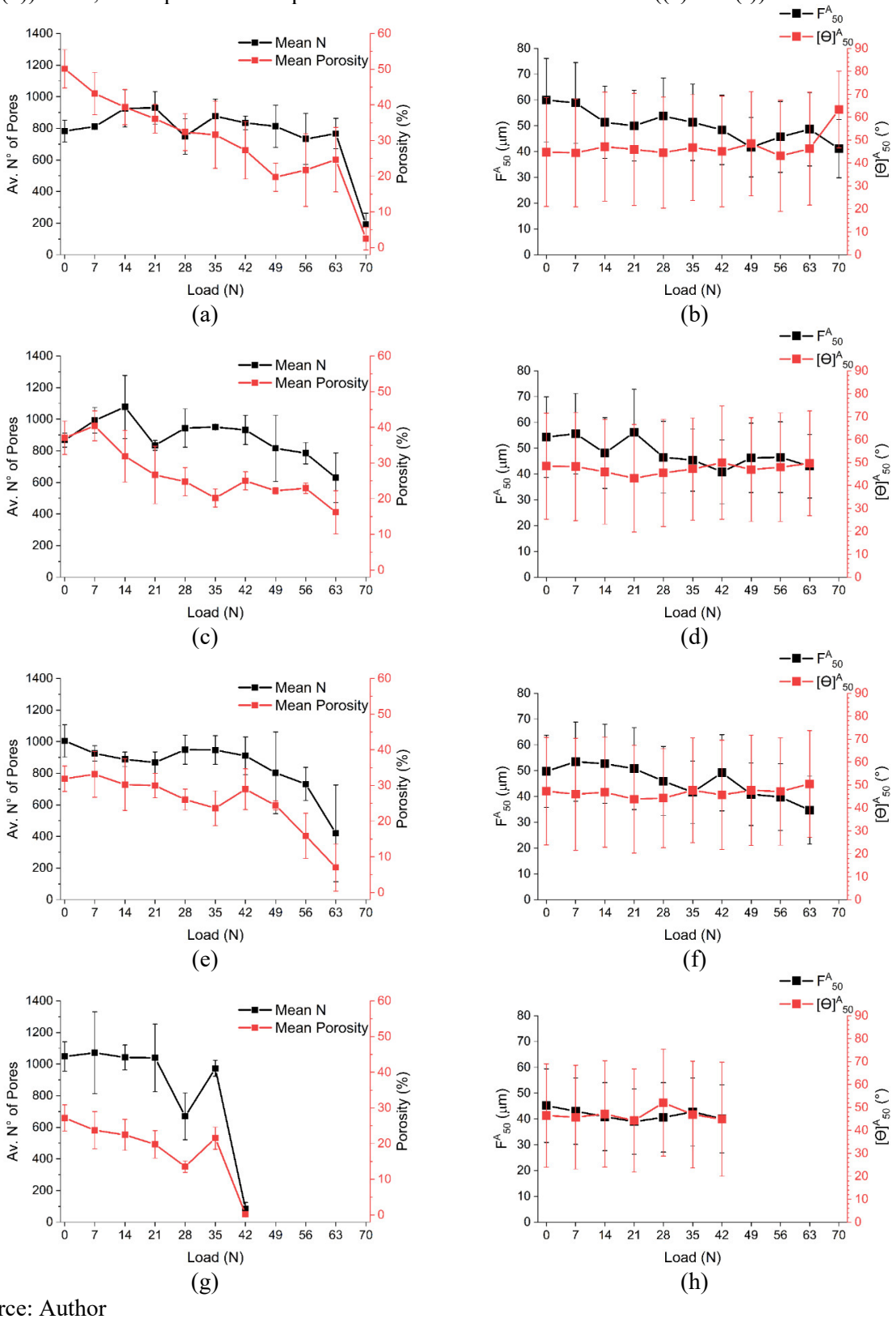

Source: Author

In figure 88 (b), (d), (f) and (h) the median Feret diameter and pore orientation were weighted by the area of the pore in order to better represent the pores that were providing graphite for larger areas in the wear tracks. Kruskal-Wallis analyses of variance (K-W ANOVA) paired with post-hoc analyses were performed on the data obtained to determine if the difference between the medians of the Feret diameters and orientation angle were significant, these statistical analyses were chosen due to the data being not normally distributed and to have a parameter (the sig value from the post-hoc analyses) that help to interpret the behaviour of the means as a functions of the pores characteristics. From the statistical analyses (see Appendix A for details), it was concluded that for all the specimens, but the ones compacted at 600 MPa, the Feret diameter diminishes as a function of the load. On the other hand, the orientation angle doesn't have significative changes with load except for the sample compacted at 200MPa where the difference between the first 9 loads (lubricity regime) and the last load was significant.

For all the conditions except for the samples compacted at 600 MPa, the total number of pores remains stable for the first load and then decreases. This behaviour does not correspond to the behaviour of total porosity which consistently decreases as a function of load. Taking into account that the Feret diameter (shown in figure 88 (b), (d), (f) and (h)) decreases as a function of load the following model is proposed:

1. The bigger pores start to be closed by their narrowest regions, this reduces their Feret diameter and creates two separated smaller pores.

2. This effect compensates the closing of small pores in the first loads, thus maintaining the overall number of pores but reducing overall porosity and pore size.

A SEM image of a pore undergoing this process is shown in figure 89. The green circle shows an area that was previously connecting two adjacent pores (making them only count as one larger pore). The deformation in this area caused the division of one big pore into two smaller ones without a significant effect on the area covered by pores. The red arrows marks points where deformation is closing the connection between two regions of a pore, when this connection gets closed, the pore will divide again into two smaller pores. Bearing this is mind the fact that the images were processed using a watershedding algorithm must be considered, so besides a physical phaenomena there is the influence of the analysis method itself that can

introduce noise to the measures however, this fact does not affect the core idea of the model that is being proposed.

Figure 89: Zoomed SEM image of a pore containing graphite (from a sample compacted at 400 MPa and sintered at 1100 °C) being divided into smaller pores by plastic deformation induced by the action of the counter-body

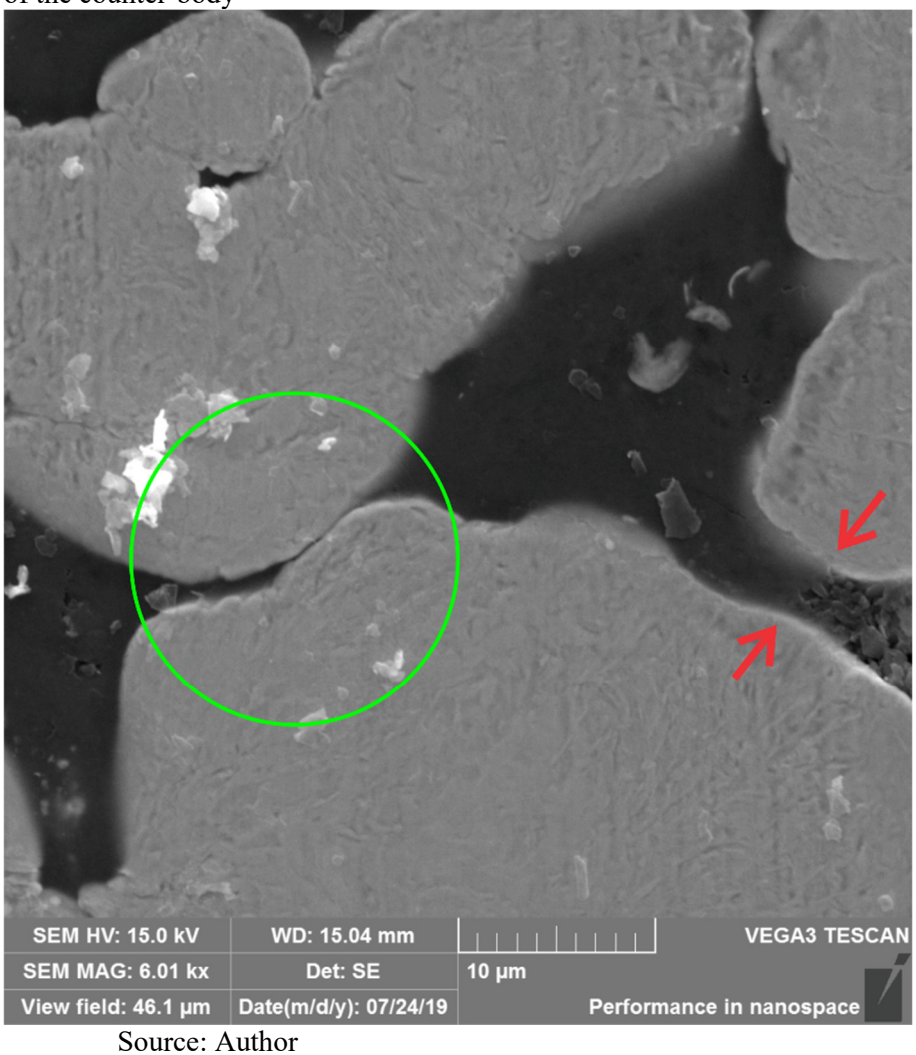

Source: Author

Figure 90 shows the histograms of the Feret diameters of pores from the specimens compacted at 400 MPa and sintered at 1100°C. The histograms show the pore size distributions in the conditions as sintered, after the 3rd, 6th and 9th load to further support the model proposed. Additional size distribution histograms for all the conditions can be found in appendix B. From the histograms of figure 90, it can be noticed that the percent of pores in the bigger size classes is reduced as a function of the load in the scuffing resistance test while the per cent of pores in the smaller size classes rises. This paired with the fact that the average number of pores remain

almost constant for the first 7 loads for this condition supports the idea that big pores get divided into smaller pores by the action of the counter-body before being completely sealed.

Figure 90: Histograms of the Feret diameter of pores from the specimens compacted at 400 MPa and sintered at 1100 °C as sintered (a) and before the 3rd (b), 6th (c) and 9th (d) load of the scuffing resistance test

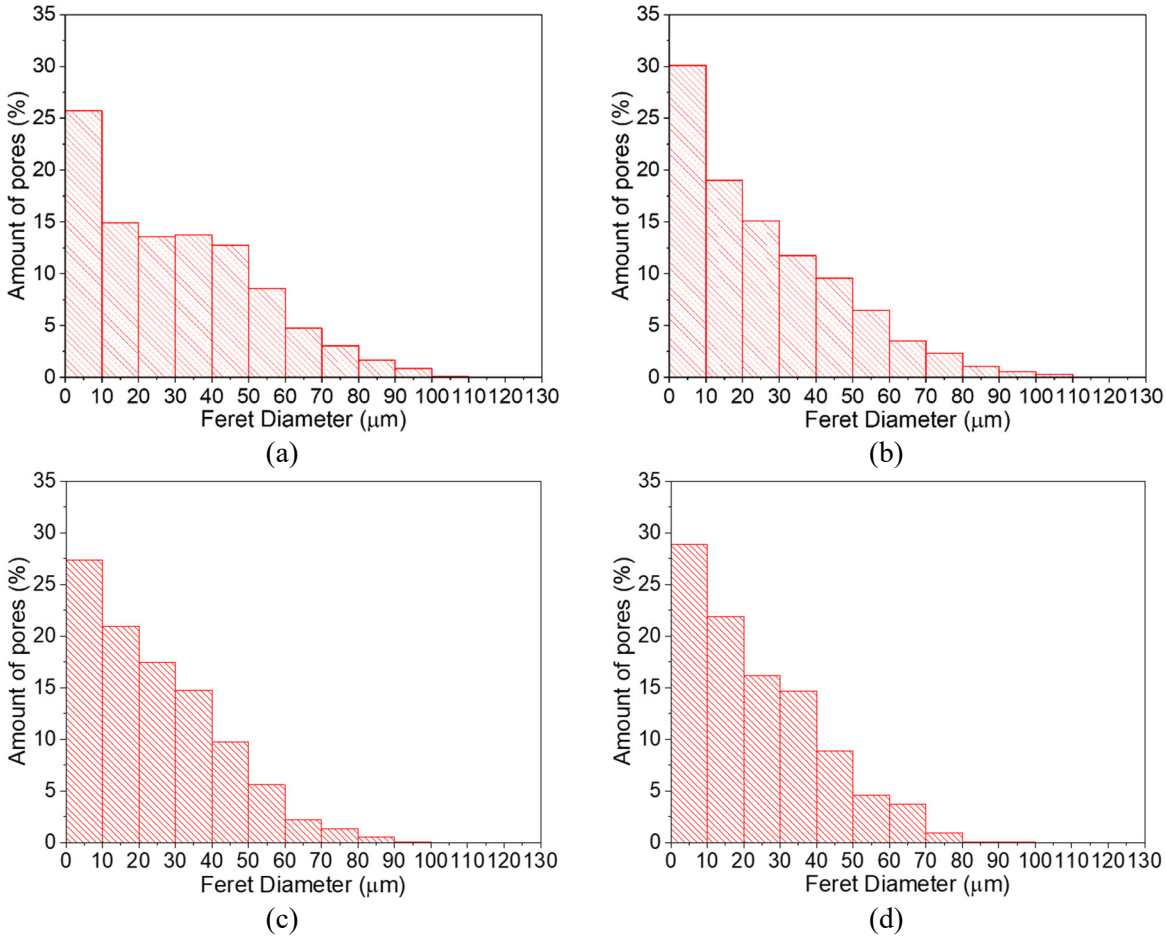

Source: Author

Figure 91 shows the evolution of circularity, solidity and eccentricity for specimens compacted at 200, 400 and 600 MPa and sintered at 1100°C ((a), (b) and (d) respectively) and for those compacted at 400 MPa and sintered at 1200°C (c). The analysis of figure 91 shows that for all the specimens, eccentricity does not change as a function of the load. The pores from the specimens compacted at 400 and 600 MPa and sintered at 1100 °C do not show any statistically significant change in solidity nor circularity as function of the load. However, for samples compacted at 200 MPa pores became less solid in the first half of the test (as product of the deformation of big pores) and then the trend reversed in the second half of the test as

pores began to become smaller (small pores tend to be more solid). Finally, the circularity from pores of specimens compacted at 400 MPa and sintered at 1200°C increases as function of load since pores become more regular as they get sealed. Statistical analysis for this data can be found in appendix A.

Figure 91: Evolution of the eccentricity, solidity and circularity of pores as a function of the load from specimens sintered at 1100°C and compacted at 200 (a), 400 (b) and 600 MPa (d). Also, for a specimen compacted at 400 and sintered at 1200 °C (c)

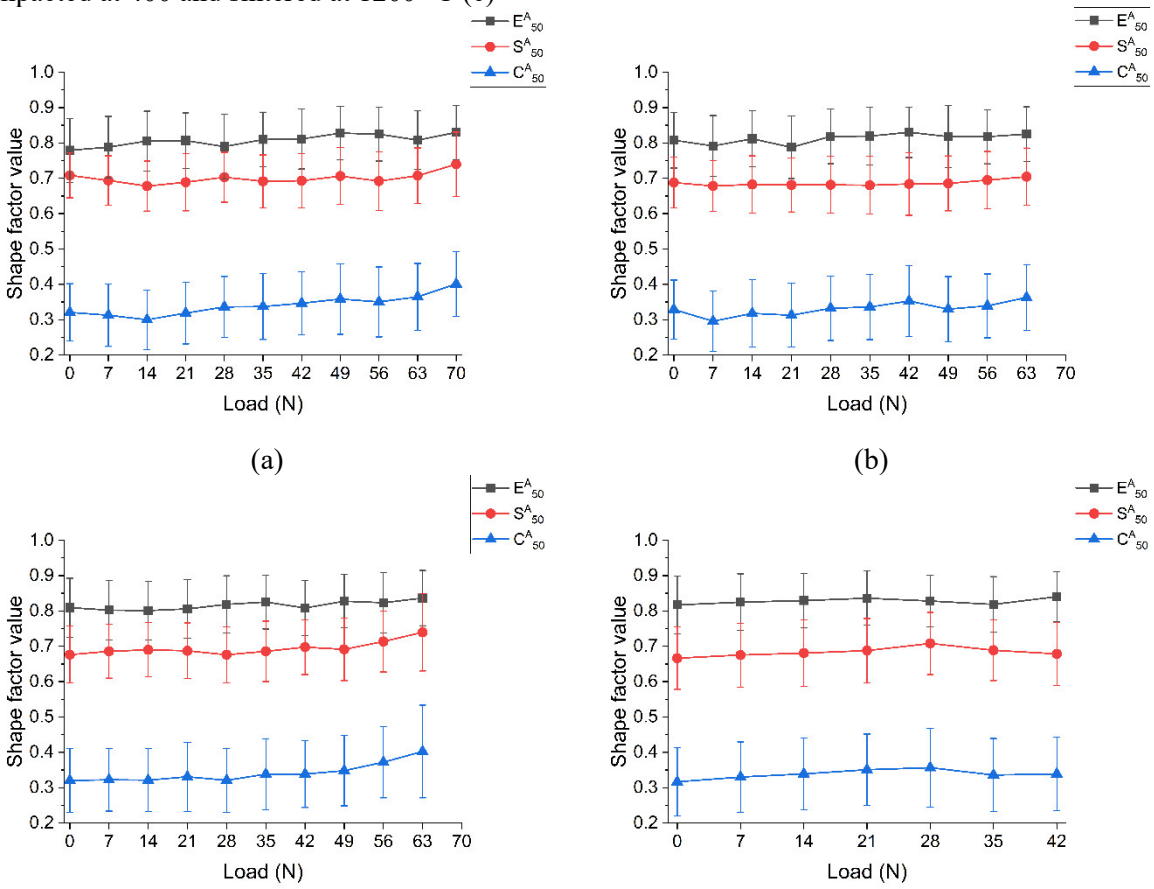

Source: Author

From the image analysis, it can be concluded that specimens with low porosity (600 MPa – 1100°C) resist the deformation process during the incremental load test. These specimens retain the size and shape of their pores up to the end of the tests. On the other hand, the pores from specimens with high porosity (200 MPa – 1100°C) rapidly change their size and shape distributions as they get sealed. At the end of the test, even the orientation of the pores tends to be perpendicular to the sliding direction. Finally, specimens of intermediate porosity (those compacted at 400 MPa) were in between these two tendencies; their pores retain their shape but not their size. Considering that the microhardness of the metallic phase of all the

specimens was practically the same, the results indicate that to avoid the sealing of pores and retain lubricity, the control of porosity is a critical factor. High porosity guarantees the supply of lubricant to the surface which reduces wear, adhesion and deformation of pores at the surface but is prejudicial to the resistance of the pores to be sealed. Because of that, for impregnated specimens, there must be an equilibrium between the number of lubricant stocks (pores) and the mechanical properties at the surface, in the case of this work, that equilibrium is represented by the samples compacted at 400 MPa, which provided lubrication for almost as long as the specimens compacted at 200 MPa by a combination of availability of lubricant and resistance to deformation. From the analysis of the wear tracks from the scuffing resistance test, it was noted that even if some pores were open inside the wear track, graphite was not always available at the surface. An example of this situation is shown in figure 92.

Figure 92: SEM image of a wear track from a sample compacted at 200 MPa and sintered at 1100 °C showing pores with graphite at surface level (red arrows) and graphite below the surface level (green arrows)

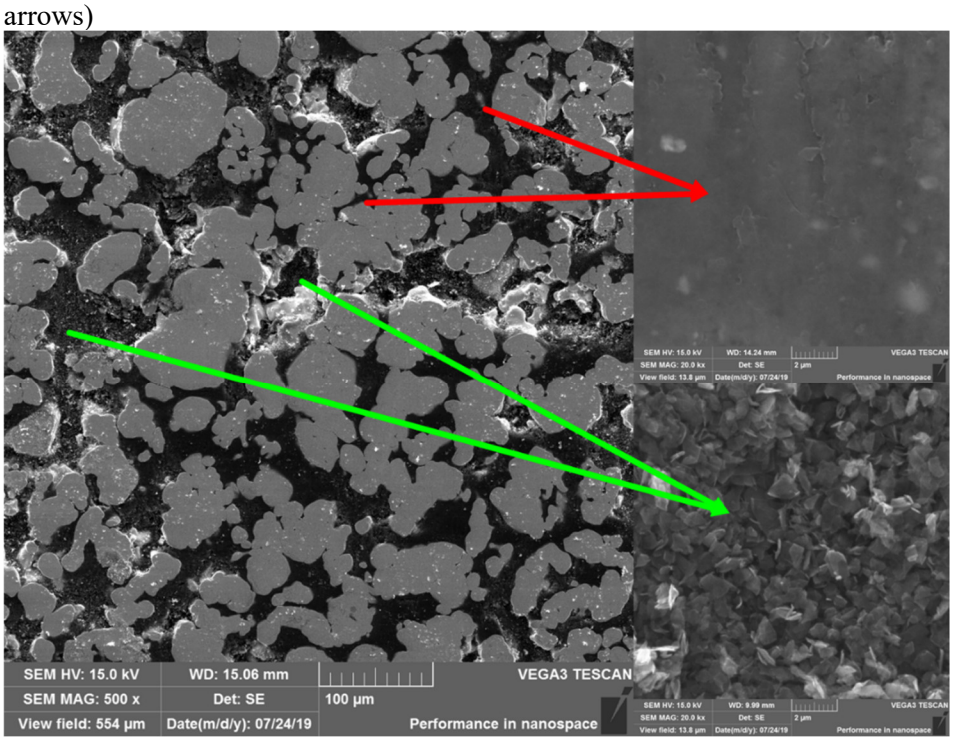

Source: Author

The red arrows point to pores opened to the surface inside a wear track. As shown by the inset, the graphite inside the pore is sheared, which means that it was supplying lubricant during the tribological test. The green arrows mark pores where graphite was below the surface

of the wear track. As seen in the zoomed image, the graphite inside these pores was not sheared, meaning that it was not participating in the healing of the tribolayer. In order to elucidate if the presence of graphite at the surface or below depended on the size or shape of pores, the EDS carbon maps obtained from the wear tracks were superimposed to the binarized images and analysis by using the method described in section 3.5.4. The carbon intensity obtained in the EDS maps as function of the size, solidity, circularity and eccentricity of the pores from specimens compacted at 400 MPa and sintered at 1100°C before the tribological tests is shown in figure 93.

Figure 93: Carbon intensity obtained in the elemental maps as a function of the size (a) and as a function of the solidity, circularity and eccentricity of the pores (b) from specimens compacted at 400 MPa and sintered at 1100°C

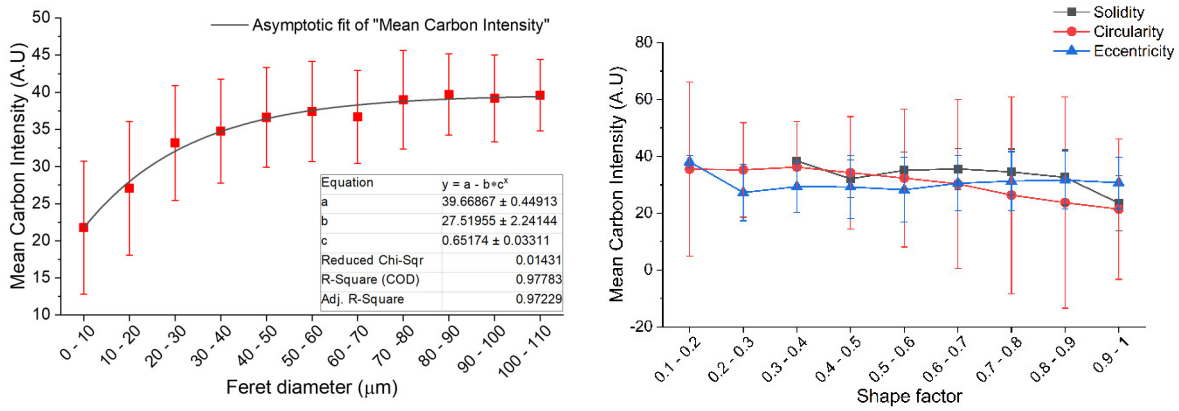

(a) (b)

Source: Author

The data in figure 93 shows that the mean carbon intensity is sensitive to the size of pores rather than their shape. The EDS probe detects less graphite in the first three size classes than in the rest of the pores. This can be expected because the region activated by the electron beam forms a pear shaped volume below the surface, for small pores this volume will include not only the carbon contained inside the pores but also iron from the surroundings, giving the mean carbon intensity vs Feret diameter curve its asymptotic behaviour as shown in the figure. These analyses were taken as baselines, meaning that when no tribological test is performed in the specimens, the variation of the carbon intensity detected by the EDS probe is distributed as shown in figure 93. Considering this, the changes on the mean carbon intensity distribution as a function of load in the scuffing resistance test can be calculated using the following equation:

$$\Delta\ Carbon\ Intensity\ (A.U) = \frac{I_{pl} - I_{p0}}{I_{p0}} \qquad (9)$$

Where I_{pl} is the mean carbon intensity as a function of the size or shape of pores from the wear tracks of scuffing resistance tests and I_{p0} is the mean carbon intensity from pores before the tribological tests. Plots for Δ Carbon Intensity as a function of the size, circularity, solidity and eccentricity of pores from specimens compacted at 400 MPa and sintered at 1100°C are shown in figure 94 (The Δ Carbon Intensity parameter was normalized from o to 100 for visualization purposes).

.

Figure 94: Δ Carbon Intensity as a function of the size (a), circularity (b), solidity (c) and eccentricity (d) of pores from specimens compacted at 400 MPa and sintered at 1100°C

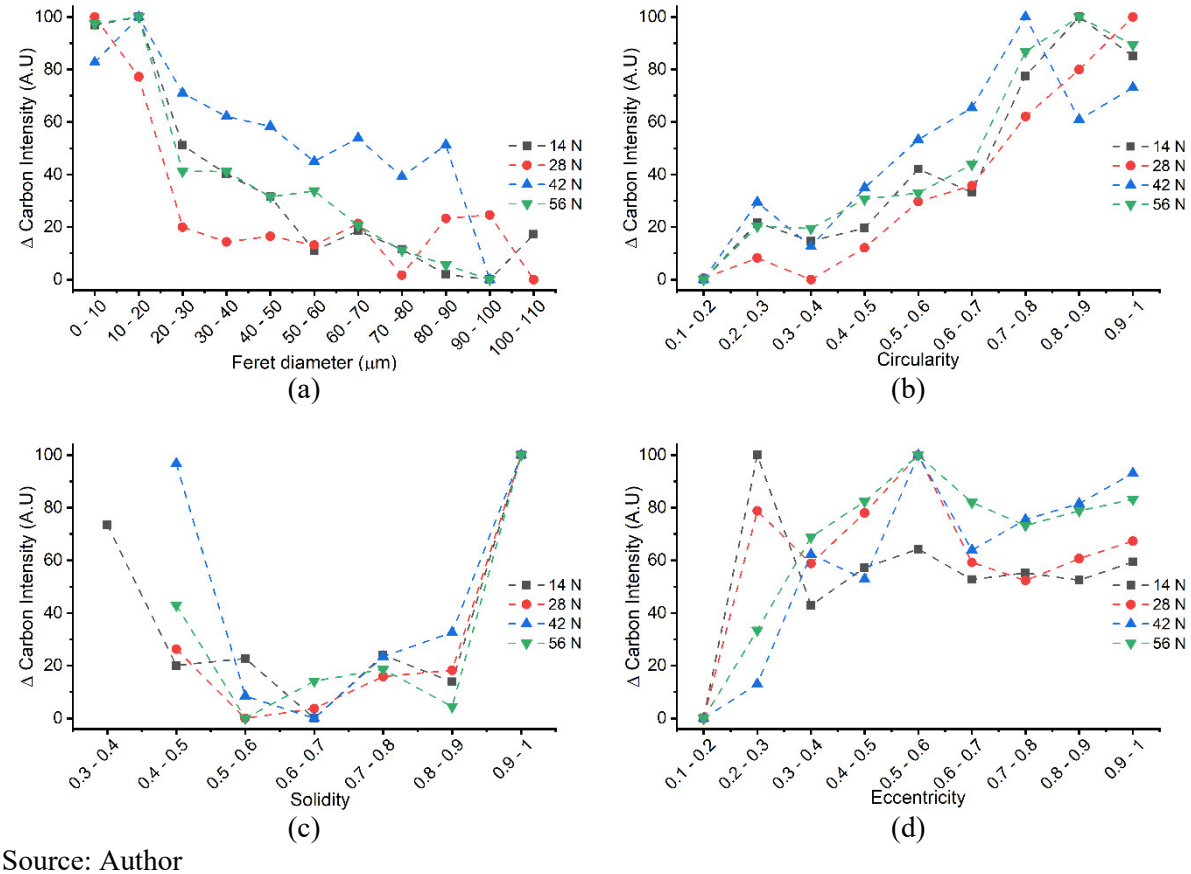

Source: Author

From figure 94, it can be noticed that pore size had a significant impact on the distribution of carbon inside the pores. Before the specimens were subjected to the tribological tests, the carbon intensity was lower for the smaller pores as was shown in figure 95 however, when the wear tracks are analysed, the small pores present a greater increase in carbon intensity,

meaning that carbon is more readily available at the surface level of these small pores and that larger pores were losing carbon during to the tribological test. Figure 95 shows a SEM image from a wear track to better understand this analysis. Small pores strongly retain the graphite inside them, slowly releasing it during the test (red circles in figure 95). Big pores on the other hand release graphite in large blocks which depletes them faster (green circles in figure 95).

Figure 95: SEM image from a wear track of a specimen compacted at 400 MPa and sintered at 1100 °C showing regions with small pores retaining graphite (red circles), big pores that quickly released graphite (green circles) and pores with narrow sections that also retained graphite (blue circles)

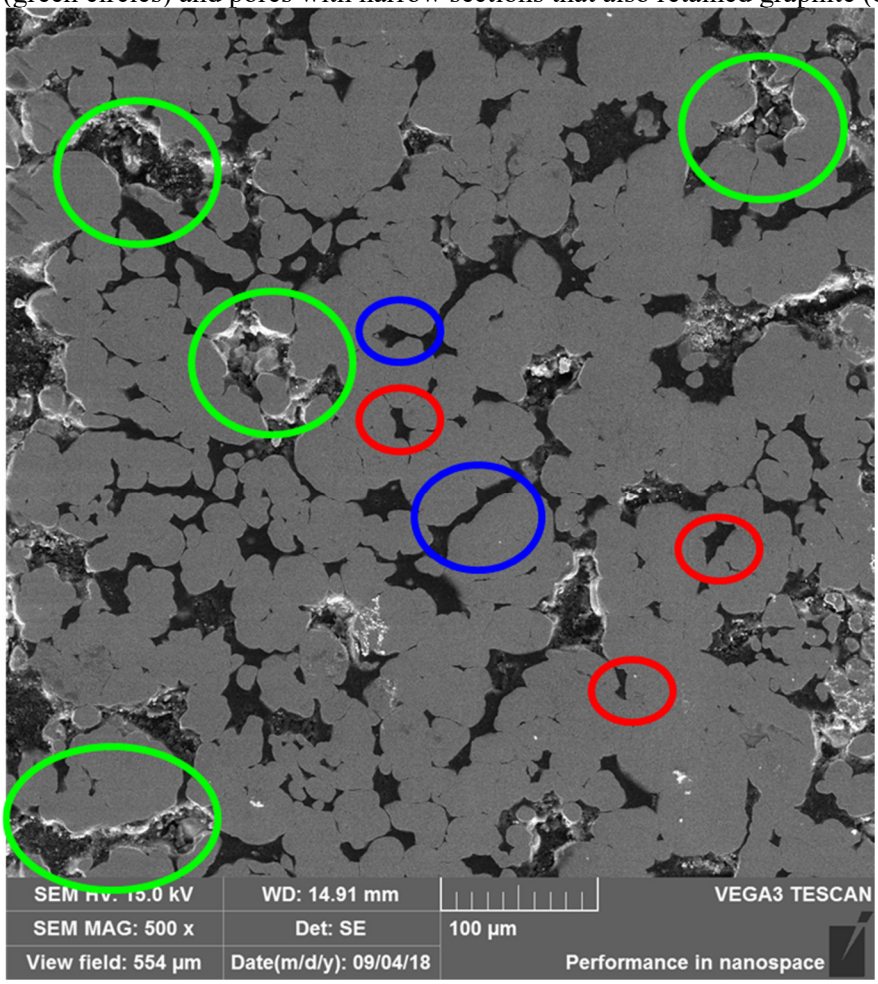

Source: Author

Circularity had a strong effect on the carbon intensity, but this might simply be because small pores also tend to be more circular (and solid). Solidity and eccentricity also might play a role in retaining graphite during the test. Pores with low solidity and highly eccentric are composed by narrow sections, these narrow sections (blue circles in figure 95) offer enough interaction between the graphite and the pore walls to prevent graphite from being quickly released from the pore. On the other hand, if the notion of powders acting as fluid and therefore

flowing from the pores that was proposed in step 3 is considered, it can be argued that small and narrow pores act as the narrow sections of a pipe, hampering the flow of solid lubricant from the pores to the contact, causing it to be slowly release due to the resistance exerted by the small flow area provided by these pores. For the analysis of samples compacted at 200 and 600 MPa and sintered at 1100°C please refer to appendix B.

The final part of this step was to analyse the tribolayers generated by the scuffing resistance test using micro-Raman spectroscopy and the method developed by Cançado et al. (CANÇADO et al., 2017) to determine the crystallite size (La) and point-defect density (σ) of the graphite left in the tribolayers. This method was detailed in section 2.4.The amorphization diagram σ vs. La of graphite by the action of the scuffing resistance test in specimens compacted at 200 MPA and sintered at 1100 °C is shown in figure 96 (the same plot for the other conditions can be found in appendix B). As a frame of reference, the crystallite size (L_a) for the impregnated graphite was 159 +/- 42 nm (determined using the Tuinstra-Koenig/Cançado relation (CANÇADO, 2006)). The point-defect density (σ) cannot be estimated from the Raman spectra of crystalline graphite and is considered as being less than 10^{-5} nm^{-2} (CANÇADO et al., 2017).

Figure 96: Raman amorphization diagram σ vs L_a of graphite by the action of the scuffing resistance test in specimens compacted at 200 MPa sintered at 1100 °C, the numbers above the symbols indicate the load where the tests were stopped.

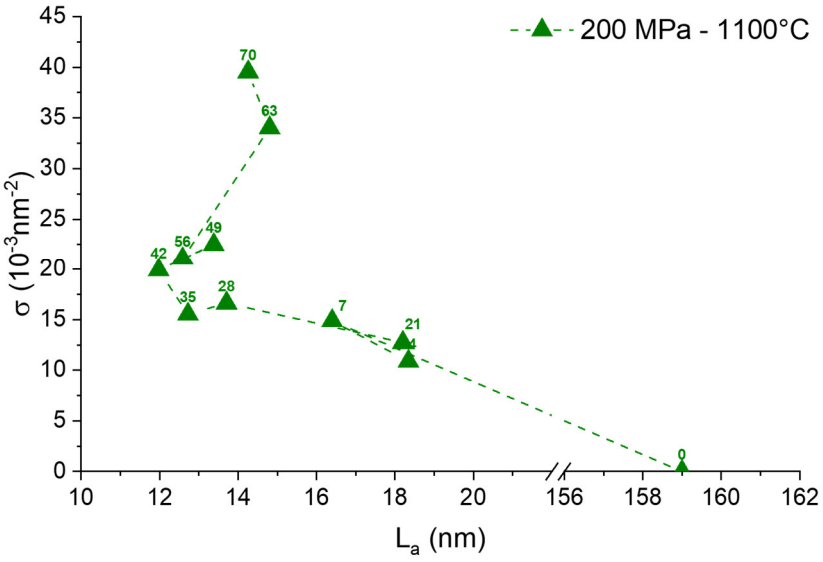

Source: Author

In figure 96, the numbers above the symbols show the load on the scuffing resistance test at where the Raman analyses were performed (the 0 value shows the conditions of the graphite before the tribological tests). From figure 96, it was determined that apart from the initial reduction of crystallite size from 159 to the 11 – 19 nm range, increments in load did not significatively reduce this parameter. This decrease in crystallite size corresponds to the nanometric nature of the tribolayer (REBELO DE FIGUEIREDO et al., 2008; ÖSTERLE et al., 2013; WANG et al., 2013). On the other hand, the overall tendency of point-defect density was to increase with load, this is best shown in figure 97.

Figure 97: Evolution of point-defect density (σ) as a function of load for impregnated samples sintered at 1100 °C in scuffing resistance test

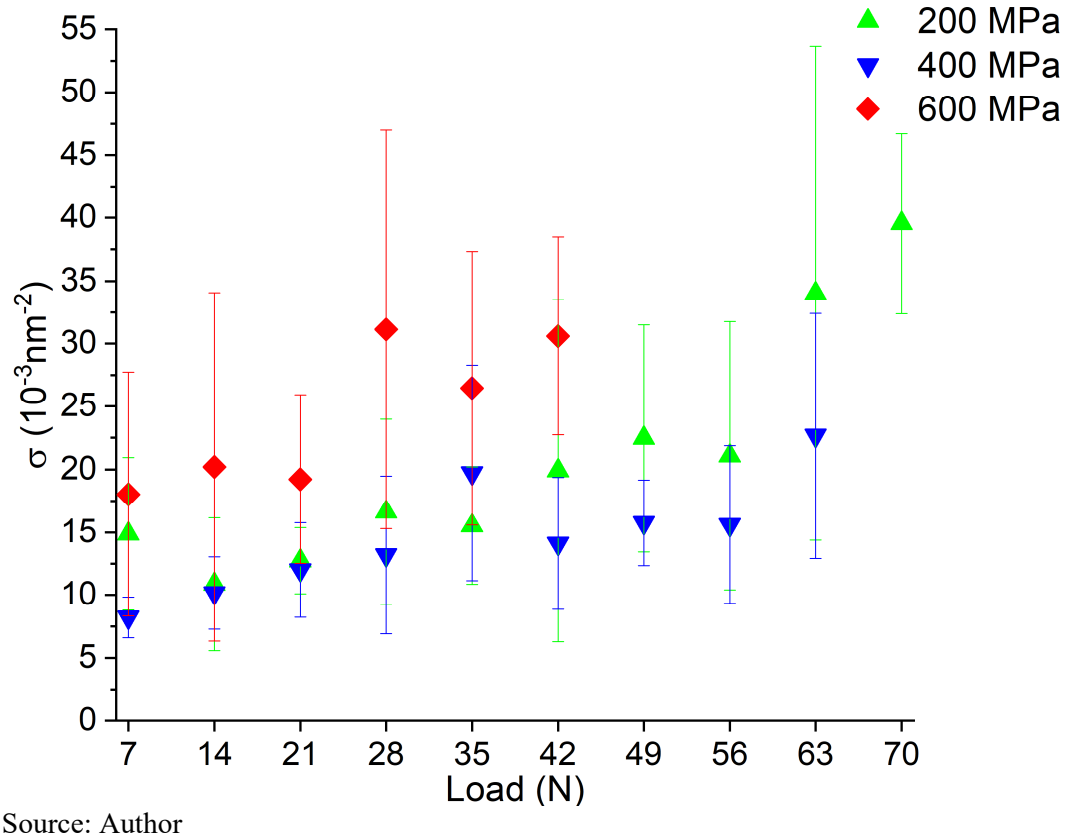

Source: Author

Oscillations and dispersion of La and σ during the tests may come from the fact that as long pores are open, sheared graphite is constantly being mixed with “fresh” graphite from the pores, and the Raman spectra of the wear tracks are showing an average of the Raman-active species in the track. It would be recommended for future works to perform the same analysis in systems without self-replenishment of the lubricating layer like dip coating, spray casting or similar techniques.

The analysis of variance revealed that there were no significant changes in the crystallite sizes. However, the increase in point-defect density with load is statistically significant (for more details please refer to appendix A). Point-defect density in graphite (also called 0D defects) can come from vacancies, dopants, or impurities (PIMENTA et al., 2007; CANÇADO et al., 2017). If it is assumed that defect density is rising mainly due to vacancies the following model (shown in figure 98) can be proposed:

1. In the first step, crystallite size is drastically reduced by the action of the counter-body (mixing, intense plastic deformation, comminution). This reduction occurs in the contact points between specimen and counter-body (real contact area) and allows to dissipate energy that would be otherwise applied in the process described in step 2.
2. The energy coming from the mechanical action from the counter-body induce the formation of vacancies and dangling bonds (blue arrows in figure 98 (b)) inside the basal planes of graphite.
3. sp^2 hexagonal carbon rearranges to sp^3 amorphous carbon (a-C) due to the high number of dangling bonds (figure 98 (c)). Once this process reaches a critical point, no shearing between basal planes is possible, and lubrication stops.

To complement the analysis, figure 99 shows some exemplary Raman spectra from specimens compacted at 400 MPa and sintered at 1100 °C after the 14, 28, 42 and 63 N loads. In figure 99, the typical bands related to sp^2 carbon D, G and 2D are present. The disorder-induced D+G band is also present for all the spectra along with the G+2D band that is not present in the last loads. As discussed in section 4.3, the T band is related to the presence of sp^3 carbon which starts to form early in the test. The intensity of the 2D band which is related to 3D stacking order declines as the load increases meaning that long-range order in the c axis is being lost as graphite is being sheared by the action of the counter-body. The number of peaks that fit in the 2D band is also indicative of stacking order.

Figure 98: Transformations in graphite during the tribological test: Crystallite size reduction to cover the surfaces (a), the formation of vacancies (b) and sp3 hybridization (c).

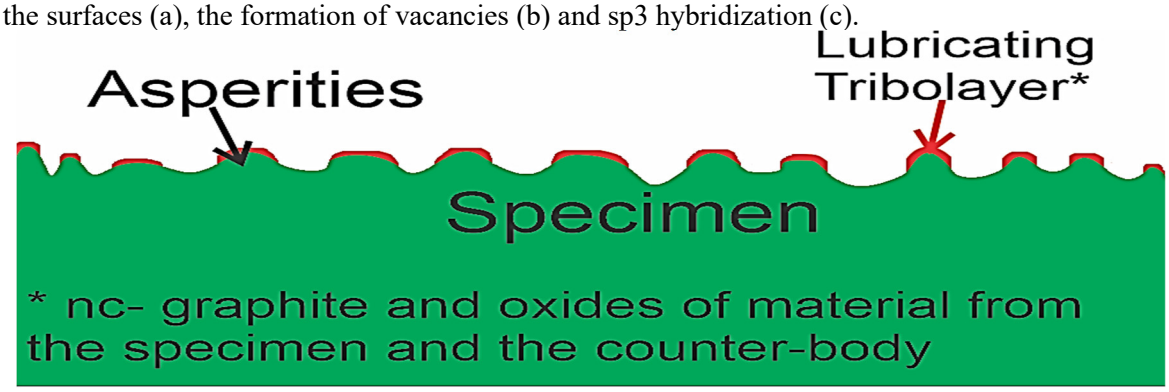

(a)

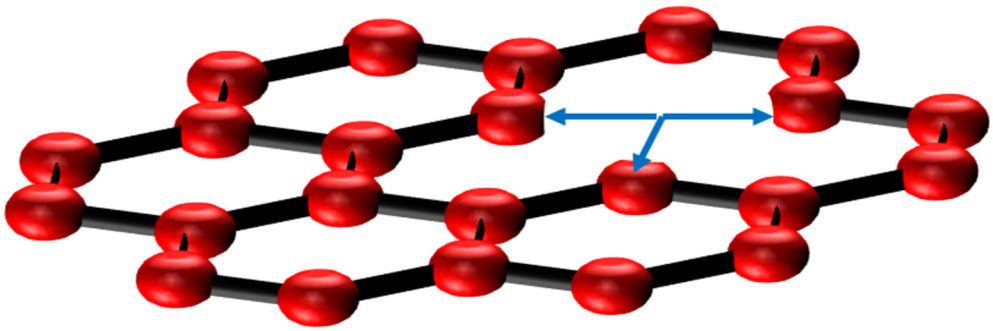

(b)

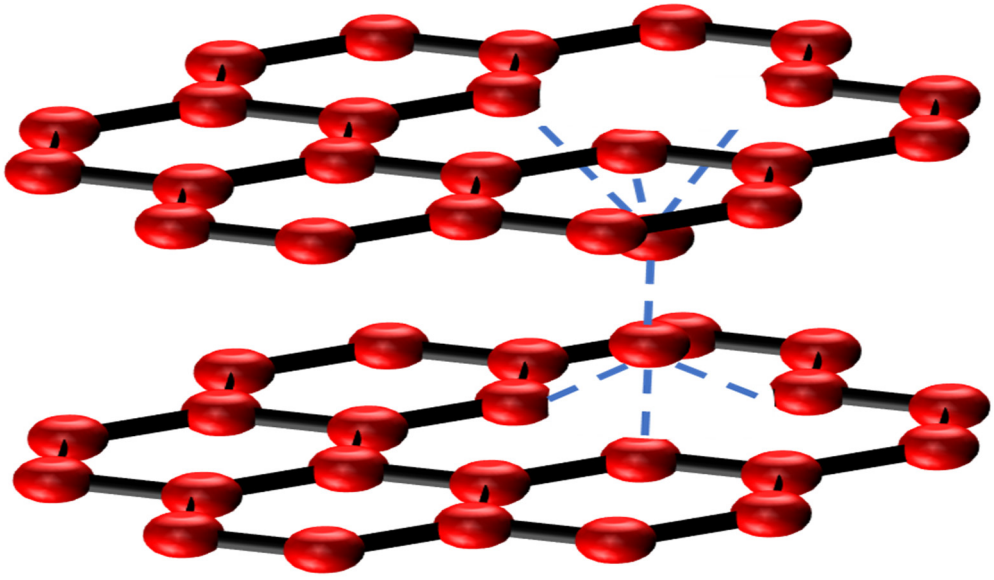

(c)

Source: Author

Figure 99: exemplary Raman spectra from specimens compacted at 400 MPa and sintered at 1100 °C after the 14, 28, 42 and 63 N loads.

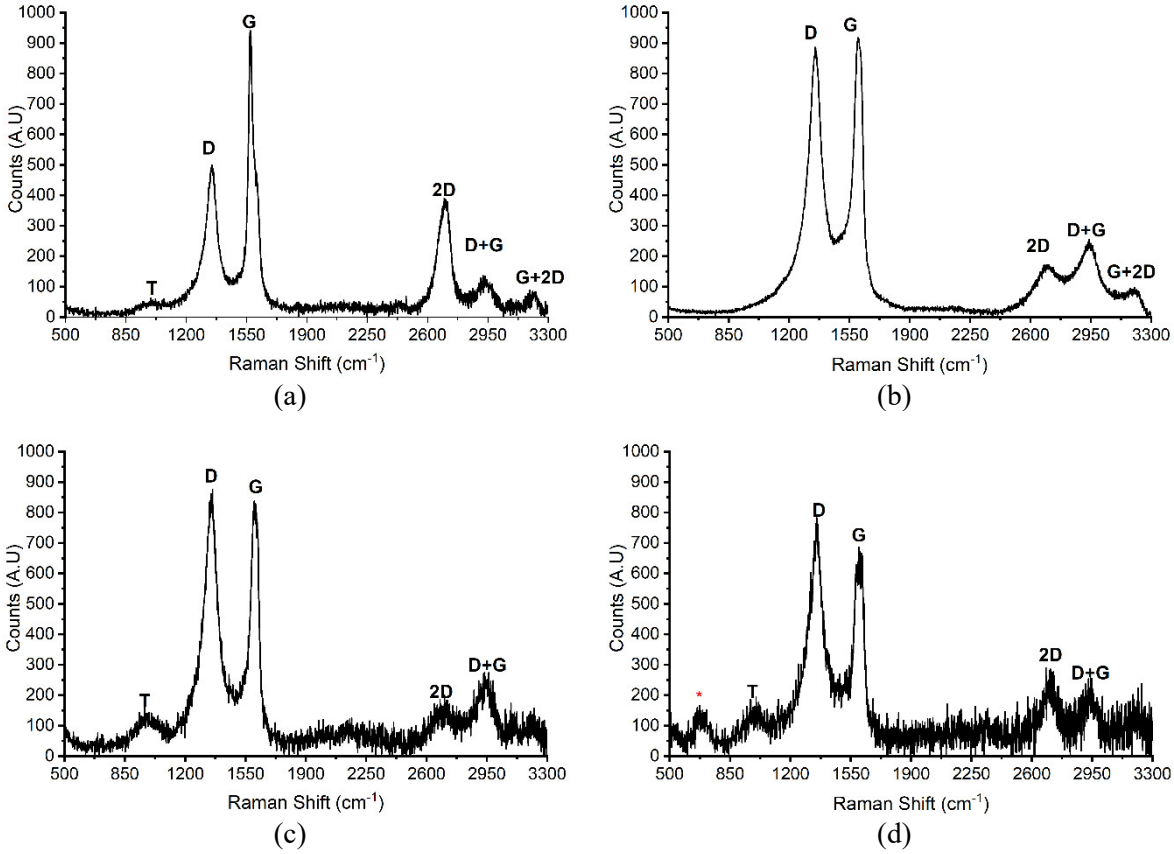

Source: Author

Figure 100 shows the fitting of the 2D band of wear tracks after the 2nd load of the scuffing resistance tests. From figure 100, it can be noticed that, even when the crystallite size was greatly reduced at the start of the test the 2D band can be fitted using two peaks (2D1 and 2D2), meaning that stacking order was not lost at the 14 N load. If the 2D could be fitted by only one peak it would mean that the tribological phenomena were transforming crystalline graphite into turbostratic graphite which was not the case. For the other spectra, the intensity of the D+G band does not allow to correctly fit the 2D band as the bands start to merge.

Figure 100: Exemplary 2D band obtained from the Raman spectrum of a wear track of a sample compacted at 400 MPa and sintered at 1100 °C after the second load of the scuffing resistance test.

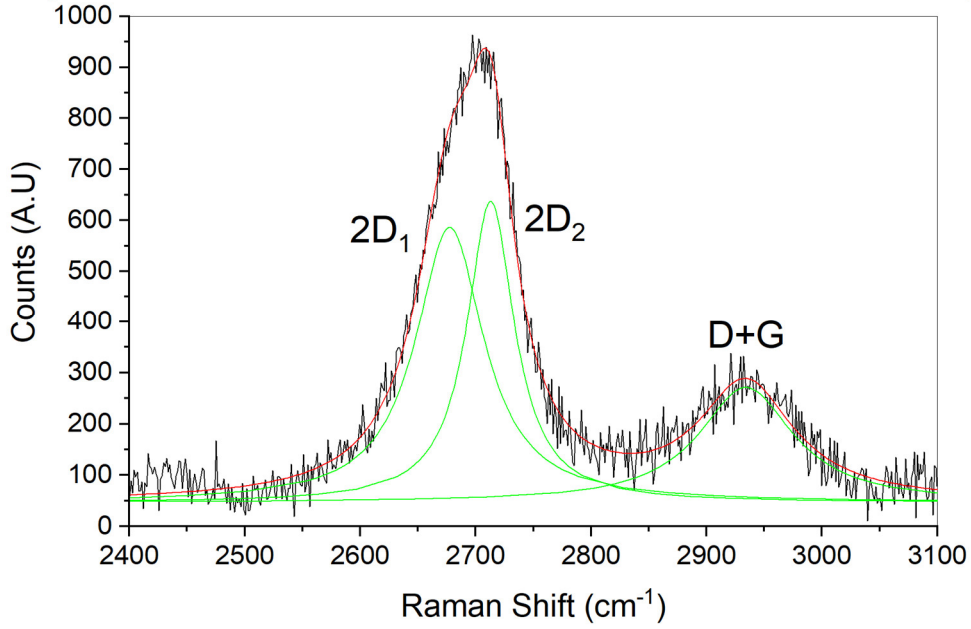

Source: Author

In this step, the sealing of the impregnated pores, the release of graphite and the amorphization process of graphite during scuffing resistance tests were studied. Knowing that the crystallite size is quickly reduced by the tribological phaenomena and the defect density increases up to the point where no more lubrication is possible, it is of interest to study how the crystalline structure of the graphite before the test influences its tribological behaviour. For these reasons, in step 5 the effect of the crystalline structure of graphite was studied using the new developed solid-state reaction CDCs.

5.5 TRIBOLOGICAL PERFORMANCE OF CARBIDE DERIVED CARBON

In this step, the tribological behaviour of sintered steel impregnated with graphite derived from the reaction between Cr_3C_2 and B_4C was studied. The method of production of this CDC was presented in section 5.2; more details about the synthesis and characteristics of this material can be found in reference (NEVES et al., 2020).

For the tribological tests, samples compacted at 400 MPa and sintered 1 hour at 1100°C were impregnated with CDCs synthesized at 1200, 1300, 1400 and 1500 °C which from now on are referred as CDC XXXX where “XXXX” is the synthesis temperature. The D50 of these materials are presented in figure 101.

Figure 101: D_{50} of CDCs synthesised at 1200, 1300, 1400 and 1500 °C and of 1.10 μm crystalline graphite

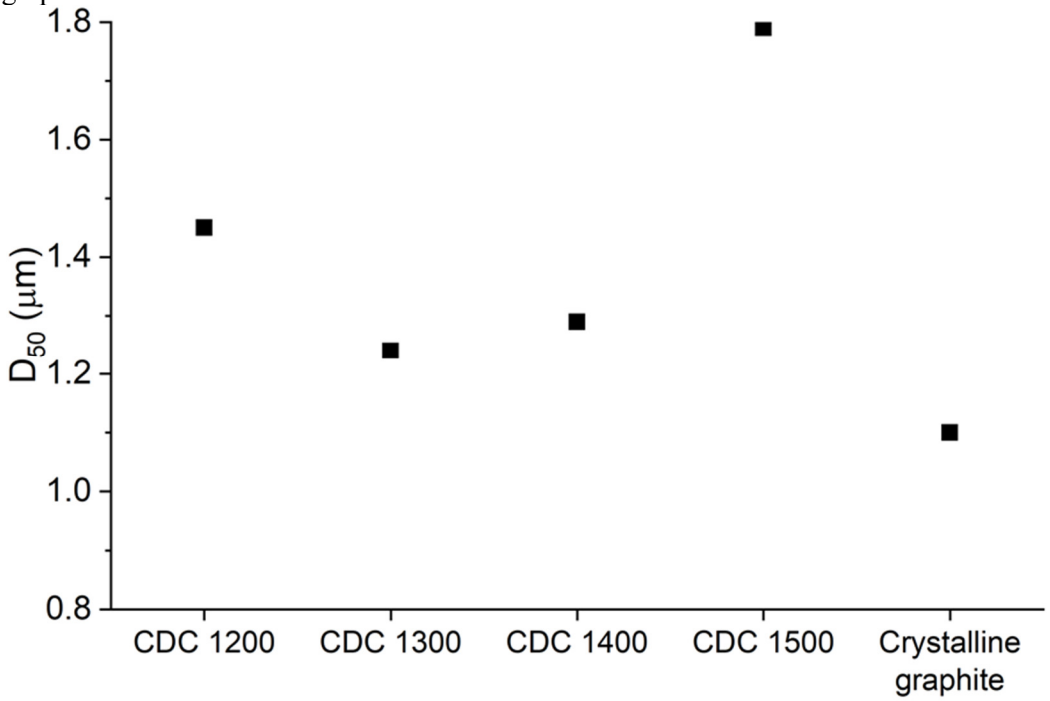

Source: Author

Figure 101 shows that the D_{50} of the CDC and the crystalline graphite were in the range of 1.1 – 1.8 μm. This allowed the use of 1.10 μm graphite for comparison purposes as its size was close to the size of the CDCs. As was demonstrated in section 4.3, the particle size of graphite plays an important role on its tribological behaviour, so to isolate the effect of the crystalline structure of graphite in its tribological behaviour, working with similar particle sizes was crucial.

X-ray diffraction was used to obtain information about the crystalline structure of the graphite used in this step; the XRD spectra are shown in figure 102. The dashed orange line marks the T peak and the dashed black line the G peak. According to literature, the T peak corresponds to highly turbostratic graphite while the G peak corresponds to ordered crystalline graphite (JONES; THROWER, 1991; QIN et al., 2012). For the CDCs, the G peak is found at higher angles than for crystalline graphite; this was attributed to the presence of boron inside the graphite lattice. Since boron atoms are smaller than carbon atoms, their presence in the graphite lattice decreases the distance between the (002) planes, shifting the G peak to higher angles (NEVES, 2020).

Figure 102: X-ray diffraction pattern zoomed in the region corresponding to the (002) plane of crystalline graphite and of CDCs synthesised at 1200, 1300, 1400 and 1500 °C

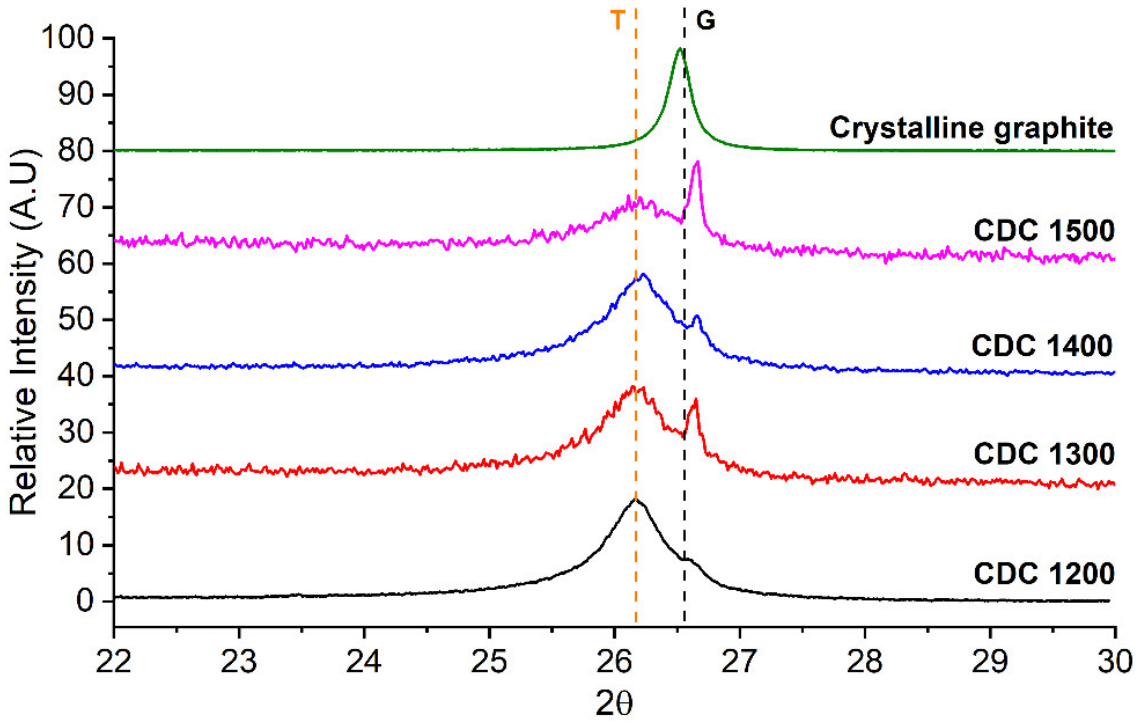

Source: Adapted by the author from Neves (2020)

On the other hand, the T peaks are located at lower angles because the interplanar distance for turbostratic graphite is greater than for crystalline graphite (KUMAR et al., 2011; CONSONI, 2014; DE MELLO et al., 2017b). Synthesis temperature had the effect of decreasing the intensity of the T peak in favour of the G peak intensity. In order to completely elucidate the crystalline structure of these materials, more sophisticated analyses such as XPS to determine the amount of sp^2 and sp^3 bonds and TEM to understand their atomic arrangement are required, however these analyses are not available at this point (and are beyond the scope of this work).

The Raman spectra obtained from the CDC and an exemplary 2D band fitted by a single Lorentzian peak are shown in figures 103 and 104 respectively.

Figure 103: Exemplary Raman spectra of CDCs synthesised at 1200 (a), 1300 (b), 1400 (c) and 1500 °C (d)

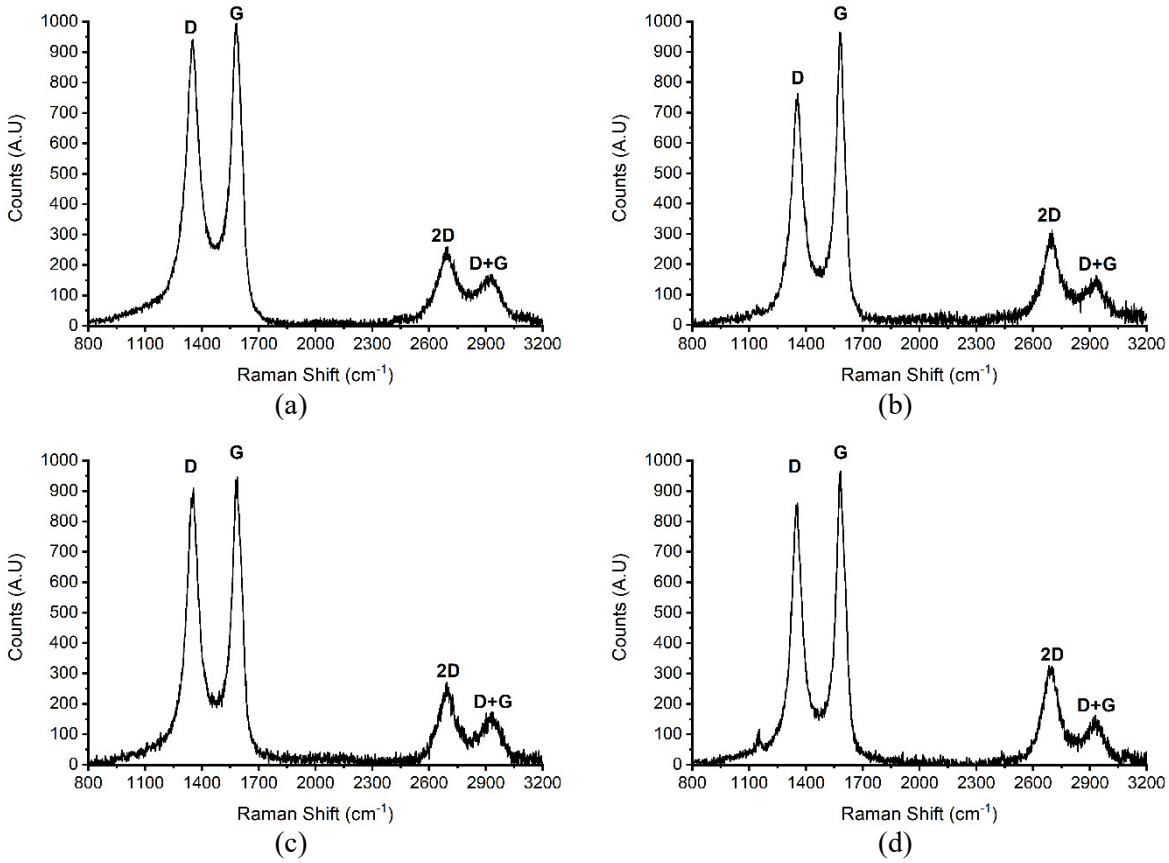

Source: Author

For all the synthesis conditions, the Raman spectra had the same basic features (the D, G, 2D and D + G bands). The high intensity of the D band relative to the G band indicates the presence of defects within the crystalline structure. This is further confirmed by the presence of the D + G band that, as was discussed in the previous section, appears when the defect density is high. These crystalline defects can be attributed to the presence of boron derived from the synthesis process (WANG; GAO, 2009) and/or to the high fraction of amorphous phase present in the CDCs as solid-state graphitization of carbon requires temperatures close to 3000°C (WELZ, 2003). As shown in figure 104, the 2D band of the CDCs studied can be fitted by a single Lorentzian peak which reinforces the idea that some of the graphite in the CDC is turbostratic.

Figure 104: 2D and D + G bands from the Raman spectra of CDC powder synthesised at 1400 °C showing how each band is fitted by a single Lorentzian peak

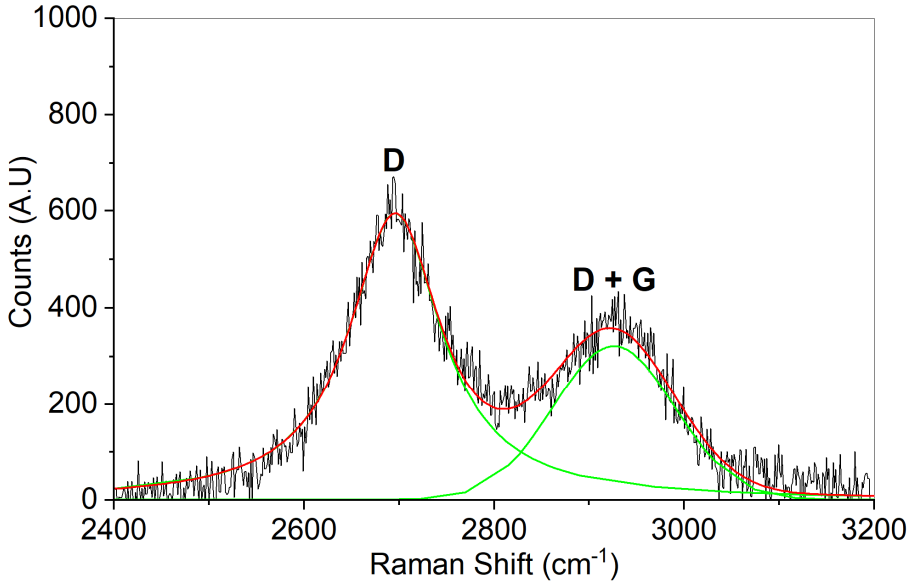

Source: Author

To start the tribological characterization of the CDCs, scuffing resistance tests were performed (shown in figure 105 (a)) on specimens compacted at 400 MPa, sintered 1 hour at 1100 °C and impregnated with CDCs. To determine the influence of the synthesis temperature in the coefficient of friction and wear rates constant load tests of 1 hour and 14 N were performed (shown in figure 105 (b)). These results were compared with those obtained for the 1.10 μm graphite.

From figure 105 it is noticeable that the specimens impregnated with the CDC synthesised at 1300 °C presented high dispersion in its scuffing resistance, wear rate and coefficient of friction, but overall it can be noticed that:

1. The scuffing resistance of the samples impregnated with CDC increased with the synthesis temperature.
2. The coefficient of friction decreased as a function of the crystallinity of the graphite.
3. Specimens impregnated with CDC synthesised at 1400°C had the lowest wear rate.
4. The tribological response of the CDC synthesised at 1500°C was close to that of crystalline graphite.

Figure 105: Scuffing resistance (a); wear rates and COF (b) of specimens compacted at 400 MPa and sintered at 1100 °C impregnated with crystalline graphite and CDCs

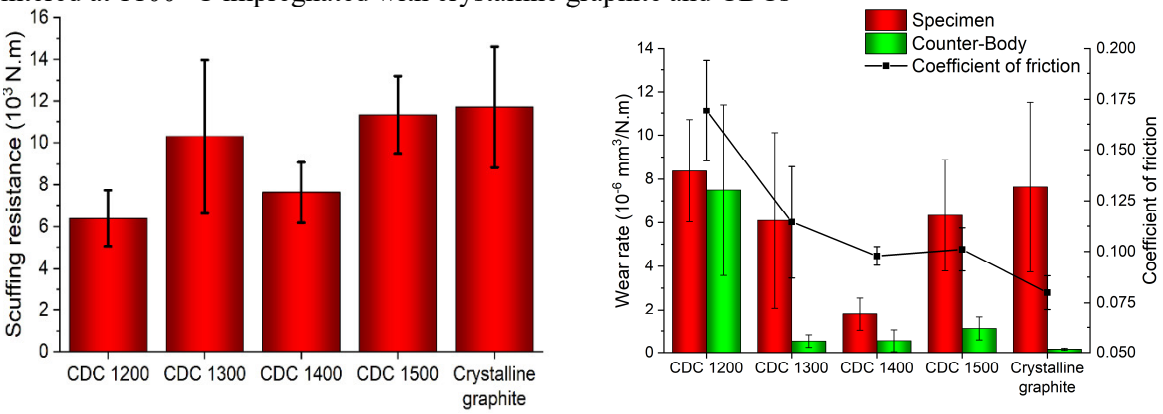

(a) (b)

Source: Author

The wear tracks from the constant load test were analysed using micro-Raman spectroscopy. Figure 106 shows the σ vs La Raman diagram for the raw CDC powders and for the wear tracks. From figure 106, it comes to attention that the CDCs are nanocrystalline with sizes close to those found in the crystalline carbon tribolayers. Defect density is also high when compared with crystalline graphite ($\sigma < 10^{-5}$ nm^{-2}) being in the same order of magnitude that was found in the tribolayers of step 4. In this analysis, the synthesis temperature did not have a clear influence in both σ and La. This can be because this material presents both turbostratic and crystalline graphite whose relative fractions change as a function of the synthesis temperature, which can be altering the results extracted from the Raman spectra. The crystallite size of the CDC in the wear tracks did not exhibit statistically significant differences before and after the wear tests. Still, there was a sensible increase in defect density for all the conditions; this again can be attributed to the generation of defects inside the basal planes of graphite induced by the tribological phaenomenon. As was commented in section 4.4, the high dispersion of La and σ after the wear test might be due to the mixture of sheared and fresh graphite coming from the pores (this can be proven in systems without self-healing of the lubricating tribo-layer as commented in section 4.4). Finally, an hypothesis of this work was that the crystalline structure of the CDC would have a significative impact in its tribological performances as it has been found for other forms of carbon (KUMAR et al., 2011, 2013) however, no correlation was found between the tribological performance of these CDCs and the results found in the σ vs. La plot meaning that the quantity of crystalline defects in graphite

cannot be used to “predict” a good or bad tribological performance. This indicates that there are other variables at the macro level such as particle size, particle shape, surface energy, etc. that have a more definitive impact in the performance of these solid lubricants than the number of crystalline defects.

Figure 106: σ vs La Raman diagram for raw CDC powders and the wear tracks from the constant load tests.

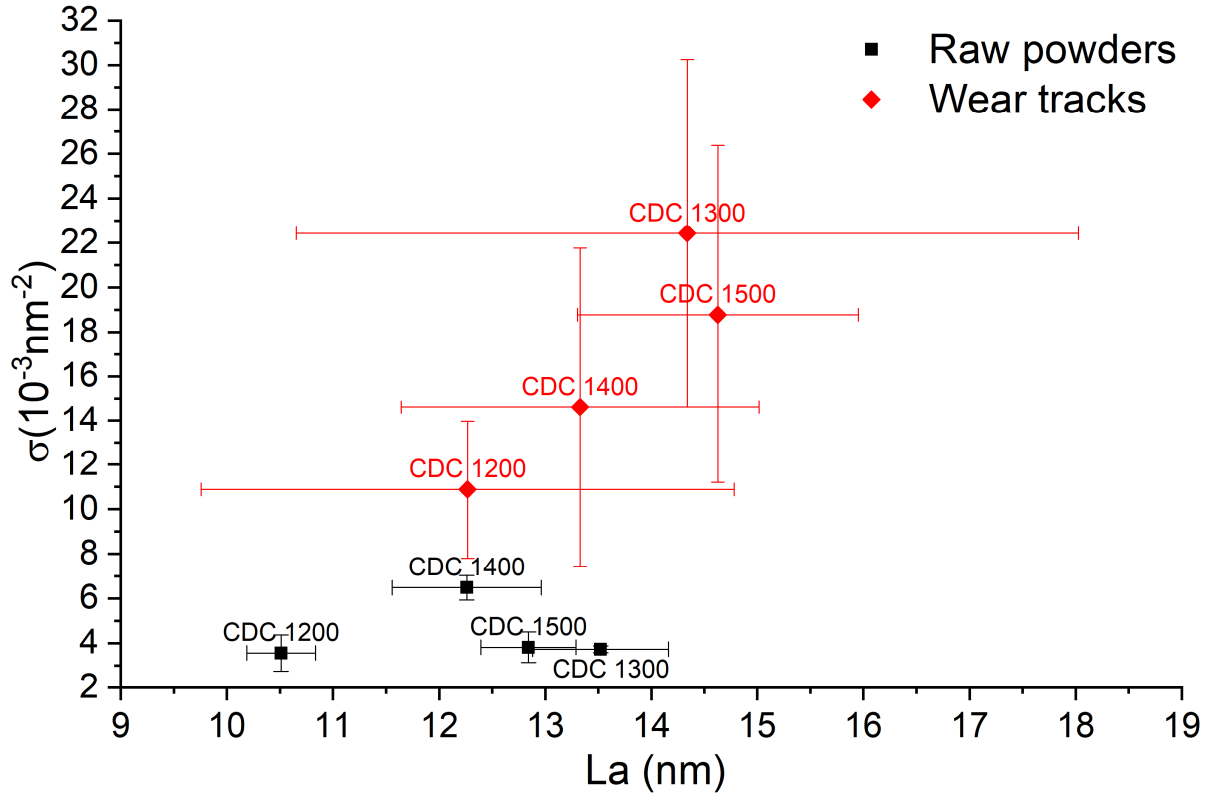

Source: Author

To understand the difference in the tribological behaviour exhibited by the CDCs, the wear tracks from the constant load test were observed using SEM and analysed using elemental maps (shown in figure 107).

Figure 107: SEM images and elemental maps from the wear tracks of specimens impregnated with CDCs synthesised at 1200 (a), 1300 (b), 1400 (c) and 1500 °C (d)

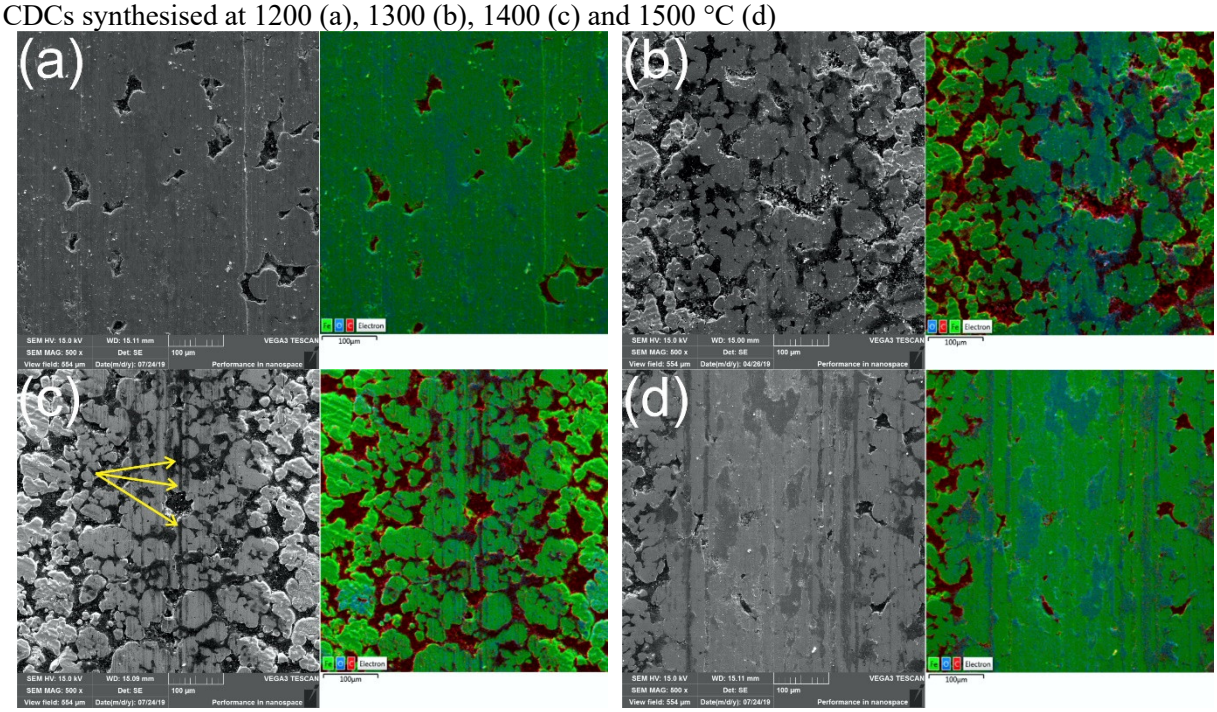

Source: Author

From 107 it can be noticed that the wear tracks from specimens impregnated with CDC synthesised at 1200 °C (figure 109 (a)) and 1500 °C (figure 107 (d)) had the majority of their pores sealed at the end of test, despite that, the CDC synthesised at 1500 °C was able to induce lower coefficient of friction and wear rates than the CDC synthesised at 1200 °C. This indicates that the crystallinity of graphite plays a role in reducing friction and wear however, it is not the only variable to be considered (as previously discussed) as CDCs synthesised at 1300 and 1400 °C (figure 107 (b) and (c)) had lower wear rates and remained with the majority of their pores opened at the end of the test. The specimen with the lowest wear rate also presents marks of abrasion inside the wear tracks (pointed by the yellow arrows in figure 107 (c)). To understand the difference in the tribological responses induced by the CDCs synthesised at 1300 and 1400 °C, zoomed SEM images and carbon maps of the wear tracks are presented in figure 108.

The yellow arrows in figure 108 show abrasion marks present in the wear tracks of both specimens. By comparing figure 108 (a) and (b), it is noticeable that there is less graphite left in the pores of the specimens impregnated with the 1300 °C CDC. Overall the wear tracks of the specimens impregnated with the 1400 °C CDC had their pores filled with graphite which was available at the surface level. No residual carbides were found in the raw powders (NEVES,

2020) nor in the wear tracks that could explain the mild abrasion found in these specimens, so they are attributed to the formation of abrasive debris during the tests. The differences in tribological behaviour between the 1300 and the 1400 °C CDC can be explained by how the graphite is distributed inside the wear tracks. The 1400 °C CDC had the lowest coefficient of friction and wear rate and presented more graphite inside the pores and at surface level. By considering the notion of powder flow presented in section 4.3, CDC synthesised at 1400 °C must have more surface interaction between its particles (making it more "viscous"), thus granting it the ability to be slowly released from the pores during the tribological tests.

Figure 108: Zoomed SEM image and carbon maps of the wear tracks from specimens impregnated with CDC synthesised at 1300 (a) and 1400 °C (b).

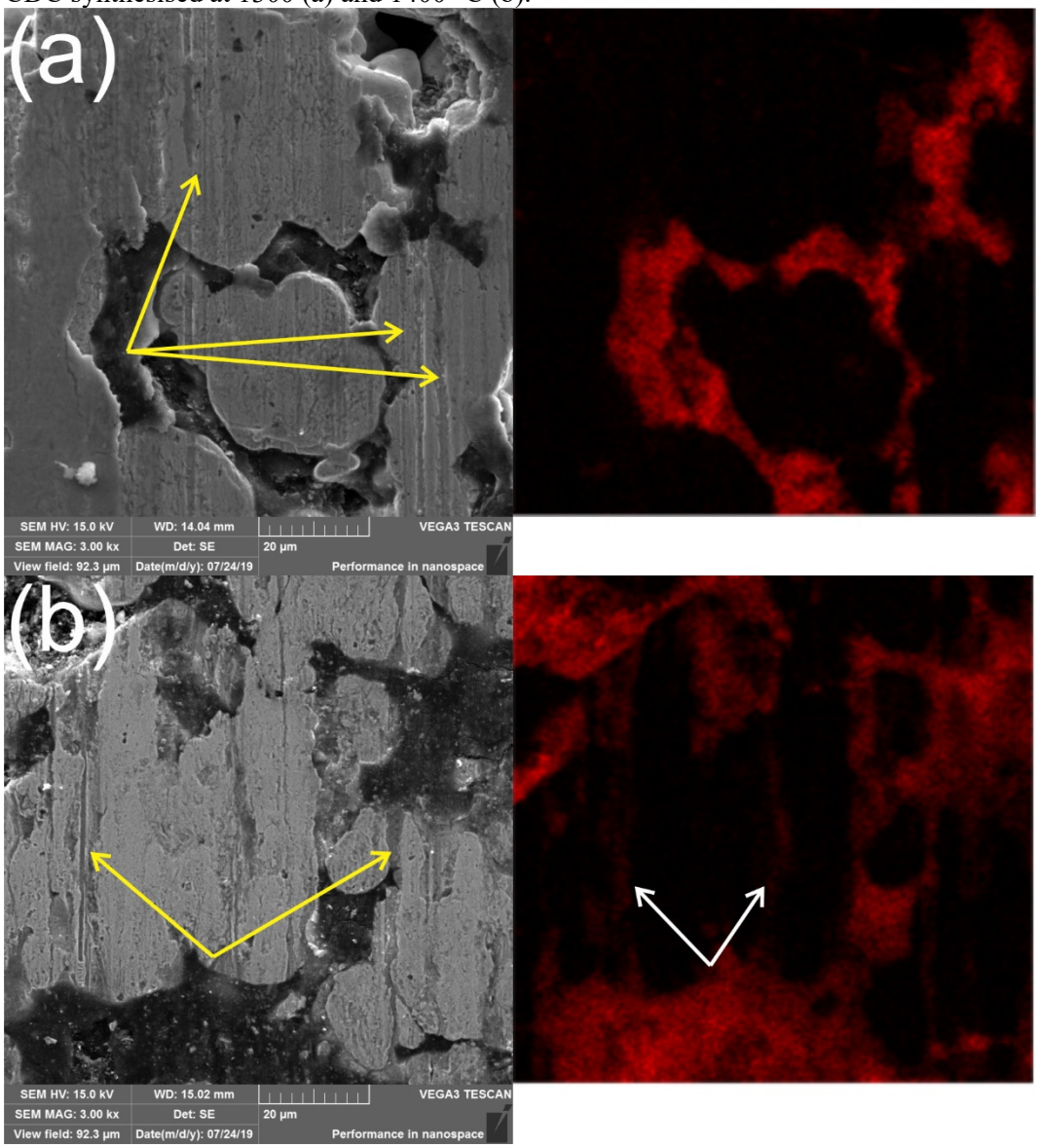

Source: Author

Finally, to put the results into perspective, a comparison between the materials characterised in this step (in red) and the solid lubricants presented in section 2.1 is shown in table 7. The impregnation of sintered steel with both crystalline graphite and CDC allowed the obtention of a self-lubricating composite with friction coefficients lower than many commonly used solid lubricants paired with wear rates in the order of 10^{-6} $mm^3/N.m$ which is considered low for dry lubricated iron based materials (SHARMA; ANAND, 2016). These results make these materials viable candidates for industrial applications.

Table 7: Comparison between the materials studied in this step and some commonly used solid lubricants

Classification	Key Examples	Typical friction coefficients*
Sintered steel impregnated with graphite	Crystalline graphite (D50 = 1.10 µm)	0.065 – 0.08
	Cr_3C_2/B_4C CDC 1200-1500	0.17 – 0.085
Lamellar solids	MoS_2	0.002 - 0.24
	h-BN	0.15 - 0.7
	Graphite	0.07 - 0.5
	Graphite fluoride	0.05 - 0.15
	H_3BO_3	0.02 - 0.2
Soft metals	Ag	0.2 - 0.35
	Pb	0.15 - 0.2
	Au	0.2 - 0.3
	Sn	0.2
Single oxides	B_2O_3	0.15 - 0.6
	Re_2O_7	0.2
	MoO_3	0.2
	ZnO	0.1 - 0.6
Halides and sulphates from alkaline metals	CaF_2, BaF_2, SrF_2	0.2 - 0.4
	$CaSO_4$, $BaSO_4$, $SrSO_4$	0.15 - 0.2
Carbon-based solids	Diamond	0.02 - 1
	DLC	0.003 - 0.5
	Vitreous carbon	0.15
Organic materials/polymers	Zinc stearate	0.1 - 0.2
	Waxes	0.2 - 0.4
	Soaps	0.15 - 0.25
	PTFE	0.04 - 0.15
Bulk or thick-film composites (> 50 µm)	Metal-, polymer-, and ceramic-matrix composites consisting of graphite WS_2, MoS_2, Ag, CaF_2, BaF_2, etc.	0.05 - 0.4
Thin films (< 50 µm)	Nanocomposite or multilayer coatings consisting of MoS_2, DLC, Ti, etc.	0.05 - 0.15
	Electroplated Ni and CR films consisting of PTFE, graphite, diamond, B_4C, etc., particles as lubricants	0.1 - 0.5

Source: Adapted by the author from Erdemir (2000).

6 SUMMARY AND CONCLUSIONS

The main objective of this work was to advance the knowledge about the interaction of solid lubricant and the lubricant stocks (pores) and its influence on the tribological behaviour of the composite. For this, a model system (graphite / sintered steel) was used.

In order to achieve this, an impregnation method was developed which can successfully fill the pores of sintered steel with various degrees of porosity with graphite of different particle sizes and crystalline structures. The main impact of this research is not only to develop a simple procedure to impregnate porous materials with solid lubricant, thus promoting lubricity, but also to demonstrate that the tribological response of the impregnated materials will be a function of the characteristics of the lubricant, the mechanical properties of the porous specimens and of how the lubricant is being released during the tribological phenomena. This development marks a significative advance in the TRL (technology readiness level) of sintered steel impregnated with graphite and will allow the further exploration of this technique for industrial applications.

Differently from other works involving self-lubricating composites, the methodology used in this work makes it that the mechanical properties of the matrix are independent of the properties of the lubricating phase. This allows using the same methodology to evaluate a wide range of combinations of solid lubricant – porous matrix which will enable engineers to find the most suitable combination of materials depending on the application.

Another product of this work was the development of a Python script to perform image analysis and superposition of secondary electron images and EDS elemental maps. This script can be used to analyse the evolution of the stocks of lubricants in several self-lubricating composites as well as in materials impregnated with other solid lubricants besides graphite. It can also be used to differentiate pores from nodules in self-lubricating materials containing graphite.

This work presents the first use of the Raman diagram developed by Cançado et al. in 2017 to analyse graphitic tribolayers. This diagram proved to be a powerful tool to understand the changes in crystallinity of graphite during the tribological tests and is a contribution to the application of Raman spectroscopy in tribology overall.

Finally, this work also presents the first tribological evaluation of the new CDCs derived from the solid-state reaction between Cr_3C_2 and B_4C. The CDCs derived from metal/carbide or carbide/carbide reactions are new materials developed in the LABMAT which derived in the deposit of patent BR1020200007483.

Based on the results obtained in the present work, the main conclusions are:

1) For mixtures of Astaloy CRL + 0.6 wt.% C, a cooling rate of 60 °C/min inside a tubular furnace is enough to promote hardening. Microhardness above 3000 MPa can be achieved using this method.
2) Impregnation of porous steels with graphite can successfully promote lubricity being possible to obtain friction coefficients as low as 0.065.
3) The scuffing resistance of impregnated steels is inversely proportional to the D50 of graphite. This is attributed to the ability of powders to remain inside the pores during the tribological testing. Smaller size pores have more particle-particle interactions, which diminishes their flowability and makes them remain inside the pores (and provide lubricity) for longer.
4) The D50 6.07 and 21.54 μm graphite cannot maintain lubricity for 100 meters at constant load. This is also attributed to the higher flowability of these powders when compared with the 1.10 μm graphite. The difference between the constant and the incremental load test is attributed to the fact that when the load increases, new lubricant stocks are accessed.
5) For samples impregnated with 1.10 μm graphite, the scuffing resistance is proportional to the porosity (namely, the amount of lubricant available) while the wear resistance is proportional to the mechanical properties of the matrix, in other words, inversely proportional to the porosity.
6) During tribological testing, the impregnated pores start to get sealed by the action of the counter body. First, the narrow sections connecting pores deform and close which reduces porosity and the Feret diameter of individual pores but increases the overall pore count. Then pores start to get smaller and sealed up to the point where not enough lubricant is available, and the lubricity regime ends.
7) Small and narrow pores better retain graphite during the tribological test, slowly releasing it, which helps to maintain the lubricating tribolayer. This is because (as it happens with fluids) it is harder for powders to flow through narrow spaces, this

again points towards flowability being a critical variable to be taken into account for the tribological behaviour of impregnated materials.

8) The Raman diagram and Raman spectra revealed that the tribolayers generated by crystalline graphite and CDCs are both nanocrystalline and remain between 10 and 20 nm. Degradation of the graphite inside the tribolayers occurs by the increase in the point-defect density and the formation of sp^3 hybridized carbon.
9) The CDC derived from the reaction between Cr_3C_2 and B_4C consists of nanocrystalline turbostratic and ordered graphite and can promote lubricity when impregnated in sintered steel.
10) The tribological behaviour of sintered steels impregnated with these CDCs is not directly related to the synthesis temperature, and more variables besides its crystalline structure must be considered.
11) The CDC synthesised at 1400°C induced the lower wear rate of all the conditions studied in the present work. In these specimens, most of the pores in the wear tracks were opened at the end of the test and had graphite available at the surface, which again points towards the slow release of lubricant from the pores as a critical variable to achieve optimal lubrication in impregnated materials.

7 SUGGESTIONS FOR FUTURE RESEARCH

This work addressed the main parameters involving the tribological behaviour of sintered steels impregnated with graphite and at the same time, opened some questions that can be addressed in future research. Considering this, the suggestions for future research are:

- To study the effect of the microhardness of the matrix in the tribological performance of impregnated porous steels.
- To develop an automatized impregnation cycle for technological applications
- To optimize the sintering and impregnation cycles to obtain the best mechanical properties – amount of lubricant combination. In this line, suggestions include using pre-sintering – impregnation – repressing and sintering or similar methods.
- To study in detail the behaviour of the contact resistance in the constant and incremental load tests as it can help to understand how the tribolayers and being healed by the release of lubricant from the pores.
- To perform the Raman analyses used in this work in materials without self-replenishment of the lubricating layer in order to reduce the impact of the "fresh" graphite coming from the pores in the Raman spectra of the wear tracks.
- To use space-holders to obtain materials with narrow pore sizes distributions in order to get a definitive understanding of the effect of this isolated variable in the tribological behaviour of impregnated steels.
- To use powders graphite with sizes smaller than 1.10 μm to confirm the relation between size – flowability – tribological performance.
- To further the characterization of the Cr_3C_2-B_4C CDCs in terms of flowability and other physicochemical properties that can be related to its tribological behaviour.
- To use the impregnation technique to characterize other CDCs developed in the LABMAT like the Fe-SiC, Fe_3C-SiC and the Fe-B_4C graphite as well as other solid lubricants like MoS_2. WS_2. h-BN, etc.

REFERENCES

ASM INTERNATIONAL HANDBOOK COMMITTEE. **Powder Metal Technologies and Applications**. 1. ed. Ohio: ASM International, 1998.

ASM INTERNATIONAL HANDBOOK COMMITTEE. **Failure Analysis and Prevention Handbook**. Ohio: ASM International, 2002. v. 11

BACKHAUS-RICOULT, M. Solid State Reactions Between Silicon Carbide and Various Transition Metals. **Berichte der Bunsengesellschaft für physikalische Chemie**, v. 93, n. 11, p. 1277–1281, nov. 1989. Disponível em: <http://doi.wiley.com/10.1002/bbpc.19890931127>.

BARBOSA, M. . et al. Physicochemical characterisation of tribolayers by micro-Raman and GDOES analyses. **Tribology International**, v. 81, p. 223–230, jan. 2015. Disponível em: <http://linkinghub.elsevier.com/retrieve/pii/S0301679X14003326>. Acesso em: 18 out. 2014.

BEDOLLA-JACUINDE, A. et al. Sliding wear behavior of austempered ductile iron microalloyed with boron. **Wear**, v. 330–331, p. 1–9, 2015. Disponível em: <http://linkinghub.elsevier.com/retrieve/pii/S0043164815000113>.

BEISS, P. Iron and steel: manufacturing route. In: LANDOLT-BÖRNSTEIN (Ed.). **Landolt-Börnstein—Group VIII Advanced Materials and Technologies**. 1. ed. London: Springer Materials, 2003. p. 5–20.

BHUSHAN, B.; GUPTA, B. K. **Friction and wear of ion-implanted diamondlike carbon and fullerene films for thin-film rigid disksJournal of Applied Physics**, 1994. .

BINDER, C. **Desenvolvimento de novos tipos de aços sinterizados autolubrificantes a seco com elevada resistência mecânica aliada a baixo coeficiente de atrito vía moldagem de pós por injecão**. 2009. Universidade Federal de Santa Catarina, 2009.

BINDER, C. et al. 'Fine tuned' steels point the way to a focused future. **Metal Powder Report**, v. 65, n. 4, p. 29–37, maio 2010. Disponível em: <http://linkinghub.elsevier.com/retrieve/pii/S0026065710701089>. Acesso em: 30 jul. 2014.

BINDER, C. et al. Structure and properties of in situ-generated two-dimensional turbostratic graphite nodules. **Carbon**, v. 124, p. 685–692, 2017. Disponível em: <https://doi.org/10.1016/j.carbon.2017.09.036>.

BOHNING, J. J. **The Raman effect**. 1st. ed. Jadavpur, Calcutta: ACS, 1998.

BP P.L.C. **BP Energy Outlook 2035**. Disponível em:

<http://www.bp.com/content/dam/bp/pdf/Energy-economics/energy-outlook-2015/Energy_Outlook_2035_booklet.pdf>.

BRAITHWAITE, E. R. TECHNIQUES FOR EXAMINING SURFACES. In: BRAITHWAITE, E. R. (Ed.). **Solid Lubricants and Surfaces**. 1st. ed. London: Elsevier, 1964. p. 77–119.

BRISCOE, B. Tribology — Friction and wear of engineering materials. **Tribology International**, v. 25, n. 5, p. 357, jan. 1992. Disponível em: <https://linkinghub.elsevier.com/retrieve/pii/0301679X9290040T>.

BUSHAN, B. Fluid Film Lubrication. In: SONS, J. W. & (Ed.). **Principles and Applications to Tribology**. 2nd. ed. Chicheste-UK: John Wiley & Sons, Ltd, 2013. p. 545–653.

CAMPOS, J. L. E. et al. Applications of Raman spectroscopy in graphene-related materials and the development of parameterized PCA for large-scale data analysis. **Journal of Raman Spectroscopy**, v. 49, n. 1, p. 54–65, jan. 2018. Disponível em: <http://doi.wiley.com/10.1002/jrs.5225>.

CANÇADO, L. et al. Disentangling contributions of point and line defects in the Raman spectra of graphene-related materials. **2D Materials**, v. 4, n. 2, p. 025039, 24 fev. 2017. Disponível em: <http://stacks.iop.org/2053-1583/4/i=2/a=025039?key=crossref.376f8e0c03840738868cf8e19cbc341a>.

CANÇADO, L. G. et al. Influence of the atomic structure on the Raman spectra of graphite edges. **Physical Review Letters**, v. 93, n. 24, p. 5–8, 2004.

CANÇADO, L. G. et al. Quantifying defects in graphene via Raman spectroscopy at different excitation energies. **Nano Letters**, v. 11, n. 8, p. 3190–3196, 2011.

CANÇADO, L. G. et al. General equation for the determination of the crystallite size la of nanographite by Raman spectroscopy. **Applied Physics Letters**, v. 88, n. 16, p. 1998–2001, 2006.

CANÇADO, L. G. D. O. L. **RAMAN SPECTROSCOPY OF NANOGRAPHITES**. 2006. Universidade Federal de Minas Gerais, 2006. Disponível em: <http://www13.fisica.ufmg.br/~posgrad/Teses_Doutorado/decada2000/luiz-cancado>.

CAPUS, J. M. Introduction. In: CAPUS, J. (Ed.). **Metal Powders**. 4th. ed. New York: Elsevier, 2005a. p. 5–17.

CAPUS, J. M. Summary. In: CAPUS, J. M. (Ed.). **Metal Powders**. 4th. ed. New York: Elsevier, 2005b. p. 1–4.

CHAGNON, F.; TRUDEL, Y. Effect of Sintering Parameters on Mechanical Properties of

Sinter Hardened Materials. (PM2TEC, Ed.) In: PM2TEC Chicago Conference, Chicago. **Anais**... Chicago: 1997.

CHAMBERLAIN, M. B. Solid state reaction of titanium and (0001) α-SiC. **Thin Solid Films**, v. 72, n. 2, p. 305–311, out. 1980. Disponível em: <https://linkinghub.elsevier.com/retrieve/pii/0040609080900127>.

CHAWLA, N.; DENG, X. Microstructure and mechanical behavior of porous sintered steels. **Materials Science and Engineering A**, v. 390, n. 1–2, p. 98–112, 2005.

CHEN, Q.; LI, D. Y.; COOK, B. Is porosity always detrimental to the wear resistance of materials?-A computational study on the effect of porosity on erosive wear of TiC/Cu composites. **Wear**, v. 267, n. 5–8, p. 1153–1159, 2009.

CHOU, T. C.; JOSHI, A.; WADSWORTH, J. Solid state reactions of SiC with Co, Ni, and Pt. **Journal of Materials Research**, v. 6, n. 04, p. 796–809, 1991.

CHUN, Y.; LIM, D. Carbide derived carbon: from growth to tribological application. **Journal of the Ceramic Society of Japan**, v. 122, n. 1428, p. 577–585, 2014. Disponível em: <http://jlc.jst.go.jp/DN/JST.JSTAGE/jcersj2/122.P8-1?lang=en&from=CrossRef&type=abstract%5Cnhttp://jlc.jst.go.jp/DN/JST.JSTAGE/jcersj2/122.577?lang=en&from=CrossRef&type=abstract>.

CLAUSS, F. J. **Solid Lubricants and Self-Lubricating Solids**. I ed. New York: Academic Press Inc., 1972.

CONSONI, D. R. Morfologia e Estrutura dos Nódulos de Grafite Gerados pela Dissociação de SiC na Sinterização (Tese de Doutorado). p. 159, 2014.

CUI, G. et al. Tribological properties of bronze-graphite composites under sea water condition. **Tribology International**, v. 53, p. 76–86, 2012. Disponível em: <http://dx.doi.org/10.1016/j.triboint.2012.04.023>.

CUI, G. et al. The bronze–silver self-lubricating composite under sea water condition. **Tribology International**, v. 60, p. 83–92, abr. 2013. Disponível em: <http://linkinghub.elsevier.com/retrieve/pii/S0301679X1200360X>. Acesso em: 19 out. 2014.

DA SILVA, W. M.; BINDER, R.; DE MELLO, J. D. B. Abrasive wear of steam-treated sintered iron. **Wear**, v. 258, n. 1–4, p. 166–177, jan. 2005. Disponível em: <http://linkinghub.elsevier.com/retrieve/pii/S0043164804002546>.

DE MELLO, J. D. B. et al. Effect of compaction pressure and powder grade on microstructure

and hardness of steam oxidised sintered iron. **Powder Metallurgy**, v. 44, n. 1, p. 53–61, 2001. Disponível em: <http://www.tandfonline.com/doi/full/10.1179/003258901666176>.

DE MELLO, J. D. B. et al. Effect of precursor content and sintering temperature on the scuffing resistance of sintered self lubricating steel. **Wear**, v. 271, n. 9–10, p. 1862–1867, jul. 2011. Disponível em: <http://linkinghub.elsevier.com/retrieve/pii/S0043164811001943>. Acesso em: 30 jul. 2014.

DE MELLO, J. D. B. et al. Effect of the metallic matrix on the sliding wear of plasma assisted debinded and sintered MIM self-lubricating steel. **Wear**, v. 301, n. 1–2, p. 648–655, abr. 2013. Disponível em: <http://linkinghub.elsevier.com/retrieve/pii/S0043164813000215>. Acesso em: 30 jul. 2014.

DE MELLO, J. D. B. et al. Tribological behaviour of sintered iron based self-lubricating composites. **Friction**, v. 5, n. 3, p. 285–307, 2017a.

DE MELLO, J. D. B. et al. In situ created 2D turbostratic graphite : a new way to obtain high performance self lubricating composites . In: World Tribology Congress, Beijing. **Anais**... Beijing: 2017b.

DE MELLO, J. D. B.; BINDER, R. A methodology to determine surface durability in multifunctional coatings applied to soft substrates. **Tribology International**, v. 39, n. 8, p. 769–773, ago. 2006. Disponível em: <http://linkinghub.elsevier.com/retrieve/pii/S0301679X05001787>. Acesso em: 30 jul. 2014.

DE MELLO, J. D. B.; HUTCHINGS, I. M. Effect of processing parameters on the surface durability of steam-oxidized sintered iron. **Wear**, v. 250, n. 1–12, p. 435–448, out. 2001. Disponível em: <http://www.scielo.br/scielo.php?script=sci_arttext&pid=S1516-14392005000200007&lng=en&tlng=en>.

DESHPANDE, P. K.; LIN, R. Y. Wear resistance of WC particle reinforced copper matrix composites and the effect of porosity. **Materials Science and Engineering: A**, v. 418, n. 1–2, p. 137–145, fev. 2006. Disponível em: <https://linkinghub.elsevier.com/retrieve/pii/S0921509305014590>.

DIENWIEBEL, M. et al. Superlubricity of graphite. **Physical Review Letters**, v. 92, n. 12, p. 126101–1, 2004.

DINCER, I. Renewable energy and sustainable development: a crucial review. **Renewable and Sustainable Energy Reviews**, v. 4, n. 2, p. 157–175, 2000. Disponível em: <http://linkinghub.elsevier.com/retrieve/pii/S1364032199000118>.

DOBRZAŃSKI, L. A. et al. Influence of sintering parameters on the properties of duplex

stainless steel. **Journal of Achievements in Materials and Manufacturing Engineering**, v. 20, n. 2, p. 231–234, 2007.

DRESSELHAUS, M. S. Future directions in carbon science. **Annu. Rev. Mater. Sci.**, v. 27, p. 1–34, 28 mar. 1997.

DUBRUJEAUD, B.; VARDAVOULIAS, M.; JEANDIN, M. The role of porosity in the dry sliding wear of a sintered ferrous alloy. **Wear**, v. 174, n. 1–2, p. 155–161, 1994.

DULLIEN, F. A. L. Pore Structure. In: **Porous Media**. Toronto: Elsevier, 1992. p. 5–115.

ERDEMIR, A. Solid Lubricants and Self-Lubricating Films. In: BUSHAN, B. (Ed.). **Modern Tribology Handbook**. 1st. ed. Boca Raton: CRC Press, 2000. p. 787–818.

ERDEMIR, A. et al. Effects of high-temperature hydrogenation treatment on sliding friction and wear behavior of carbide-derived carbon films. **Surface and Coatings Technology**, v. 188–189, n. 1- 3 SPEC.ISS., p. 588–593, 2004.

ERDEMIR, A.; ERYILMAZ, O. Achieving superlubricity in DLC films by controlling bulk, surface, and tribochemistry. **Friction**, v. 2, n. 2, p. 140–155, 2014.

FERRARI, A. C. Raman spectroscopy of graphene and graphite: Disorder, electron-phonon coupling, doping and nonadiabatic effects. **Solid State Communications**, v. 143, n. 1–2, p. 47–57, 2007.

FERRARI, A. C.; BASKO, D. M. Raman spectroscopy as a versatile tool for studying the properties of graphene. **Nature Nanotechnology**, v. 8, n. 4, p. 235–246, 2013. Disponível em: <http://dx.doi.org/10.1038/nnano.2013.46>.

FERRARI, A. C.; ROBERTSON, J. Interpretation of Raman spectra of disordered and amorphous carbon. v. 61, n. 20, p. 95–107, 2000.

FERRARI, A. C.; ROBERTSON, J. Resonant Raman spectroscopy of disordered, amorphous, and diamondlike carbon. **Physical Review B**, v. 64, n. 7, p. 075414, 2001. Disponível em: <http://link.aps.org/doi/10.1103/PhysRevB.64.075414%5Cnhttp://journals.aps.org/prb/abstract/10.1103/PhysRevB.64.075414>.

FERRARO, J. R.; NAKAMOTO, K.; BROWN, C. **Introductory Raman Spectroscopy**. 2nd. ed. San Diego: Elsevier, 2003a.

FERRARO, J. R.; NAKAMOTO, K.; BROWN, C. W. Basic Theory. In: ACADEMIC PRESS (Ed.). **Introductory Raman Spectroscopy**. 2nd. ed. San Diego: Elsevier, 2003b. p. 1–94.

FRIEL, J. J. et al. **Practical Guide to Image Analysis**. Washington DC: ASM International,

2000.

FU, X. et al. Effect of particle shape and size on flow properties of lactose powders. **Particuology**, v. 10, n. 2, p. 203–208, 2012. Disponível em: <http://dx.doi.org/10.1016/j.partic.2011.11.003>.

FURLAN et al. Metallurgical Aspects of Self-lubricating Composites Containing Graphite and MoS2. **Journal of Materials Engineering and Performance**, v. 26, n. March, p. 1135–1145, 2017. Disponível em: <http://link.springer.com/10.1007/s11665-017-2563-4>.

FURLAN, K. P. et al. Thermal Stability of the MoS2 Phase in Injection Moulded 17-4 PH Stainless Steel. **Journal of Materials Research and Technology**, v. 1, n. 3, p. 134–140, out. 2012. Disponível em: <http://linkinghub.elsevier.com/retrieve/pii/S2238785412700248>. Acesso em: 18 out. 2014.

GERMAN, R. M. **Powder Metallurgy & Particulate Materials Processing**. Princeton: Metal Powder Industries Federation, 2005.

GHADERI, A. R.; NILI AHMADABADI, M.; GHASEMI, H. M. Effect of graphite morphologies on the tribological behavior of austempered cast iron. **Wear**, v. 255, n. 1–6, p. 410–416, 2003.

GOODALL, R. **Porous metals: foams and sponges**. 1sd. ed. Sheffield: Woodhead Publishing Limited, 2013.

GOSTICK, J. et al. PoreSpy: A Python Toolkit for Quantitative Analysis of Porous Media Images. **Journal of Open Source Software**, v. 4, n. 37, p. 1296, 2019.

GOUESBET, G.; GRÉHAN, G. **Optical Particle Sizing**. Boston, MA: Springer US, 1988.

GÜLSOY, H. Ö.; GERMAN, R. M. Production of micro-porous austenitic stainless steel by powder injection molding. **Scripta Materialia**, v. 58, n. 4, p. 295–298, 2008.

HAMMES, G. et al. Effect of double pressing/double sintering on the sliding wear of self-lubricating sintered composites. **Tribology International**, v. 70, p. 119–127, fev. 2014. Disponível em: <http://dx.doi.org/10.1016/j.triboint.2013.09.016>.

HANESCH, M. Raman spectroscopy of iron oxides and (oxy)hydroxides at low laser power and possible applications in environmental magnetic studies. **Geophysical Journal International**, v. 177, n. 3, p. 941–948, 2009.

HAO, T. Analogous viscosity equations of granular powders based on Eyring's rate process theory and free volume concept. **RSC Advances**, v. 5, n. 115, p. 95318–95333, 2015.

HATATE, M. et al. Influences of graphite shapes on wear characteristics of austempered cast iron. **Wear**, v. 251, n. 1–12, p. 885–889, 2001.

HAYNES, R. Effect of Porosity Content on the Tensile Strength of Porous Materials. **Powder Metallurgy**, v. 14, n. 27, p. 64–70, 1971. Disponível em: <http://www.tandfonline.com/doi/full/10.1179/pom.1971.14.27.004>.

HAYNES, R. Effects of porosity on the tensile strengths of sintered irons. **Metal Powder Report**, v. 46, n. 2, p. 49–51, 1991.

HAYNES, R.; EGEDIEGE, J. T. Effect of porosity and sintering conditions on elastic constants of sintered irons. v. 32, n. 1, p. 47–52, 1989.

HÖGANAS. Compacting of metal powders. In: HÖGANAS (Ed.). **PM-School Handbook 2: Production of Sintered Components**. 1st. ed. Höganäs: Höganas, 2013a.

HÖGANAS. Sintering. In: HÖGANAS (Ed.). **PM-School Handbook 2: Production of Sintered Components**. 1st. ed. Höganäs: Höganas, 2013b.

HÖGANÄS AB. Sintered Iron Based Materials. In: HÖGANÄS (Ed.). **Höganäs Handbook for Sintered Components**. 1. ed. Höganäs: Höganäs, 2004. p. 3–4.

HOLMBERG, K. et al. Global energy consumption due to friction in trucks and buses. **Tribology International**, v. 78, p. 94–114, 2014. Disponível em: <http://dx.doi.org/10.1016/j.triboint.2014.05.004>.

HOLMBERG, K.; ANDERSSON, P.; ERDEMIR, A. Global energy consumption due to friction in passenger cars. **Tribology International**, v. 47, p. 221–234, mar. 2012. Disponível em: <http://dx.doi.org/10.1016/j.triboint.2011.11.022>.

HOLMBERG, K.; ERDEMIR, A. Influence of tribology on global energy consumption, costs and emissions. **Friction**, v. 5, n. 3, p. 263–284, 2017.

ISLAM, M. A.; FARHAT, Z. N. Effect of porosity on dry sliding wear of AlSi alloys. **Tribology International**, v. 44, n. 4, p. 498–504, 2011. Disponível em: <http://dx.doi.org/10.1016/j.triboint.2010.12.007>.

JACQUES DIAS, H. **EXTRAÇÃO QUÍMICA DA GRAFITA TURBOSTRÁTICA GERADA IN SITU PELA DISSOCIAÇÃO DO CARBETO DE SILÍCIO EM MATRIZ DE FERRO PURO DURANTE TRATAMENTO TÉRMICO DE SINTERIZAÇÃO**. 2019. Universidade Federal de Santa Catarina, 2019.

JONES, L. .; THROWER, P. . Influence of boron on carbon fiber microstructure, physical properties, and oxidation behavior. **Carbon**, v. 29, n. 2, p. 251–269, 1991. Disponível em: <https://linkinghub.elsevier.com/retrieve/pii/000862239190076U>.

JORIO, A. et al. **Raman Spectroscopy in Graphene Related Systems**. 1st. ed. Weinheim, Germany: Wiley-VCH Verlag GmbH & Co. KGaA, 2011a.

JORIO, A. et al. Disorder Effects in the Raman Spectra of sp2 Carbons. In: **Raman Spectroscopy in Graphene Related Systems**. Weinheim, Germany: Wiley-VCH Verlag GmbH & Co. KGaA, 2011b. p. 299–325.

JORIO, A. et al. Raman Spectroscopy: From Graphite to sp2 Nanocarbons. In: **Raman Spectroscopy in Graphene Related Systems**. Weinheim, Germany: Wiley-VCH Verlag GmbH & Co. KGaA, 2011c. p. 73–101.

JORIO, A. Raman Spectroscopy in Graphene-Based Systems: Prototypes for Nanoscience and Nanometrology. **ISRN Nanotechnology**, v. 2012, n. 2, p. 1–16, 2012. Disponível em: <http://www.hindawi.com/journals/isrn.nanotechnology/2012/234216/>.

JORIO, A.; FILHO, A. G. S. Raman Studies of Carbon Nanostructures. **Annual Review of Materials Research**, v. 46, p. 357–382, 2016.

JRADI, K.; SCHMITT, M.; BISTAC, S. Surface modifications induced by the friction of graphites against steel. **Applied Surface Science**, v. 255, n. 7, p. 4219–4224, 2009.

KANG, S. C.; CHUNG, D. W. Improvement of frictional properties and abrasive wear resistance of nylon/graphite composite by oil impregnation. **Wear**, v. 254, n. 1–2, p. 103–110, 2003.

KHAEMBA, D. N.; NEVILLE, A.; MORINA, A. A methodology for Raman characterisation of MoDTC tribofilms and its application in investigating the influence of surface chemistry on friction performance of MoDTC lubricants. **Tribology Letters**, v. 59, n. 3, p. 1–17, 2015.

KLEIN, A. N. et al. Thermodynamic aspects during the processing of sintered materials. **Powder Technology**, v. 271, p. 193–203, 2015. Disponível em: <http://dx.doi.org/10.1016/j.powtec.2014.11.022>.

KOZBIAL, A. **UNDERSTANDING THE INTRINSIC WATER WETTABILITY OF GRAPHITE**. 2016. University of Pittsburgh, 2016.

KULECKI, P. et al. Fractography and Porosity Analysis of Cr and Cr-Mo PM Steels. **Archives of Metallurgy and Materials**, v. 61, n. 3, p. 1613–1622, 2016. Disponível em: <https://www.degruyter.com/view/j/amm.2016.61.issue-3/amm-2016-0263/amm-2016-0263.xml>.

KULECKI, P.; LICHAŃSKA, E.; SUŁOWSKI, M. The Effect of Processing Parameters on Microstructure and Mechanical Properties of Sintered Structural Steels Based on Prealloyed Powders / Wpływ Parametrów Wytwarzania Na Strukturę I Własności Mechaniczne

Spiekanych Stali Wykonanych Na Bazie Proszków Sto. **Archives of Metallurgy and Materials**, v. 60, n. 4, 2015. Disponível em: <http://www.degruyter.com/view/j/amm.2015.60.issue-4/amm-2015-0411/amm-2015-0411.xml>.

KUMAR, N. et al. Tribology International Super low to high friction of turbostratic graphite under various atmospheric test conditions. **Tribiology International**, v. 44, n. 12, p. 1969–1978, 2011. Disponível em: <http://dx.doi.org/10.1016/j.triboint.2011.08.012>.

KUMAR, N. et al. High-temperature phase transformation and low friction behaviour in highly disordered turbostratic graphite. **Journal of Physics D: Applied Physics**, v. 46, n. 39, p. 395305, 2013. Disponível em: <http://stacks.iop.org/0022-3727/46/i=39/a=395305?key=crossref.b461c093e1da20ee34be913511203890>.

LARKIN, P. **Infrared and Raman Spectroscopy**. 1st. ed. San Diego: Elsevier, 2011.

LEHEUP, E. R.; ZHANG, D.; MOON, J. R. Low amplitude reciprocating wear of sintered iron. **Wear**, v. 176, n. 1, p. 121–130, jul. 1994. Disponível em: <http://linkinghub.elsevier.com/retrieve/pii/0043164894902054>.

LEHEUP, E. R.; ZHANG, D.; MOON, J. R. Fretting wear of sintered iron under low normal pressure. **Wear**, v. 221, n. 2, p. 86–92, 1998.

LÉONARD, L. et al. Characterizing powders in order to determine their flow behavior in a mixer: From small scale observations to macroscopic in-mixer rheology for powders of various flowabilities. **Powder Technology**, v. 322, p. 314–331, 2017. Disponível em: <https://doi.org/10.1016/j.powtec.2017.07.075>.

LESHCHINSKY, V. et al. Inorganic nanoparticle impregnation of self lubricated materials. **International Journal of Powder Metallurgy (Princeton, New Jersey)**, v. 38, n. 5, p. 50–57, 2002.

LI, X.; OLOFSSON, U. A study on friction and wear reduction due to porosity in powder metallurgic gear materials. **Tribology International**, v. 110, n. February, p. 86–95, 2017. Disponível em: <http://dx.doi.org/10.1016/j.triboint.2017.02.008>.

LIU, P. S.; CHEN, G. F. Characterization Methods: Basic Factors. In: **Porous Materials**. 1st. ed. Oxford: Elsevier, 2014a. p. 411–492.

LIU, P. S.; CHEN, G. F. Making Porous Metals. In: **Porous Materials**. 1st. ed. Oxford: Elsevier, 2014b. p. 21–112.

LIU, P. S.; CHEN, G. F. General Introduction to Porous Materials. In: LIU, P. S.; CHEN, G. F. (Ed.). **Porous Materials**. 1st. ed. Oxford: Elsevier, 2014c. p. 1–20.

MABUCHI, Y.; HIGUCHI, T.; WEIHNACHT, V. Effect of sp2/sp3bonding ratio and nitrogen content on friction properties of hydrogen-free DLC coatings. **Tribology International**, v. 62, n. October 2017, p. 130–140, 2013. Disponível em: <http://dx.doi.org/10.1016/j.triboint.2013.02.007>.

MARTIN, F.; GARCÍA, C.; BLANCO, Y. Influence of residual porosity on the dry and lubricated sliding wear of a powder metallurgy austenitic stainless steel. **Wear**, v. 328–329, p. 1–7, 2015. Disponível em: <http://dx.doi.org/10.1016/j.wear.2015.01.025>.

MARTINS FERREIRA, E. H. et al. Evolution of the Raman spectra from single-, few-, and many-layer graphene with increasing disorder. **Physical Review B - Condensed Matter and Materials Physics**, v. 82, n. 12, 2010.

MARUYAMA, T.; HOKAO, M. Mechanism of Fretting Wear Reduction using Magnesium Stearate as Lubricant Additive under Oil Lubrication. In: 6th World Tribology Congress Proceedings, Beijing. **Anais**... Beijing: World Tribology Congress, 2017.

MIYOSHI, K. **Solid Lubrication Fundamentals and Applications**. 1st. ed. Cleveland: CRC Press, 2001a.

MIYOSHI, K. Friction and wear properties of selected solid lubricating films. In: NASA (Ed.). **Solid Lubrication Fundamentals and Applications**. 1st. ed. Cleveland: CRC Press, 2001b. p. 266–271.

MOGERA, U. et al. Highly Decoupled Graphene Multilayers: Turbostraticity at its Best. **Journal of Physical Chemistry Letters**, v. 6, n. 21, p. 4437–4443, 2015.

MOLINARI, A.; STRAFFELINI, G. Surface durability of steam treated sintered iron alloys. **Wear**, v. 181–183, n. PART 1, p. 334–341, 1995.

MONDAL, D. P. et al. Stainless steel foams made through powder metallurgy route using NH4HCO3 as space holder. **Materials and Design**, v. 88, p. 430–437, 2015. Disponível em: <http://dx.doi.org/10.1016/j.matdes.2015.09.020>.

MOUSTAFA, S. . et al. Friction and wear of copper–graphite composites made with Cu-coated and uncoated graphite powders. **Wear**, v. 253, n. 7–8, p. 699–710, out. 2002. Disponível em: <http://linkinghub.elsevier.com/retrieve/pii/S0043164802000388>.

NAVARRO-LÓPEZ, A. et al. Characterization of bainitic/martensitic structures formed in isothermal treatments below the Ms temperature. **Materials Characterization**, v. 128, n. March, p. 248–256, 2017.

NEVES, G. O. **Sintese de particulas de carbono nanoestructurado a partir da reação entre carbetos precursores**. 2020. Universidade Federal de Santa Catarina, 2020.

NISHIYABU, K. Powder space holder metal injection molding (PSH-MIM) of micro-porous metals. **Handbook of Metal Injection Molding**, n. Mim, p. 349–390, 2012. Disponível em: <http://linkinghub.elsevier.com/retrieve/pii/B9780857090669500157>.

NISHIYABU, K.; MATSUZAKI, S.; TANAKA, S. Net-Shape Manufacturing of Micro Porous Metal Components by Powder Injection Molding. **Materials Science Forum**, v. 534–536, p. 981–984, 2007.

NOWACKI, J.; KLIMEK, L. The mechanism of reaction sintering of iron-iron boride cermets. **Journal of Materials Science**, v. 28, n. 14, p. 3939–3944, 1993.

OSS GIACOMELLI, R. et al. DLC deposited onto nitrided grey and nodular cast iron substrates: An unexpected tribological behaviour. **Tribology International**, v. 121, p. 460–467, maio 2018. Disponível em: <https://linkinghub.elsevier.com/retrieve/pii/S0301679X18300860>.

ÖSTERLE, W. et al. Verification of nanometre-scale modelling of tribofilm sliding behaviour. **Tribology International**, v. 62, p. 155–162, jun. 2013. Disponível em: <https://linkinghub.elsevier.com/retrieve/pii/S0301679X13000698>.

PANWAR, N. L.; KAUSHIK, S. C.; KOTHARI, S. Role of renewable energy sources in environmental protection: A review. **Renewable and Sustainable Energy Reviews**, v. 15, n. 3, p. 1513–1524, 2011. Disponível em: <http://dx.doi.org/10.1016/j.rser.2010.11.037>.

PARUCKER, M. L. et al. Development of self-lubricating composite materials of nickel with molybdenum disulfide, graphite and hexagonal boron nitride processed by powder metallurgy: preliminary study. **Materials Research**, v. 17, p. 180–185, 2013. Disponível em: <http://www.scielo.br/scielo.php?script=sci_arttext&pid=S1516-14392013005000185&nrm=iso>.

PAVLINA, E. J.; VAN TYNE, C. J. Correlation of Yield strength and Tensile strength with hardness for steels. **Journal of Materials Engineering and Performance**, v. 17, n. 6, p. 888–893, 2008.

PEREIRA, R. V. **SEPARAÇÃO MECÂNICA DE GRAFITA GERADA POR DISSOCIAÇÃO DE CARBONETOS EM TRATAMENTO TÉRMICO DE HOMOGENEIZAÇÃO DE MISTURA DE PÓS.** 2019. Universidade Federal de Santa

Catarina, 2019.

PIECZONKA, T.; SUŁOWSKI, M.; CIAŚ, A. Atmosphere Effect on Sintering Behaviour of Astaloy CrM and Astaloy CrL Höganäs Powders with Manganese and Carbon Additions. **Archives of Metallurgy and Materials**, v. 57, n. 4, 2012. Disponível em: <http://www.degruyter.com/view/j/amm.2012.57.issue-4/v10172-012-0112-6/v10172-012-0112-6.xml>.

PIMENTA, M. A. et al. Studying disorder in graphite-based systems by Raman spectroscopy. **Physical Chemistry Chemical Physics**, v. 9, n. 11, p. 1276–1291, 2007. Disponível em: <http://www.scopus.com/inward/record.url?eid=2-s2.0-33947263695&partnerID=tZOtx3y1>.

PODCZECK, F.; MIA, Y. The influence of particle size and shape on the angle of internal friction and the flow factor of unlubricated and lubricated powders. **International Journal of Pharmaceutics**, v. 144, n. 2, p. 187–194, nov. 1996. Disponível em: <https://linkinghub.elsevier.com/retrieve/pii/S0378517396047552>.

POQUILLON, D. et al. Cold compaction of iron powders—relations between powder morphology and mechanical properties. **Powder Technology**, v. 126, n. 1, p. 75–84, 2002.

PRABU, S. S. et al. Experimental Study on Dry Sliding Wear Behaviour of Sintered Fe-C-W P/M Low Alloy Steels. **Procedia Materials Science**, v. 5, p. 809–816, 2014. Disponível em: <http://linkinghub.elsevier.com/retrieve/pii/S221181281400697X>.

PYTHON SOFTWARE FOUNDATION. **What is Python? Executive Summary**. Disponível em: <https://www.python.org/doc/essays/blurb/>.

QIN, X. et al. A comparison of the effect of graphitization on microstructures and properties of polyacrylonitrile and mesophase pitch-based carbon fibers. **Carbon**, v. 50, n. 12, p. 4459–4469, out. 2012. Disponível em: <http://dx.doi.org/10.1016/j.carbon.2012.05.024>.

RAPOPORT, L. et al. Hollow nanoparticles of WS2 as potential solid-state lubricants. **Nature**, v. 387, n. 1993, p. 791–793, 1997. Disponível em: <http://www.nature.com/nature/journal/v387/n6635/abs/387791a0.html>.

RAPOPORT, L. et al. Slow Release of Fullerene-like WS2 Nanoparticles from Fe-Ni Graphite Matrix: A Self-Lubricating Nanocomposite. **Nano Letters**, v. 1, n. 3, p. 137–140, 2001.

RAPOPORT, L. et al. Friction and wear of powdered composites impregnated with WS2 inorganic fullerene-like nanoparticles. **Wear**, v. 252, n. 5–6, p. 518–527, 2002.

RAPOPORT, L. et al. Superior tribological properties of powder materials with solid lubricant nanoparticles. **Wear**, v. 255, n. 7–12, p. 794–800, 2003.

REBELO, D. **MORFOLOGIA E ESTRUTURA DOS NÓDULOS DE GRAFITE**

GERADOS PELA DISSOCIAÇÃO DE SiC NA SINTERIZAÇÃO DE LIGAS FERROSAS. 2014. Universidade Federal de Santa Catarina, 2014.

REBELO DE FIGUEIREDO, M. et al. Formation mechanisms of low-friction tribo-layers on arc-evaporated TiC1-xNx hard coatings. **Wear**, v. 265, n. 3–4, p. 525–532, 2008.

RIBEIRO-SOARES, J. et al. Supplemental Material to " Structural analysis of polycrystalline graphene systems by Raman spectroscopy ". **Carbon**, v. 55, n. 31, 2015.

ROHATGI, P. K.; RAY, S.; LIU, Y. Tribological properties of metal matrix-graphite particle composites. **International Materials Reviews**, v. 37, n. 1, p. 129–152, 1992. Disponível em: <http://www.maneyonline.com/doi/abs/10.1179/imr.1992.37.1.129>.

SAKKA, M. M. et al. Tribological response of an epoxy matrix filled with graphite and/or carbon nanotubes. **Friction**, v. 5, n. 2, p. 171–182, 2017.

SCIKIT-IMAGE. **Scikit-image: image processing in python**. Disponível em: <https://scikit-image.org/docs/dev/api/skimage.measure.html>. Acesso em: 14 out. 2019.

SHARMA, S. M.; ANAND, A. Solid lubrication in iron based materials – A review. **Tribology in Industry**, v. 38, n. 3, p. 318–331, 2016.

SHI, H. et al. Effect of particle size and cohesion on powder yielding and flow. **KONA Powder and Particle Journal**, v. 2018, n. 35, p. 226–250, 2018.

SIMCHI, a.; DANNINGER, H. Effects of porosity on delamination wear behaviour of sintered plain iron. **Powder Metallurgy**, v. 47, n. 1, p. 73–80, 2004. Disponível em: <https://doi.org/10.1179/003258904225015545>.

SLINEY, H. E. Solid lubricant materials for high temperatures - a review. **Tribology International**, v. 15, n. 5, p. 303–315, 1982.

STACHOWIAK, G. W.; BATCHELOR, A. W. Physical Properties of Lubricants. In: STACHOWIAK, G. W.; BATCHELOR, A. W. (Ed.). **Engineering Tribology**. 2nd. ed. Amsterdam: Elsevier Ltd, 1993. p. 11–57.

STACHOWIAK, G. W.; BATCHELOR, A. W. Solid Lubrication and Surface Treatments. In: STACHOWIAK, G. W.; BATCHELOR, A. W. (Ed.). **Engineering Tribology**. 4th. ed. New York: Elsevier, 2014a. p. 429–474.

STACHOWIAK, G. W.; BATCHELOR, A. W. Hydrodynamic Lubrication. In: INTERGOVERNMENTAL PANEL ON CLIMATE CHANGE (Ed.). **Engineering Tribology**. Cambridge: Elsevier, 2014b. p. 105–210.

SUGIMURA, J. Tribology and Materials for Hydrogen Energy Society. In: World Tribology Congress, Beijing. **Anais**... Beijing: World Tribology Congress, 2017.

SUŁOWSKI, M.; KULECKI, P.; RADZISZEWSKA, A. Sintered Structural Pm Cr and Cr-Mo Steels/ Spiekane Stale Konstrukcyjne Chromowe I Chromowo-Molibdenowe. **Archives of Metallurgy and Materials**, v. 59, n. 4, p. 1–6, 2014. Disponível em: <http://www.degruyter.com/view/j/amm.2014.59.issue-4/amm-2014-0256/amm-2014-0256.xml>.

TAN, P.-H. **Raman Spectroscopy of Two-Dimensional Materials**. 1st. ed. Singapore: Springer Singapore, 2019. v. 276

TANG, W. M. et al. A study of the solid state reaction between silicon carbide and iron. **Materials Chemistry and Physics**, v. 74, n. 3, p. 258–264, 2002.

TUINSTRA, F.; KOENIG, J. L. Characterization of Graphite Fiber Surfaces with Raman Spectroscopy. **Journal of Composite Materials**, v. 4, n. 4, p. 492–499, 27 out. 1970a. Disponível em: <http://journals.sagepub.com/doi/abs/10.1177/002199837000400405?related-urls=yes&cited-by=yes&legid=spjcm%3B4%2F4%2F492&legid=spjcm%3B4%2F4%2F492&legid=spjcm%3B4%2F4%2F492&patientinform-links=yes&journalCode=jcma>.

TUINSTRA, F.; KOENIG, L. J. Raman Spectrum of Graphite. **The Journal of Chemical Physics**, v. 53, n. 5, p. 1126–1130, 1970b. Disponível em: <http://link.aip.org/link/?JCPSA6/53/1126/1>.

TUNG, S. C.; MCMILLAN, M. L. Automotive tribology overview of current advances and challenges for the future. **Tribology International**, v. 37, n. 7, p. 517–536, 2004.

URBONAITE, S. **Synthesis and Characterisation of Carbide Derived Carbons**. 1st. ed. Stockholm: US-AB, 2008.

URBONAITE, S.; HÄLLDAHL, L.; SVENSSON, G. Raman spectroscopy studies of carbide derived carbons. **Carbon**, v. 46, n. 14, p. 1942–1947, nov. 2008. Disponível em: <http://linkinghub.elsevier.com/retrieve/pii/S0008622308004089>.

VAN DER WALT, S. et al. scikit-image: image processing in Python. **PeerJ**, v. 2, p. e453, 19 jun. 2014. Disponível em: <https://peerj.com/articles/453>.

VARDAVOULIAS, M.; JOUANNY-TRESY, C.; JEANDIN, M. Sliding-wear behaviour of ceramic particle-reinforced high-speed steel obtained by powder metallurgy. **Wear**, v. 165, n. 2, p. 141–149, 1993.

WANG, H.; GAO, Q. Synthesis, characterization and energy-related applications of carbide-

derived carbons obtained by the chlorination of boron carbide. **Carbon**, v. 47, n. 3, p. 820–828, 2009. Disponível em: <http://dx.doi.org/10.1016/j.carbon.2008.11.030>.

WANG, P. et al. Carbon tribo-layer for super-low friction of amorphous carbon nitride coatings in inert gas environments. **Surface and Coatings Technology**, v. 221, p. 163–172, 2013. Disponível em: <http://dx.doi.org/10.1016/j.surfcoat.2013.01.045>.

WANG, Q. Z. et al. Open-celled porous Cu prepared by replication of a new space-holder. **Materials Letters**, v. 142, n. 4–5, p. 52–55, 2015. Disponível em: <http://dx.doi.org/10.1016/j.msea.2009.10.062>.

WANG, Y.; ALSMEYER, D. C.; MC CREERY, R. L. Raman spectroscopy of carbon materials: structural basis of observed spectra. **Chemistry of Materials**, v. 2, n. 5, p. 557–563, set. 1990. Disponível em: <https://pubs.acs.org/doi/abs/10.1021/cm00011a018>.

WELZ, S. **Identification of carbon allotropes in carbide derived carbon using electron microscopy**. 2003. University of Illinois, Chicago, 2003. Disponível em: <http://search.proquest.com/docview/305265766>. Acesso em: 20 fev. 2017.

WELZ, S.; MCNALLAN, M. J.; GOGOTSI, Y. Carbon structures in silicon carbide derived carbon. **Journal of Materials Processing Technology**, v. 179, n. 1–3, p. 11–22, out. 2006. Disponível em: <http://linkinghub.elsevier.com/retrieve/pii/S0924013606002329>. Acesso em: 30 jul. 2014.

WIESE, G. R.; HEALY, T. W. Effect of particle size on colloid stability. **Transactions of the Faraday Society**, v. 66, n. 13, p. 490, 1970. Disponível em: <http://xlink.rsc.org/?DOI=tf9706600490>.

WIŚNIEWSKA-WEINERT, H. Deposition of MoS2 particulate layers by pressure impregnation of porous sliding bearings. **Archives of Civil and Mechanical Engineering**, v. 14, n. 2, p. 255–261, 2014.

WOJNAR, L. **Image analysis application in materials engineering**. 1st. ed. Florida: CRC Press, 1999. v. 7

WORNYOH, E. Y. A.; JASTI, V. K.; FRED HIGGS, C. A Review of Dry Particulate Lubrication: Powder and Granular Materials. **Journal of Tribology**, v. 129, n. 2, p. 438, 2007. Disponível em: <http://tribology.asmedigitalcollection.asme.org/article.aspx?articleid=1467828>.

WU, J.-B.; LIN, M.-L.; TAN, P.-H. Raman Spectroscopy of Monolayer and Multilayer

Graphenes. In: TAN, P.-H. (Ed.). **Raman Spectroscopy of Two-Dimensional Materials**. 1st. ed. Singapore: Springer Singapore, 2019. p. 1–27.

XU, L. et al. Mechanical properties of CFF/MC/SF composite prepared using vacuum infusion impregnation method. **Results in Physics**, v. 7, p. 1016–1021, 2017. Disponível em: <http://linkinghub.elsevier.com/retrieve/pii/S2211379717303273>.

YALCIN, B. Effect of porosity on the mechanical properties and wear performance of 2% copper reinforced sintered steel used in shock absorber piston production. **Journal of materials science & technology**, v. 25, n. 5, p. 577–582, 2009. Disponível em: <http://www.jmst.org/fileup/PDF/2009367.pdf>.

YE, H. Z.; LI, D. Y.; EADIE, R. L. Influences of porosity on mechanical and wear performance of pseudoelastic TiNi-matrix composites. **Journal of Materials Engineering and Performance**, v. 10, n. 2, p. 178–185, 2001.

ZENG, S. et al. A review of renewable energy investment in the BRICS countries: History, models, problems and solutions. **Renewable and Sustainable Energy Reviews**, v. 74, n. March 2016, p. 860–872, 2017. Disponível em: <http://dx.doi.org/10.1016/j.rser.2017.03.016>.

ZHAI, W. et al. Carbon nanomaterials in tribology. **Carbon**, v. 119, p. 150–171, 2017. Disponível em: <http://dx.doi.org/10.1016/j.carbon.2017.04.027>.

ZHANG, G. et al. Tribological properties of graphene oxide sheets as water-based lubricant additives in artificial knee joint. In: 6th World Tribology Congress Proceedings, Beijing. **Anais**... Beijing: World Tribology Congress, 2017.

ZHANG, Q. **Study on the sliding wear response of cast iron**. 2011. Univerisity of Wollongong, 2011.

ZHANG, W. et al. Tribological properties of oleic acid-modified graphene as lubricant oil additives. **Journal of Physics D: Applied Physics**, v. 44, n. 20, p. 205303, 25 maio 2011. Disponível em: <http://stacks.iop.org/0022-3727/44/i=20/a=205303?key=crossref.87a6f704dd08ae3a2564c955c63e26f5>.

APPENDIX A – VARIANCE AND POS-HOC ANALYSES

The Kruskal-Wallis non-parametric analyses of variance (ANOVA) was used to analyse the data obtained for hardness, Feret diameter, orientation angle, circularity, solidity and eccentricity from the sintered specimens and their wear tracks of specimens tested in incremental load tests. This method was chosen because the data was not normally distributed. Post-hoc analyses were performed to evaluate if the differences between the medians between two datasets were significatively different. This analysis helps to determine if there is a relationship between the independent variable (load) and the independent variables (the parameters obtained from the image analysis).

Statistical analysis for the image analysis of samples produced in step 1

Tables 8 and 9 presents the ANOVA and post-hoc analysis for the Feret diameter of samples compacted and sintered in step 1 of this work. In the ANOVA analysis if the Prob > Chi-Square value is less than 0.05 then the difference between the means is significant at the 0.05 level. In the post-hoc analysis a Sig value of 1 means that at the 0.05 level the difference between the mean is significant.

Table 8: ANOVA for Feret diameter of samples compacted at 200, 400 and 600 MPa and sintered 1h at 1100, 1150 and 1200°C

	Feret diameter ANOVA	
Dataset	**Mean Rank**	**Sum Rank**
200 MPa - 1100 °C	14077.82	4,37E+12
400 MPa - 1100 °C	12275.73	6,67E+12
400 MPa - 1150°C	11631.12	7,71E+12
400 MPa - 1200°C	13581.10	5,82E+12
600 MPa - 1100°C	12448.23	7,14E+12
	Chi-Square	**Prob > Chi-Square**
	337.26	9,86E-67

Source: Author

Table 9: Post-hoc analysis for Feret diameter of samples compacted at 200, 400 and 600 MPa and sintered 1h at 1100, 1150 and 1200°C

Pair of datasets	Mean Rank Diff	z	Prob	Sig
200 MPa - 1100 °C; 400 MPa - 1100 °C	1802.08857	11.01681	3.1711E-27	1
200 MPa - 1100 °C; 400 MPa - 1150°C	2446.69577	15.47298	5.28031E-53	1
200 MPa - 1100 °C; 400 MPa - 1200°C	496.71627	2.89866	0.03748	1
200 MPa - 1100 °C; 600 MPa - 1100°C	1629.58635	10.06025	8.27872E-23	1
400 MPa - 1100 °C; 400 MPa - 1150°C	644.60719	4.84503	1.26596E-5	1
400 MPa - 1100 °C; 400 MPa - 1200°C	-1305.37231	-8.78859	1.51455E-17	1
400 MPa - 1100 °C; 600 MPa - 1100°C	-172.50222	-1.2536	1	0
400 MPa - 1150°C; 400 MPa - 1200°C	-1949.9795	-13.6834	1.27579E-41	1
400 MPa - 1150°C; 600 MPa - 1100°C	-817.10941	-6.23363	4.55754E-9	1
400 MPa - 1200°C; 600 MPa - 1100°C	1132.87009	7.71849	1.17715E-13	1

Source: Author

Statistical analyses of data obtained from the analyses of the wear tracks from the scuffing resistance tests performed in step 4

Table 10 presents the ANOVA for the hardness as a function of the load in the scuffing resistance test from the data presented in figure 89.

Table 10: ANOVA for hardness of the wear tracks as a function of load in the scuffing resistance tests

	200 MPa – 1100°C		400 MPa – 1100°C		400 MPa – 1200°C		600 MPa – 1100°C	
Dataset	Mean Rank	Sum Rank	Mean Rank	Sum Rank	Mean Rank	Sum Rank	Mean Rank	Sum Rank
0N	7.9	39.5	11.6	58	16.4	82	14.8	74
7N	16.5	82.5	6.5	32.5	13.4	67	10.3	51.5
14N	17.8	89	17.5	70	25	125	20.4	102
21N	20.5	102.5	17.4	87	14.7	73.5	21.6	108
28N	26.8	134	22.2	111	21.7	108.5	15.2	76
35N	31.8	159	29.3	146.5	19.8	99	10.7	53.5
42N	33.7	168.5	31.7	158.5	25.1	125.5		
49N	32.9	164.5	30.7	153.5	31	155		
56N	27.6	138	34.6	173	39.9	199.5		
63N	39.5	197.5						
	Chi-Square	Prob>Chi-Square	Chi-Square	Prob>Chi-Square	Chi-Square	Prob>Chi-Square	Chi-Square	Prob>Chi-Square
	19.76	0.02	23.24	0.003	16.67	0.03	7.22	0.2

Source: Author

Table 11 presents the ANOVA for Feret diameter and orientation angle of samples compacted at 200 MPa and sintered 1h at 1100°C.

Table 11: ANOVA for Feret diameter and orientation angle of samples compacted at 200 MPa and sintered 1h at 1100°C

	Feret diameter ANOVA		**Orientation angle ANOVA**	
Dataset	**Mean Rank**	**Sum Rank**	**Mean Rank**	**Sum Rank**
0N	14709.40766	3.45671E7	12295.64596	2.88948E7
7N	13875.43385	3.37728E7	12400.17666	3.0182E7
14N	13245.29975	3.68087E7	12645.39043	3.51415E7
21N	12976.89677	3.62055E7	12457.19928	3.47556E7
28N	13703.66259	3.08058E7	12170.90547	2.73602E7
35N	12102.22834	3.18531E7	12569.04483	3.30817E7
42N	11794.22125	2.95327E7	12445.07089	3.11625E7
49N	10484.51763	2.55717E7	12901.01271	3.14656E7
56N	11473.91106	2.52197E7	12413.87511	2.72857E7
63N	11400.59587	2.62214E7	12622.52978	2.90318E7
70N	8784.18325	3.35556E6	14535.8822	5.55271E6
	Chi-Square	**Prob>Chi-Square**	**Chi-Square**	**Prob>Chi-Square**
	830.15556	6.76881E-172	46.93963	9.68447E-7

Source: Author

Table 12 and 13 presents the post-hoc analyses for the Feret diameter and the orientation angle respectively.

Table 12: Post-hoc analysis for Feret diameter of samples compacted at 200 MPa and sintered 1h at 1100°C

Pair of datasets	**Mean Rank Diff**	**z**	**Prob**	**Sig**
0N; 7N	833.97381	3.98687	0.00368	1
0N; 14N	1464.10791	7.22297	2.79762E-11	1
0N 21N	1732.51089	8.55482	6.4927E-16	1
0N 28N	1005.74507	4.7132	1.34119E-4	1
0N 35N	2607.17932	12.70067	3.22454E-35	1
0N 42N	2915.18641	14.03292	5.39144E-43	1
0N 49N	4224.89003	20.20754	4.62189E-89	1
0N 56N	3235.4966	15.07506	1.29962E-49	1

Continues from table 12

Pair of datasets	Mean Rank Diff	z	Prob	Sig
0N 63N	3308.81179	15.59639	4.23666E-53	1
0N; 70N	5925.22441	14.84946	3.85719E-48	1
7N 14N	630.13411	3.13815	0.09351	0
7N 21N	898.53708	4.47896	4.12537E-4	1
7N 28N	171.77126	0.81185	1	0
7N 35N	1773.20551	8.71787	1.55918E-16	1
7N 42N	2081.21261	10.10879	2.77787E-22	1
7N 49N	3390.91622	16.3631	1.92935E-58	1
7N 56N	2401.5228	11.28385	8.67329E-28	1
7N 63N	2474.83798	11.76623	3.20476E-30	1
7N 70N	5091.25061	12.7903	1.02166E-35	1
14N 21N	268.40297	1.3846	1	0
14N 28N	-458.36284	-2.23397	1	0
14N 35N	1143.0714	5.81035	3.4288E-7	1
14N 42N	1451.0785	7.28103	1.82208E-11	1
14N 49N	2760.78212	13.75659	2.5571E-41	1
14N 56N	1771.38869	8.57963	5.23464E-16	1
14N 63N	1844.70388	9.04745	8.04877E-18	1
14N 70N	4461.1165	11.30285	6.98668E-28	1
21N 28N	-726.76581	-3.54525	0.02157	1
21N 35N	874.66843	4.4503	4.71626E-4	1
21N 42N	1182.67553	5.93982	1.56931E-7	1
21N 49N	2492.37914	12.43064	9.80142E-34	1
21N 56N	1502.98572	7.28598	1.75633E-11	1
21N 63N	1576.3009	7.73797	5.55606E-13	1
21N 70N	4192.71353	10.62534	1.24945E-24	1
28N 35N	1601.43425	7.70941	6.95227E-13	1
28N 42N	1909.44134	9.08582	5.6607E-18	1
28N 56N	2229.75153	10.27695	4.92323E-23	1
28N 63N	2303.06672	10.73591	3.79684E-25	1
28N 70N	4919.47934	12.29	5.63817E-33	1
35N 42N	308.0071	1.52542	1	0
35N 49N	1617.71071	7.95763	9.64545E-14	1
35N 56N	628.31729	3.00637	0.14541	0
35N 63N	701.63247	3.39849	0.03727	1
35N 70N	3318.0451	8.37849	2.94854E-15	1
42N 49N	1309.70362	6.36475	1.07584E-8	1
42N 56N	320.31019	1.5151	1	0
42N 63N	393.62538	1.88427	1	0
42N 70N	3010.038	7.57623	1.95654E-12	1
49N 56N	-989.39343	-4.65105	1.81639E-4	1
49N 63N	-916.07824	-4.35752	7.23486E-4	1

Continues from table 12

49N 70N	1700.33438	4.27219	0.00106	1
56N 63N	73.31519	0.33982	1	0
56N 70N	2689.72781	6.70849	1.08159E-9	1
63N 70N	2616.41262	6.54716	3.22525E-9	1

Source: Author

Table 13: Post-hoc analysis for orientation angle of samples compacted at 200 MPa and sintered 1h at 1100°C

Pairs of datasets	**Mean Rank Diff**	**z**	**Prob**	**Sig**
0N; 7N	-104.53071	-0.4997	1	0
0N; 14N	-349.74447	-1.72537	1	0
0N; 21N	-161.55333	-0.7977	1	0
0N; 28N	124.74049	0.58455	1	0
0N; 35N	-273.39888	-1.33181	1	0
0N; 42N	-149.42493	-0.71927	1	0
0N; 49N	-605.36675	-2.89538	0.20828	0
0N; 56N	-118.22916	-0.55085	1	0
0N; 63N	-326.88383	-1.54076	1	0
0N; 70N	-2240.23624	-5.61422	1.08599E-6	1
7N; 14N	-245.21376	-1.22117	1	0
7N; 21N	-57.02262	-0.28424	1	0
7N; 28N	229.27119	1.08358	1	0
7N; 35N	-168.86817	-0.83021	1	0
7N; 42N	-44.89422	-0.21805	1	0
7N; 49N	-500.83605	-2.41676	0.86126	0
7N; 56N	-13.69845	-0.06436	1	0
7N; 63N	-222.35312	-1.05712	1	0
7N; 70N	-2135.70554	-5.36522	4.44688E-6	1
14N; 21N	188.19115	0.97079	1	0
14N; 28N	474.48496	2.31249	1	0
14N; 35N	76.3456	0.38806	1	0
14N; 42N	200.31954	1.00511	1	0
14N; 49N	-255.62228	-1.2737	1	0
14N; 56N	231.51531	1.12131	1	0
14N; 63N	22.86065	0.11212	1	0
14N; 70N	-1890.49177	-4.7897	9.18649E-5	1
21N; 28N	286.29381	1.39654	1	0
21N; 35N	-111.84555	-0.56905	1	0
21N; 42N	12.1284	0.06091	1	0

Continues from table 13

Pair of datasets	Mean Rank Diff	z	Prob	Sig
21N; 49N	-443.81343	-2.21345	1	0
21N; 56N	43.32417	0.21002	1	0
21N; 63N	-165.3305	-0.81158	1	0
21N; 70N	-2078.68292	-5.26776	7.59558E-6	1
28N; 35N	-398.13936	-1.91662	1	0
28N; 42N	-274.16542	-1.30455	1	0
28N; 49N	-730.10724	-3.45234	0.03057	1
28N; 56N	-242.96964	-1.11982	1	0
28N; 63N	-451.62431	-2.10523	1	0
28N; 70N	-2364.97673	-5.90812	1.90323E-7	1
35N; 42N	123.97395	0.61397	1	0
35N; 49N	-331.96788	-1.63293	1	0
35N; 56N	155.16972	0.74244	1	0
35N; 63N	-53.48495	-0.25906	1	0
35N; 70N	-1966.83737	-4.9664	3.7514E-5	1
42N; 49N	-455.94182	-2.21568	1	0
42N; 56N	31.19577	0.14756	1	0
42N; 63N	-177.4589	-0.84947	1	0
42N; 70N	-2090.81131	-5.26242	7.81932E-6	1
49N; 56N	487.1376	2.28993	1	0
49N; 63N	278.48293	1.32463	1	0
49N; 70N	-1634.86949	-4.10761	0.0022	1
56N; 63N	-208.65467	-0.96709	1	0
56N; 70N	-2122.00709	-5.2924	6.63966E-6	1
63N; 70N	-1913.35242	-4.78775	9.27642E-5	1

Source: Author

Table 14 presents the ANOVA for Feret diameter and orientation angle of samples compacted at 400 MPa and sintered 1h at 1100°C.

Table 14: ANOVA for Feret diameter and orientation angle of samples compacted at 400 MPa and sintered 1h at 1100°C

	Feret diameter ANOVA		Orientation angle ANOVA	
Dataset	**Mean Rank**	**Sum Rank**	**Mean Rank**	**Sum Rank**
0N	14416.79063	3.75269E7	13158.24337	3.42509E7
7N	14002.24933	4.16987E7	12953.3405	3.8575E7
14N	12806.10616	4.13765E7	13049.57335	4.21632E7
21N	14321.17212	3.58602E7	13121.73143	3.28568E7
28N	12940.61829	3.66478E7	12935.1619	3.66324E7
35N	13208.93266	3.76587E7	13230.23185	3.77194E7
42N	12101.39042	3.38476E7	13437.23543	3.75839E7
49N	13144.50572	3.21646E7	13572.6177	3.32122E7
56N	12926.54266	3.04549E7	13399.07067	3.15682E7
63N	12470.25199	2.35314E7	13887.26842	2.62053E7
	Chi-Square	**Prob>Chi-Square**	**Chi-Square**	**Prob>Chi-Square**
	24162153	5,84704E-12	32.62217	1.55362E-4

Source: Author

Tables 15 and 16 show the post-hoc analyses for the Feret diameter and orientation angle of samples compacted at 400 MPa and sintered 1 h at 1100°C.

Table 15: Post-hoc analysis for Feret diameter of samples compacted at 400 MPa and sintered 1h at 1100°C

Pair of datasets	**Mean Rank Diff**	**z**	**Prob**	**Sig**
0N; 7N	414.5413	2.02065	1	0
0N; 14N	1610.68447	7.99859	5.66356E-14	1
0N; 21N	95.6185	0.44678	1	0
0N; 28N	1476.17234	7.11052	5.2023E-11	1
0N; 35N	1207.85797	5.82739	2.53349E-7	1
0N; 42N	2315.40021	11.11969	4.52771E-27	1
0N; 49N	1272.2849	5.9098	1.54131E-7	1
0N; 56N	1490.24797	6.85435	3.22358E-10	1
0N; 63N	1946.53864	8.4206	1.68547E-15	1
7N; 14N	1196.14317	6.15862	3.30214E-8	1
7N; 21N	-318.9228	-1.53842	1	0
7N; 35N	793.31667	3.95996	0.00337	1
7N; 42N	1900.85891	9.44197	1.64619E-19	1
7N; 49N	857.74361	4.11166	0.00177	1

Continues from table 15

Pair of datasets	Mean Rank Diff	z	Prob	Sig
7N; 56N	1075.70667	5.10267	1.50701E-5	1
7N; 63N	1531.99734	6.80997	4.39284E-10	1
14N; 21N	-1515.06597	-7.44271	4.43897E-12	1
14N; 28N	-134.51213	-0.68346	1	0
14N; 35N	-402.8265	-2.05042	1	0
14N; 42N	704.71574	3.5688	0.01614	1
14N; 49N	-338.39956	-1.65157	1	0
14N; 56N	-120.4365	-0.58144	1	0
14N; 63N	335.85417	1.51613	1	0
21N; 28N	1380.55383	6.58248	2.08199E-9	1
21N; 35N	1112.23947	5.31147	4.89351E-6	1
21N; 42N	2219.78171	10.55298	2.21449E-24	1
21N; 49N	1176.6664	5.41404	2.77284E-6	1
21N; 56N	1394.62947	6.35515	9.37E-9	1
21N; 63N	1850.92014	7.94126	9.00617E-14	1
28N; 35N	-268.31436	-1.32276	1	0
28N; 42N	839.22787	4.11754	0.00172	1
28N; 49N	-203.88743	-0.96618	1	0
28N; 56N	14.07563	0.06602	1	0
28N; 63N	470.3663	2.07026	1	0
35N; 42N	1107.54224	5.443	2.35761E-6	1
35N; 49N	64.42693	0.30578	1	0
35N; 56N	282.39	1.32655	1	0
35N; 63N	738.68067	3.25555	0.05093	0
42N; 56N	-825.15224	-3.85939	0.00512	1
42N; 49N	-1043.1153	-4.92884	3.7224E-5	1
42N; 63N	-368.86157	-1.61945	1	0
49N; 56N	217.96306	0.98767	1	0
49N; 63N	674.25373	2.87847	0.17982	0
56N; 63N	456.29067	1.93179	1	0
7N; 28N	1061.63104	5.29023	5.4972E-6	1

Source: Author

Table 16: Post-hoc analysis for orientation angle of samples compacted at 400 MPa and sintered 1h at 1100°C

Pair of datasets	Mean Rank Diff	z	Prob	Sig
0N; 7N	204.90288	0.99875	1	0
0N; 14N	108.67002	0.53963	1	0
0N; 21N	36.51194	0.1706	1	0
0N; 28N	223.08147	1.07452	1	0
0N; 35N	-71.98848	-0.3473	1	0
0N; 42N	-278.99206	-1.33981	1	0
0N; 49N	-414.37432	-1.92472	1	0
0N; 56N	-240.8273	-1.10764	1	0
0N; 63N	-729.02504	-3.15361	0.07257	0
7N; 14N	-96.23285	-0.49546	1	0
7N; 21N	-168.39093	-0.81226	1	0
7N; 28N	18.1786	0.09058	1	0
7N; 35N	-276.89135	-1.3821	1	0
7N; 42N	-483.89493	-2.40353	0.73069	0
7N; 49N	-619.2772	-2.96846	0.13469	0
7N; 56N	-445.73017	-2.11428	1	0
7N; 63N	-933.92792	-4.15132	0.00149	1
14N; 21N	-72.15808	-0.35446	1	0
14N; 28N	114.41145	0.58131	1	0
14N; 35N	-180.6585	-0.91954	1	0
14N; 42N	-387.66208	-1.96312	1	0
14N; 49N	-523.04434	-2.55266	0.48107	0
14N; 56N	-349.49732	-1.68724	1	0
14N; 63N	-837.69506	-3.78143	0.00702	1
21N; 28N	186.56953	0.88953	1	0
21N; 35N	-108.50042	-0.51812	1	0
21N; 42N	-315.504	-1.49988	1	0
21N; 49N	-450.88627	-2.07453	1	0
21N; 63N	-765.53699	-3.28438	0.04599	1
21N; 56N	-277.33924	-1.26376	1	0
28N; 35N	-295.06995	-1.45461	1	0
28N; 42N	-502.07353	-2.46326	0.61956	0
28N; 49N	-637.4558	-3.02067	0.1135	0
28N; 56N	-463.90877	-2.17587	1	0
28N; 63N	-952.10652	-4.19044	0.00125	1
35N; 42N	-207.00358	-1.01728	1	0
35N; 49N	-342.38585	-1.62496	1	0

Continues from table 16

Pair of datasets	Mean Rank Diff	z	Prob	Sig
35N; 56N	-168.83882	-0.79311	1	0
35N; 63N	-657.03657	-2.89563	0.17028	0
42N; 49N	-135.38226	-0.63968	1	0
42N; 56N	38.16476	0.1785	1	0
42N; 63N	-450.03298	-1.97576	1	0
49N; 56N	173.54702	0.78638	1	0
49N; 63N	-314.65072	-1.34324	1	0
56N; 63N	-488.19774	-2.0668	1	0

Source: Author

Table 17 presents the ANOVA for Feret diameter and orientation angle of samples compacted at 400 MPa and sintered 1h at 1200°C

Table 17: ANOVA for Feret diameter and orientation angle of samples compacted at 400 MPa and sintered 1h at 1200°C

	Feret diameter ANOVA		Orientation angle ANOVA	
Dataset	**Mean Rank**	**Sum Rank**	**Mean Rank**	**Sum Rank**
0	13123.81055	3.95552E7	12721.89798	3.83438E7
7	13034.04482	3.62086E7	12299.31875	3.41675E7
14	13003.7714	3.4642E7	12531.16911	3.3383E7
21	12857.52821	3.34939E7	12368.24184	3.22193E7
28	12617.86359	3.59357E7	12561.00053	3.57737E7
35	12622.88613	3.58616E7	12881.44984	3.65962E7
42	13602.30666	3.71479E7	12757.76089	3.48414E7
49	12533.74471	3.01938E7	12679.91781	3.05459E7
56	11368.70378	2.49657E7	12981.62227	2.85076E7
63	10478.85346	1.31929E7	13358.72478	1.68186E7
	Chi-Square	Prob>Chi-Square	Chi-Square	Prob>Chi-Square
	253.56187	1.7654E-49	31.20943	2.72511E-4

Source: Author.

Tables 18 and 19 show the post-hoc analyses for the Feret diameter and orientation angle of samples compacted at 400 MPa and sintered 1 h at 1200°C.

Table 18: Post-hoc analysis for Feret diameter of samples compacted at 400 MPa and sintered 1h at 1200°C

Pair of datasets	Mean Rank Diff	z	Prob	Sig
0N; 7N	89.76573	0.46649	1	0
0N; 14N	120.03915	0.61698	1	0
0N; 21N	266.28234	1.36049	1	0
0N; 28N	505.94696	2.64625	0.36626	0
0N; 35N	500.92442	2.61832	0.39764	0
0N; 42N	-478.49611	-2.47555	0.59863	0
0N; 49N	590.06584	2.95105	0.14251	0
0N; 56N	1755.10677	8.55025	5.5268E-16	1
0N; 63N	2644.9571	10.77316	2.07401E-25	1
7N; 14N	30.27342	0.15259	1	0
7N; 21N	176.5166	0.88461	1	0
7N; 28N	416.18123	2.13317	1	0
7N; 35N	411.15868	2.10614	1	0
7N; 42N	-568.26185	-2.88234	0.17763	0
7N; 49N	500.30011	2.4562	0.63187	0
7N; 56N	1665.34104	7.97148	7.05516E-14	1
7N; 63N	2555.19136	10.27968	3.91573E-23	1
14N; 21N	146.24318	0.72542	1	0
14N; 28N	385.90781	1.95692	1	0
14N; 35N	380.88526	1.9303	1	0
14N; 42N	-598.53527	-3.0042	0.11983	0
14N; 49N	470.02669	2.28498	1	0
14N; 56N	1635.06762	7.75367	4.01728E-13	1
14N; 63N	2524.91794	10.09078	2.73091E-22	1
21N; 28N	239.66463	1.20828	1	0
21N; 35N	234.64208	1.18226	1	0
21N; 42N	-744.77845	-3.71698	0.00907	1
21N; 49N	323.78351	1.56564	1	0
21N; 56N	1488.82444	7.02432	9.68009E-11	1
21N; 63N	2378.67476	9.47196	1.2359E-19	1
28N; 35N	-5.02254	-0.02589	1	0
28N; 42N	-984.44308	-5.024	2.27725E-5	1
28N; 49N	84.11888	0.41535	1	0
28N; 56N	1249.15981	6.01206	8.24322E-8	1
28N; 63N	2139.01013	8.63853	2.56232E-16	1
35N; 42N	-979.42053	-4.99536	2.6427E-5	1
35N; 49N	89.14142	0.43991	1	0
35N; 56N	1254.18235	6.033	7.24263E-8	1

Continues from table 18

Pair of datasets	Mean Rank Diff	z	Prob	Sig
35N; 63N	2144.03268	8.65555	2.2075E-16	1
42N; 49N	1068.56196	5.22521	7.82799E-6	1
42N; 56N	2233.60288	10.65119	7.74652E-25	1
42N; 63N	3123.45321	12.53224	2.2381E-34	1
49N; 56N	1165.04093	5.39719	3.04622E-6	1
49N; 63N	2054.89125	8.07629	3.00447E-14	1
56N; 63N	889.85032	3.44056	0.02612	1

Source: Author

Table 19: Post-hoc analysis for orientation angle of samples compacted at 400 MPa and sintered 1h at 1200°C

Pair of datasets	Mean Rank Diff	z	Prob	Sig
0N; 7N	422.57922	2.19594	1	0
0N; 14N	190.72887	0.98027	1	0
0N; 21N	353.65613	1.80683	1	0
0N; 28N	160.89745	0.84151	1	0
0N; 35N	-159.55187	-0.83394	1	0
0N; 42N	-35.86292	-0.18553	1	0
0N; 49N	41.98017	0.20994	1	0
0N; 56N	-259.72429	-1.26524	1	0
0N; 63N	-636.82681	-2.59376	0.4272	0
7N; 14N	-231.85035	-1.16856	1	0
7N; 21N	-68.92309	-0.34539	1	0
7N; 28N	-261.68177	-1.34122	1	0
7N; 35N	-582.13109	-2.98183	0.12894	0
7N; 42N	-458.44214	-2.32522	0.9027	0
7N; 49N	-380.59905	-1.86846	1	0
7N; 56N	-682.30351	-3.26585	0.04911	1
7N; 63N	-1059.40603	-4.26189	9.12191E-4	1
14N; 21N	162.92726	0.80815	1	0
14N; 28N	-29.83142	-0.15127	1	0
14N; 35N	-350.28073	-1.77513	1	0
14N; 42N	-226.59179	-1.13728	1	0
14N; 49N	-148.7487	-0.7231	1	0
14N; 56N	-450.45316	-2.13602	1	0
14N; 63N	-827.55567	-3.30718	0.04241	1
21N; 28N	-192.75868	-0.97176	1	0
21N; 35N	-513.208	-2.58573	0.43727	0
21N; 42N	-389.51905	-1.94391	1	0

Continues from table 19

Pair of datasets	Mean Rank Diff	z	Prob	Sig
21N; 49N	-311.67597	-1.50703	1	0
21N; 56N	-613.38043	-2.89384	0.17126	0
21N; 63N	-990.48294	-3.94398	0.00361	1
28N; 35N	-320.44931	-1.65172	1	0
28N; 42N	-196.76037	-1.00411	1	0
28N; 49N	-118.91728	-0.58716	1	0
28N; 56N	-420.62174	-2.02432	1	0
28N; 63N	-797.72425	-3.22154	0.05738	0
35N; 42N	123.68895	0.63083	1	0
35N; 49N	201.53203	0.99451	1	0
35N; 56N	-100.17243	-0.48184	1	0
35N; 63N	-477.27494	-1.9267	1	0
42N; 49N	77.84309	0.38063	1	0
42N; 56N	-223.86137	-1.06747	1	0
42N; 63N	-600.96389	-2.41116	0.71559	0
49N; 56N	-301.70446	-1.39763	1	0
49N; 63N	-678.80697	-2.6678	0.34358	0
56N; 63N	-377.10251	-1.45799	1	0

Source: Author

Table 20 presents the ANOVA for Feret diameter and orientation angle of samples compacted at 600 MPa and sintered 1h at 1100°C

Table 20: ANOVA for Feret diameter and orientation angle of samples compacted at 600 MPa and sintered 1h at 1100°C

		Feret diameter ANOVA		Orientation angle ANOVA	
Dataset	**N**	**Mean Rank**	**Sum Rank**	**Mean Rank**	**Sum Rank**
0	3196	9788.12437	3.12828E7	9384.85717	2.9994E7
7	3215	9537.3661	3.06626E7	9230.99876	2.96777E7
14	3127	9500.83994	2.97091E7	9489.88839	2.96749E7
21	3119	9099.91872	2.83826E7	9302.56829	2.90147E7
28	2008	9080.91708	1.82345E7	9649.90239	1.9377E7
35	2919	9499.51182	2.77291E7	9530.59421	2.78198E7
42	1203	8715.10474	1.04843E7	9083.13674	1.0927E7
	DF	**Chi-Square**	**Prob>Chi-Square**	**Chi-Square**	**Prob>Chi-Square**
	6	56.16	2.69989E-10	15.05141	0.01986

Source: Author

Tables 21 and 22 show the post-hoc analyses for the Feret diameter and orientation angle of samples compacted at 600 MPa and sintered 1 h at 1100°C.

Table 21: Post-hoc analysis for Feret diameter of samples compacted at 600 MPa and sintered 1h at 1100°C

Pair of datasets	Mean Rank Diff	z	Prob	Sig
0N; 7N	250.75828	1.85112	1	0
0N; 14N	287.28443	2.10604	0.73923	0
0N; 21N	688.20565	5.04186	9.6817E-6	1
0N; 28N	707.20729	4.57943	9.7912E-5	1
0N; 35N	288.61256	2.07867	0.7906	0
0N; 42N	1073.01964	5.84945	1.03574E-7	1
7N; 14N	36.52615	0.26816	1	0
7N; 21N	437.44737	3.20947	0.02793	1
7N; 28N	456.44901	2.95905	0.0648	0
7N; 35N	37.85428	0.27302	1	0
7N; 42N	822.26136	4.48609	1.52336E-4	1
14N; 21N	400.92122	2.92131	0.0732	0
14N; 28N	419.92286	2.70765	0.1423	0
14N; 35N	1.32812	0.00952	1	0
14N; 42N	785.7352	4.27048	4.09605E-4	1
21N; 28N	19.00164	0.12246	1	0
21N; 35N	-399.5931	-2.86117	0.08864	0
21N; 42N	384.81399	2.09073	0.76761	0
28N; 35N	-418.59474	-2.66225	0.163	0
28N; 42N	365.81234	1.85012	1	0
35N; 42N	784.40708	4.22168	5.09224E-4	1

Source: Author

Table 22: Post-hoc analysis for orientation angle of samples compacted at 600 MPa and sintered 1h at 1100°C

Pair of datasets	Mean Rank Diff	z	Prob	Sig
0N; 7N	153.85841	1.13573	1	0
0N; 14N	-105.03123	-0.76992	1	0
0N; 21N	82.28887	0.60282	1	0
0N; 28N	-265.04523	-1.71616	1	0
0N; 35N	-145.73705	-1.04958	1	0
0N; 42N	301.72042	1.6447	1	0
7N; 14N	-258.88964	-1.90054	1	0

Continues from table 22

Pair of datasets	Mean Rank Diff	z	Prob	Sig
7N; 21N	-71.56954	-0.52506	1	0
7N; 28N	-418.90363	-2.71549	0.13897	0
7N; 35N	-299.59545	-2.16069	0.6451	0
7N; 42N	147.86201	0.80666	1	0
14N; 21N	187.3201	1.36482	1	0
14N; 28N	-160.014	-1.0317	1	0
14N; 35N	-40.70582	-0.29163	1	0
14N; 42N	406.75165	2.21057	0.56838	0
21N; 28N	-347.3341	-2.23834	0.52917	0
21N; 35N	-228.02592	-1.63262	1	0
21N; 42N	219.43155	1.19212	1	0
28N; 35N	119.30818	0.75875	1	0
28N; 42N	566.76565	2.86629	0.08722	0
35N; 42N	447.45747	2.40807	0.33678	0

Source: Author

Table 23 presents the ANOVA for circularity, solidity and eccentricity of samples compacted at 200 MPa and sintered 1h at 1100°C

Table 23: ANOVA for circularity, solidity and eccentricity of samples compacted at 200 MPa and sintered 1h at 1100°C

		Circularity ANOVA		Solidity ANOVA		Eccentricity ANOVA	
Dataset	**N**	**Mean Rank**	**Sum Rank**	**Mean Rank**	**Sum Rank**	**Mean Rank**	**Sum Rank**
0	2350	11531.71809	2.70995E7	12205.51404	2.8683E7	11264.02511	2.64705E7
7	2434	11789.6668	2.8696E7	12037.27486	2.92987E7	12018.15489	2.92522E7
14	2779	11326.8172	3.14772E7	11527.45664	3.20348E7	12466.84581	3.46454E7
21	2790	11658.10663	3.25261E7	11659.19803	3.25292E7	12693.90072	3.5416E7
28	2248	12047.10254	2.70819E7	12079.74021	2.71553E7	12012.41281	2.70039E7
35	2632	12913.25665	3.39877E7	12757.81459	3.35786E7	12648.45745	3.32907E7
42	2504	13074.73662	3.27391E7	12848.98183	3.21739E7	12921.84944	3.23563E7
49	2439	13913.85404	3.39359E7	13608.28229	3.31906E7	13127.91923	3.2019E7
56	2198	13158.76206	2.8923E7	12891.46474	2.83354E7	13051.15946	2.86864E7
63	2300	13605.65891	3.1293E7	13388.00261	3.07924E7	13039.30304	2.99904E7
70	382	16111.47644	6.15458E6	16079.38743	6.14233E6	12521.74084	4.78331E6
	DF	**Chi-Square**	**Prob>Chi-Square**	**Chi-Square**	**Prob>Chi-Square**	**Chi-Square**	**Prob>Chi-Square**
	10	469.70729	1.302E-94	310.07687	1.149E-60	144.86501	4.235E-26

Source: Author

Tables 24, 25 and 26 presents the post-hoc analyses for circularity, solidity and eccentricity of samples compacted at 200 MPa and sintered 1h at 1100°C.

Table 24: Post-hoc analysis for circularity in samples compacted at 200 MPa and sintered 1h at 1100°C

Pairs of datasets	**Mean Rank Diff**	**z**	**Prob**	**Sig**
0N; 7N	-257.94872	-1.23311	1	0
0N; 14N	204.90088	1.01082	1	0
0N; 21N	-126.38855	-0.62407	1	0
0N; 28N	-515.38445	-2.41518	0.86501	0
0N; 35N	-1381.53856	-6.72989	9.33825E-10	1
0N; 42N	-1543.01854	-7.4275	6.08689E-12	1
0N; 49N	-2382.13595	-11.39342	2.4801E-28	1
0N; 56N	-1627.04397	-7.58066	1.8909E-12	1
0N; 63N	-2073.94083	-9.77548	7.8914E-21	1
0N; 70N	-4579.75835	-11.47726	9.44036E-29	1
7N; 14N	462.8496	2.305	1	0
7N; 21N	131.56017	0.65578	1	0
7N; 28N	-257.43573	-1.2167	1	0
7N; 35N	-1123.58985	-5.52394	1.82318E-6	1
7N; 42N	-1285.06982	-6.24164	2.38151E-8	1
7N; 49N	-2124.18723	-10.25017	6.49758E-23	1
7N; 56N	-1369.09525	-6.43271	6.89434E-9	1
7N; 63N	-1815.99211	-8.63365	3.26846E-16	1
7N; 70N	-4321.80964	-10.85704	1.01549E-25	1
14N; 21N	-331.28943	-1.70897	1	0
14N; 28N	-720.28534	-3.51045	0.0246	1
14N; 35N	-1586.43945	-8.06384	4.06623E-14	1
14N; 42N	-1747.91942	-8.77027	9.80348E-17	1
14N; 49N	-2587.03684	-12.89054	2.7989E-36	1
14N; 56N	-1831.94486	-8.87272	3.92584E-17	1
14N; 63N	-2278.84171	-11.17644	2.92497E-27	1
14N; 70N	-4784.65924	-12.1223	4.42592E-32	1
21N; 28N	-388.9959	-1.89752	1	0
21N; 35N	-1255.15002	-6.38603	9.36345E-9	1
21N; 42N	-1416.62999	-7.11466	6.17055E-11	1
21N; 49N	-2255.74741	-11.25018	1.2712E-27	1
21N; 56N	-1500.65543	-7.27451	1.9122E-11	1
21N; 63N	-1947.55228	-9.56019	6.46481E-20	1
21N; 70N	-4453.36981	-11.28564	8.49826E-28	1
28N; 35N	-866.15411	-4.16962	0.00168	1
28N; 42N	-1027.63409	-4.88974	5.55329E-5	1

Continues from table 24

Pairs of datasets	Mean Rank Diff	z	Prob	Sig
28N; 49N	-1866.7515	-8.827	5.91345E-17	1
28N; 56N	-1111.65952	-5.12353	1.64927E-5	1
28N; 63N	-1558.55638	-7.26515	2.04944E-11	1
28N; 70N	-4064.3739	-10.1535	1.75826E-22	1
35N; 42N	-161.47997	-0.79972	1	0
35N; 49N	-1000.59739	-4.92189	4.71426E-5	1
35N; 56N	-245.50541	-1.17467	1	0
35N; 63N	-692.40226	-3.3537	0.04386	1
35N; 70N	-3198.21979	-8.07573	3.68923E-14	1
42N; 49N	-839.11742	-4.07775	0.0025	1
42N; 56N	-84.02544	-0.39744	1	0
42N; 63N	-530.92229	-2.54145	0.60717	0
42N; 70N	-3036.73982	-7.64326	1.16487E-12	1
49N; 56N	755.09198	3.54953	0.02123	1
49N; 63N	308.19513	1.46596	1	0
49N; 70N	-2197.6224	-5.52153	1.84835E-6	1
56N; 63N	-446.89686	-2.07131	1	0
56N; 70N	-2952.71438	-7.36423	9.79949E-12	1
63N; 70N	-2505.81753	-6.27026	1.98239E-8	1

Source: Author

Table 25: Post-hoc analysis for solidity in samples compacted at 200 MPa and sintered 1h at 1100°C

Pairs of datasets	Mean Rank Diff	z	Prob	Sig
0N; 7N	168.23919	0.80426	1	0
0N; 14N	678.0574	3.34502	0.04525	1
0N; 21N	546.31601	2.69754	0.38419	0
0N; 28N	125.77383	0.5894	1	0
0N; 35N	-552.30055	-2.69042	0.39249	0
0N; 42N	-643.46779	-3.09741	0.10737	0
0N; 49N	-1402.76825	-6.70924	1.07599E-9	1
0N; 56N	-685.9507	-3.19596	0.07665	0
0N; 63N	-1182.48857	-5.57364	1.37213E-6	1
0N; 70N	-3873.87339	-9.70825	1.52939E-20	1
7N; 14N	509.81822	2.5389	0.6116	0
7N; 21N	378.07683	1.88456	1	0
7N; 28N	-42.46536	-0.2007	1	0
7N; 35N	-720.53973	-3.54241	0.02181	1

Continues from table 25

Pairs of datasets	Mean Rank Diff	z	Prob	Sig
7N; 49N	-1571.00743	-7.58082	1.8885E-12	1
7N; 56N	-854.18988	-4.01342	0.00329	1
7N; 63N	-1350.72775	-6.42167	7.41319E-9	1
7N; 70N	-4042.11258	-10.1544	1.74213E-22	1
14N; 21N	-131.74139	-0.6796	1	0
14N; 28N	-552.28357	-2.69166	0.39103	0
14N; 35N	-1230.35795	-6.25389	2.20195E-8	1
14N; 42N	-1321.52519	-6.63081	1.83613E-9	1
14N; 49N	-2080.82565	-10.36822	1.90255E-23	1
14N; 56N	-1364.0081	-6.60635	2.16653E-9	1
14N; 63N	-1860.54597	-9.12493	3.94789E-18	1
14N; 70N	-4551.9308	-11.53266	4.96684E-29	1
21N; 28N	-420.54218	-2.0514	1	0
21N; 35N	-1098.61656	-5.58961	1.25168E-6	1
21N; 42N	-1189.7838	-5.97538	1.26254E-7	1
21N; 49N	-1949.08426	-9.72074	1.35287E-20	1
21N; 56N	-1232.26671	-5.97348	1.27732E-7	1
21N; 63N	-1728.80458	-8.4864	1.1723E-15	1
21N; 70N	-4420.18941	-11.20156	2.20351E-27	1
28N; 35N	-678.07438	-3.26422	0.06037	0
28N; 42N	-769.24162	-3.66024	0.01386	1
28N; 49N	-1528.54207	-7.22777	2.70047E-11	1
28N; 56N	-811.72453	-3.74116	0.01007	1
28N; 63N	-1308.2624	-6.09841	5.89191E-8	1
28N; 70N	-3999.64722	-9.9918	9.10478E-22	1
35N; 42N	-91.16724	-0.4515	1	0
35N; 49N	-850.4677	-4.18341	0.00158	1
35N; 56N	-133.65015	-0.63947	1	0
35N; 63N	-630.18802	-3.05236	0.12488	0
35N; 70N	-3321.57284	-8.3872	2.7382E-15	1
42N; 49N	-759.30046	-3.68988	0.01234	1
42N; 56N	-42.48291	-0.20094	1	0
42N; 63N	-539.02078	-2.58021	0.54307	0
42N; 70N	-3230.40561	-8.1307	2.34748E-14	1
49N; 56N	716.81755	3.36961	0.0414	1
49N; 63N	220.27968	1.04778	1	0
49N; 70N	-2471.10515	-6.20865	2.9392E-8	1
56N; 63N	-496.53787	-2.30139	1	0
56N; 70N	-3187.92269	-7.95085	1.01878E-13	1
63N; 70N	-2691.38483	-6.73461	9.04054E-10	1

Source: Author

Table 26: Post-hoc analysis for eccentricity in samples compacted at 200 MPa and sintered 1h at 1100°C

Pairs of datasets	Mean Rank Diff	z	Prob	Sig
0N; 7N	-754.12978	-3.60508	0.01716	1
0N; 14N	-1202.8207	-5.9338	1.628E-7	1
0N; 21N	-1429.87561	-7.0603	9.13811E-11	1
0N; 28N	-748.38771	-3.50707	0.02492	1
0N; 35N	-1384.43234	-6.74399	8.47519E-10	1
0N; 42N	-1657.82433	-7.98013	8.0399E-14	1
0N; 49N	-1863.89412	-8.91474	2.6892E-17	1
0N; 56N	-1787.13436	-8.32655	4.57788E-15	1
0N; 63N	-1775.27794	-8.36774	3.23048E-15	1
0N; 70N	-1257.71573	-3.15194	0.0892	0
7N; 14N	-448.69092	-2.23449	1	0
7N; 21N	-675.74583	-3.36833	0.04159	1
7N; 28N	5.74208	0.02714	1	0
7N; 35N	-630.30256	-3.09877	0.10688	0
7N; 42N	-903.69455	-4.38929	6.25482E-4	1
7N; 49N	-1109.76434	-5.35512	4.70256E-6	1
7N; 56N	-1033.00457	-4.85358	6.66884E-5	1
7N; 63N	-1021.14815	-4.85477	6.62881E-5	1
7N; 70N	-503.58595	-1.26508	1	0
14N; 21N	-227.05491	-1.17128	1	0
14N; 28N	454.433	2.21477	1	0
14N; 35N	-181.61164	-0.92313	1	0
14N; 42N	-455.00363	-2.283	1	0
14N; 49N	-661.07342	-3.29396	0.05433	0
14N; 56N	-584.31366	-2.83003	0.25599	0
14N; 63N	-572.45724	-2.80758	0.27453	0
14N; 70N	-54.89503	-0.13908	1	0
21N; 28N	681.48791	3.32429	0.04875	1
21N; 35N	45.44327	0.23121	1	0
21N; 42N	-227.94872	-1.14481	1	0
21N; 49N	-434.01851	-2.1646	1	0
21N; 56N	-357.25875	-1.73183	1	0
21N; 63N	-345.40233	-1.69552	1	0
21N; 70N	172.15988	0.43628	1	0
28N; 35N	-636.04464	-3.06189	0.12097	0
28N; 42N	-909.43663	-4.32733	8.30112E-4	1
28N; 49N	-1115.50642	-5.27471	7.313E-6	1

Continues from table 26

Pairs of datasets	Mean Rank Diff	z	Prob	Sig
28N; 56N	-1038.74665	-4.78748	9.28879E-5	1
28N; 63N	-1026.89023	-4.78681	9.31998E-5	1
28N; 70N	-509.32803	-1.27239	1	0
35N; 42N	-273.39199	-1.35395	1	0
35N; 49N	-479.46178	-2.35845	1	0
35N; 56N	-402.70202	-1.9268	1	0
35N; 63N	-390.8456	-1.89309	1	0
35N; 70N	126.71661	0.31997	1	0
42N; 49N	-206.06979	-1.00141	1	0
42N; 56N	-129.31002	-0.61163	1	0
42N; 63N	-117.4536	-0.56223	1	0
42N; 70N	400.1086	1.00704	1	0
49N; 56N	76.75977	0.36083	1	0
49N; 63N	88.61619	0.42151	1	0
49N; 70N	606.17839	1.52302	1	0
56N; 63N	11.85642	0.05495	1	0
56N; 70N	529.41863	1.3204	1	0
63N; 70N	517.56221	1.29509	1	0

Source: Author

Table 27 presents the ANOVA for circularity, solidity and eccentricity of samples compacted at 400 MPa and sintered 1h at 1100°C.

Table 27: ANOVA for circularity, solidity and eccentricity of samples compacted at 400 MPa and sintered 1h at 1100°C

	Circularity ANOVA		Solidity ANOVA		Eccentricity ANOVA	
Dataset	**Mean Rank**	**Sum Rank**	**Mean Rank**	**Sum Rank**	**Mean Rank**	**Sum Rank**
0	12750.692	3.31901E7	12887.621	3.35465E7	12941.410	3.36865E7
7	12692.859	3.77993E7	12927.513	3.84981E7	12601.886	3.75284E7
14	13349.634	4.31327E7	13379.020	4.32276E7	13199.425	4.26473E7
21	12775.217	3.19891E7	12944.693	3.24135E7	12550.976	3.14276E7
28	13227.311	3.74597E7	13145.311	3.72275E7	13551.875	3.83789E7
35	13228.823	3.77154E7	13055.508	3.72213E7	13375.135	3.81325E7
42	13927.494	3.89552E7	13714.176	3.83586E7	13697.205	3.83111E7
49	13294.870	3.25325E7	13225.184	3.2362E7	13295.482	3.2534E7
56	13533.107	3.1884E7	13537.423	3.18942E7	13485.539	3.17719E7
63	13836.389	2.61093E7	13788.061	2.60181E7	13963.412	2.6349E7
	Chi-Square	**Prob>Chi-Square**	**Chi-Square**	**Prob>Chi-Square**	**Chi-Square**	**Prob>Chi-Square**
	73.55431	3.045E-12	41.42185	4.174E-6	80.18565	1.485E-13

Source: Author

Tables 28, 29 and 30 present the post-hoc analyses for circularity, solidity and eccentricity of samples compacted at 400 MPa and sintered 1h at 1100°C.

Table 28: Post-hoc analysis for circularity in samples compacted at 400 MPa and sintered 1h at 1100°C

Pairs of datasets	**Mean Rank Diff**	**z**	**Prob**	**Sig**
0N; 7N	57.83302	0.28189	1	0
0N; 14N	-598.94197	-2.97422	0.13218	0
0N; 21N	-24.52459	-0.11459	1	0
0N; 28N	-476.61843	-2.29573	0.97611	0
0N; 35N	-478.13073	-2.3067	0.94822	0
0N; 42N	-1176.80144	-5.6514	7.16178E-7	1
0N; 49N	-544.178	-2.52764	0.51674	0
0N; 56N	-782.41472	-3.59858	0.0144	1
0N; 63N	-1085.69711	-4.6965	1.19094E-4	1

Continues from table 28

Pairs of datasets	Mean Rank Diff	z	Prob	Sig
7N; 14N	-656.775	-3.38145	0.03245	1
7N; 21N	-82.35762	-0.39726	1	0
7N; 28N	-534.45145	-2.66315	0.34836	0
7N; 35N	-535.96376	-2.67526	0.33602	0
7N; 42N	-1234.63446	-6.13249	3.89307E-8	1
7N; 49N	-602.01102	-2.88569	0.17575	0
7N; 56N	-840.24775	-3.98563	0.00303	1
7N; 63N	-1143.53013	-5.08301	1.67179E-5	1
14N; 21N	574.41738	2.82171	0.21496	0
14N; 28N	122.32355	0.62151	1	0
14N; 35N	120.81124	0.61492	1	0
14N; 42N	-577.85947	-2.92628	0.15437	0
14N; 49N	54.76398	0.26727	1	0
14N; 56N	-183.47275	-0.88574	1	0
14N; 63N	-486.75514	-2.19726	1	0
21N; 28N	-452.09384	-2.15551	1	0
21N; 35N	-453.60614	-2.16611	1	0
21N; 42N	-1152.27685	-5.47782	1.93774E-6	1
21N; 49N	-519.65341	-2.39093	0.75625	0
21N; 56N	-757.89013	-3.4535	0.0249	1
21N; 63N	-1061.17252	-4.55275	2.38276E-4	1
28N; 35N	-1.51231	-0.00746	1	0
28N; 42N	-700.18301	-3.43522	0.02664	1
28N; 49N	-67.55957	-0.32014	1	0
28N; 56N	-305.7963	-1.43428	1	0
28N; 63N	-609.07868	-2.68069	0.33061	0
35N; 42N	-698.67071	-3.43349	0.02681	1
35N; 49N	-66.04726	-0.31346	1	0
35N; 56N	-304.28399	-1.42935	1	0
35N; 63N	-607.56638	-2.67761	0.33368	0
42N; 49N	632.62344	2.98912	0.1259	0
42N; 56N	394.38672	1.84456	1	0
42N; 63N	91.10433	0.39997	1	0
49N; 56N	-238.23673	-1.0795	1	0
49N; 63N	-541.51911	-2.31174	0.93565	0
56N; 63N	-303.28239	-1.28396	1	0

Source: Author

Table 29: Post-hoc analysis for solidity in samples compacted at 400 MPa and sintered 1h at 1100°C

Pairs of datasets	Mean Rank Diff	z	Prob	Sig
0N; 7N	-39.89148	-0.19444	1	0
0N; 14N	-491.39864	-2.44018	0.66059	0
0N; 21N	-57.07211	-0.26666	1	0
0N; 28N	-257.69001	-1.24122	1	0
0N; 35N	-167.88716	-0.80996	1	0
0N; 42N	-826.55519	-3.9694	0.00324	1
0N; 49N	-337.56232	-1.56794	1	0
0N; 56N	-649.80139	-2.98865	0.1261	0
0N; 63N	-900.43969	-3.89512	0.00442	1
7N; 14N	-451.50716	-2.32461	0.90417	0
7N; 21N	-17.18063	-0.08287	1	0
7N; 28N	-217.79853	-1.08528	1	0
7N; 35N	-127.99568	-0.63889	1	0
7N; 42N	-786.66371	-3.9074	0.0042	1
7N; 49N	-297.67084	-1.42686	1	0
7N; 56N	-609.90991	-2.89305	0.17169	0
7N; 63N	-860.54821	-3.82515	0.00588	1
14N; 21N	434.32654	2.13354	1	0
14N; 28N	233.70863	1.18744	1	0
14N; 35N	323.51148	1.64664	1	0
14N; 42N	-335.15655	-1.69723	1	0
14N; 49N	153.83632	0.75078	1	0
14N; 56N	-158.40275	-0.76471	1	0
14N; 63N	-409.04105	-1.84645	1	0
21N; 28N	-200.6179	-0.95651	1	0
21N; 35N	-110.81505	-0.52918	1	0
21N; 42N	-769.48309	-3.65805	0.01144	1
21N; 49N	-280.49021	-1.29054	1	0
21N; 56N	-592.72929	-2.7009	0.31118	0
21N; 63N	-843.36758	-3.6183	0.01334	1
28N; 35N	89.80285	0.4427	1	0
28N; 42N	-568.86518	-2.79095	0.23649	0
28N; 49N	-79.87231	-0.37849	1	0
28N; 56N	-392.11138	-1.83912	1	0
28N; 63N	-642.74968	-2.82889	0.2102	0
35N; 49N	-169.67516	-0.80527	1	0
35N; 56N	-481.91423	-2.26375	1	0
35N; 63N	-732.55253	-3.22843	0.05601	0

Continues from table 29

Pairs of datasets	Mean Rank Diff	z	Prob	Sig
35N; 42N	-658.66803	-3.23691	0.05437	0
42N; 49N	488.99287	2.31047	0.93879	0
42N; 56N	176.7538	0.82668	1	0
42N; 63N	-73.8845	-0.32437	1	0
49N; 56N	-312.23907	-1.41482	1	0
49N; 63N	-562.87737	-2.40291	0.73192	0
56N; 63N	-250.6383	-1.06109	1	0

Source: Author

Table 30: Post-hoc analysis for eccentricity in samples compacted at 400 MPa and sintered 1h at 1100°C

Pairs of datasets	Mean Rank Diff	z	Prob	Sig
0N; 7N	339.5243	1.65493	1	0
0N; 14N	-258.015	-1.28125	1	0
0N; 21N	390.43426	1.82425	1	0
0N; 28N	-610.46559	-2.94043	0.14749	0
0N; 35N	-433.72527	-2.09247	1	0
0N; 42N	-755.79528	-3.62958	0.01277	1
0N; 49N	-354.07254	-1.64462	1	0
0N; 56N	-544.12918	-2.50262	0.55474	0
0N; 63N	-1022.0022	-4.42097	4.4216E-4	1
7N; 14N	-597.53972	-3.07647	0.09426	0
7N; 21N	50.90996	0.24557	1	0
7N; 28N	-949.98989	-4.73376	9.91808E-5	1
7N; 35N	-773.24957	-3.85967	0.00511	1
7N; 42N	-1095.3958	-5.44051	2.39079E-6	1
7N; 49N	-693.59684	-3.3247	0.03983	1
7N; 56N	-883.65348	-4.19152	0.00125	1
7N; 63N	-1361.5266	-6.052	6.43756E-8	1
14N; 21N	648.44968	3.18538	0.06505	0
14N; 28N	-352.45016	-1.79075	1	0
14N; 35N	-175.70985	-0.89435	1	0
14N; 42N	-497.77986	-2.52076	0.52696	0
14N; 49N	-96.05712	-0.4688	1	0
14N; 56N	-286.11375	-1.38125	1	0
14N; 63N	-763.98684	-3.44871	0.02535	1
21N; 28N	-1000.8998	-4.77213	8.20282E-5	1
21N; 35N	-824.15953	-3.93562	0.00373	1
21N; 42N	-1146.2294	-5.44907	2.27856E-6	1
21N; 49N	-744.5068	-3.42549	0.02762	1

Continues from table 30

Pairs of datasets	Mean Rank Diff	z	Prob	Sig
21N; 56N	-934.56344	-4.25855	9.25917E-4	1
21N; 63N	-1412.4362	-6.05977	6.13411E-8	1
28N; 35N	176.74032	0.87128	1	0
28N; 42N	-145.32969	-0.71301	1	0
28N; 49N	256.39305	1.21495	1	0
28N; 56N	66.33641	0.31114	1	0
28N; 63N	-411.53668	-1.81127	1	0
35N; 42N	-322.07001	-1.58276	1	0
35N; 49N	79.65273	0.37803	1	0
35N; 56N	-110.40391	-0.51861	1	0
35N; 63N	-588.27699	-2.5926	0.42864	0
42N; 49N	401.72274	1.89812	1	0
42N; 56N	211.6661	0.98997	1	0
42N; 63N	-266.20698	-1.16872	1	0
49N; 56N	-190.05664	-0.86119	1	0
49N; 63N	-667.92972	-2.85138	0.19588	0
56N; 63N	-477.87309	-2.02309	1	0

Source: Author

Table 31 presents the ANOVA for circularity, solidity and eccentricity of samples compacted at 400 MPa and sintered 1h at 1200°C.

Table 31: ANOVA for circularity, solidity and eccentricity of samples compacted at 400 MPa and sintered 1h at 1200°C

	Circularity ANOVA		Solidity ANOVA		Eccentricity ANOVA	
Dataset	Mean Rank	Sum Rank	Mean Rank	Sum Rank	Mean Rank	Sum Rank
0	12274.147	3.69943E7	12348.097	3.72172E7	12425.986	3.74519E7
7	12625.695	3.50742E7	12787.502	3.55237E7	12243.704	3.4013E7
14	12551.736	3.34378E7	12588.971	3.3537E7	12313.442	3.2803E7
21	12642.528	3.29338E7	12637.598	3.29209E7	12632.744	3.29083E7
28	12466.919	3.55058E7	12421.099	3.53753E7	12673.221	3.60933E7
35	12447.936	3.53646E7	12353.624	3.50966E7	13012.684	3.6969E7
42	12088.350	3.30133E7	12116.642	3.30906E7	12770.074	3.48751E7
49	12551.442	3.02364E7	12497.723	3.0107E7	13032.531	3.13954E7
56	13670.494	3.00204E7	13569.370	2.97983E7	13088.484	2.87423E7
63	14786.830	1.86166E7	14718.453	1.85305E7	12665.458	1.59458E7
	Chi-Square	Prob>Chi-Square	Chi-Square	Prob>Chi-Square	Chi-Square	Prob>Chi-Square
	178.93203	8.466E-34	164.35671	9.227E-31	39.0153	1.144E-5

Source: Author

Tables 32, 33 and 34 present the post-hoc analyses for circularity, solidity and eccentricity of samples compacted at 400 MPa and sintered 1h at 1200°C.

Table 32: Post-hoc analysis for circularity in samples compacted at 400 MPa and sintered 1h at 1200°C

Pair of datasets	**Mean Rank Diff**	**z**	**Prob**	**Sig**
0N; 7N	-351.54868	-1.82683	1	0
0N; 14N	-277.58915	-1.4267	1	0
0N; 21N	-368.38184	-1.88206	1	0
0N; 28N	-192.77192	-1.00821	1	0
0N; 35N	-173.78985	-0.90836	1	0
0N; 42N	185.79673	0.9612	1	0
0N; 49N	-277.29557	-1.38677	1	0
0N; 56N	-1396.346	-6.80224	4.638E-10	1
0N; 63N	-2512.688	-10.234	6.2835E-23	1
7N; 14N	73.95953	0.37277	1	0
7N; 21N	-16.83316	-0.08436	1	0
7N; 28N	158.77676	0.81379	1	0
7N; 35N	177.75883	0.91053	1	0
7N; 42N	537.3454	2.72542	0.28899	0
7N; 49N	74.25311	0.36453	1	0
7N; 56N	-1044.798	-5	2.56732E-5	1
7N; 63N	-2161.1342	-8.69403	1.5713E-16	1
14N; 21N	-90.79268	-0.45035	1	0
14N; 28N	84.81723	0.43009	1	0
14N; 35N	103.7993	0.52603	1	0
14N; 42N	463.38588	2.32576	0.90141	0
14N; 49N	0.29358	0.00143	1	0
14N; 56N	-1118.7577	-5.30507	5.06839E-6	1
14N; 63N	-2235.0933	-8.93216	1.8803E-17	1
21N; 28N	175.60992	0.88531	1	0

Continues from table 32

Pair of datasets	Mean Rank Diff	z	Prob	Sig
21N; 35N	194.59199	0.98043	1	0
21N; 42N	554.17856	2.76564	0.25565	0
21N; 49N	91.08627	0.44043	1	0
21N; 56N	-1027.9651	-4.84978	5.56185E-5	1
21N; 63N	-2144.3010	-8.53834	6.1272E-16	1
28N; 35N	18.98207	0.09784	1	0
28N; 42N	378.56864	1.93191	1	0
28N; 49N	-84.52365	-0.41734	1	0
28N; 56N	-1203.575	-5.79244	3.121E-7	1
28N; 63N	-2319.910	-9.36875	3.3029E-19	1
35N; 42N	359.58657	1.83394	1	0
35N; 49N	-103.50572	-0.51077	1	0
35N; 56N	-1222.557	-5.88064	1.83906E-7	1
35N; 63N	-2338.893	-9.44184	1.648E-19	1
42N; 49N	-463.09229	-2.26441	1	0
42N; 56N	-1582.143	-7.54434	2.045E-12	1
42N; 63N	-2698.4796	-10.8267	1.157E-25	1
49N; 56N	-1119.051	-5.18393	9.77638E-6	1
49N; 63N	-2235.3873	-8.78535	7.014E-17	1
56N; 63N	-1116.335	-4.31608	7.14704E-4	1

Source: Author

Table 33: Post-hoc analysis for solidity in samples compacted at 400 MPa and sintered 1h at 1200°C

Pair of datasets	Mean Rank Diff	z	Prob	Sig
0N; 7N	-439.40547	-2.28338	1	0
0N; 14N	-240.87424	-1.238	1	0
0N; 21N	-289.5018	-1.47906	1	0
0N; 28N	-73.0025	-0.38181	1	0
0N; 35N	-5.5272	-0.02889	1	0
0N; 42N	231.45424	1.19741	1	0
0N; 49N	-149.62607	-0.74829	1	0
0N; 56N	-1221.27317	-5.94938	1,21E-02	1
0N; 63N	-2370.35609	-9.65431	2,12E-15	1
7N; 14N	198.53124	1.00063	1	0
7N; 21N	149.90367	0.75121	1	0
7N; 28N	366.40298	1.87795	1	0
7N; 35N	433.87827	2.22244	1	0
7N; 42N	670.85971	3.40261	0.03004	1
7N; 49N	289.7794	1.4226	1	0
7N; 56N	-781.8677	-3.74242	0.0082	1
7N; 63N	-1930.95062	-7.76802	3,59E-08	1
14N; 21N	-48.62756	-0.2412	1	0
14N; 28N	167.87174	0.85124	1	0
14N; 35N	235.34703	1.19268	1	0
14N; 42N	472.32848	2.37064	0.79907	0
14N; 49N	91.24816	0.44357	1	0
14N; 56N	-980.39893	-4.64898	1,50E+00	1
14N; 63N	-2129.48185	-8.5101	7,82E-11	1
21N; 28N	216.4993	1.09145	1	0
21N; 35N	283.9746	1.43077	1	0
21N; 42N	520.95604	2.59985	0.41969	0
21N; 49N	139.87573	0.67634	1	0
21N; 56N	-931.77137	-4.39596	4,96E+01	1
21N; 63N	-2080.85429	-8.28571	5,28E-10	1
28N; 35N	67.47529	0.34779	1	0
28N; 42N	304.45674	1.5537	1	0
28N; 49N	-76.62358	-0.37833	1	0
28N; 56N	-1148.27068	-5.52628	1,47E-01	1
28N; 63N	-2297.35359	-9.27765	7,80E-15	1
35N; 42N	236.98145	1.20863	1	0
35N; 49N	-144.09887	-0.71109	1	0
35N; 56N	-1215.74597	-5.84788	2,24E-02	1
35N; 63N	-2364.82889	-9.54654	6,03E-15	1
42N; 49N	-381.08032	-1.86339	1	0

Continues from table 33

Pair of datasets	Mean Rank Diff	z	Prob	Sig
42N; 56N	-1452.72741	-6.92723	1,93E-06	1
49N; 63N	-2220.73002	-8.72775	1,17E-11	1
56N; 63N	-1149.08292	-4.44269	4,00E+01	1

Source: Author

Table 34: Post-hoc analysis for eccentricity in samples compacted at 400 MPa and sintered 1h at 1200°C

Pair of datasets	Mean Rank Diff	z	Prob	Sig
0N; 7N	182.28141	0.94723	1	0
0N; 14N	112.54366	0.57843	1	0
0N; 21N	-206.75849	-1.05633	1	0
0N; 28N	-247.23568	-1.29306	1	0
0N; 35N	-586.69839	-3.06654	0.09745	0
0N; 42N	-344.08847	-1.78011	1	0
0N; 49N	-606.54511	-3.03335	0.10883	0
0N; 56N	-662.49851	-3.22733	0.05623	0
0N; 63N	-239.47207	-0.97535	1	0
7N; 14N	-69.73774	-0.35149	1	0
7N; 21N	-389.0399	-1.94958	1	0
7N; 28N	-429.51709	-2.20144	1	0
7N; 35N	-768.97979	-3.93892	0.00368	1
7N; 42N	-526.36987	-2.66975	0.34158	0
7N; 49N	-788.82652	-3.87256	0.00485	1
7N; 56N	-844.77992	-4.04355	0.00237	1
7N; 63N	-421.75348	-1.69667	1	0
14N; 21N	-319.30215	-1.58379	1	0
14N; 28N	-359.77934	-1.82435	1	0
14N; 35N	-699.24205	-3.54357	0.01776	1
14N; 42N	-456.63213	-2.29186	0.98611	0
14N; 49N	-719.08877	-3.49563	0.02128	1
14N; 56N	-775.04218	-3.67519	0.0107	1
14N; 63N	-352.01573	-1.40677	1	0
21N; 28N	-40.47719	-0.20406	1	0
21N; 35N	-379.9399	-1.91428	1	0
21N; 42N	-137.32998	-0.68535	1	0
21N; 49N	-399.78662	-1.93307	1	0
21N; 56N	-455.74002	-2.15011	1	0
21N; 63N	-32.71358	-0.13026	1	0

Continues from table 34

Pair of datasets	Mean Rank Diff	z	Prob	Sig
28N; 35N	-339.46271	-1.74972	1	0
28N; 42N	-96.85279	-0.49426	1	0
28N; 49N	-359.30943	-1.7741	1	0
28N; 56N	-415.26283	-1.99853	1	0
28N; 63N	7.76361	0.03135	1	0
35N; 42N	242.60992	1.23734	1	0
35N; 49N	-19.84672	-0.09794	1	0
35N; 56N	-75.80013	-0.36461	1	0
35N; 63N	347.22632	1.40171	1	0
42N; 49N	-262.45664	-1.28335	1	0
42N; 56N	-318.41005	-1.51832	1	0
42N; 63N	104.6164	0.41974	1	0
49N; 56N	-55.9534	-0.2592	1	0
49N; 63N	367.07304	1.44264	1	0
56N; 63N	423.02644	1.63554	1	0

Source: Author

Table 35 presents the ANOVA for circularity, solidity and eccentricity of samples compacted at 600 MPa and sintered 1h at 1200°C.

Table 35: ANOVA for circularity, solidity and eccentricity of samples compacted at 600 MPa and sintered 1h at 1100°C

	Circularity ANOVA		Solidity ANOVA		Eccentricity ANOVA	
Dataset	Mean Rank	Sum Rank	Mean Rank	Sum Rank	Mean Rank	Sum Rank
0	9216.4216	2.94557E7	9191.898	2.93773E7	9092.6880	2.90602E7
7	9249.1471	2.9736E7	9241.0328	2.97099E7	9347.1398	3.00511E7
14	9314.9120	2.91277E7	9291.7494	2.90553E7	9458.4705	2.95766E7
21	9664.8719	3.01447E7	9605.3533	2.99591E7	9518.9459	2.96896E7
28	9589.9315	1.92566E7	9748.0963	1.95742E7	9565.0709	1.92067E7
35	9229.1692	2.69399E7	9276.7343	2.70788E7	9460.0561	2.76139E7
42	9829.0885	1.18244E7	9751.0299	1.17305E7	9382.3740	1.1287E7
	Chi-Square	Prob>Chi-Square	Chi-Square	Prob>Chi-Square	Chi-Square	Prob>Chi-Square
	27.22391	1.314E-4	27.98146	9.472E-5	14.63834	0.02326

Source: Author

Tables 36, 37 and 38 present the post-hoc analyses for circularity, solidity and eccentricity of samples compacted at 600 MPa and sintered 1h at 1100°C.

Table 36: Post-hoc analysis for circularity in samples compacted at 600 MPa and sintered 1h at 1100°C

Pair of datasets	Mean Rank Diff	z	Prob	Sig
0N; 7N	-32.7255	-0.24157	1	0
0N; 14N	-98.49044	-0.72197	1	0
0N; 21N	-448.45029	-3.28519	0.0214	1
0N; 28N	-373.5099	-2.41847	0.32731	0
0N; 35N	-12.74762	-0.09181	1	0
0N; 42N	-612.66691	-3.33968	0.01761	1
7N; 14N	-65.76493	-0.48279	1	0
7N; 21N	-415.72479	-3.04991	0.04807	1
7N; 28N	-340.7844	-2.20909	0.57053	0
7N; 35N	19.97789	0.14408	1	0
7N; 42N	-579.94141	-3.16385	0.0327	1
14N; 21N	-349.95986	-2.54983	0.22633	0
14N; 28N	-275.01947	-1.77321	1	0
14N; 35N	85.74282	0.61428	1	0
14N; 42N	-514.17647	-2.79439	0.1092	0
21N; 28N	74.94039	0.48294	1	0
21N; 35N	435.70268	3.11954	0.03804	1
21N; 42N	-164.21661	-0.89215	1	0
28N; 35N	360.76229	2.2943	0.45724	0
28N; 42N	-239.157	-1.20948	1	0
35N; 42N	-599.91929	-3.22857	0.02613	1

Source: Author

Table 37: Post-hoc analysis for solidity in samples compacted at 600 MPa and sintered 1h at 1100°C

Pair of datasets	Mean Rank Diff	z	Prob	Sig
0N; 7N	-49.13482	-0.3627	1	0
0N; 14N	-99.85144	-0.73195	1	0
0N; 21N	-413.45532	-3.02883	0.05156	0
0N; 28N	-556.19837	-3.60137	0.00665	1
0N; 35N	-84.83633	-0.61098	1	0
0N; 42N	-559.13193	-3.04786	0.0484	1
7N; 14N	-50.71663	-0.37232	1	0
7N; 21N	-364.3205	-2.67279	0.15797	0
7N; 28N	-507.06355	-3.28698	0.02127	1
7N; 35N	-35.70151	-0.25748	1	0

Continues from table 37

Pair of datasets	Mean Rank Diff	z	Prob	Sig
7N; 42N	-509.99711	-2.78227	0.11336	0
14N; 21N	-313.60388	-2.28493	0.46865	0
14N; 28N	-456.34692	-2.94234	0.06841	0
14N; 35N	15.01511	0.10757	1	0
14N; 42N	-459.28048	-2.49605	0.26373	0
21N; 28N	-142.74305	-0.91989	1	0
21N; 35N	328.61899	2.35284	0.39124	0
21N; 42N	-145.67661	-0.79142	1	0
28N; 35N	471.36204	2.99767	0.05713	0
28N; 42N	-2.93356	-0.01484	1	0
35N; 42N	-474.2956	-2.55251	0.2246	0

Source: Author

Table 38: Post-hoc analysis for eccentricity in samples compacted at 600 MPa and sintered 1h at 1100°C

Pair of datasets	Mean Rank Diff	z	Prob	Sig
0N; 7N	-254.45177	-1.87827	1	0
0N; 14N	-365.78253	-2.68133	0.15399	0
0N; 21N	-426.25793	-3.12262	0.03764	1
0N; 28N	-472.38292	-3.05867	0.04669	1
0N; 35N	-367.36814	-2.64573	0.17118	0
0N; 42N	-289.68602	-1.5791	1	0
7N; 14N	-111.33077	-0.81729	1	0
7N; 21N	-171.80616	-1.26043	1	0
7N; 28N	-217.93115	-1.41271	1	0
7N; 35N	-112.91637	-0.81436	1	0
7N; 42N	-35.23425	-0.19222	1	0
14N; 21N	-60.4754	-0.44063	1	0
14N; 28N	-106.60039	-0.68732	1	0
14N; 35N	-1.5856	-0.01136	1	0
14N; 42N	76.09651	0.41356	1	0
21N; 28N	-46.12499	-0.29725	1	0
21N; 35N	58.88979	0.42164	1	0
21N; 42N	136.57191	0.74196	1	0
28N; 35N	105.01478	0.66785	1	0
28N; 42N	182.6969	0.92395	1	0
35N; 42N	77.68212	0.41806	1	0

Source: Author

Determination of La and σ through Raman spectroscopy.

The data for La and σ obtained from the Raman spectra of the wear tracks and powders was normally distributed so conventional analyses of variance were used. The Fisher-SD test was used to perform the post-hoc analyses of the data. Table 39 shows the ANOVA for the La of graphite inside the wear tracks of samples compacted at 200, 400 and 600 MPa and sintered at 1100°C. In these analyses, if the Prob > F value is lower than 0.05, the means are different at the 0.05 level of significance.

Table 39: ANOVA for the La of graphite inside the wear tracks of samples compacted at 200, 400 and 600 MPa and sintered at 1100°C

	200 MPa – 1100°C		**400 MPa – 1100°C**		**600 MPa – 1100°C**	
Dataset	**Mean**	**Standard Deviation**	**Mean**	**Standard Deviation**	**Mean**	**Standard Deviation**
7N	14.258	5.97501	12.21711	1.66509	13.57057	2.71171
14N	14.80447	3.77163	11.56638	2.56187	11.58533	2.81701
21N	12.58777	2.76144	12.14876	2.24087	13.10079	2.68752
28N	13.38113	3.78761	14.17274	2.87698	11.37078	1.86169
35N	11.97755	2.98126	11.9071	3.09819	11.07917	2.40912
42N	12.72484	3.0726	12.75764	3.95364	12.92841	4.40694
49N	13.70681	4.67274	12.71533	1.70336		
56N	18.20119	4.77172	11.12485	3.49463		
63N	18.34546	5.85272	13.40813	3.60101		
70N	16.3984	4.85769				
	F Value	Prob>F	F Value	Prob>F	F Value	Prob>F
	1.89845	0.06979	0.88194	0.535	1.3941	0.23915

Source: Author

Table 40 shows the ANOVA for σ of graphite inside the wear tracks of samples compacted at 200, 400 and 600 MPa and sintered at 1100°C. As the means were significatively different, tables 41, 42 and 43 show the post-hoc analyses for these samples.

Table 40: ANOVA for σ of graphite inside the wear tracks of samples compacted at 200, 400 and 600 MPa and sintered at 1100°C

	200 MPa – 1100°C		**400 MPa – 1100°C**		**600 MPa – 1100°C**	
Dataset	**Mean**	**Standard Deviation**	**Mean**	**Standard Deviation**	**Mean**	**Standard Deviation**
7N	0.01487	0.00656	0.00821	0.0017	0.01803	0.01001
14N	0.01087	0.00581	0.01016	0.00304	0.02021	0.01444
21N	0.01273	0.00286	0.012	0.00392	0.01922	0.00716
28N	0.01662	0.00769	0.01319	0.00679	0.03308	0.01529
35N	0.01552	0.00492	0.01852	0.00892	0.02646	0.01152
42N	0.01991	0.01471	0.01411	0.00545	0.0306	0.00821
49N	0.02248	0.01044	0.01575	0.00365		
56N	0.02108	0.01171	0.01559	0.00662		
63N	0.03403	0.02197	0.02267	0.01028		
70N	0.03954	0.00784				
	F Value	Prob>F	F Value	Prob>F	F Value	Prob>F
	27.22391	1.314E-4	4.87027	5.408E-5	3.34665	0.00987

Source: Author

Table 41: Post-hoc analyses for the σ of graphite inside the wear tracks of the scuffing resistance tests performed on samples compacted at 200 MPa and sintered at 1100°C

Pair of datasets	**Mean Diff**	**Prob**	**Sig**
7N; 14N	0.004	0.47202	0
7N; 21N	0.00214	0.6885	0
7N; 28N	-0.00175	0.71337	0
7N; 35N	-6,50E+01	0.89493	0
7N; 42N	-0.00503	0.34737	0
7N; 49N	-0.0076	0.22748	0
7N; 56N	-0.00621	0.26631	0
7N; 63N	-0.01915	0.0017	1
7N; 70N	-0.02467	8,07E+00	1
14N; 21N	-0.00186	0.73748	0
14N; 28N	-0.00575	0.25213	0
14N; 35N	-0.00465	0.36839	0
14N; 42N	-0.00904	0.1076	0
14N; 49N	-0.01161	0.07569	0
14N; 56N	-0.01021	0.0804	0
14N; 63N	-0.02316	2,97E+01	1
14N; 70N	-0.02867	1,29E+00	1
21N; 28N	-0.00389	0.41444	0
21N; 35N	-0.00279	0.5711	0

Continues from table 41

Pair of datasets	Mean Diff	Prob	Sig
21N; 42N	-0.00718	0.18213	0
21N; 49N	-0.00974	0.12337	0
21N; 56N	-0.00835	0.13656	0
21N; 63N	-0.0213	5,45E+00	1
21N; 70N	-0.02681	2,25E+00	1
28N; 35N	0.0011	0.79782	0
28N; 42N	-0.00329	0.48947	0
28N; 49N	-0.00586	0.31193	0
28N; 56N	-0.00446	0.37304	0
28N; 63N	-0.01741	0.0017	1
28N; 70N	-0.02292	5,84E+00	1
35N; 42N	-0.00438	0.37453	0
35N; 49N	-0.00695	0.24211	0
35N; 56N	-0.00556	0.28345	0
35N; 63N	-0.0185	0.00122	1
35N; 70N	-0.02402	4,45E+00	1
42N; 49N	-0.00257	0.68202	0
42N; 56N	-0.00117	0.83273	0
42N; 63N	-0.01412	0.0184	1
42N; 70N	-0.01963	0.00132	1
49N; 56N	0.00139	0.82899	0
49N; 63N	-0.01155	0.08852	0
49N; 70N	-0.01707	0.01309	1
56N; 63N	-0.01295	0.03568	1
56N; 70N	-0.01846	0.00327	1
63N; 70N	-0.00552	0.38403	0

Source: Author

Table 42: Post-hoc analyses for the σ of graphite inside the wear tracks of the scuffing resistance tests performed on samples compacted at 400 MPa and sintered at 1100°C

Pair of datasets	Mean Diff	Prob	Sig
7N; 14N	-0.00195	0.507	0
7N; 21N	-0.00379	0.17435	0
7N; 28N	-0.00498	0.12527	0
7N; 35N	-0.01031	2,03E+00	1
7N; 42N	-0.0059	0.03322	1

Continues from table 42

Pair of datasets	Mean Diff	Prob	Sig
7N; 49N	-0.00754	0.01701	1
7N; 56N	-0.00738	0.0136	1
7N; 63N	-0.01446	3,80E-01	1
14N; 21N	-0.00184	0.49576	0
14N; 28N	-0.00302	0.33888	0
14N; 35N	-0.00836	0.00164	1
14N; 42N	-0.00394	0.13899	0
14N; 49N	-0.00559	0.06816	0
14N; 56N	-0.00543	0.06032	0
14N; 63N	-0.01251	3,22E+00	1
21N; 28N	-0.00119	0.69224	0
21N; 35N	-0.00652	0.00752	1
21N; 42N	-0.00211	0.39321	0
21N; 49N	-0.00375	0.19392	0
21N; 56N	-0.00359	0.18395	0
21N; 63N	-0.01067	1,43E+01	1
28N; 35N	-0.00533	0.06858	0
28N; 42N	-9,21E+01	0.75597	0
28N; 49N	-0.00257	0.43932	0
28N; 56N	-0.00241	0.44616	0
28N; 63N	-0.00949	0.00334	1
35N; 42N	0.00441	0.06221	0
35N; 49N	0.00277	0.31954	0
35N; 56N	0.00293	0.25855	0
35N; 63N	-0.00415	0.10993	0
42N; 49N	-0.00164	0.56234	0
42N; 56N	-0.00149	0.57534	0
42N; 63N	-0.00856	0.00168	1
49N; 56N	1,59E+01	0.95819	0
49N; 63N	-0.00692	0.02465	1
56N; 63N	-0.00708	0.01502	1

Source: Author

Table 43: Post-hoc analyses for the σ of graphite inside the wear tracks of the scuffing resistance tests performed on samples compacted at 600 MPa and sintered at 1100°C

Pair of datasets	**Mean Diff**	**Prob**	**Sig**
7N; 14N	-0.00414	0.41324	0
7N; 21N	0.00248	0.63527	0
7N; 28N	0.00663	0.23658	0
7N; 35N	-0.01138	0.03276	1
7N; 42N	-0.00723	0.19679	0
14N; 21N	-0.01386	0.01809	1
14N; 28N	-0.0104	0.02636	1
14N; 35N	-0.00625	0.21102	0
14N; 42N	-0.01288	0.01468	1
21N; 28N	9,81E+01	0.84886	0
21N; 35N	-0.01257	0.0054	1
21N; 42N	-0.00843	0.08112	0
28N; 35N	-0.01506	0.00342	1
28N; 42N	-0.0012	0.80929	0
35N; 42N	-0.00218	0.61091	0

APPENDIX B – ADDITIONAL PLOTS AND ANALYSES

Figures 109, 110 and 111 shows the histograms of the Feret diameter as a function of load in the scuffing resistance tests performed in samples compacted at 200, 400 and 600 MPa and sintered at 1100°C

Figure 109: Histograms of Feret diameter for specimens compacted at 200 MPa and sintered at 1100 °C after de scuffing resistance tests (a) and after the 7 (b), 14 (c), 21 (d), 28 (e), 35 (f), 42 (g), 49 (h), 56 (i), 63 (j) and 70N loads (k)

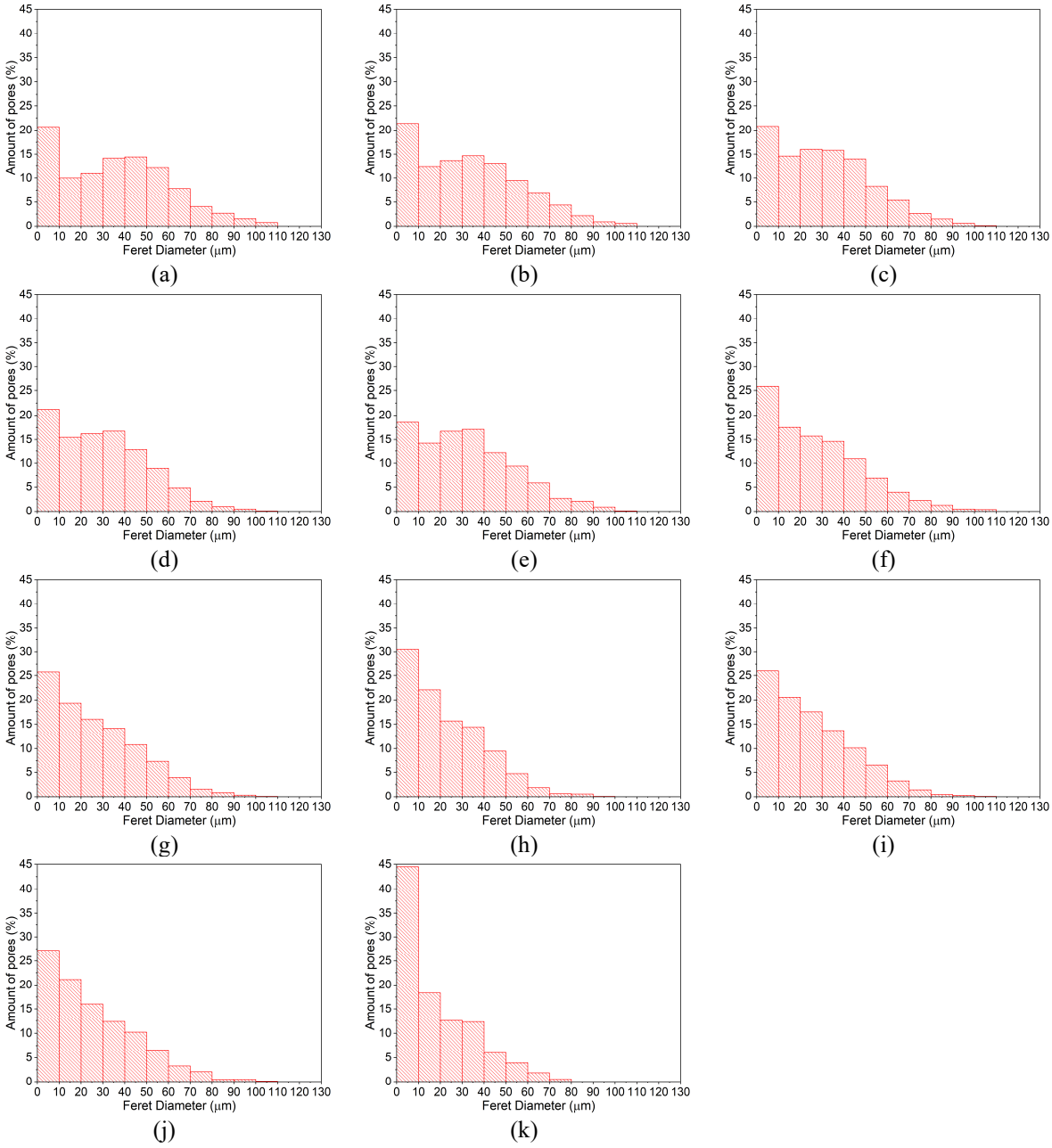

Source: Author

Figure 110: Histograms of Feret diameter for specimens compacted at 200 MPa and sintered at 1100 °C after de scuffing resistance tests (a) and after the 7 (b), 14 (c), 21 (d), 28 (e), 35 (f), 42 (g), 49 (h), 56 (i), 63N loads (j)

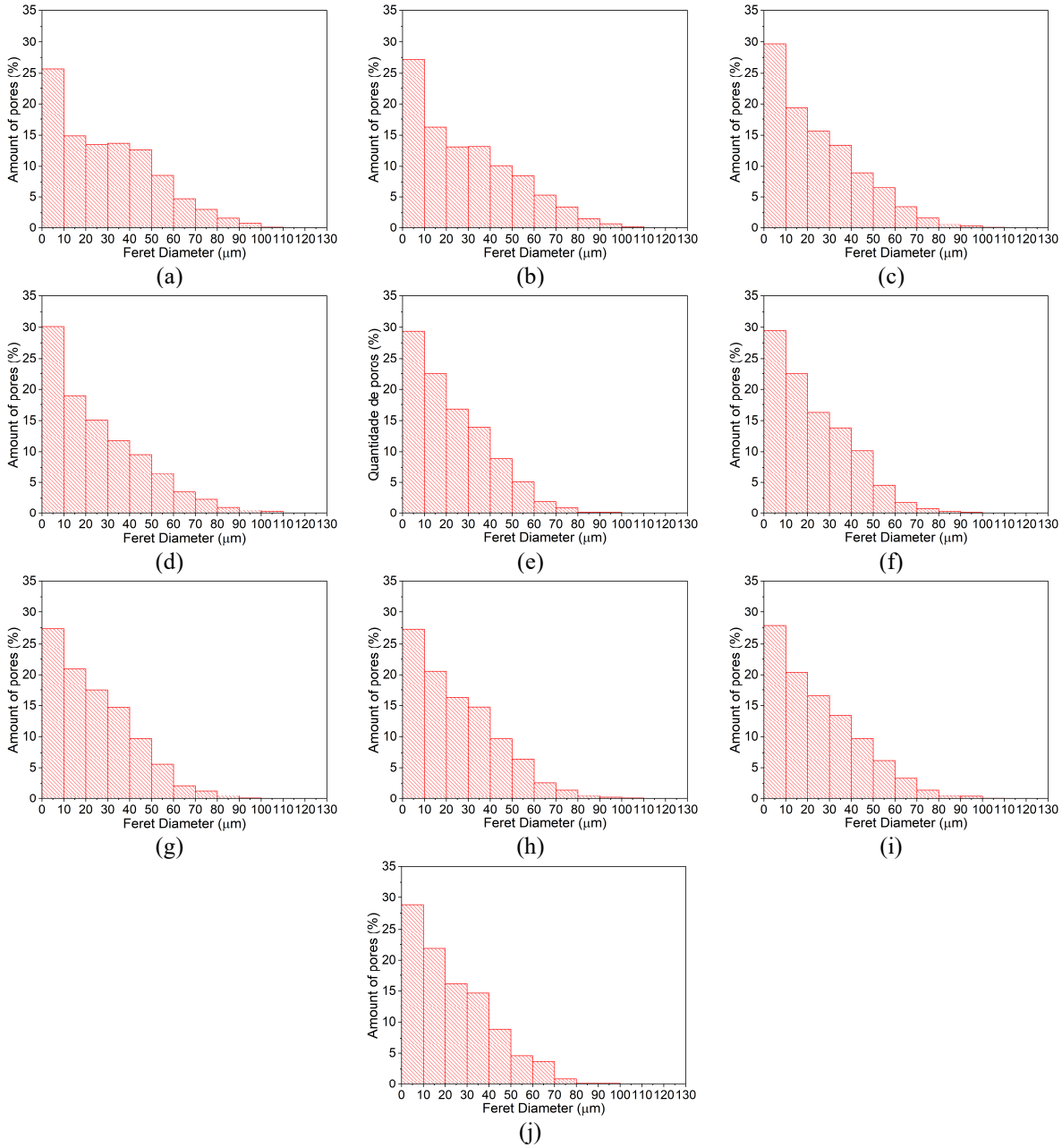

Source: Author

Figure 111: Histograms of Feret diameter for specimens compacted at 600 MPa and sintered at 1100 °C after de scuffing resistance tests (a) and after the 7 (b), 14 (c), 21 (d), 28 (e), 35 (f), 42N loads (g)

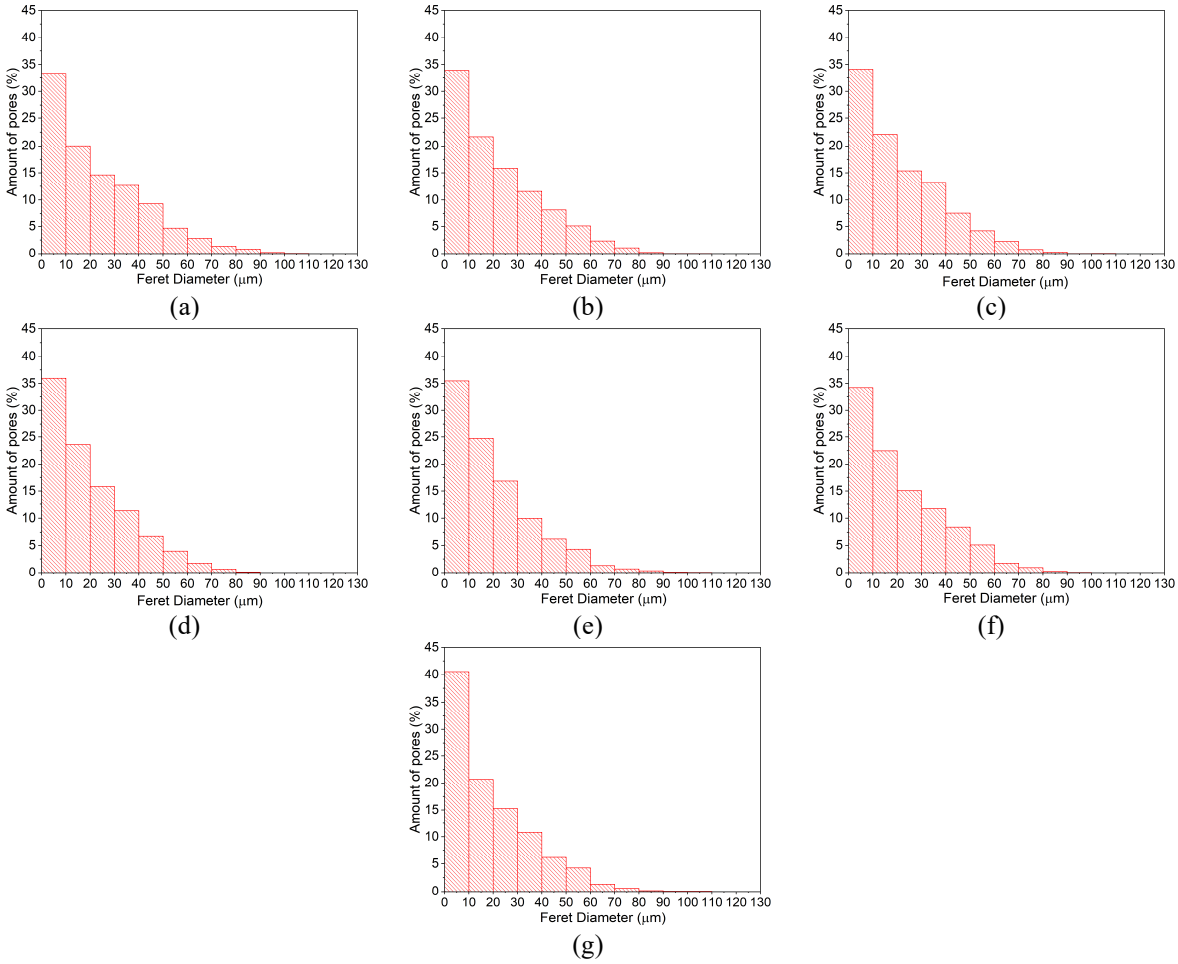

Source: Author

Figures 112 and 113 shows the plots for Δ Carbon Intensity as function of the size, circularity, solidity and eccentricity of pores from specimens compacted sintered at 1100°C and compacted at 200 and 600 MPa respectively. The amorphization diagram obtained from the wear tracks of samples sintered at 1100 °C and compacted at 200, 400 and 600 MPa is shown in figure 114.

Figure 112: Δ Carbon Intensity as a function of the size (a), circularity (b), solidity (c) and eccentricity (d) of pores from specimens compacted at 200 MPa and sintered at 1100°C

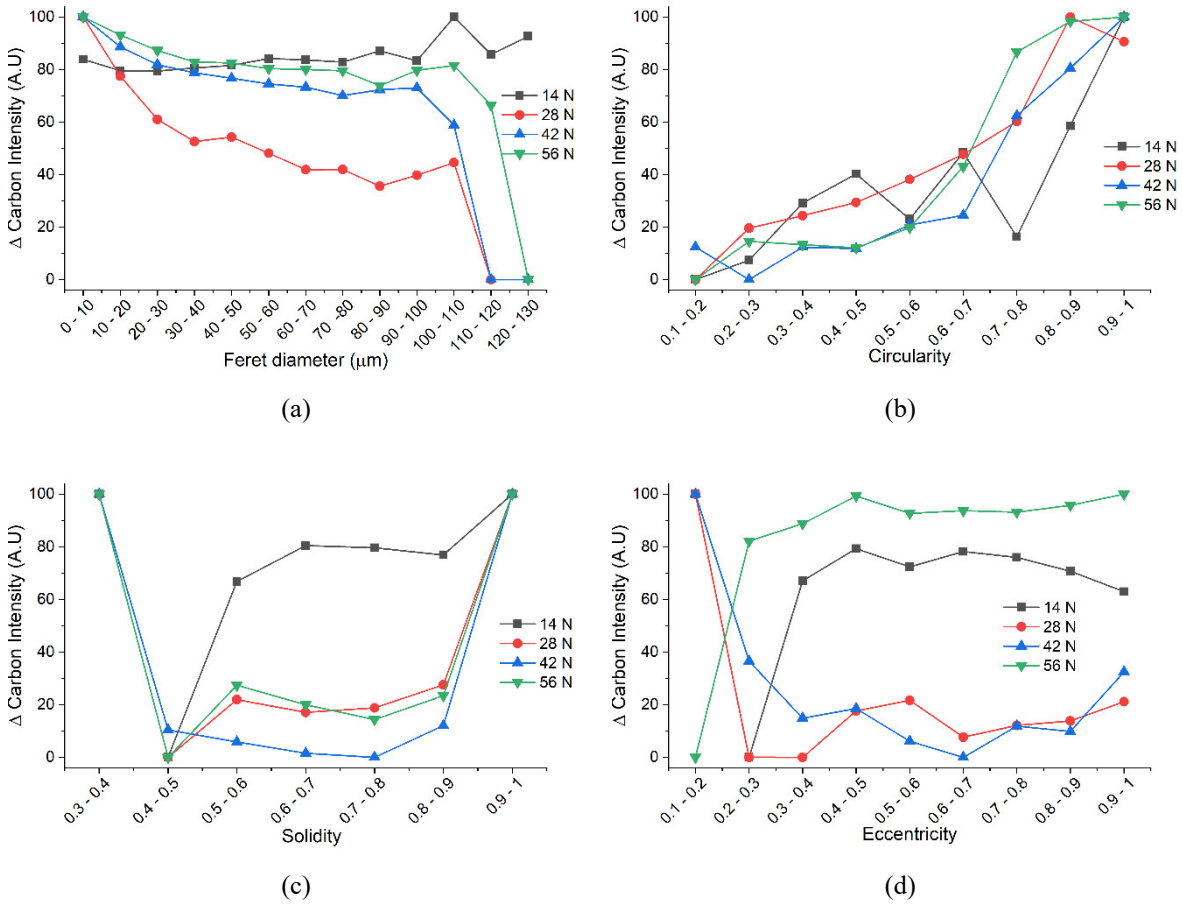

Source: Author

Figure 113: □ Carbon Intensity as a function of the size (a), circularity (b), solidity (c) and eccentricity (d) of pores from specimens compacted at 600 MPa and sintered at 1100°C

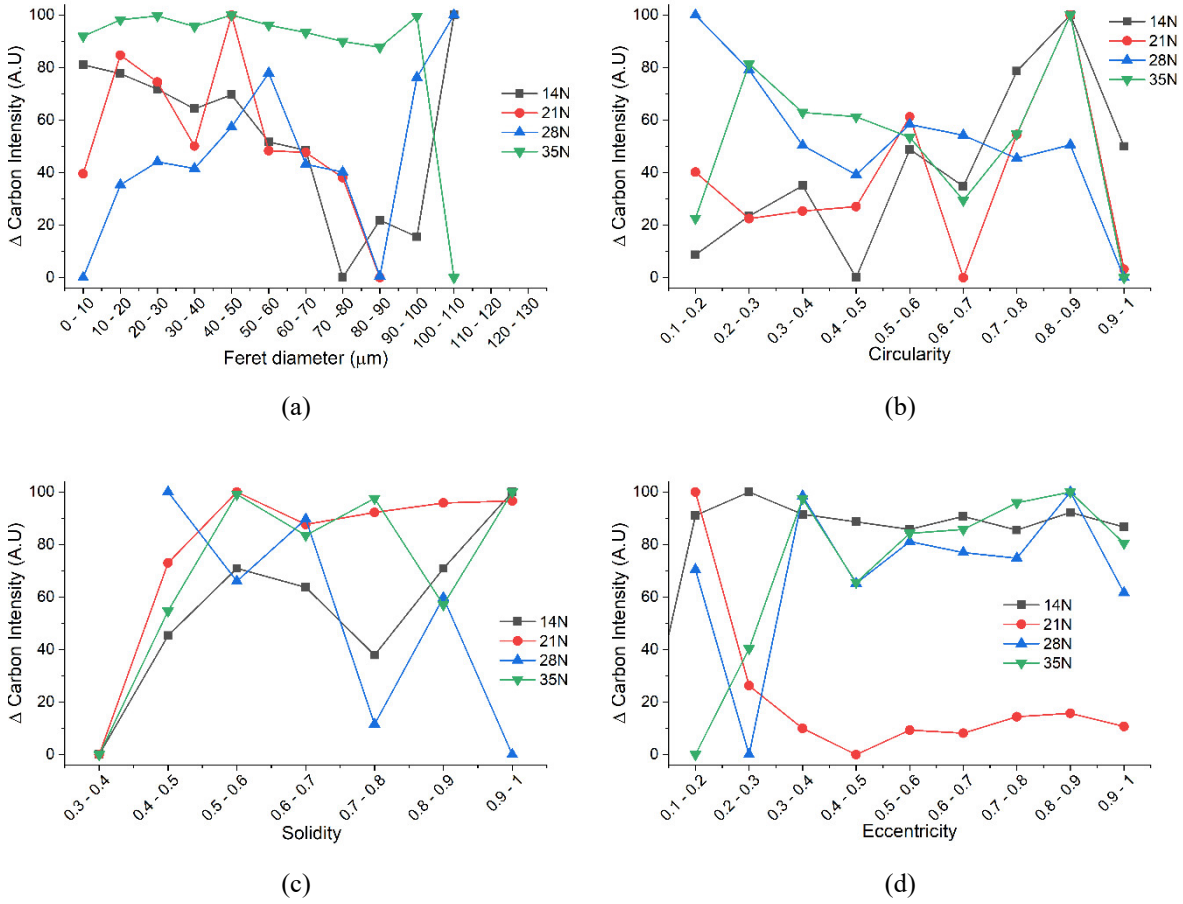

Source: Author

Figure 114: Raman amorphization diagram □ vs L_a of graphite by the action of the scuffing resistance test in specimens sintered at 1100 °C, the numbers above the symbols indicate the load where the tests were stopped.

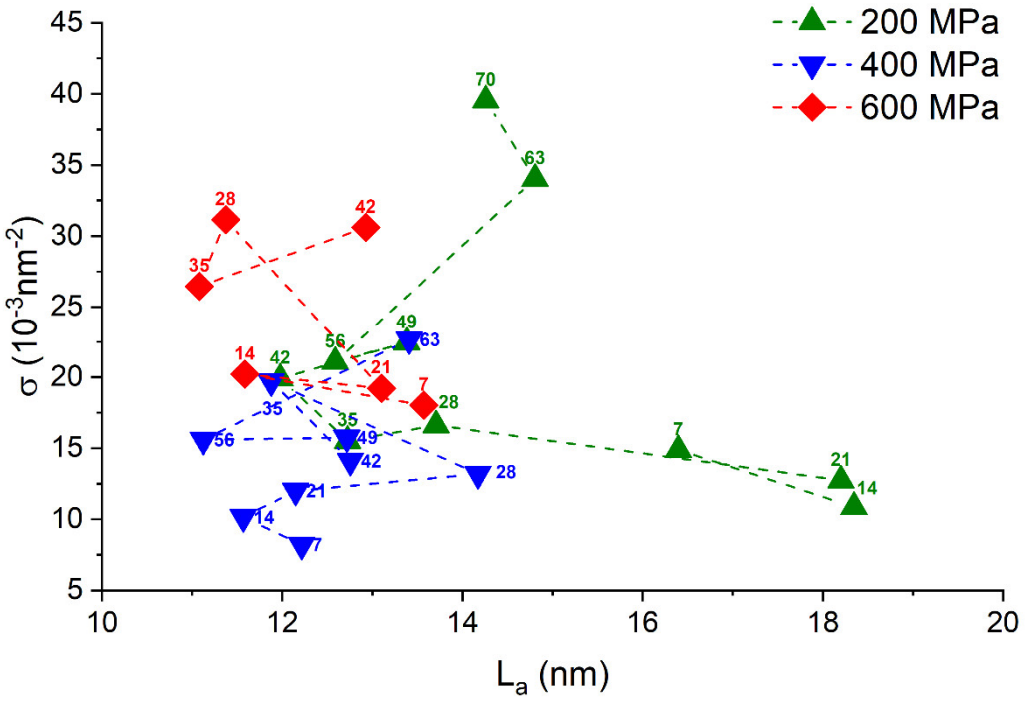

Source: Author